

ADVANCED STEEL CONSTRUCTION

An International Journal

Volume 12 Number 3

September 2016

CONTENTS

Technical Papers

Static Strength of Square Tubular Y-Joints with Reinforced Chord under Axial Compression
Y. Chen and Y.B. Shao

Eccentric Loading Behavior of L-Shaped Columns Composed of Concrete-Filled Steel Tubes
Ting Zhou, Minyang Xu, Zhihua Chen, Xiaodun Wang and
Yawen Wang

Advancement and Applications of Japanese High Performance Steel in Structural Engineering
Ping Xiang, Hanbin Ge and Liang-Jiu Jia

Static Behavior of Axially Compressed Circular Concrete Filled CFRP-Steel Tubular
(C-CF-CFRP-ST) Columns with Moderate Slenderness Ration
Q.L. Wang, S.E. Qu, Y.B. Shao and L.M. Feng

A Pseudo-Dynamic Test Study on a Self-Centering Prefabricated Steel Frame with
a Column Base Connected by Semi-Rigid Joints
Yanxia Zhang, Zongyang Wang, Wei Zhao, Wenzhan Zhao and Yuanyuan Chen

Analysis of Door-Type Modular Steel Scaffolds based on a Novel Numerical Method
Zhongwei Zhao and Zhihua Chen

Safety Assessment of Eurocode 3 Stability Design Rules for the Flexural Buckling of Columns
Luís Simões da Silva, Trayana Tankova, Liliana Marques and Carlos Rebelo

Announcement by IJASC :
Announcement for ICSAS 2016
Announcement for ICTWS'18

Copyright © 2016 by :
The Hong Kong Institute of Steel Construction
Website: <http://www.hkisc.org>
ISSN 1816-112X
Science Citation Index Expanded, Materials Science Citation Index and ISI Alerting

Cover: 1000ton+ temporary steel platform in support of heavy-duty mobile cranes, designed by second-order direct analysis
without effective length

e-copy of IJASC is free to download at "www.ascjournal.com" in internet and mobile apps.

ADVANCED STEEL CONSTRUCTION

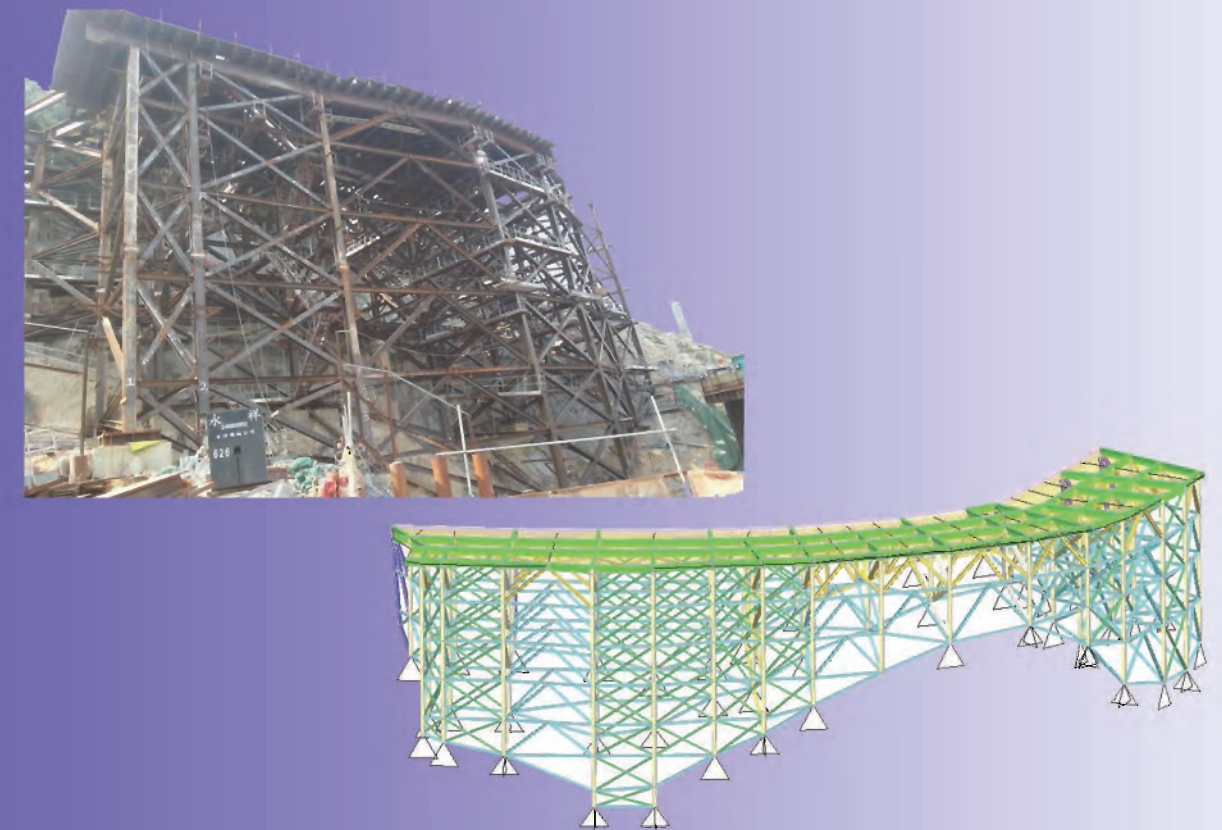
ADVANCED STEEL CONSTRUCTION

an International Journal

ISSN 1816-112X

Volume 12 Number 3

September 2016



Editors-in-Chief

S.L. Chan, The Hong Kong Polytechnic University, Hong Kong

W.F. Chen, University of Hawaii at Manoa, USA

R. Zandonini, Trento University, Italy

VOL.12, NO.3 (2016)

ISSN 1816-112X

Science Citation Index Expanded,
Materials Science Citation Index
and ISI Alerting

EDITORS-IN-CHIEF

Asian Pacific, African and organizing Editor

S.L. Chan
*The Hong Kong Polyt. Univ.,
Hong Kong*

American Editor

W.F. Chen
Univ. of Hawaii at Manoa, USA

European Editor

R. Zandonini
Trento Univ., Italy

INTERNATIONAL EDITORIAL BOARD

F.G. Albermani
The Univ. of Queensland, Australia

I. Burgess
Univ. of Sheffield, UK

F.S.K. Bijlaard
Delft Univ. of Technology, The Netherlands

R. Bjorhovde
The Bjorhovde Group, USA

M.A. Bradford
The Univ. of New South Wales, Australia

D. Camotim
Technical Univ. of Lisbon, Portugal

C.M. Chan
Hong Kong Univ. of Science & Technology, Hong Kong

T.H.T. Chan
Queensland Univ. of Technology, Australia

T.M. Chan
The Hong Kong Polyt. Univ., Hong Kong

S.P. Chiew
Singapore Institute of Technology, Singapore

W.K. Chow
The Hong Kong Polyt. Univ., Hong Kong

G.G. Deierlein
Stanford Univ., California, USA

L. Dezi
Univ. of Ancona, Italy

D. Dubina
The Politehnica Univ. of Timisoara, Romania

L. Gardner
Imperial College of Science, Technology and Medicine, UK

R. Greiner
Technical Univ. of Graz, Austria

Y. Goto
Nagoya Institute of Technology

L.H. Han
Tsinghua Univ. China

S. Herion
University of Karlsruhe, Germany

G.W.M. Ho
Ove Arup & Partners Hong Kong Ltd., Hong Kong

B.A. Izzuddin
*Imperial College of Science, Technology and
Medicine, UK*

J.P. Jaspart
Univ. of Liege, Belgium

S. A. Jayachandran
IIT Madras, Chennai, India

S.E. Kim
Sejong Univ., South Korea

S. Kitipornchai
The Univ., of Queensland, Australia

D. Lam
Univ. of Bradford, UK

G.Q. Li
Tongji Univ., China

J.Y.R. Liew
National Univ. of Singapore, Singapore

Y.P. Liu
The Hong Kong Polyt. Univ., Hong Kong

S.W. Liu
NIDA EUROPE Ltd., UK

E.M. Lui
Syracuse Univ., USA

Y.L. Mo
Univ. of Houston, USA

J.P. Muzeau
CUST, Clermont Ferrand, France

D.A. Nethercot
*Imperial College of Science, Technology and
Medicine, UK*

Y.Q. Ni
The Hong Kong Polyt. Univ., Hong Kong

D.J. Oehlers
The Univ. of Adelaide, Australia

J.L. Peng
Yunlin Uni. of Science & Technology, Taiwan

K. Rasmussen
The Univ. of Sydney, Australia

J.M. Rotter
The Univ. of Edinburgh, UK

C. Scawthorn
Scawthorn Porter Associates, USA

P. Schaumann
Univ. of Hannover, Germany

Y.J. Shi
Tsinghua Univ., China

G.P. Shu
Southeast Univ. China

L. Simões da Silva
*Department of Civil Engineering, University of
Coimbra, Portugal*

J.G. Teng
The Hong Kong Polyt. Univ., Hong Kong

G.S. Tong
Zhejiang Univ., China

K.C. Tsai
National Taiwan Univ., Taiwan

C.M. Uang
Univ. of California, USA

B. Uy
The University of New South Wales, Australia

M. Veljkovic
Univ. of Lulea, Sweden

F. Wald
Czech Technical Univ. in Prague, Czech

Y.C. Wang
The Univ. of Manchester, UK

Y.L. Xu
The Hong Kong Polyt. Univ., Hong Kong

D. White
Georgia Institute of Technology, USA

E. Yamaguchi
Kyushu Institute of Technology, Japan

Y.B. Yang
National Taiwan Univ., Taiwan

Y.Y. Yang
China Academy of Building Research, Beijing, China

B. Young
The Univ. of Hong Kong, Hong Kong

X.L. Zhao
Monash Univ., Australia

X.H. Zhou
Chongqing University, China

Z.H. Zhou
Alpha Consultant Ltd., Hong Kong

R.D. Ziemian
Bucknell University, USA

*Cover: 1000ton+ temporary steel platform in support of heavy-duty mobile cranes, designed by second-order direct analysis
without effective length*

e-copy of IJASC is free to download at "www.ascjournal.com" in internet and mobile apps.

General Information

Advanced Steel Construction, an international journal

Aims and scope

The International Journal of Advanced Steel Construction provides a platform for the publication and rapid dissemination of original and up-to-date research and technological developments in steel construction, design and analysis. Scope of research papers published in this journal includes but is not limited to theoretical and experimental research on elements, assemblages, systems, material, design philosophy and codification, standards, fabrication, projects of innovative nature and computer techniques. The journal is specifically tailored to channel the exchange of technological know-how between researchers and practitioners. Contributions from all aspects related to the recent developments of advanced steel construction are welcome.

Instructions to authors

Submission of the manuscript. Authors may submit on-line at www.hkisc.org

Asian Pacific, African and organizing editor : Professor S.L. Chan, Email: ceslchan@polyu.edu.hk

American editor : Professor W.F. Chen, Email: waifah@hawaii.edu

European editor : Professor R. Zandonini, Email: riccardo_zandonini@ing.unitn.it

All manuscripts submitted to the journal are recommended to accompany with a list of four potential reviewers suggested by the author(s). This list should include the complete name, address, telephone and fax numbers, email address, and at least five keywords that identify the expertise of each reviewer. This scheme will improve the process of review.

Style of manuscript

General. Author(s) should provide full postal and email addresses and fax number for correspondence. The manuscript including abstract, keywords, references, figures and tables should be in English with pages numbered and typed with double line spacing on single side of A4 or letter-sized paper. The front page of the article should contain:

- a) a short title (reflecting the content of the paper);
- b) all the name(s) and postal and email addresses of author(s) specifying the author to whom correspondence and proofs should be sent;
- c) an abstract of 100-200 words; and
- d) 5 to 8 keywords.

The paper must contain an introduction and a conclusion. The length of paper should not exceed 25 journal pages (approximately 15,000 words equivalents).

Tables and figures. Tables and figures including photographs should be typed, numbered consecutively in Arabic numerals and with short titles. They should be referred in the text as Figure 1, Table 2, etc. Originally drawn figures and photographs should be provided in a form suitable for photographic reproduction and reduction in the journal.

Mathematical expressions and units. The Systeme Internationale (SI) should be followed whenever possible. The numbers identifying the displayed mathematical expression should be referred to in the text as Eq. 1, Eq. 2.

References. References to published literature should be referred in the text, in the order of citation with Arabic numerals, by the last name(s) of the author(s) (e.g. Zandonini and Zanon [3]) or if more than three authors (e.g. Zandonini et al. [4]). References should be in English with occasional allowance of 1-2 exceptional references in local languages and reflect the current state-of-technology. Journal titles should be abbreviated in the style of the Word List of Scientific Periodicals. References should be cited in the following style [1, 2, 3].

Journal: [1] Chen, W.F. and Kishi, N., "Semi-rigid Steel Beam-to-column Connections, Data Base and Modelling", Journal of Structural Engineering, ASCE, 1989, Vol. 115, No. 1, pp. 105-119.

Book: [2] Chan, S.L. and Chui, P.P.T., "Non-linear Static and Cyclic Analysis of Semi-rigid Steel Frames", Elsevier Science, 2000.

Proceedings: [3] Zandonini, R. and Zanon, P., "Experimental Analysis of Steel Beams with Semi-rigid Joints", Proceedings of International Conference on Advances in Steel Structures, Hong Kong, 1996, Vol. 1, pp. 356-364.

Proofs. Proof will be sent to the corresponding author to correct any typesetting errors. Alternations to the original manuscript at this stage will not be accepted. Proofs should be returned within 48 hours of receipt on-line.

Copyright. Submission of an article to "Advanced Steel Construction" implies that it presents the original and unpublished work, and not under consideration for publication nor published elsewhere. On acceptance of a manuscript submitted, the copyright thereof is transferred to the publisher by the Transfer of Copyright Agreement and upon the acceptance of publication for the papers, the corresponding author must sign the form for Transfer of Copyright.

Permission. Quoting from this journal is granted provided that the customary acknowledgement is given to the source.

Page charge and Reprints. There will be no page charges if the length of paper is within the limit of 25 journal pages. A total of 30 free offprints will be supplied free of charge to the corresponding author. Purchasing orders for additional offprints can be made on order forms which will be sent to the authors. These instructions can be obtained at the Hong Kong Institute of Steel Construction,

Journal website: <http://www.hkisc.org>

The International Journal of Advanced Steel Construction is published quarterly by learnt society, The Hong Kong Institute of Steel Construction, c/o Department of Civil & Environmental Engineering, The Hong Kong Polytechnic University, Hung Hom, Kowloon, Hong Kong.

Disclaimer. No responsibility is assumed for any injury and / or damage to persons or property as a matter of products liability, negligence or otherwise, or from any use or operation of any methods, products, instructions or ideas contained in the material herein.

Subscription inquiries and change of address. Address all subscription inquiries and correspondence to Member Records, IJASC. Notify an address change as soon as possible. All communications should include both old and new addresses with zip codes and be accompanied by a mailing label from a recent issue. Allow six weeks for all changes to become effective.

The Hong Kong Institute of Steel Construction

HKISC

c/o Department of Civil and Environmental Engineering,

The Hong Kong Polytechnic University,

Hunghom, Kowloon, Hong Kong, China.

Tel: 852- 2766 6047 Fax: 852- 2334 6389

Email: ceslchan@polyu.edu.hk Website: <http://www.hkisc.org/>

ISSN 1816-112X

Science Citation Index Expanded, Materials Science Citation Index and ISI Alerting

Copyright © 2016 by:

The Hong Kong Institute of Steel Construction.



ISSN 1816-112X

Science Citation Index Expanded,
Materials Science Citation Index and
ISI Alerting

EDITORS-IN-CHIEF

Asian Pacific, African and organizing Editor

S.L. Chan

*The Hong Kong Polytech Univ.,
Hong Kong*

Email: ceslchan@polyu.edu.hk

American Editor

W.F. Chen

Univ. of Hawaii at Manoa, USA

Email: waifah@hawaii.edu

European Editor

R. Zandonini

Trento Univ., Italy

Email: riccardo.zandonini@ing.unitn.it

Advanced Steel Construction

an international journal

VOLUME 12 NUMBER 3

SEPTEMBER 2016

Technical Papers

Static Strength of Square Tubular Y-Joints with Reinforced Chord under Axial Compression 211

Y. Chen and Y.B. Shao

Eccentric Loading Behavior of L-Shaped Columns Composed of Concrete-Filled Steel Tubes 227

Ting Zhou, Minyang Xu, Zhihua Chen, Xiaodun Wang and Yawen Wang

Advancement and Applications of Japanese High Performance Steel in Structural Engineering 245

Ping Xiang, Hanbin Ge and Liang-Jiu Jia

Static Behavior of Axially Compressed Circular Concrete Filled CFRP-Steel Tubular (C-CF-CFRP-ST) Columns with Moderate Slenderness Ratio 263

Q.L. Wang, S.E. Qu, Y.B. Shao and L.M. Feng

A Pseudo-Dynamic Test Study on a Self-Centering Prefabricated Steel Frame with a Column Base Connected by Semi-Rigid Joints 296

Yanxia Zhang, Zongyang Wang, Wei Zhao, Wenzhan Zhao and Yuanyuan Chen

Analysis of Door-Type Modular Steel Scaffolds based on a Novel Numerical Method 316

Zhongwei Zhao and Zhihua Chen

Safety Assessment of Eurocode 3 Stability Design Rules for the Flexural Buckling of Columns 328

Luís Simões da Silva, Trayana Tankova, Liliana Marques and Carlos Rebelo

Announcement by IJASC :

Announcement for ICSAS 2016

Announcement for ICTWS'18

STATIC STRENGTH OF SQUARE TUBULAR Y-JOINTS WITH REINFORCED CHORD UNDER AXIAL COMPRESSION

Y. Chen ¹ and Y.B. Shao ^{2,*}

¹Graduate student, China Ministry of Education Key Laboratory of Building Safety and Energy Efficiency, College of Civil Engineering, Hunan University, Changsha, China

²Professor, School of Mechatronic Engineering, Southwest Petroleum University, Chengdu, China
*(Corresponding author: E-mail: cybshao2009@hotmail.com)

Received: 26 June 2012; Revised: 9 September 2012; Accepted: 9 October 2012

ABSTRACT: Chord reinforcement is an available alternative to improve the static strength of the welded square tubular joints. Four full-scaled square tubular Y-joints are studied experimentally to investigate the effect of local chord reinforcement on their static strength. From experimental results, it is found that the static strength of a square tubular Y-joint can be improved greatly by increasing the chord thickness locally near the brace/chord intersection. The failure mode of an un-reinforced Y-joint can be changed from local yielding around the brace/chord intersection to flexural yielding of the chord member when the local chord thickness is increased to a critical value. In addition, finite element (FE) models for analyzing the static behavior of square tubular Y-joints are also presented, and the accuracy and reliability of these models have been evaluated by comparing the FE results with experimental results. Finally, influence of some parameters (L/d , β , γ and T_c/t_o) on the static strength of square tubular Y-joints with local chord reinforcement is studied, and a parametric equation for predicting the static strength of square tubular Y-joints with local chord reinforcement under axial compression is presented. The accuracy of the presented equation is verified through error analysis.

Keywords: Square tubular T-joints, chord reinforcement, finite element, static strength, parametric equation

DOI:10.18057/IJASC.2016.12.3.1

1. INTRODUCTION

The static strength of welded steel tubular joints is of considerable importance, both in the design stage and during servicing time. One of the primary design concerns for steel tubular structures is the static strength of the connection between different tubular members (namely tubular joint). As high stress concentration exists at the weld toe, failure generally occurs on the chord surface around the weld. For a tubular joint, the brace members are mainly subjected to axial loads, and thus the chord is frequently subjected to the load in its radial direction. Due to the hollow section, the radial stiffness of the chord is much smaller than the axial stiffness of the brace. If the static strength of a joint is found to be inadequate, various methods are available to reinforce it. The most commonly used reinforcements in tubular structures, such as doubler-plate, collar-plate, internally stiffened ring and infilled concrete, have been reported in the literature.

The fatigue behavior of internally ring-stiffened welded steel tubular joints was investigated by Gandhi et al. [1], who created an extensive database on internally ring-stiffened steel tubular joints, and experimental investigations on internally ring-stiffened steel tubular joints with different geometries were conducted under various loading conditions and environments. Van der Vegte et al. [2] studied the static strength of Y-joints reinforced with doubler- or collar-plates by using both numerical and experimental methods, and the numerically and experimentally determined load-ovalization curves reveal a very good correlation. The results show that a significant strength enhancement can be achieved through proportioning the doubler-plate. Lee and Llewelyn-Parry [3] conducted a detailed parametric study on the static strength of axially loaded tubular T-joints with internal ring-stiffeners, and they carried out nonlinear finite element analyses to evaluate the

accuracy and the validity of the numerical procedure through comparison with tested results in other literature. Nazari et al. [4] presented parametric equations for predicting the stress concentration factors (SCF) for tubular T-, Y-, K-, X-, and DT-joints reinforced with doubler-plate, and a sensitivity analysis is performed for describing the effect of joint types on the SCF stress concentration factors. The numerical study of doubler-plate stiffened CHS T- and X-joints subjected to in-plane bending was carried out by Choo et al. [5] to investigate the failure modes and the load transferring mechanisms of such joints with different sizes of doubler-plate, and the design recommendations were presented for the doubler-plate reinforced X-joints. The hysteretic behavior of circular tubular T-joint reinforced with collar-plate under quasi-static cyclic loading was studied experimentally by Shao et al. [6]. Through experimental observation, the failure position was found to be transferred from the weld toe along the brace/chord intersection to the corner of the collar-plate, and therefore the reinforced circular tubular T-joints can dissipate more energy and have better ductility. Gao et al. [7] carried out experimental study on concrete-filled steel tubular arches with corrugated steel webs. It was found that the infilled concrete can improve the local and global buckling of the steel tube, and the static strength of the joint is then increased efficiently.

As a novel and innovative reinforcing measure, local chord reinforcement is an alternative in improving the static strength of tubular joints. The significant effectiveness of this reinforcing method has been studied by Shao et al. [8]-[9]. This method remedies the defect that a doubler- or a collar-plate cannot be used for multi-planar tubular joints with several brace members connecting to the chord, and it does not influence the joint appearance. This reinforcing method has been applied in engineering practice such as Guangdong Science Center in China. However, it is still necessary to conduct further study on the reinforcing efficiency of this method for design purpose.

This study then aims to carry out detailed investigation to propose convenient yet accurate estimation on the static strength of a square tubular Y-joint with local chord reinforcement under axial compression. The overall research program involves both experimental tests and finite element (FE) studies. Through verifying the reliability of the FE model against the experiments described, an extensive parametric analysis is conducted, and finally a parametric equation is presented to be possibly used in practical design stage.

2. EXPERIMENTAL TEST

2.1 Specimen Details

Generally, a tubular joint is consisted of two or more hollow section tubes. The large through member is called chord, and the other branch members are called braces which are welded directly onto the chord surface. Figure 1 shows the fabrication of a square tubular Y-joint, in which the brace end is profiled firstly, and then it is welded onto the chord surface directly by using full penetration welds. Because welding process can produce uneven temperature distribution around the brace/chord intersection, it is carried out on-site after installation to avoid large residual deformation.



Figure 1. Fabrication of A Square Tubular Y-joint

The schematic arrangement of a square tubular Y-joint specimen is illustrated in Figure 2. The chord is strengthened near the brace/chord intersection by increasing the tube thickness locally, and the outer width of reinforced tube is same to that of the un-reinforced tube to keep the outer surface of the two tubes are coplanar. The locally reinforced segment is connected to the un-reinforced one by using butt weld in which a gradient of 1:2.5 is used to connect the different tube thicknesses. The reinforcing efficiency of this method can be controlled by varying the thickness T_c and the length L_c of the enhanced segment. The joint is considered not to be reinforced when $T_c=t_0$ and $L_c=L_0$. The geometries of all the specimens used in the experimental tests are summarized in Table 1. The specimens include two reinforced models and two corresponding un-reinforced ones. The reinforced square tubular Y-joints have same dimensions as the un-reinforced specimens except that the chord of the reinforced segment has a larger value of thickness and length. The chord and the brace of each square tubular Y-joint specimen are fabricated by seamed carbon steel pipe while the reinforced segment is obtained by welding four steel plates together. It is noted that the reinforced segment can be also fabricated by rolling a steel plate into a square tube when the thickness of the reinforced tube is not quite big and the fabrication is easily processed. However, four steel plates are suggested to be welded together when such thickness is quite big due to easy fabrication. When four steel plates are welded together to form a square tube, the welding side of each steel plate is also profiled to be a slope, and partial butt weld is used to connect two adjacent plates together. Both chord ends are welded onto a steel plate, and each plate is welded two ear plates pinned to the supports to produce hinged boundary conditions at the chord ends.

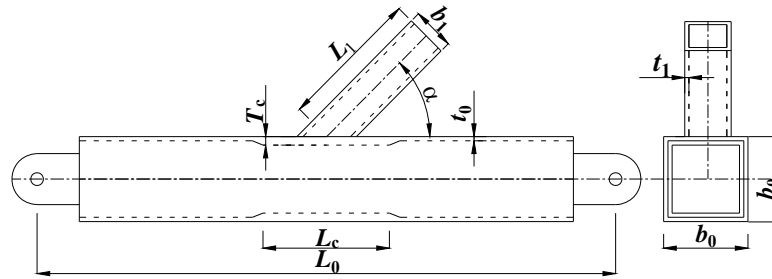


Figure 2. A Chord Reinforced Y-joint

Table 1. Geometry of Specimens

NO.	b_0 (mm)	b_1 (mm)	t_0 (mm)	t_1 (mm)	L_0 (mm)	L_1 (mm)	L_c (mm)	T_c (mm)	β	2γ	α ($^\circ$)
Ex-1	180	70	8	8	2437	467	—	—	0.389	22.5	50.5
Ex-2	180	70	8	8	2437	467	200	16	0.389	22.5	50.5
Ex-3	160	100	8	8	1959	550	—	—	0.625	20.0	74.5
Ex-4	160	100	8	8	1959	550	200	16	0.625	20.0	74.5

The specimens are made up of Q235 steel which is widely used in steel structures in China. A uni-axial tensile test is conducted to measure the mechanical properties of the steel materials, such as steel yield stress, tensile stress, elastic modulus and elongation percentage. The measured results are listed in Table 2. The coupons used in the uni-axial tensile tests are shown in Figure 3. The steel materials of the pipes used in the square tubular Y-joint specimens have good plasticity as shown in Figure 4, in which the experimentally measured stress-strain curves are plotted. The material properties of the reinforced segments are obtained from the manufacturers.

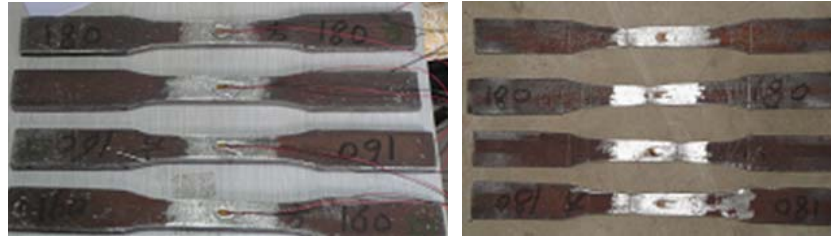


Figure 3. The Standard Coupon Test

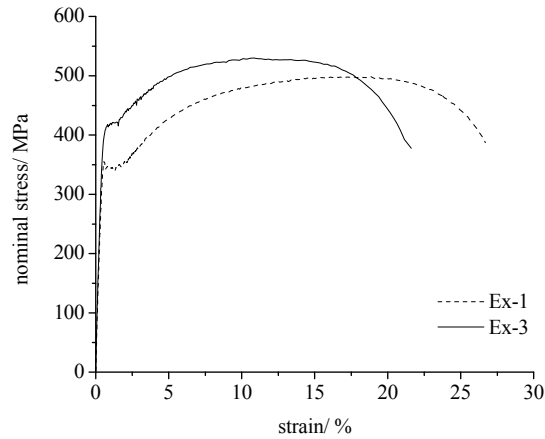


Figure 4. Stress-Strain Curves

Table 2. Material Properties

NO.	Yield stress (N/mm ²)	Ultimate stress (N/mm ²)	Elongation (%)
EX-1	340	499	26
EX-2	348	527	22
EX-3	415	529	22
EX-4	417	529	23
Reinforced segment	280	455	26

2.2 Test Setup

All experimental tests are conducted in a test rig as shown in Figure 5. The test rig has a maximum loading capacity of 500 kN, and the maximum magnitude of the axial displacement is ± 75 mm. The test rig has a special data acquisition system which can collect and export real-time applied load and the axial displacement at the brace end. During the experimental test, the specimens are pinned at both ends of the chord, and the load is applied at the brace end in axial direction.



Figure 5. Test Setup

During the tests on the un-reinforced specimens, LVDTs are placed on both the upper and lower surface of the chord at the brace/chord intersection, as shown in Figure 6(a), to measure the deformation of the chord in transverse direction. However, for the reinforced specimens, LVDTs are placed on a location near the chord intersection which is the maximum deformation position and is estimated from finite element analysis, as shown in Figure 6(b).

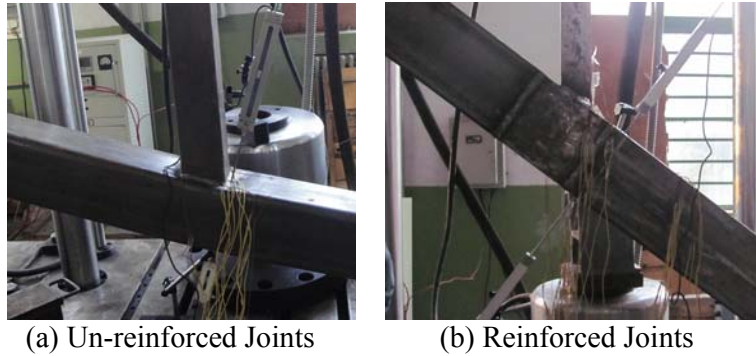


Figure 6. Arrangement of LVDTs

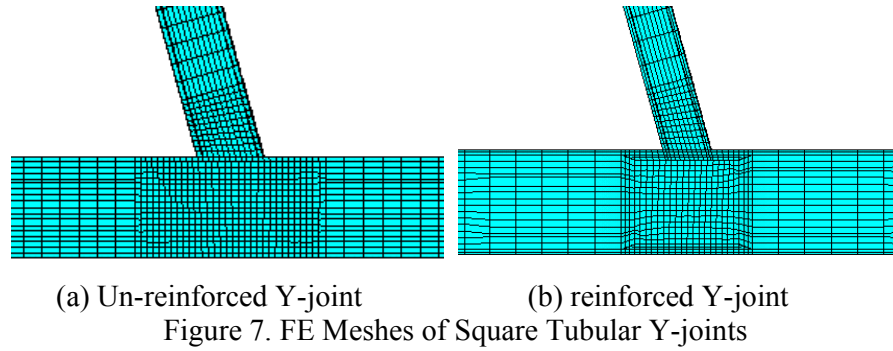
2.3 Loading Scheme

In the elastic stage, loading is controlled gradually at a speed of 10kN/min. The loading control is changed to displacement control at a speed of 0.5mm/min when a critical point in the load-displacement curve initiates and nonlinear stage begins. Displacement control is used in this stage because a large deformation may occur even though only a small loading increment is applied. During the tests, the applied loads and the axial displacement at the brace end can be both recorded automatically from the data acquisition system. The deformation of the joint can be measured from the LVDTs.

3. FINITE ELEMENT ANALYSIS

3.1 Finite Element Modeling

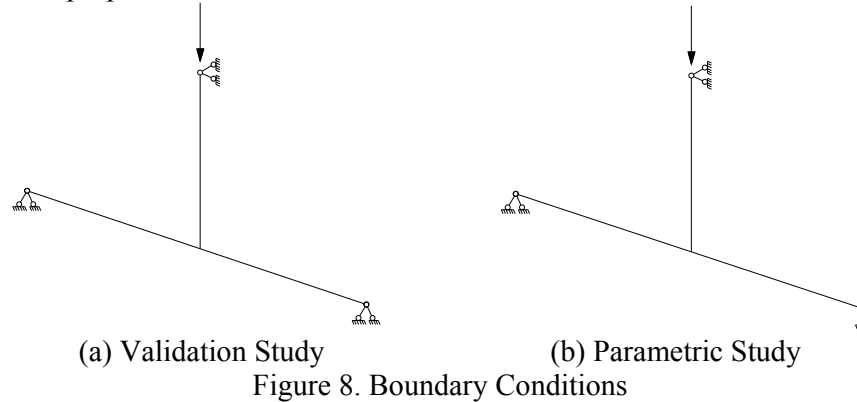
The numerical study is carried out from non-linear finite element analysis by using software ANSYS. 20-node hexahedral element is used to model the entire structure. In the vicinity of the brace/chord intersection, a refined mesh is used to simulate a high stress gradient, and a relatively coarse mesh is used in the regions far away from the intersection to save computing time. Although residual stress exists at the weld of the brace/chord intersection, the distribution of the residual stress along the weld is very complicated because it is affected by welding sequence, welding method, techniques of welders and so on. It is difficult to put all the situations into consideration. Fortunately, previous study shows the ignorance of the weld in analyzing the static strength of a tubular joint can still produce accurate enough results. In addition, omission of the weld produces underestimation for the radial stiffness of the chord, and thus the calculated result of the static strength is conservative. Based on these considerations, Weld is not considered in the FE model. Figure 7 shows the detailed FE mesh of both an un-reinforced square tubular Y-joint and a chord reinforced one.



3.2 Boundary Conditions and Material Properties

In the FE models, loading is applied to the center of the steel plate at the brace end. To simulate an actual boundary condition in the experimental tests, pins are set to be at both ends of the chord, as shown in Figure 8(a). However, one end is released to be a roller in following parametric study, as shown in Figure 8(b). Pin-roller constraints are set to the chord ends to avoid axial tensile stresses in the chord because such stresses can increase the static strength of the Y-joint. This treatment is safe and reasonable for estimating the static strength of a tubular joint since it is impossible to acquire accurate information on the exact level of the axial stress in the chord.

In the following parametric study, the steel material has a yielding stress of 235 N/mm^2 and a Poisson's ratio of 0.3. However, the experimental results are obtained based on the experimentally measured material properties as listed in Table 2.



3.3 Convergence and Validation Studies

Although the FE model can be benchmarked from experimental results, it must be evaluated from convergence study firstly. The convergence study is conducted by comparing the results obtained from FE models with different mesh densities because the FE results will converge to a fixed value if the mesh density is high enough. In the convergence study, two tested Y-joint specimens, including an un-stiffened one and a stiffened one, are analyzed with various mesh layouts and densities. The details are tabulated in Table 3 and Table 4.

As seen from Table 3, the ultimate load of the un-reinforced model or the reinforced model tends to be a fixed value when the mesh density increases gradually in the FE analyses. The results are more accurate with the increase of the mesh density. The results in Table 4 show that there is only a difference of 2% in the ultimate load between models EX-4-3 and EX-4-1, even though the mesh density of EX-4-3 is 9.5 times greater than that of EX-4-1. It indicates that accurate result can be

obtained by using the mesh density of EX-4-1 or EX-4-2. As a result, an approximate element size in the regions around the brace/chord intersection and around the chord/chord intersection can be determined to guarantee the convergence of the FE results.

Table 3. Convergence Study for Un-stiffened Joint EX-3

Mesh reference	Number of elements	Ultimate load (kN)
EX-3-1	2283	251.82
EX-3-2	3745	245.59
EX-3-3	4805	242.83
EX-3-4	6781	239.17
EX-3-5	8594	237.20

Table 4. Convergence Study for Stiffened Joint EX-4

Mesh reference	Number of elements in reinforced chord	Ultimate load (kN)
EX-4-1	616	291.01
EX-4-2	916	289.65
EX-4-3	5939	284.13

After the cost-effective mesh layout is determined, numerical models of two further joints are analyzed to validate the FE procedure. The results of the validation study are shown in Table 5. The definitions of the static strength of the joints are classified into three types: the maximum axial force at the brace end, the axial force at the brace end with a defined deformation limit and the axial force at the brace end obtained from the twice-elastic-slope (TES) method [10]. Figure 9 shows the definition on the TES. The above three definitions on the static strength are dependent on the load-displacement/deformation curves. When there is a clear loading drop after the linear stage in the load-displacement curve, the peak load is taken as the static strength of the joint. However, the peak load cannot be located from the load-displacement/ deformation curve if there is no loading drop in the curve. In this case, the second (deformation limit) or the third definition (TES) will be used to locate the static strength of the joint.

The difference between the deformation limit and the TES is determined from the local deformation of the chord around the brace/chord intersection. For example, there is clear local deformation in this position for the un-reinforced square tubular Y-joint because the transverse stiffness of the chord is smaller than the axial stiffness of the brace. For a square tubular Y-joint with $0.6 \leq \beta \leq 0.8$, the load at a joint deformation of $3\%b_0$ is defined as the static strength of this joint (Zhao [11]), and it is easily obtained from the load-deformation curve. It is different for the Y-joint with local chord reinforcement because the joint deformation may be much smaller. Due to the increased chord thickness around the brace/chord intersection, the transverse stiffness of the chord in this region is improved greatly. TES method is then used for this situation. In Figure 9, the static strength of a tubular joint is determined from a point with an angle φ in the load-displacement curve. The value of φ is determined from the following relationship: $\tan \varphi = 2 \tan \theta$. As the tested results of all specimens benefit the TES method, they are obtained based on this method.

Table 5. Validation Study

Model	Ultimate load (kN)		
	Test	FE	Test/FE
EX-1	171.75	160.27	1.07
EX-2	289.44	280.05	1.03
EX-3	230.01	228.64	1.01
EX-4	261.26	282.60	0.92

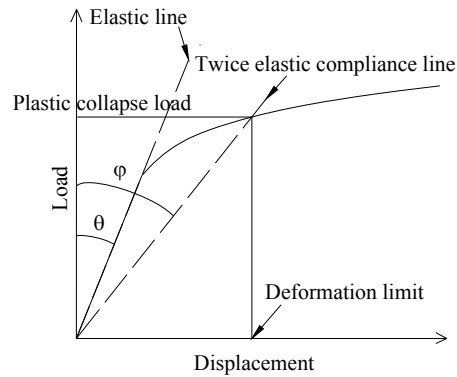


Figure 9. Twice-elastic-slope (TES) Method

According to the above three definitions, the static strength of the analyzed models in Table 5 can be obtained both from experimental tests and from FE analyses. Table 5 shows the comparison between the two results. The agreement shows reasonably well as the maximum relative error is only 8%. To evaluate the accuracy of the FE model in more details, the load-displacement curves of the un-stiffened Y-joints and the Y-joints stiffened with chord reinforcement obtained from both FE analyses and experimental measurements are plotted together in Figure 10.

It is found that the FE and the experimental results of the stiffness in the linear stage of the load-displacement curves are some different. However, the results of the static strength between the two methods are much closer. The stiffness in the linear stage obtained from the FE analyses is always bigger than that obtained from experimental measurements. Such difference is caused by the actual pinned constraints at the ends of the chord in experimental tests. To simulate a pinned constraint, the chord is hinged at both ends by inserting a pin into a drilled hole in the end plate. As the hole diameter is a little bigger than the diameter of the pin, there is a sliding shift between the hole and the pin. For the FE analyses, the pinned constraint at the chord end is only implemented by restricting the freedoms of a node of the end plate in three directions, and such modeling cannot reflect the actual sliding in experimental tests. Due to the above reason, the stiffness of the load-displacement curve in the linear stage of the experimental results is smaller. However, such difference does not affect the static strength significantly.

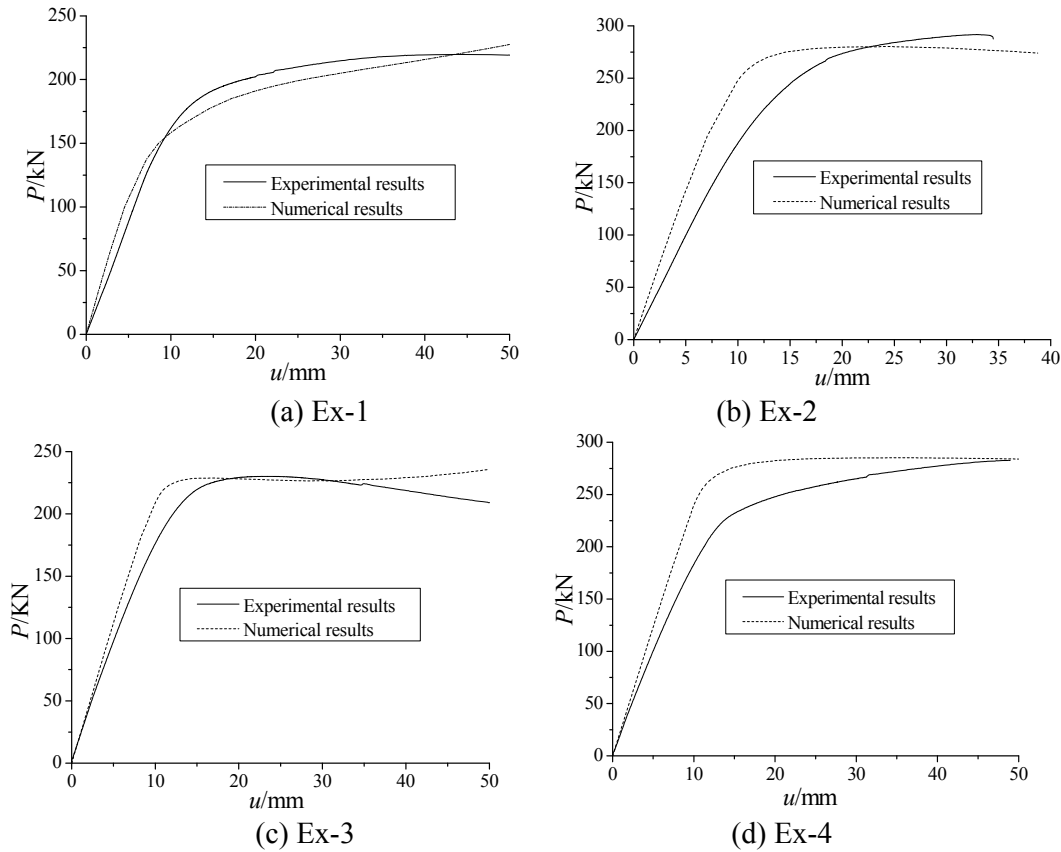


Figure 10. Load-Displacement Curves of the Y-joint Specimens

3.4 Failure Mode

The good correlation between the experimental and the numerical results can also be illustrated by the deformed shapes at failure as shown in Figure 11. The equivalent failure mode obtained from FE calculations indicates that the presented FE model can predict the final failure mode of both the un-reinforced and the reinforced tubular Y-joints reliably. From experimental tests and FE analyses, it can be found that the failure mode of a tubular Y-joint may be changed if suitable chord reinforcement is taken. When the local chord thickness near the brace/chord intersection is increased properly, the chord stiffness in transverse direction can be improved efficiently. As can be seen from Figures 11(a) and 11(c), there is clear concaved deformation around the weld toe for the un-reinforced Y-joint specimens, which indicates that the un-reinforced specimens fail due to local yielding. However, if the local radial stiffness of the chord near the weld is improved enough by increasing the local chord thickness, the failure location may move to the chord/chord intersection as shown in Figures 11(b) and 11(d). In this situation, the chord behaves much like a bending beam, and the final failure is caused by the flexural yielding on the top and on the bottom surfaces at the chord/chord intersection.

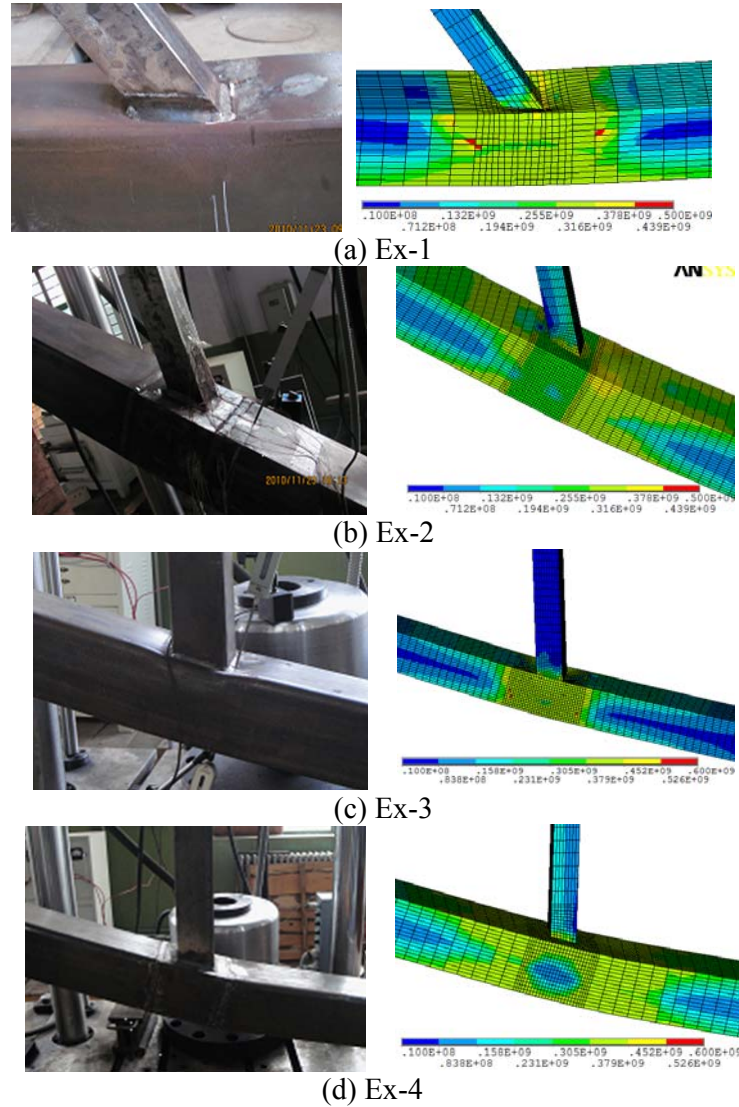


Figure 11. Failure Modes

4. PARAMETRIC STUDY

Although the static strength of a square tubular Y-joint can be improved efficiently by increasing the local chord thickness near the brace/chord intersection as mentioned previously, the reinforcing efficiency must be studied from a parametric investigation. The parameters considered in numerically parametric study include the following ones: (1) chord width to wall thickness ratio 2γ ; (2) brace to chord width ratio β ; (3) the reinforced to the un-reinforced chord thickness ratio T_c/t_0 ; (4) the intersecting angle α between the chord and the brace. Table 6 shows the detailed values of the above parameters in the FE analyses.

Table 6. Parameter Values

B	γ	α	T_c/t_0
0.4,0.6,0.8	6,8,10,12	30,45,60,75	1.25,1.5,1.75,2.0

In the parametric study, overall 102 square tubular Y-joint models with a validity range of the parameters tabulated in Table 6 are analyzed. Based on the FE results, the efficiency of the chord reinforcement is then investigated.

4.1 Effect of Chord Reinforced Length

From the parametric study, it has been found that the effect of L_c/b (b is the length of the brace intersected on the chord surface) on the reinforcing efficiency is much ineffective than the effect of T_c/t_0 as seen in Figure 12. Although Figure 12 only shows the effect of the chord reinforcement of a single typical Y-joint, it represents the general pattern. As L_c/b has little influence on the static strength of a square tubular Y-joint, it is not necessary to increase the reinforced chord length considerably in practical design. The applicable value of this parameter can be taken based on the consideration of easy construction, especially the effect of the welding process on the residual deformation. Due to this reason, the value of L_c/b is taken with $L_c/b = 2$ in parametric study.

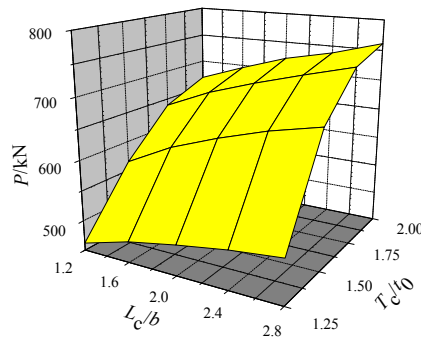


Figure 12. Efficiency of Chord Thickness Reinforcement

4.2 Effect of Other Parameters

From the results of the parametric study, the effects of the prescribed 4 parameters on the static strength of a chord reinforced square tubular Y-joint (P) under axial compression are obtained, and they are plotted in Figure 13. Some conclusions can be generalized based on the results in Figure 13 as follows: (1) It is significantly effective to improve the static strength of a square tubular Y-joint by increasing the local chord thickness. However, such effective improvement only exists when the T_c/t_0 is less than a critical value, i.e. $T_c/t_0 \leq 1.5$ for the models shown in Figure 13(a). Beyond this value, T_c/t_0 has a little influence. This phenomenon can be explained from the failure mechanism of the tubular Y-joint which will be introduced in the following section in details. (2) The effect of parameter β on the static strength of a square tubular Y-joint presents basically a linear relationship as illustrated in Figure 13(b). (3) The relationship between P and γ changes from nonlinearity into linearity with the increase of the reinforced chord thickness, which can be seen in Figure 13(c). (4) The effect of α on the static strength can be seen in Figure 13(d), which shows that P reduces greatly with the increase of α .

4.3 Failure Mechanism

Based on the parametric investigation, it can be found that a very small increment of the chord thickness near the brace/chord intersection can significantly improve the static strength of square tubular Y-joints when β is relatively small. As β represents the width ratio of the brace to the chord, a smaller value of β means the width of the brace is much smaller than the chord's width. Hence, the contact area of the brace/chord intersection is small in this situation. When the Y-joint is subjected to brace axial loading, such smaller contact area causes high stress around the intersection, and the joint then fails much easily. The typical failure mode of the un-reinforced

square tubular Y-joint is shown in Figure 14(a) and 14(c). The hollow section of the chord causes the chord stiffness in transverse direction to be much smaller than the brace stiffness in axial direction. As the chord has to sustain the load in transverse direction when the brace is subjected to axial loading, failure generally occurs on the chord surface around the weld toe. Definitely, increasing the local chord thickness near the weld toe can improve the chord stiffness in transverse direction significantly, especially when β has a small value.

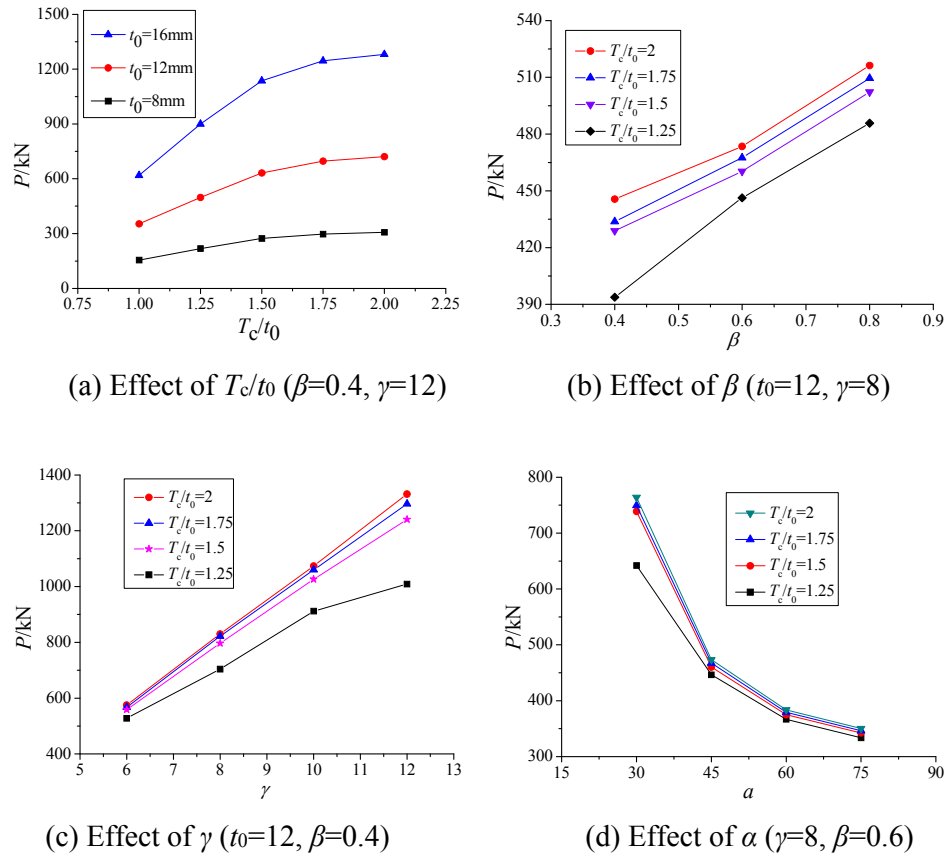


Figure 13. Effect of Parameters on Static Strength

Similarly, it is more effective to improve the static strength of a square tubular Y-joint when the value of γ is much bigger. γ is the ratio of the chord width to the chord thickness of the un-reinforced joint. A bigger value of γ means a thin-walled chord. When the chord thickness is small, the chord stiffness in transverse direction must be very weak, and the static strength of the joint is then very low. In overall, increasing the chord thickness locally near the weld toe is much effective when the chord thickness is much smaller.

The improvement of the static strength of a square tubular Y-joint can be explained in details by analyzing the failure mechanism of a reinforced model. As seen from Figure 14(b) and 14(d), the failure mechanism of a square tubular Y-joint with reinforcement is much different when the local chord thickness is increased to a certain value. If the local chord is reinforced enough, the chord stiffness in transverse direction can exceed the brace stiffness in axial direction. At this time, it is ineffective to improve the static strength by continuing to increase the local chord thickness, which is proved in Figure 13(a). Such ineffectiveness can be also explained from Figure 14(b) and 14(d). Due to the over-strengthening of the local chord near the brace/chord intersection, the reinforced chord has enough transverse stiffness, and then the failure location moves to the chord/chord intersection. In this case, the chord behaves much like a flexural beam, and failure of the joint now

is caused due to large flexural deformation. When the chord is hinged at both ends, the chord can be taken as a simply supported beam. The failure mechanism of the square tubular Y-joint is now explained as chord flexural failure.

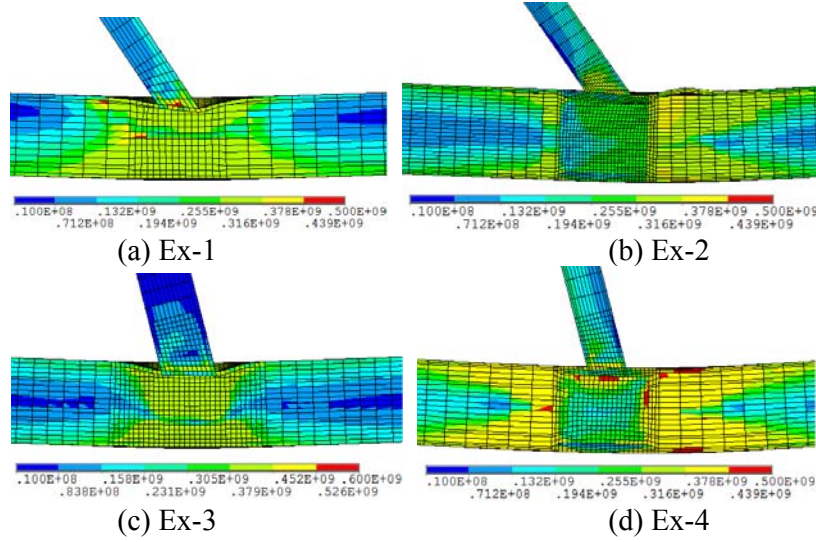


Figure 14. Deformed Shapes of Both Stiffened and Un-stiffened Y-joint Models

5. PARAMETRIC EQUATION FOR PREDICTING STATIC STRENGTHS OF A Y-JOINT

Based on the above parametric study, a parametric equation for predicting the static strength of a square tubular Y-joint under axial compression (P_c) is proposed. The equation is developed by examining the influence of the different sizes of reinforcement and various geometric parameters. Curve fitting technique and regression analysis are used to obtain the following parametric equation

$$P_c = \left\{ 0.021\beta_c\gamma_c \left(\alpha^{0.051} + 0.174 \right) \left[1 - (T_c/t_0)^{-1.907} \right] + 1 \right\} P_0 \quad (1)$$

where P_0 is the static strength of the un-reinforced square tubular Y-joint, which can be found in many design guidelines such as CIDECT [12]. The unit of the intersecting angle α is in radian. Other geometric parameters in Eq. (1) are listed as follows:

$$\beta_c = 0.171 - 0.134\beta \quad (2)$$

$$\gamma_c = \gamma^{2.51} + 42.18 \quad (3)$$

It is specified here that the value of T_c/t_0 is taken to be 1.5 when such value is greater than 1.5 in Eq. (1), which can be found from Fig. 13(a) that the reinforcing efficiency is very minor when T_c/t_0 is greater than 1.5.

To verify the accuracy of Eq. (1), a comparison between the predicted results and the FE results is conducted, and the evaluation can be given from Figure 15. P_f and P_c are the results of FE simulation and the equation's prediction respectively. From the comparison, the FE results have reasonable agreement with the predicted results, which implies that Eq. (1) has good accuracy and reliability.

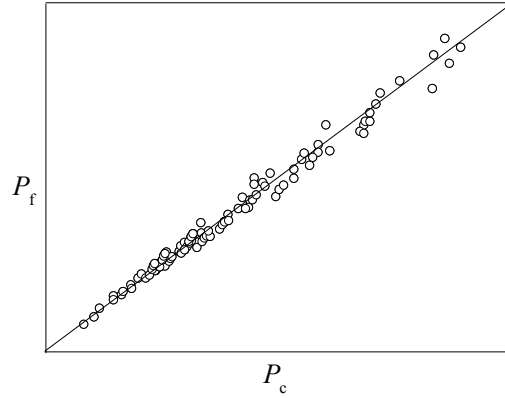


Figure 15. Comparing of Predicted and FE Results

The accuracy of Eq. (1) can be also assessed from error analyses. The relative error e_i^* , the averaged relative error e , the relative standard variance s^* and the relative average standard variance s are defined and listed as follows:

$$e_i^* = \frac{P_{fi} - P_{ci}}{P_{fi}} \quad (i=1, 2, 3 \dots n) \quad (4)$$

$$e = \frac{\sum_{i=1}^n |e_i^*|}{n} \quad (5)$$

$$s^* = \sqrt{\frac{\sum_{i=1}^n |e_i^*|^2}{n-1}} \quad (6)$$

$$s = \sqrt{\frac{\sum_{i=1}^n (|e_i^*| - e)^2}{n-1}} \quad (7)$$

P_{fi} and P_{ci} are the results of FE simulation and equation's prediction respectively. The total number of the models is n . The values of e , s^* , s are calculated to be 5.54%, 6.79%, 6.41% respectively. Such small error values can also prove the accuracy of Eq. 1 in estimating the static strength of a square tubular Y-joint with chord reinforcement.

Using Eq. a, the static strengths of the reinforced specimens Ex-2 and Ex-4 can be also calculated, and the results are 326kN and 226kN respectively. Compared to the experimental results, i.e., 289.4kN and 261.3kN, the relatively errors are 12.8% and -13.4%, which indicates that the estimation is acceptable.

As Eq. 1 is obtained based on the above parametric study, it has to be satisfied with a validity range. This range is listed as follows: $0.4 \leq \beta \leq 0.8$, $6 \leq \gamma \leq 12$, $1 \leq T_c/t_0 \leq 1.5$ (when $T_c/t_0 > 1.5$, its value is taken to be 1.5 in Eq. (1)), $30^\circ \leq \alpha \leq 75^\circ$.

6. CONCLUSIONS

Experimental tests and FE analyses have both proved that the static strength of a square tubular Y-joint can be improved effectively by increasing the local chord thickness near the brace/chord intersection. Based on a parametric study, the effect of some parameters including β , γ , T_c/t_0 , α , and L_c/b on improving the static strength is carried out. Finally, a parametric for predicting the static strength is presented. Generally, the following conclusions can be obtained:

- (1) There is a remarkable improvement on the static strength of a square tubular Y-joint under axial compression with reinforced chord. However, T_c/t_0 should not exceed a certain value (it is advised to be not larger than 1.5) otherwise there is ineffective improvement.
- (2) It is ineffective to increase the static strength of a square tubular Y-joint under axial compression by increasing the length of the reinforced chord segment.
- (3) The proposed parametric equation can provide accurate and reliable prediction on the static strength of a chord reinforced square tubular Y-joint in a validity range of joint geometry.

REFERENCES

- [1] Ganhi, P., Raghava, G. and Ramachandra Murthy, D.S., "Fatigue Behavior of Internally Ring-stiffened Welded Steel Tubular Joints", *Journal of structural engineering*, 2000, Vol. 126, No. 7, pp. 809-815.
- [2] Van der Vegte, G.J., Choo, Y.S., Liang, J.X., Zettlemoyer, N., Liew, J.Y.R., "Static Strength of T-joints Reinforced with Doubler or Collar Plates, II: Numerical Simulations", *Journal of Structural Engineering*, ASCE, 2005, Vol. 131, No.1, pp. 129-138.
- [3] Lee, M.M.K., and Llewelyn-Parry, A., "Strength of Ring-stiffened Tubular T-joints in Offshore Structures—A Numerical Parametric Study", *Journal of Constructional Steel Research*, 1999, Vol. 51, pp. 239–264.
- [4] Nazari, A. Guan, Z., Daniel, W.J.T., Gurgenci, H., "Parametric Study of Hot Spot Stresses around Yubular Joints with Doubler Plates", *Practice Periodical on Structural Design and Construction*, ASCE, 2007, Vol. 12, No.1, pp. 38-47.
- [5] Choo, Y.S., Liang, J.X., Van der Vegte, G.J., Liew, J.Y.R., "Static Strength of Doubler Plate Reinforced CHS X-joints Loaded by in-plane Bending", *Journal of Constructional Steel Research*, 2004, Vol. 60, pp. 1725–1744.
- [6] Shao, Y.B., Yue, Y.S., and Cai, Y.Q., "Experimental Study on Hysteretic Behavior of Circular Tubular T-joints Reinforced with Collar-plate", *Engineering Mechanics*, 2011, Vol. 28, No.10, pp. 209-215.
- [7] Gao, J., Su, J.Z., Xia, Y., Chen, B.C., "Experimental Study of Concrete-filled Steel Tubular Arches with Corrugated Steel Webs", *Advanced Steel Construction*, 2014, Vol. 10, No. 1, pp. 99-115.
- [8] Shao, Y.B., Li, T., Seng, T. L., Chiew S.P., "Hysteretic Behavior of Square Tubular T-joints with Chord Reinforcement under Axial Cyclic Loading", *Journal of Constructional Steel Research*, 2011, Vol. 67, No.1, pp. 140-149.
- [9] Shao, Y.B., Lie, S.T., and Chiew S.P., "Static Strength of Tubular T-joints with Reinforced Chord under Axial Compression", *Advances in Structural Engineering*, 2010, Vol. 13 No.2, pp. 369-377.
- [10] Moffat, D.G., Hsieh, M.F., and Lynch, M., "An Assessment of ASME III and CEN TC54 Methods of Determining Plastic and Limit Loads for Pressure System Components", *Journal of Strain Analysis*, 2001, Vol. 36 No. 3, pp. 301-312.

- [11] Zhao, X.L., “Deformation Limit and Ultimate Strength of Welded T-joints in Cold-formed RHS Sections”, *Journal of Constructional Steel Research*, 2000, Vol. 53, pp. 149-165.
- [12] CIDECT, “Design Guide 3: For Rectangular Hollow Section (RHS) Joints under Predominantly Static Loading”, Second Edition. 2009.

ECCENTRIC LOADING BEHAVIOR OF L-SHAPED COLUMNS COMPOSED OF CONCRETE-FILLED STEEL TUBES

T. Zhou¹, M.Y. Xu², Z.H. Chen³, X.D. Wang^{4,*} and Y.W. Wang⁵

¹ Lecturer, School of Architecture, Tianjin University, China

² Master Candidate, School of Civil Engineering, Tianjin University, China

³ Professor, School of Civil Engineering, Tianjin University, China

⁴ Associate Professor, School of Civil Engineering, Tianjin University, China

⁵ Structural Designer, Tianjin University Research Institute of Architectural Design and Urban Planning, China

*(Corresponding author: E-mail: maodun2004@126.com)

Received: 24 November 2014; Revised: 12 June 2015; Accepted: 9 November 2015

ABSTRACT: Concrete special-shaped columns have been studied and used in China for twenty years, and can be incorporated into walls to widen indoor areas. However, concrete special-shaped columns do not perform well under seismic action. In addition, special-shaped concrete-filled steel tubular columns were put forward and researched as well because of their high strength and ductility, but the interaction between steel and inner concrete is small. Tie rods are often set to solve the problem, which in turn affect the architectural appearance. To solve the above problems, a special-shaped column composed of concrete-filled steel tubes (SCFT) was proposed and studied. Axial loading behavior, seismic behavior, and whole structure behavior were studied. This type of special-shaped column has been used in residential buildings, and the structural behavior performed well. This paper experimentally investigated the biaxial loading behavior of L-shaped SCFT columns. Failure modes, cooperation of mono-columns, and the effects of eccentric angle and distance on column behavior were studied. Test results were compared with those of finite element analysis. A reasonable simplified calculating formula was proposed based on the study and was proved effectively through the comparison with test results. Mono-columns of SCFT columns proved to work well together. This kind of special-shaped column proved to be a good structure type.

Keywords: L-shaped column, concrete-filled steel tube, composite columns, biaxial loading test, finite element analysis, calculating formula

DOI:10.18057/IJASC.2016.12.3.2

1. INTRODUCTION

Rapid population growth has led to many problems around the world, especially in China. An increasing number of people have moved from urban to rural areas, and the price of residential buildings has risen rapidly. Therefore, the effective use of land is an important problem. Most residential buildings are built with a concrete structure, and the section of columns is always much larger than the thickness of walls such that columns always occupy inner areas. In recent years, special-shaped columns have been studied to increase utilization areas.

Special-shaped columns are divided according to different construction materials: concrete special-shaped columns (Ramamurthy et al. [1]), steel-reinforced concrete special-shaped columns (Xue et al. [2]), steel fiber high-strength reinforced-concrete and composite columns (Tokgoz et al. [3]), special-shaped concrete-filled steel tube columns (Shen et al. [4]), and special-shaped columns composed of concrete-filled steel tube mono-columns (SCFT columns)(Zhou et al. [5]).

SCFT columns are composed of several small sections of concrete-filled steel tube columns called mono-columns, which are connected by connection plates. This type of special-shaped column has the advantages of high ductility and low construction cost. SCFT columns have been used in more than 200 residential buildings. In the process of being used, axial loading tests and seismic behavior tests were studied, and the structural static and dynamic behaviors were analyzed using 3D finite element software (Chen et al. [6-7], Zhou et al. [8]). However, eccentric loading behavior has not been researched.

Eccentric loading is one of the most important effect factors of ultimate bearing capacity for columns or walls. For any new structure, eccentric loading behavior should be tested and studied. Kim et al. [9] studied the eccentric loading capacity of high-strength steel-concrete composite columns of various sectional shapes. Halabi et al. [10] studied the behavior of reinforced concrete (RC) slab-column connections strengthened with external carbon fiber-reinforced polymer (CFRP) sheets subjected to eccentric loading. Ernest et al. [11] studied the behavior of textile-reinforced mortar (TRM) strengthened brickwork walls under eccentric compressive loading. Song et al. [12] studied the eccentric behavior of fiber-reinforced polymer (FRP)-strengthened concrete columns. Most studies use the unidirectional bending test, but for asymmetric sections such as special-shaped columns, the real loading condition is biaxial bending.

This paper presents the results of an experimental investigation and analytical simulation of the behavior of eccentrically loaded L-shaped SCFT columns.

2. EXPERIMENTAL PROGRAM

2.1 Introduction

An experimental study was performed to assess L-shaped SCFT columns under biaxial compression. Three specimens were investigated according to eccentric angle and distance. The main objective of the test was to study the deformation process and failure modes of SCFT columns. The effects of bending direction and eccentric distance on behavior were examined. A finite element model was developed according to the test results.

The cross section shape of L-shaped SCFT columns is monosymmetric; the actual vertical load behavior of this column is compression combined with bending. Three mono-columns were placed under different axial loadings, as shown in Figure 1(a). Under unidirectional lateral force, the load condition could be simplified as uniaxial bending, as shown in Figure 1(b). If bidirectional lateral force was applied to the column, then the load condition could be simplified as biaxial bending, as shown in Figure 1(c). This study investigated the behavior of uniaxial and biaxial bending; axial loading behavior was also tested to study the effect of eccentric loading. The loading positions are shown in Figure 2. The distance between the center of gravity “O” and the loading point “P” is the eccentric distance. The eccentric distances of the uniaxial bending and biaxial bending specimens were the same, whereas the eccentric angles were different.

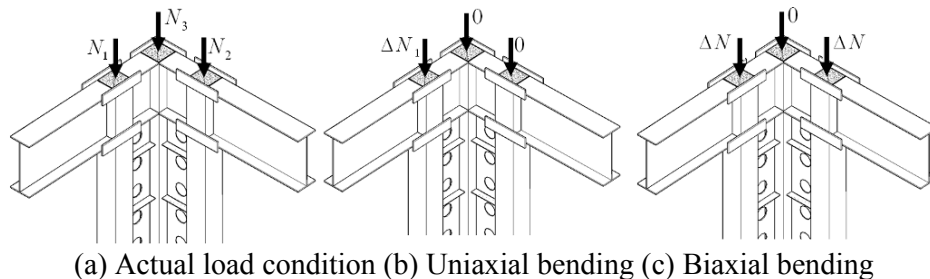
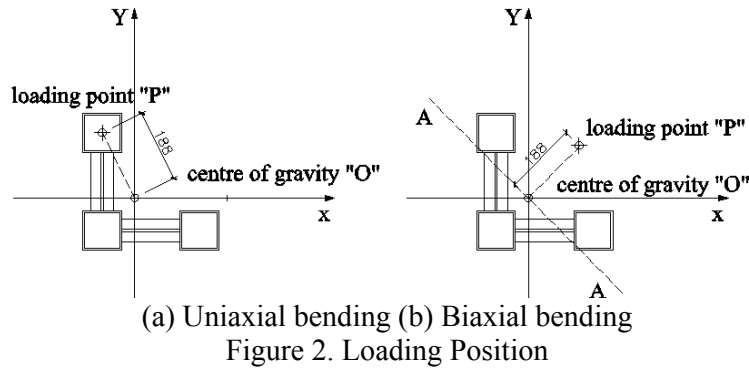


Figure 1. Simplified Load Condition



2.2 Specimens

Details of the SCFT column specimens are shown in Figure 3. Both the connection plates and stiffeners were welded onto the steel tubes. Table 1 provides a summary of the specimen details. Material properties of steel and concrete were determined using tensile tests on coupons extracted from the steel tubes and cubes, and cylinder tests on the concrete. Material test results are listed in Tables 2 and 3. Two steel plates with a thickness of 40 mm were welded to the top and end of the specimens.

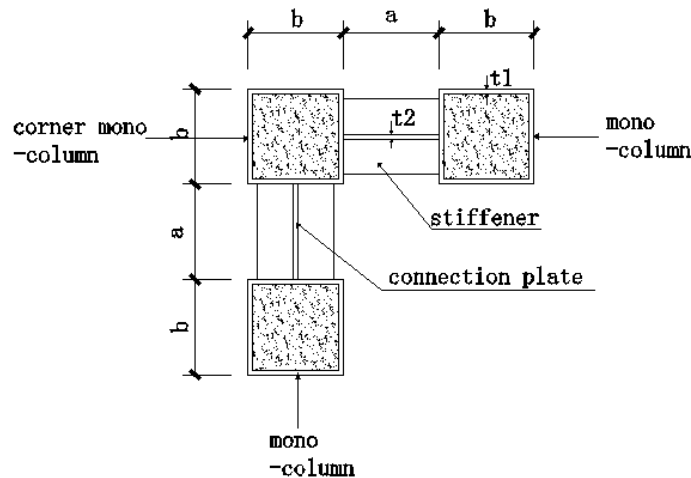


Figure 3. Details of Specimens

Table 1. Summary of Specimens

Specimen	b (mm)	a (mm)	t_1 (mm)	t_2 (mm)	A_y (mm ²)	A_c (mm ²)	f_y (MPa)	f_c (MPa)	l (mm)
S-1, S-2, S-3	100	150	4	3	1,536	8,464	269	17.336	1,500

Table 2. Properties of Steel Tube and Connection Plate

Steel	t (mm)	f_y (MPa)	f_u (MPa)	E_s (MPa)	ε_y (μ)
Connection plate	3.00	312	426	148,261	2,104
Steel tube	3.75	269	445	208,305	1,291

Table 3. Properties of Concrete

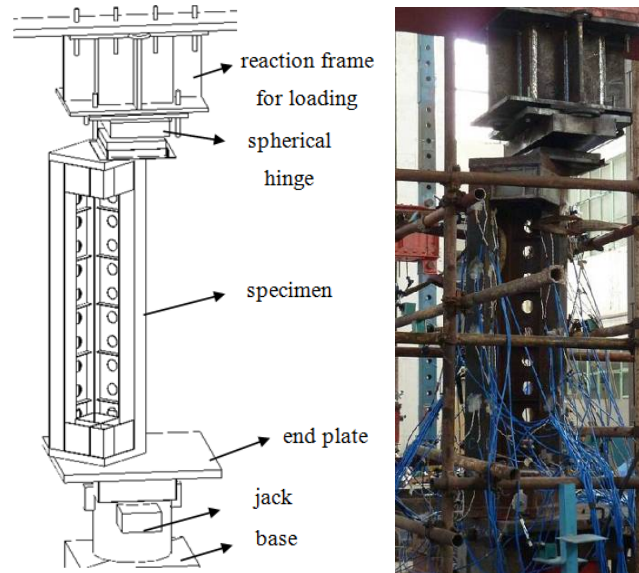
Concrete grade	f_{cu} (MPa)	f_c (MPa)	E_c (MPa)
C25	23.2	17.336	19,373

2.3 Test Setup and Procedure

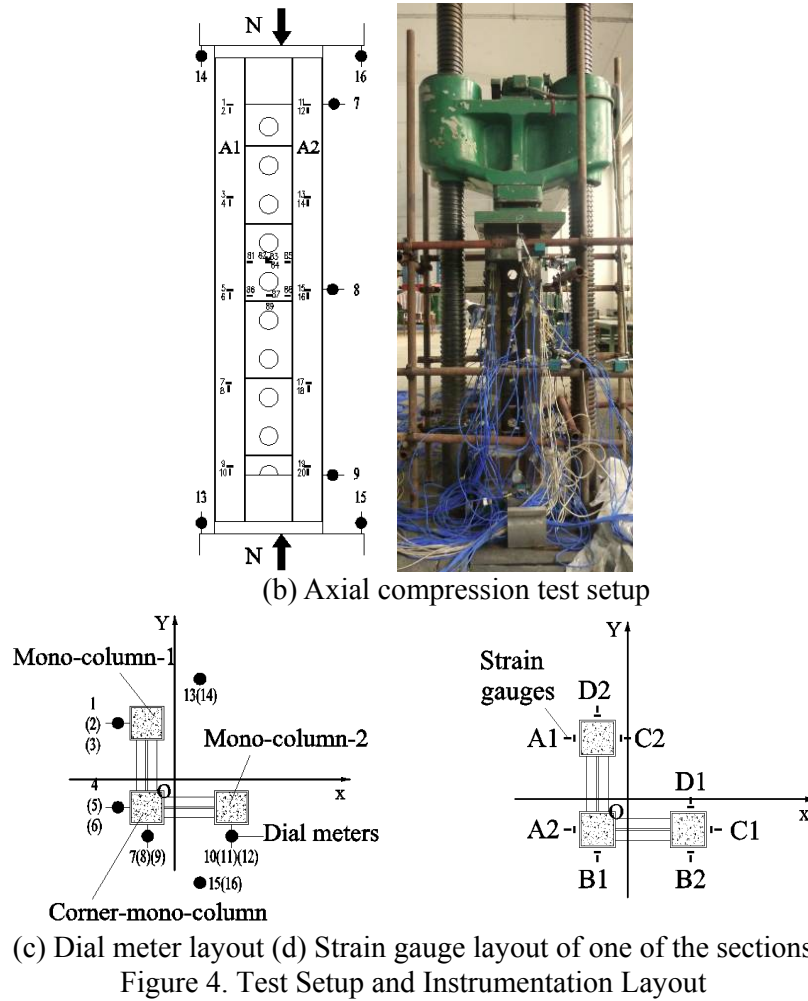
The test setup and instrumentation layouts for the L-shaped SCFT column specimens are shown in Figure 4. The uniaxial bending and biaxial bending tests were performed using a reaction frame and a 3000 kN jack, and a spherical hinge was set between the specimen and the reaction frame. To compare the difference between axial loading behavior and eccentric loading behavior, one specimen was compressed using a 5000 kN loading machine.

To describe the experimental results, each mono-column surface was numbered, as shown in Figure 4(d). Figure 4(c) shows that 12 dial meters (numbers 1 to 12) were used to measure the lateral displacements at the top, middle, and end of the specimens. In addition, two dial meters (numbers 14 and 16) were set at the top, while another two dial meters (numbers 13 and 15) were set at the ends of the specimens to measure vertical displacement. Ninety-two strain gauges and two strain rosettes were used for each specimen. Strain gauges and strain rosettes were bonded to the connection plate to determine the directions of principal strains. In addition, 80 strain gauges were bonded to the steel tube of each mono-column at five sections to measure the strains in the tubes along the specimen length. Figure 4(d) shows the strain gauge arrangement on one face of the specimen, which was the same as the other four sections.

Each specimen was loaded manually at low speed. Data were logged at 20 kN intervals before yield and at 10 kN intervals after yield. To apply uniform compressive loading on the columns, two steel plates, each having a thickness of 40 mm, were welded to the two ends of the specimens and allowed to harden under a pre-load of 20 kN.



(a) Eccentric compression test setup



3. TEST RESULTS

3.1 Deformation and Failure Mode

For Specimen S-1, the loading applied to the mono-column was considered uniaxial bending. The failure mode is shown in Figure 5(a). The entire column bent around the x-axis, whereas the bend along the y-axis was not evident. At the top of the mono-column, which was under compression load, the steel tube buckled and the concrete cracked.

For Specimen S-2, the loading position was located at the top steel plate, where no mono-column was under compression load; it was considered biaxial bending. The failure mode is shown in Figure 5(b). The entire column bent around axes x and y, which means that the column bent around the axis A-A as mentioned in Figure 2(b).

Specimen S-3 was axially compressed by a 5000 kN loading machine. Evident buckling occurred at the top, after which the load decreased rapidly. Mono-column-1 and mono-column-2 exhibited significant buckling at the top, whereas no evident deformation was observed at the corner mono-column. The failure mode is given in Figure 5(c). Although the deformation shapes of the two mono-columns were not the same because of construction error and randomness of the experiment, the failure mode of the specimen is believed to be symmetrical.

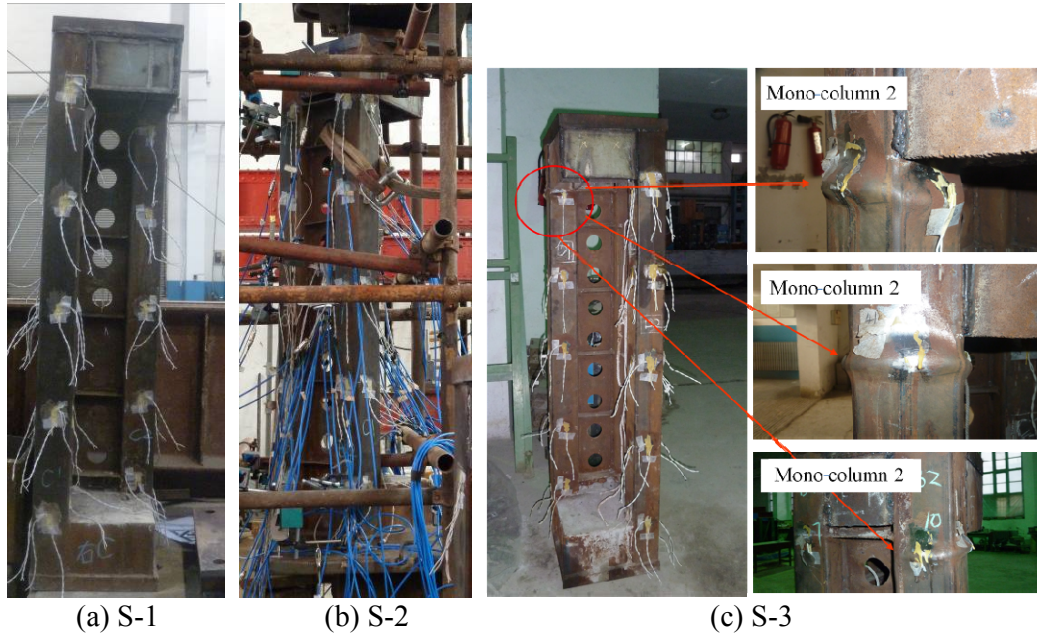


Figure 5. Failure Modes

3.2 Vertical Load-End Compressive Displacement

To gauge vertical deformation, two dial meters were set to measure the downward displacement of the top plate of the loading machine, and another two dial meters were set to measure the upward displacement of the baseboard. The average value of the two dial meters for each plate was considered its displacement. The sum of absolute values of the vertical displacements at the top plate and the baseboard of the press was the end compressive displacement of the specimen. Axial load-compressive displacement curve at the load-end of the two specimens is shown in Figure 6.

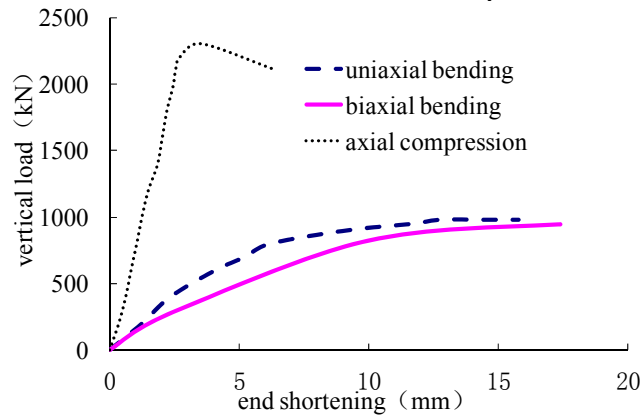


Figure 6. Axial Load-compressive Displacement Curve at Load-end.

The ultimate bearing loads of Specimen S-1 (uniaxial bending), S-2 (biaxial bending), and S-3 (axial compression) were 980, 940, and 2300 kN, respectively. The ultimate bearing capacity of Specimens S-1 and S-2 decreased by 57% compared with the ultimate bearing capacity of Specimen S-3, which means that the eccentric load was adverse. The ultimate loads of Specimens S-1 and S-2 were almost the same, which was caused by an equal eccentric distance of 188 mm for both specimens. Eccentric load angle is considered to have little influence on ultimate bearing capacity.

3.3 Load-lateral displacement curves

Out-of-plane lateral displacements of the mono-columns were obtained using lateral dial meters. Surface numbers of the mono-columns are shown in Figure 4(d). Figure 7(a) shows that the lateral displacements of areas B1 and B2 of Specimen S-1 were much larger than that of areas A1 and A2. The column section was considered to revolve around the x-axis under uniaxial bending load. However, for Specimen S-2, the lateral displacements of areas A1, A2, B1, and B2 were almost the same, which means that the column section revolved around axis A-A.

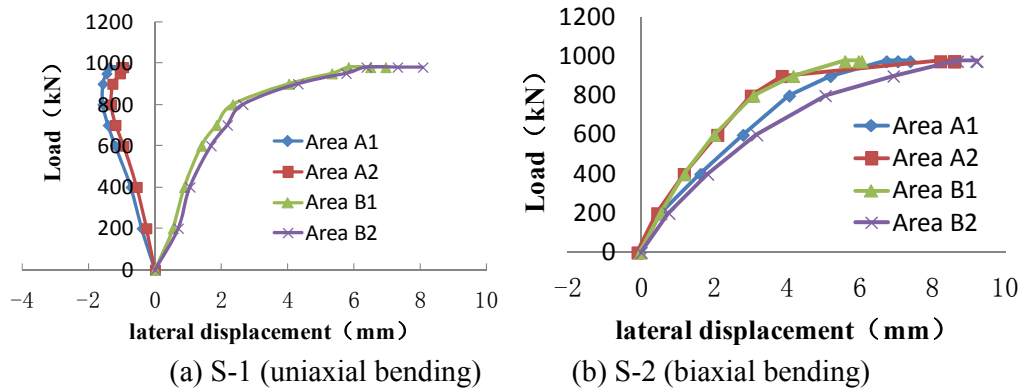


Figure 7. Axial load–lateral Displacement Curve

3.4 Lateral Strain Distribution at the Middle Section

To study strain distribution around the cross section, strain gauges were arranged in the middle section of the column, as shown in Figure 4(c). Figure 8 shows the setup of the strain gauges at the middle cross section. Three load levels (30%, 60%, and 90% of the ultimate load) were selected to study strain distribution along the cross section. The three load levels for Specimens S-1 and S-2 were set as 400, 600, and 800 kN, while those for Specimen S-3 were 600, 1200, and 1700 kN. The strain distributions for each load level are shown in Figure 9.

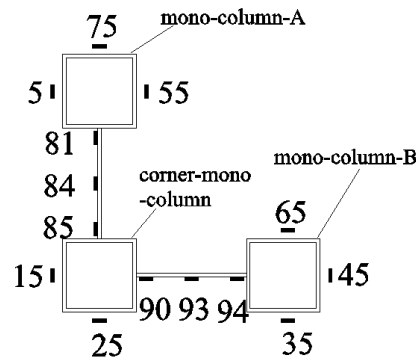


Figure 8. Strain Gauge Arrangement at the Cross Section

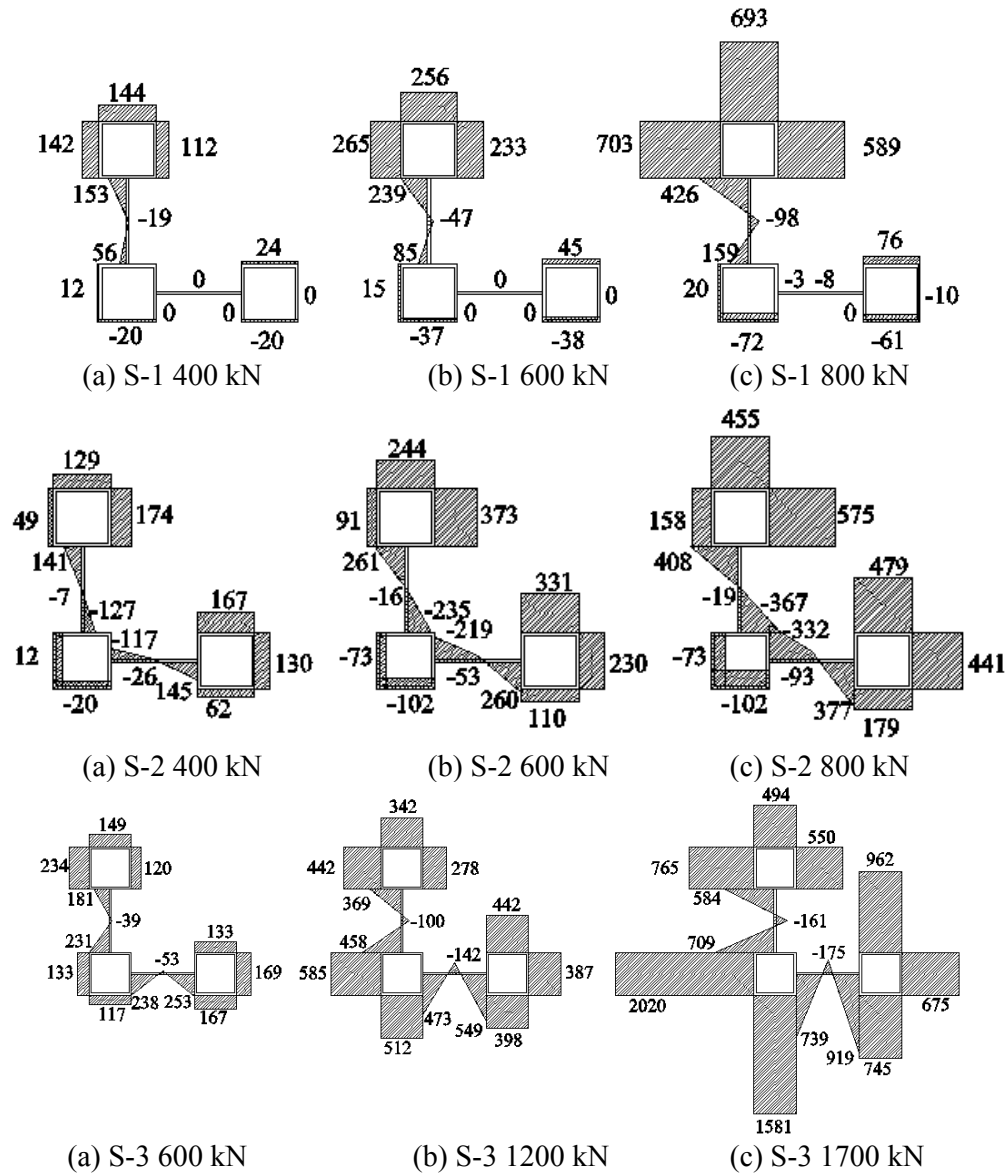


Figure 9. Strain Distribution of the Cross Section

The strain distribution of Specimen S-1 indicates that the mono-column bore almost all the compression loading. The strains of the other two mono-columns were much lower. The strain sign indicated that the entire column bent around axis $X'-X'$, as shown in Figure 10(a). Strain distribution and signs of S-2 illustrated that the three mono-columns could work together, and the entire column bent around axis $A'-A'$, as shown in Figure 10(b). Figure 10 shows the bent axes of S-1 and S-2. Hence, the accurately bent axis was found from the cross section strain distribution. The mono-column strains of S-3 were almost the same when the load reached 1200 kN, but the strain of the corner mono-column increased rapidly when the load reached 1700 kN.

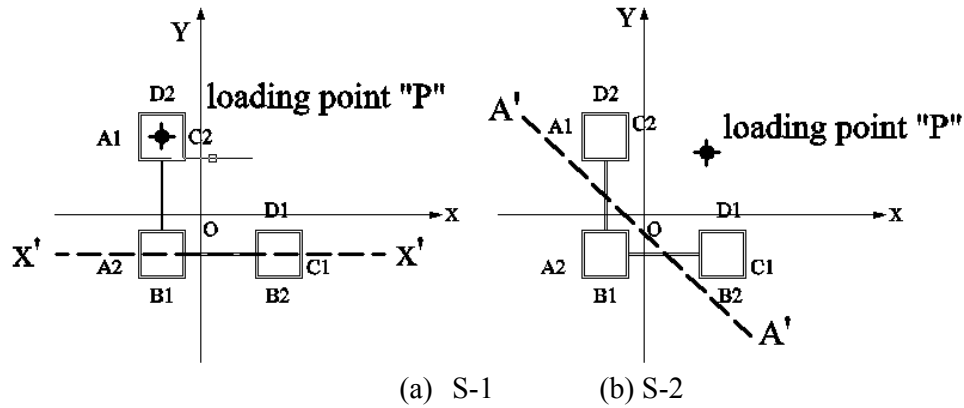


Figure 10. Bent Axis of S-1 and S-2

The maximum strains of the middle sections of S-1 and S-2 were 703 and 575 μ when the axial load was 800 kN, whereas that of S-3 was 2020 μ when the axial load reached 1700 kN. The strain of S-3 was significantly larger than that of S-1 and S-2. The steel of S-1 and S-2 did not yield when the load reached 800 kN. From the strain distribution, specimen failure under eccentric loading could be concluded to have been caused by instability, whereas that of the axial loading specimen was caused by steel yielding.

3.5 Lateral Strain Distribution at the Middle Section

To study the principal stress angle of the middle section of the connection plates, one strain rosette was bonded to the connection plate between areas A1 and A2, while the other was bonded to the connection plate between areas B1 and B2, as shown in Figure 11. The strain rosette consisted of three strain gauges with angles of 0°, 45°, and 90°. The 90° strain gauge was parallel to the length of the steel tube. Principal stress and principal strain were evaluated.

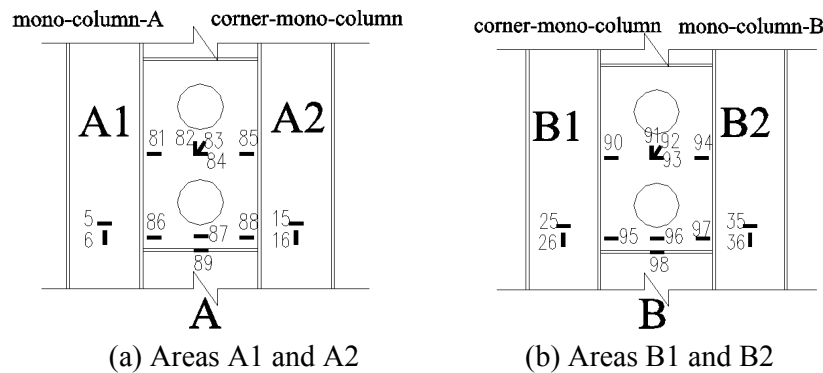
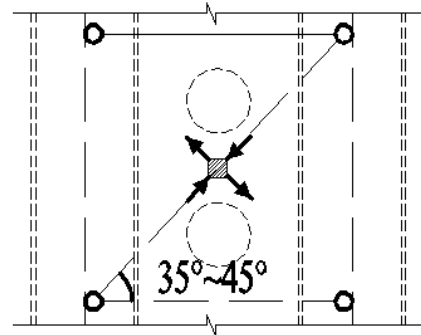
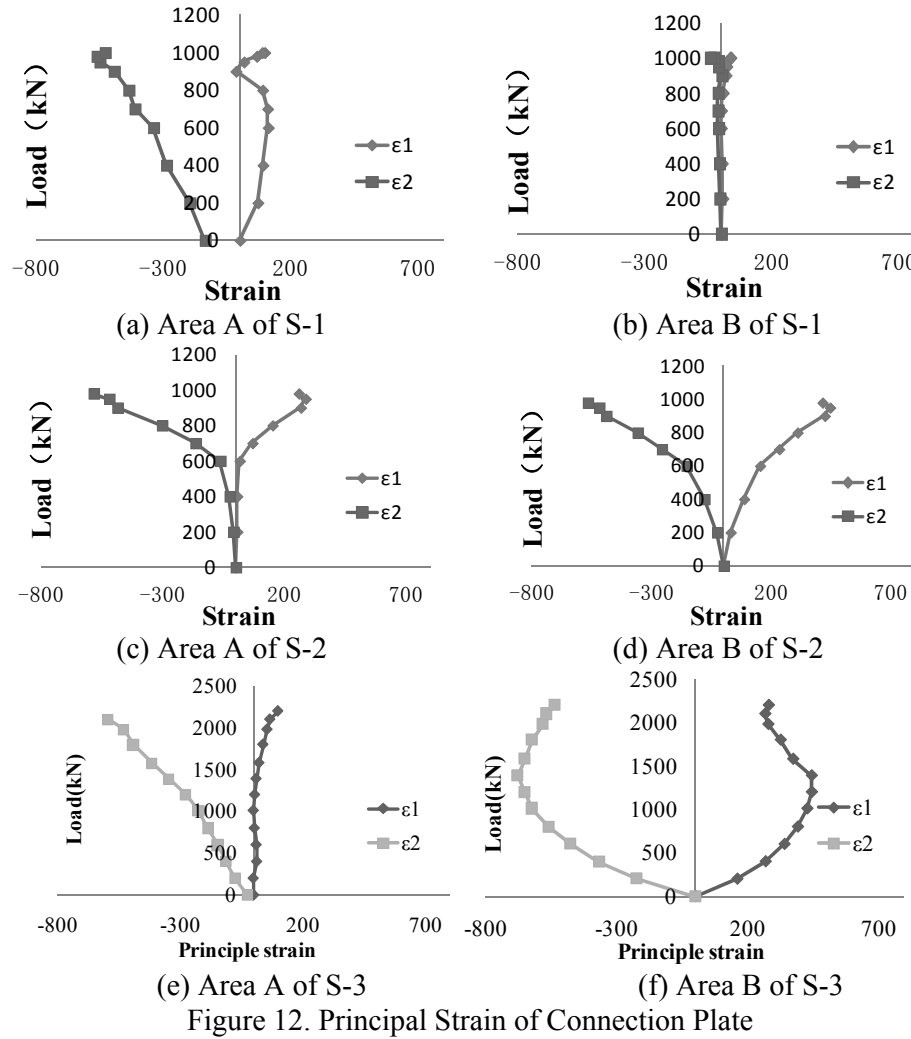


Figure 11. Strain Rosettes Bonded to the Middle Section of the Connection Plates

The first principal strain ε_1 and the second principal strain ε_2 of each specimen connection plate are shown in Figure 12. The principal strains of area A and area B were symmetrical for Specimens S-2 and S-3, which indicates that their deformations were symmetrical. The θ_p of all strain rosettes ranged from 35° to 45°. The principal strain direction of the connection plate is shown in Figure 13. The connection plate could be reduced to a lacing bar with an angle of 35° to 45°, whereas the stiffener could be reduced to a lateral lacing bar, as shown in Figure 13.



4. FINITE ELEMENT ANALYSIS

A finite element model was established. The behavior of SCFT columns was complicated because of the nonlinearity of the inner concrete and the interaction between the concrete and steel tube. Therefore, a finite element model could provide an efficient method to simulate the behavior of SCFT columns subjected to axial loading. Specimens were modeled and analyzed using the commercial finite element software ANSYS.

4.1 Modeling of SCFT columns

Four main components were modeled to simulate the behavior of SCFT columns: steel tubes, connection plate, inner-filled concrete, and the interface between the concrete and the steel tube. In addition, the selection of element type, mesh size, initial geometric deformation, boundary conditions (fixed at the top and bottom of the column), and load application were also important in simulating the SCFT columns.

SHELL 181 was used to model the steel tubes and bracings. SHELL 181 is a four-node doubly curved shell element that has six degrees of freedom per node. The constitutive law of steel tubes and bracings was assumed elastoplastic with a yielding strain equal to f_y/E_s . The three-dimensional eight-node element SOLID 65 was adopted to model infilled concrete. Each element node has three degrees of freedom. This element is capable of cracking, crushing, and plastic deformation, and can be used to achieve accurate results in simulating the behavior of concrete under axial loads.

The constitutive law of concrete is the Hognestad type. The constitutive relation of concrete was chosen according to Eqs. 1 to 3, and that of steel was chosen according to Eqs. 4 and 5. σ_{c0} is the compressive strength of concrete achieved in the material test, which equaled 23.2 MPa. E_c is the elasticity modulus of concrete, which equaled 19373 MPa. σ_{s0} is the yield strength; the yield strength of the steel tube was 269 MPa, and that of the connection plate was 312 MPa. E_s is the elasticity modulus of steel, and the elasticity modulus of the steel tube and the connection plate were 208305 and 148261 MPa, respectively.

$$\begin{cases} \sigma_c = \sigma_{c0} \left[\frac{2\varepsilon_c}{\varepsilon_{c0}} - \left(\frac{\varepsilon_c}{\varepsilon_{c0}} \right)^2 \right] & 0 \leq \varepsilon_c \leq \varepsilon_{c0} \\ \sigma_c = \sigma_{c0} \left[1 - 0.15 \left(\frac{\varepsilon_c - \varepsilon_{c0}}{\varepsilon_{cu} - \varepsilon_{c0}} \right) \right] & \varepsilon_{c0} \leq \varepsilon_c \leq \varepsilon_{cu} \end{cases} \quad (1)$$

$$\varepsilon_{c0} = 1.8\sigma_{c0}/E_c \quad (2)$$

$$\varepsilon_{cu} = 0.0038 \quad (3)$$

$$\begin{cases} \sigma_s = E_s \varepsilon_s & 0 \leq \varepsilon_s \leq \varepsilon_{s0} \\ \sigma_s = \sigma_{s0} & \varepsilon_s \geq \varepsilon_{s0} \end{cases} \quad (4)$$

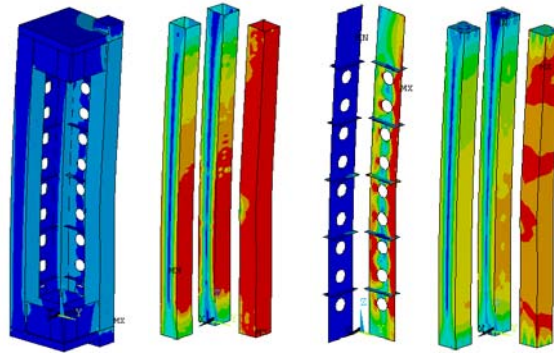
$$\varepsilon_{s0} = \sigma_{s0}/E_s \quad (5)$$

Contact action between the steel tube and the concrete was modeled by contact elements TARGE 170 and CONTA 173. These surface-to-surface contact elements consist of two matching contact faces of the steel tube and concrete elements. The friction between the two faces is maintained as long as the surfaces remain in contact. The coefficient of friction between the two faces was taken as 0.25 in the analysis. These contact elements allow the surfaces to separate under the influence of tensile force, but the contact elements were not allowed to penetrate each other. In addition, the initial imperfections were simulated as follows: compressive unit force was loaded on the

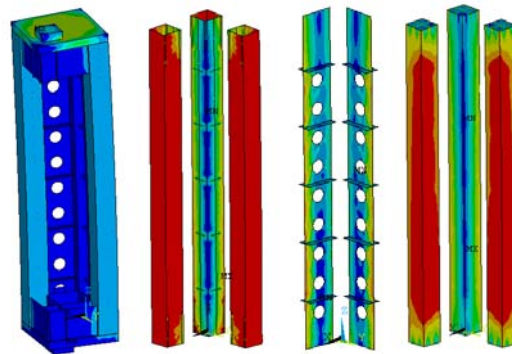
specimens; the deformation was calculated; and the buckling modal with the concerned deformation was analyzed. (Liu et al. [13])

4.2 Strain Distribution of Steel and Concrete

Strain distributions and deformations of the three specimens are shown in Figures 14, 15, and 16. The failure modes were similar to the test results. Specimen S-1 bent around axis $X'-X'$, Specimen S-2 bent around axis $A'-A'$, and Specimen S-3 deformed axially. Based on the deformation and the strain distribution, the strain of each mono-column reached the maximum value; the three mono-columns could work together.



(a) Column (b) Steel tube (c) Connection plates (d) Concrete
Figure 14. Strain and Deformation of S-1 (Uniaxial Bending)



(a) Column (b) Steel tube (c) Connection plates (d) Concrete
Figure 15. Strain and Deformation of S-2 (Biaxial Bending)



(a) Column (b) Steel tube (c) Connection plates (d) Concrete
Figure 16. Strain and Deformation of S-3 (Axial Loading)

4.3 Load-end Compressive Displacement

According to finite element method (FEM) analysis, the ultimate bearing capacity of Specimens S-1, S-2, and S-3 was 740, 699, and 2113 kN, respectively. The load-end compressive displacement curves of the specimens obtained from the experiments and FEM analysis are given in Figure 17. Some differences can be observed between the test results and FEM results of Specimens S-1 and S-2, which were caused by the difference between the real test setup and the FEM model. However, the test and FEM results of Specimen S-3 showed good agreement because the axial loading test was easier to model, which explains the higher ultimate strength gained by FEM. Considering this effect, the results of the finite element analysis agree with those of the experiment.

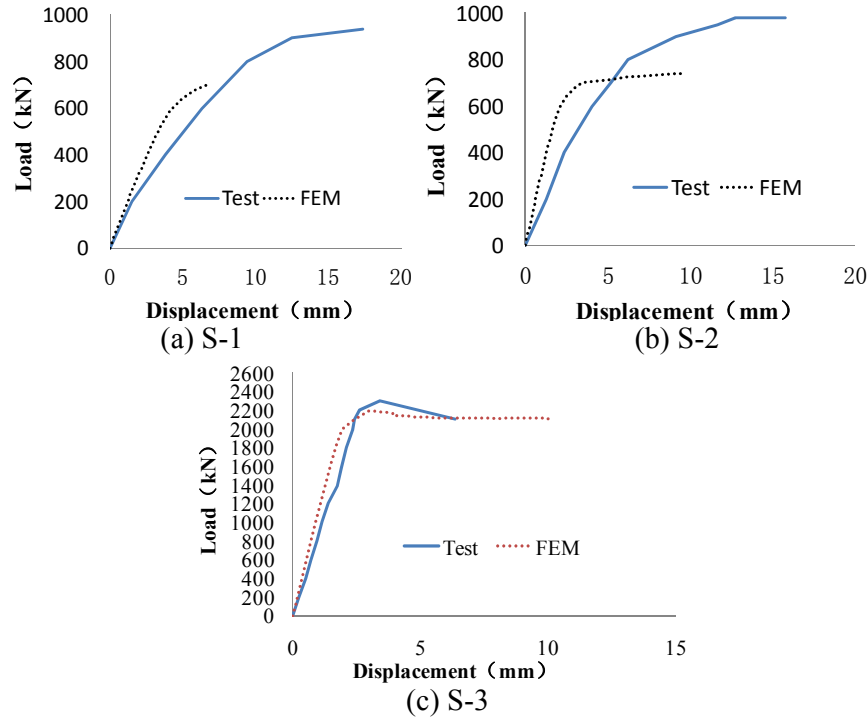


Figure 17. Comparison of Load-end Compressive Displacement Curves

5. SIMPLIFIED CALCULATING FORMULA

According to the strain on the connection plates, the connection plates could be reduced to a lacing bar, and the mono-column was connected by truss. The column is a lattice structure. Eccentric loading N will lead to bending moment in two directions (Ne_x and Ne_y). The mono-column bearing axial loading, total loading N , was divided into three axial loadings: N_1 , N_2 , and N_3 . The force diagram is shown in Figure 18, where point “O” is the center of gravity. The equilibrium equation is shown in Eq. 1. Axial loadings N_1 , N_2 , and N_3 could be calculated using Eq. 4. If one of the mono-columns failed under axial loading, then the entire column was considered to have failed. If the ultimate axial loadings of the three mono-columns are N_{1u} , N_{2u} , and N_{3u} , then the ultimate eccentric loading N_u can be calculated using Eq. 5. The bearing capacity of each mono-column could be calculated using Eqs. 6–8. If the eccentric distance is large, then the axial load of corner mono-column will be tense, and the concrete is neglected because of poor tension capacity. The stability coefficient φ was calculated according to CECS 159: 2004 (China). Calculation results are shown in Table 4. The comparison indicates that the formula results were reasonably accurate.

Rong [14] studied L-shaped, T-shaped, and X-shaped SCFT columns experimentally, and six specimens were tested under axial loading. Pictures of the test are shown in Figure 19, and test results are shown in Table 5. To verify the accuracy of the calculating formula, a comparison is shown in Table 5. If the section was L-shaped, then there were three mono-columns, and the ultimate bearing capacity could be calculated using Eq. 9. If the section was T-shaped, then we used Eq. 10. If the section was X-shaped, then the corner mono-column was braced by other mono-columns. Thus, the stability coefficient φ equaled 1.0, and we used Eq. 11. According to the comparison, the calculating formula proposed in this paper was considered reasonable.

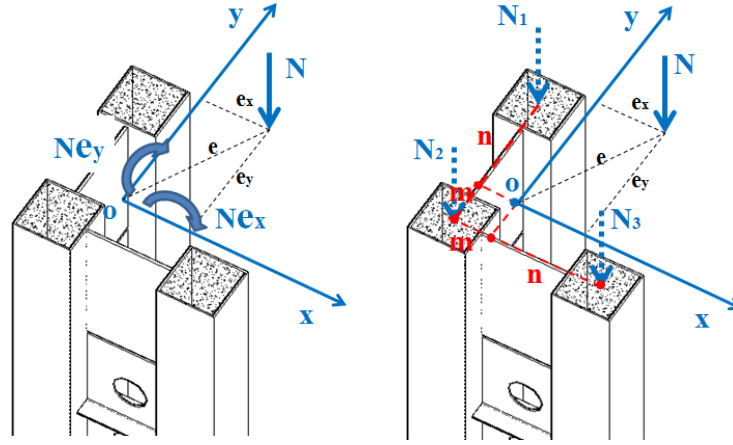


Figure 18. Force diagram.

$$\begin{cases} N = N_1 + N_2 + N_3 \\ Ne_x = N_3 n - N_1 m - N_2 m \\ Ne_y = N_1 n - N_2 m - N_3 m \end{cases} \quad (1)$$

$$\begin{cases} m = \frac{a+b}{3} \\ n = \frac{2(a+b)}{3} \end{cases} \quad (2)$$

$$\begin{cases} N = N_1 + N_2 + N_3 \\ Ne_x = N_3 n - m(N - N_3) \\ Ne_y = N_1 n - m(N - N_1) \end{cases} \quad (3)$$

$$\begin{cases} N_1 = \frac{e_y + m}{m + n} N \\ N_2 = \frac{n - m - (e_x + e_y)}{m + n} N \\ N_3 = \frac{e_x + m}{m + n} N \end{cases} \quad (4)$$

$$N_u = \min \left\{ \frac{m+n}{e_y + m} N_{1u}, \left| \frac{m+n}{n - m - (e_x + e_y)} \right| N_{2u}, \frac{m+n}{e_x + m} N_{3u} \right\} \quad (5)$$

$$N_{1u} = \varphi(A_y f_u + A_c f_{cu}) \quad (6)$$

$$N_{2u} = \begin{cases} \varphi(A_y f_u + A_c f_{cu}) & (\frac{n-m-(e_x+e_y)}{m+n} > 0 \quad \text{pressure}) \\ A_y f_u & (\frac{n-m-(e_x+e_y)}{m+n} \leq 0 \quad \text{tension}) \end{cases} \quad (7)$$

$$N_{3u} = \varphi(A_y f_u + A_c f_{cu}) \quad (8)$$

$$N_u = 3\varphi(A_y f_u + A_c f_{cu}) \quad (9)$$

$$N_u = 4\varphi(A_y f_u + A_c f_{cu}) \quad (10)$$

$$N_u = (4\varphi + 1) \times (A_y f_u + A_c f_{cu}) \quad (11)$$

Table 4. Comparison between the Test, FEM, and Formula

Specimen No	e (mm)	e_x (mm)	e_y (mm)	N_{ut} (test) (kN)	N_{uF} (FEM) (kN)	N_{uf} (formula) (kN)	$\frac{ N_{uf} - N_{ut} }{N_{ut}} \times 100\%$
Specimen-1 Uniaxial bending	186	-83	167	980	740	949	3.16%
Specimen-2 Biaxial bending	185	131	131	940	699	891	5.21%
Specimen-3 Axial compression	0	0	0	2300	2113	2280	0.87%



(a) L-shaped column (b) T-shaped column (c) X-shaped column

Figure 19. Axial Loading Test in Reference [12]

Table 5. Comparison between the Reference Test and the Proposed Formula Results

Specimen No	e (mm)	h (mm)	a (mm)	b (mm)	f_u (MPa)	f_{cu} (MPa)	N_{ut} (Test) (kN)	N_{uf} (Formula) (kN)	Error (%)
L-shaped CFST column	0	400	100	100	429	49.7	3975	3960	3.77%
L-shaped CFST column	0	2000	100	100	429	49.7	3610	3370	6.64%
T-shaped CFST column	0	400	100	100	472	49.7	5580	5280	5.37%
T-shaped CFST column	0	2000	100	100	472	49.7	4600	4500	2.17%
X-shaped CFST column	0	400	100	100	429	49.7	6830	6660	2.49%
X-shaped CFST column	0	2000	100	100	429	49.7	6390	5800	9.23%

6. CONCLUSIONS

The behavior of SCFT columns subjected to axial load and eccentric load was experimentally investigated. The effects of the eccentric angle and distance were studied. The experimental results were compared with those of FEM analysis. The following conclusions could be drawn:

- (1) Mono-columns could work together when the entire column bears the eccentric load. The SCFT column demonstrates good eccentric loading behavior. Thus, this kind of special-shaped column is suitable for residential buildings.
- (2) The ultimate bearing capacity of Specimen S-1 and S-2 decreased by 57% compared with that of Specimen S-3, which means that eccentric load was adverse.
- (3) The failure mode of Specimen S-1 was uniaxial bending around axis X'-X', that of Specimen S-2 was biaxial bending around axis A'-A', and that of Specimen S-3 was axial compression with minimal bending, as shown in Figure 10. Meanwhile, mono-columns could work together. The strain distribution and failure mode indicate that the failure of specimens under eccentric loading was caused by instability, whereas steel yielding caused the failure of axial loading specimens.
- (4) The connection plate could be reduced to a lacing bar with an angle of 35° to 45°, whereas the stiffener could be reduced to a lateral lacing bar, as shown in Figure 13.
- (5) The results obtained by FEM analysis agreed with those obtained by the test. Thus, FEM analysis can effectively simulate the behavior of SCFT columns.
- (6) According to the test and FEM analysis, eccentric load could be divided into three axial loadings subjected by mono-columns, and a simplified calculating formula was proposed to predict the ultimate bearing capacity of SCFT under compression. The calculated results were reasonably accurate.

ACKNOWLEDGMENTS

This work was sponsored by the National Natural Science Foundation of China (grant nos. NSFC51308387).

NOMENCLATURE

a	Distance between mono-columns
b	Width of mono-column
t_1	Thickness of steel tube
t_2	Thickness of connection plate
t	Thickness of steel in material tests
A_y	Steel area of mono-column
A_c	Concrete area of mono-column
l	Length of column
N	Axial compression applied to specimen
f_y	Yield strength
f_u	Ultimate strength
ε_y	Yield strain
f_{cu}	Axial compressive strength of concrete cube with a width of 150 mm
f_c	Axial compressive strength of concrete cuboids with dimensions of 150 mm \times 150 mm \times 300 mm
θ_p	Angle between the first principal and x-axis
N	Eccentric loading
e_x	Eccentric distance along x-axis
e_y	Eccentric distance along y-axis
m	Distance between the center of gravity and the center of corner mono-column along x-axis
n	Distance between the center of gravity and the center of corner mono-column along y-axis
N_u	Ultimate bearing capacity of entire column under eccentric loading
$N_{1u} N_{2u} N_{3u}$	Ultimate bearing capacity of mono-columns under axial loading
φ	Stability coefficient

References

- [1] Ramamurthy, L.N. and Hafeez, K.T.A., "L-shaped Column Design for Biaxial Eccentricity", Journal of Structural Engineering, 1983, Vol. 109, No. 8, pp. 1903-1917.
- [2] Xue, J.Y., Chen, Z.P., Zhao, H.T., Gao, L. and Liu, Z.Q., "Shear Mechanism and Bearing Capacity Calculation on Steel Reinforced Concrete Special-shaped Columns", Steel and Composite Structures, 2012, Vol. 13, No. 5, pp. 473-487.
- [3] Tokgoz, S. and Dundar, C., "Tests of Eccentrically Loaded L-shaped Section Steel Fibre High strength Reinforced Concrete and Composite Columns", Engineering Structures, 2012,

- Vol. 38, pp. 134-141.
- [4] Shen, Z.Y., Lei, M., Li, Y.Q., Lin, Z.Y. and Luo, J.H., "Experimental Study on Seismic Behavior of Concrete-Filled L-Shaped Steel Tube Columns", *Advances in Structural Engineering*, 2013, Vol. 16, No. 7, pp. 1235-1247.
 - [5] Zhou, T., Chen, Z.H. and Liu, H.B., "Seismic Behavior of Special Shaped Column Composed of Concrete-filled Steel Tubes", *Journal of Constructional Steel Research*, 2012, Vol. 75, pp.131-141.
 - [6] Chen, Z.H., Rong, B. and Apostolos, F., "Axial Compression Stability of a Crisscross Section Column Composed of Concrete-filled Square Steel Tubes", *Journal of Mechanic of Materials and Structures*, 2009, Vol. 4, No. 10, pp. 1787-1799.
 - [7] Chen, Z.H., Zhou, T. and Wang, X.D., "Application of Special Shaped Column Composed of Concrete-filled Steel Tubes", *Advanced Materials Research*, 2011, pp.196-199.
 - [8] Zhou, T., Li, X.F. and Xu, M.Y., "Heat Transfer Property of Special-shaped Column Composed of Concrete-filled Steel Tubes", *Journal of Tianjin University*, 2015, supplement, pp.74-80.
 - [9] Kim, C.S., Park, H.G., Chung, K.S. and Choi, I.R., "Eccentric Axial Load Capacity of High-strength Steel-concrete Composite Columns of Various Sectional Shapes", *Journal of Structural Engineering*, 2014, Vol. 140, No. 4.
 - [10] Halabi, Z., Ghrib, F., El-Ragaby, A. and Sennah, K., "Behavior of RC Slab-column Connections Strengthened with External CFRP Sheets and Subjected to Eccentric Loading", *Journal of Composites for Construction*, 2013, Vol. 17, No. 4, pp.488-496.
 - [11] Ernest, B., Lluís, G., Pere, R. and Christian, E., "Experimental and Analytical Study of TRM Strengthened Brickwork Walls under Eccentric Compressive Loading", *Construction and Building Materials*, 2013, Vol. 44, pp. 35-47.
 - [12] Song, X.B., Gu, X.L., Li, Y.P., Chen, T., and Zhang, W.P., "Mechanical Behavior of FRP-strengthened Concrete Columns Subjected to Concentric and Eccentric Compression Loading", *Journal of Composites for Construction*, 2013, Vol. 17, No. 3, pp. 336-346.
 - [13] Liu, H.B., Chen, Z.H., Wang, X.D. and Zhou, T., "Theoretical Analysis and Experimental Research on Stability Behavior of Structural Steel Tube and Coupler Falsework with X-bracing", *Advanced Steel Construction*, 2010, Vol. 6, No. 4, pp. 946-962.
 - [14] Rong, B., "Theoretical Analysis and Experimental Study on Special-shaped Column Composed of Concrete-filled Square Steel Tubes", *Doctoral Dissertation*, 2008, Tianjin University. (In Chinese)

ADVANCEMENT AND APPLICATIONS OF JAPANESE HIGH PERFORMANCE STEEL IN STRUCTURAL ENGINEERING

Ping Xiang¹, Hanbin Ge^{2,*} and Liang-Jiu Jia³

¹Assistant Professor, Department of Structural Engineering, Tongji University, Shanghai, 200092, China

²*Professor, Department of Civil Engineering, Meijo University, 1-501 Shiogamaguchi, Tempaku-ku, Nagoya, 468-8502, Japan

³Assistant Professor, Research Institute of Structural Engineering and Disaster Reduction, Tongji University, Shanghai, 200092, China. (Former Post Doctoral Researcher, Advanced Research Center for Natural Disaster Risk Reduction, Meijo Univ., 1-501 Shiogamaguchi, Tempaku-ku, Nagoya, 468-8502, Japan)

*(Corresponding author: E-mail: gehanbin@meijo-u.ac.jp)

Received: 14 January 2014; Revised: 12 October 2015; Accepted: 13 October 2015

ABSTRACT: Applications of steel to building structures in Japan can date back to the first steel factory, Shueisha Printing Plant, constructed in 1894. History of steel bridges in Japan can trace back to the first steel bridge, Kurogane Bridge in Nagasaki, constructed in 1868 using wrought iron. As the developments of large-scale structures, new construction technologies and demanding structural performance, a variety of high performance steels (HPSs) have been developed. In this study, history of applications of HPSs to building and bridge structures in Japan is briefly reviewed. The characteristics of typical HPSs in both buildings and bridges are introduced, respectively, and their impacts on structural engineering are also discussed.

Keywords: Steel, high performance, toughness, welding, ductility, weathering, buildings, bridges

DOI:10.18057/IJASC.2016.12.3.3

1. INTRODUCTION

Constructions of large-scale and large-span structures in developed countries tend to decrease in recent decades, and structural scales of most projects are becoming smaller in countries such as Japan and America. As a rival of reinforced concrete structures, steel structures are confronting a more and more competitive situation. Partially motivated by this concern, a number of high performance steels (HPSs) have been proposed to reduce construction cost, and employed in both building and bridge structures. As progress of new design concepts, connection details, fabrication technologies and mechanics, various properties such as higher strength, ductility, weldability, toughness, weathering and fireproofing properties, are increasingly demanded in practice. For example, design concept based on whole life cycle cost (LCC) is gaining more attention in steel bridges [1], which not only considers initial construction cost, but also maintenance expenses. From the viewpoint of LCC, durability related characteristics, such as weathering and fracture-resistant properties, are becoming more important issues for structural steels.

Before discussion on HPS, its definition is distinguished in different countries. In the USA, HPS is defined as having an optimized balance of strength, weldability, toughness, ductility, corrosion resistance and formability, to achieve the best overall performance of structures while remaining cost-effective [2-4]. A series of HPSs, HPS50W, HPS70W and HPS100W, were developed for steel bridges [3], where the aforementioned material properties are all considered through new manufacturing technologies including developments in metallurgical, rolling and heat-treatment. On the other hand, HPS in Japan commonly represents steels that have one or several virtues in strength, ductility, fire-proofing, weathering, weldability, toughness, cold formability, connecting feasibility [5, 6], etc. Therefore, the definition of HPS in Japan is broader than that in the USA, and there are more steel grades for HPS in Japan. In this study, Japanese HPSs developed respectively

for building and bridge structures are introduced in terms of specific properties, such as strength, toughness, weldability, connection feasibility, durability properties etc.

2. HIGH PERFORMANCE STEELS IN BUILDING STRUCTURES

2.1 General Comments

It is commonly acknowledged that performance of a high-rise building structure is governed by serviceability considerations such as inter-storey drift, which is mainly related with stiffness of a material, boundary conditions (connection stiffness), structural systems and loading conditions. As it is known that steel has a stable elastic modulus, currently it is still not possible to increase its value. It is thus considered not economical to increase strength of a structural steel for common structural systems. However, it is still promising to employ high strength steels in building structures when new structural systems are proposed [7].

In addition, most of past design specifications mainly focus on tensile strength properties, with some attention paid to ductility, fracture-resistant and weldability properties. The aforementioned properties were once deemed good enough to guarantee favorable performance for serviceability, capacities and ductility. However, recent strong earthquakes such as the 1994 Northridge earthquake [8, 9] and the 1995 Kobe earthquake [10, 11] shake this confident belief in steel welded moment resisting frames, especially for the connections details and fracture-resistant properties of the steels and welding materials. The catastrophic consequences of the earthquakes arouse an extensive research on fracture mechanisms of steel welded structures [12-18], and more attentions are paid to fracture-resistant and weldability properties of steels [19, 20]. As the development of new structural systems, fireproofing properties, connecting feasibility and energy dissipation capacity become more and more important in practice.

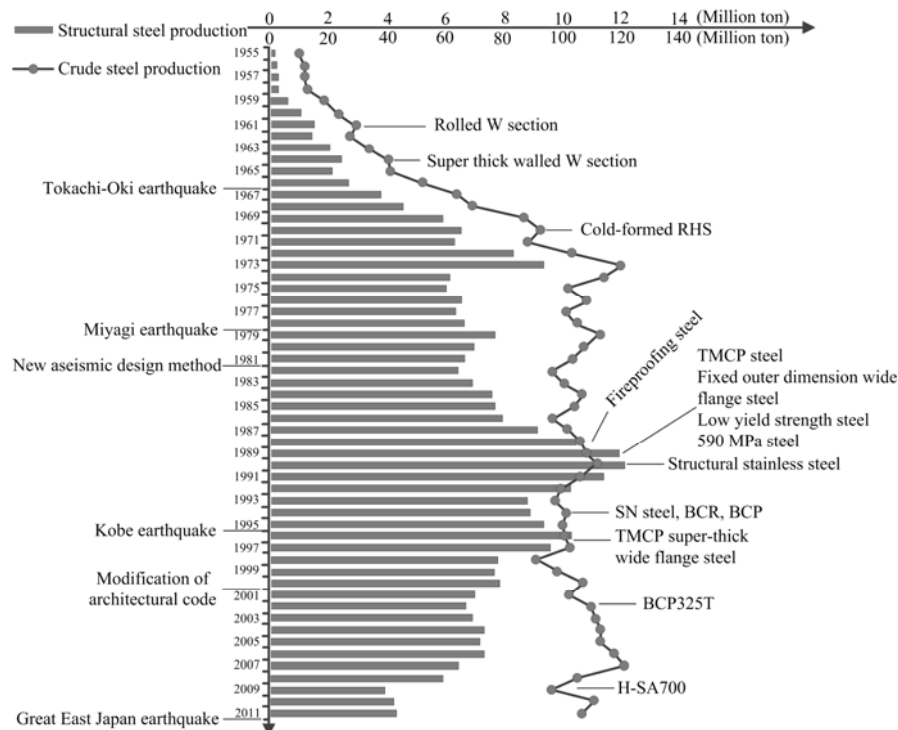


Figure 1. History of High Performance Steel in Building Structures (adapted from [21])

The Japanese crude steel and structural steel productions for building structures from the year of 1955 to 2011 are both plotted in Figure 1 [21], indicating that the structural steel production has passed its peak, while the crude steel production in recent forty years are quite stable. To promote application of steel structures, more economical structural systems, steels and corresponding manufacturing and connecting technologies are required. Strong earthquakes occurred in Japan are also marked in the figure, and a number of HPSs were developed as advancement in seismic design methods and steel manufacturing technologies etc.

2.2 Strength Related HPSs

2.2.1 SN, BCR and BCP

Before 1994, structural steels employed in buildings are SS (S: steel; S: structure) and SM (S: steel; M: Marine) series, which are also simultaneously employed in bridges and marine structures. Under the specific considerations of seismic design of building structures, deviations in the yield strength, tensile strength and yield-to-tensile strength ratio (YR) are of significant importance in the failure mechanisms of common frame structures [22]. To achieve better seismic performance and material weldability, a new series of HPS is developed for steel building structures in 1994, termed SN (S: steel; N: new) series [23]. Two corresponding series for cold formed rectangular hollow sections, BCR (box column-roll) and BCP (box column-press), are also developed, which have equivalent properties as those of the SN series. Mechanical and chemical properties of the SN steels are listed in Table 1. The SN steels has three types, A, B and C, and BCP steel has two types, B and C. For SN Types B and C, and BCR, BCP steels, the upper limit values for the yield strength is specified, and the YR has also to be less than 0.8 except for SN400A. These rules are proposed to ensure structures fail in an expected ductile mode as designed. The weldability is also considered by limiting the carbon content, equivalent carbon content, C_{eq} , carbon equivalent and composition parameter, P_{cm} . C_{eq} is widely employed to evaluate weldability of a steel, while P_{cm} is generally employed in Japan. The two variables are respectively given in Eqns. 1 and 2,

$$C_{eq} = C + \frac{Si}{24} + \frac{Mn}{6} + \frac{Ni}{40} + \frac{Cr}{5} + \frac{Mo}{4} + \frac{V}{14} \quad (1)$$

$$P_{cm} = C + \frac{Si}{30} + \frac{Mn}{20} + \frac{Cu}{20} + \frac{Ni}{60} + \frac{Cr}{20} + \frac{Mo}{15} + \frac{V}{10} + 5B \quad (2)$$

Table 1 Mechanical and Chemical Properties of SN Steels in Japan (JIS G 3136: 2012)

Steel grades	Yield strength (MPa)					Tensile strength (MPa)	Yield-to-tensile strength ratio					C_{eq} (Weight %)		Charpy impact energy at 0 ° (J)
Thickness (mm)	6≤t≤12	12≤t<16	16	16<t≤40	40<t≤100		6≤t≤12	12≤t<16	16	16<t≤40	40<t≤100	t≤40	40<t≤100	6<t≤100
SN400A	≥235	≥235	≥235	≥235	≥215	400≤σ _t ≤510	-	-	-	-	-	-	-	-
SN400B	≥235	235≤σ _y ≤355	235≤σ _y ≤355	235≤σ _y ≤355	215≤σ _y ≤335		-	≤0.8	≤0.8	≤0.8	≤0.8	≤0.36	≤0.36	≥27
SN400C	No product	No product	235<σ _y <355	235<σ _y <355	215<σ _y <335		No product	No product	≤0.8	≤0.8	≤0.8			
SN490B	≥325	325≤σ _y ≤445	325≤σ _y ≤445	325≤σ _y ≤445	295≤σ _y ≤415	490≤σ _t ≤610	-	≤0.8	≤0.8	≤0.8	≤0.8	≤0.44	≤0.46	
SN490C	No product	No product	325≤σ _y ≤445	325≤σ _y ≤445	295≤σ _y ≤415		No product	No product	≤0.8	≤0.8	≤0.8			

Charpy impact energy at 0 ° is required to be no less than 27 J for SN Types B and C, BCR and BCP steels, to improve their fracture-resistant properties. In addition, thickness direction properties

are also specified for Type C of SN and BCP steels. Applications of the SN, BCR and BCP steels in a welded steel frame (through diaphragm type) are shown in Figure 2 [21], where SN Type A steel is employed in secondary beams, SN Type B steel for beams and splice plates, SN Type C steel for diaphragms, BCR and BCP steels for columns. In Japan, the columns are commonly directly welded to the diaphragms, and the diaphragms are subjected to tensile stresses along the thickness direction under seismic loading. Thus, Type C steel is applied to the diaphragms.

2.2.2 High strength steels

High strength steels can reduce sectional size and thickness of structural members, which is correlated with reduced mass and gravity load. One of the main characteristics of high strength steels is a larger elastic domain compared with common mild steel. However, high strength steels are generally with a larger YR and a smaller elongation as illustrated in Figure 3, which are unfavorable for seismic design. For seismic design of structures, a small YR is favorable for a larger load-carrying capacity potential, and a large elongation is beneficial for its correlation with a large energy dissipation capacity. Therefore, application of high strength steels to seismic design of building structures is limited to only some structural components. On the other hand, a number of energy dissipation products have been proposed, and post-earthquake serviceability is paid more attention after the 1995 Kobe earthquake. A new design concept that main structural components such as beams and columns should remain elastic even during strong earthquakes receives more acknowledgements [7]. The seismic design concept for common steels and high strength ones are presented in Figure 4, where energy is dissipated through yielding of the beam and column ends for common steel frames, while through specific energy dissipation components for high strength steel frames. A research project aiming to develop a new damage-free structural system in intensity 7 earthquake (largest intensity in Japan) using super high strength steel has been carried out from the year of 2004 to 2008, e.g., [24-26]. To date, a number of super high strength steel grades, e.g., H-SA700 and BT-HT880, e.g., [27-29], have been proposed and recognized by the Japanese government. The mechanical and chemical properties of the high strength steels are listed in Table 2. It can be seen that the high strength steels have much larger C_{eq} and YR than SN steels, indicating poor weldability and ductility properties of the materials. The YR can reach as large as 0.98 [30]. Meanwhile, the V-notched Charpy impact energy requirements are much higher than those for SN steels, indicating favorable fracture-resistant properties.

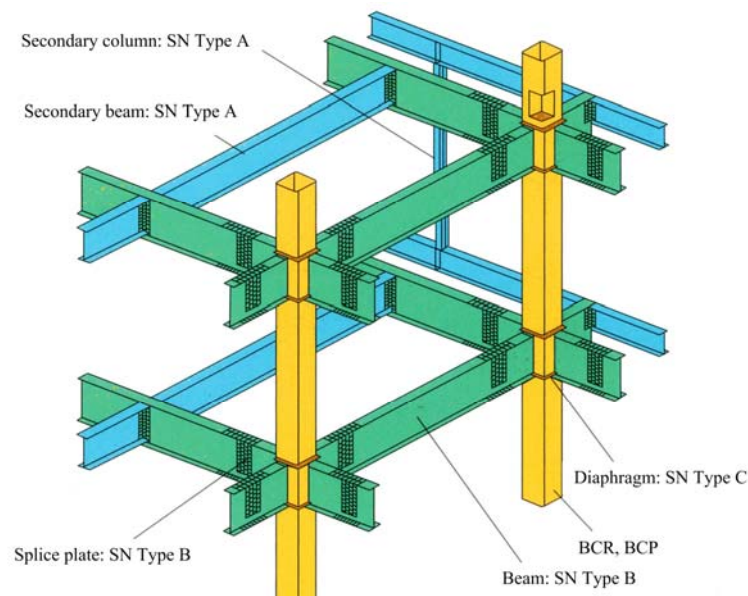


Figure 2 Application of SN and BCR, BCP Steels (adapted from [21])

Table 2 Steel Grades of High Strength Steels Qualified by Japanese Transportation Minister

Shape	Tensile Strength	Company	Grade	Size	C_{eq}	P_{cm}	Yield stress	YR	Charpy energy (J)
Steel plate	780	Kobe JFE Nippon steel	H-SA700A	$6 \leq t \leq 50$	≤ 0.65	≤ 0.32	-	≤ 98	≥ 47
			H-SA700B		≤ 0.60	≤ 0.30	-	≤ 98	≥ 47
		Kobe	KBSA630B	$6 \leq t \leq 80$	-	≤ 0.30	630	≤ 85	≥ 47
			KBSA630C	$16 \leq t \leq 80$	-	≤ 0.30	630	≤ 85	≥ 47
		JFE	JFE-HITEN780TB	$22 \leq t \leq 100$	≤ 0.60	≤ 0.30	630	≤ 85	≥ 47
			JFE-HITEN780TC	$22 \leq t \leq 100$	≤ 0.60	≤ 0.30	630	≤ 85	≥ 47
			HL630B-L	$12 \leq t \leq 40$	≤ 0.60	≤ 0.30	-	≤ 85	≥ 47
			HL630C-L	$12 \leq t \leq 40$	≤ 0.60	≤ 0.30	-	≤ 85	≥ 47
		Nippon steel	BT-HT630B	$9 \leq t \leq 100$	≤ 0.60	≤ 0.30	630	≤ 85	≥ 47
			BT-HT630C	$9 \leq t \leq 100$	≤ 0.62	≤ 0.30	630	≤ 85	≥ 47
Pipe	780	Nippon steel	SA-TT630	$\Phi 400 \sim 2200$	$19 \leq t \leq 60$	≤ 0.60	780	≤ 95	≥ 47
					$60 \leq t \leq 80$	≤ 0.63			
		Kobe	KAST630	$\Phi 400 \sim 2500$	$12 \leq t \leq 80$	-	780	≤ 90	≥ 47

Note: YR denotes yield-to-tensile strength ratio

To date, there are several applications of high strength steels to building structures. For example, concrete filled high strength steel columns (780 MPa steel) are employed in Obayashi Corporation's Technical Research Institute Main Building "Techno-Station" as illustrated in Figure 5 [31], where 160 MPa high strength concrete is adopted. The slender columns have a superior architectural effect, and large span and space is realized by the application of the high strength steel. Amagasaki Research and Development Center shown in Figure 6 [32] is the first application of the 1000 MPa high strength steel in the world, and the high strength steels are employed in columns of the first floor, where buckling restrained braces (BRBs) are also employed to absorb seismic energy during a strong earthquake. Sliding column bases and shear panels with the details shown in Figure 7 [32] are employed to prevent the beams and columns from yielding, and the beams and columns are designed to remain elastic even during a strong earthquake.

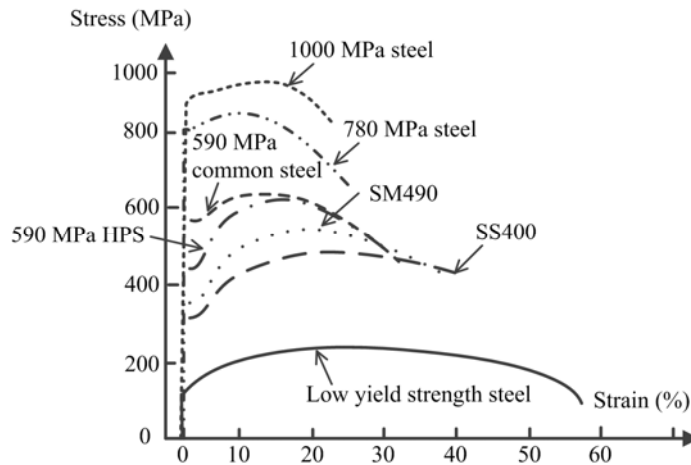


Figure 3. Stress-strain Curves of Common and High Performance Steels

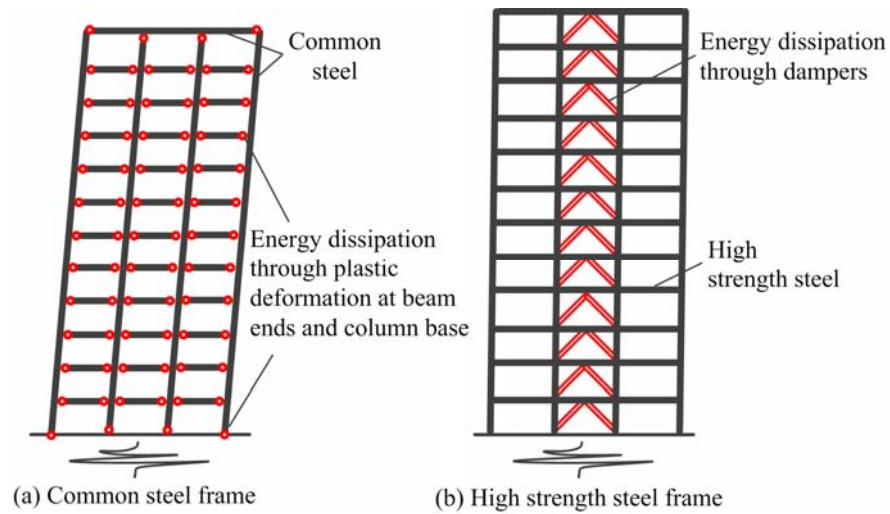


Figure 4. Seismic Design Concept for Framed Structures Made of Common Steel and High Strength Steel



Figure 5. Application of 780 MPa High Strength Steel (adapted from [31])

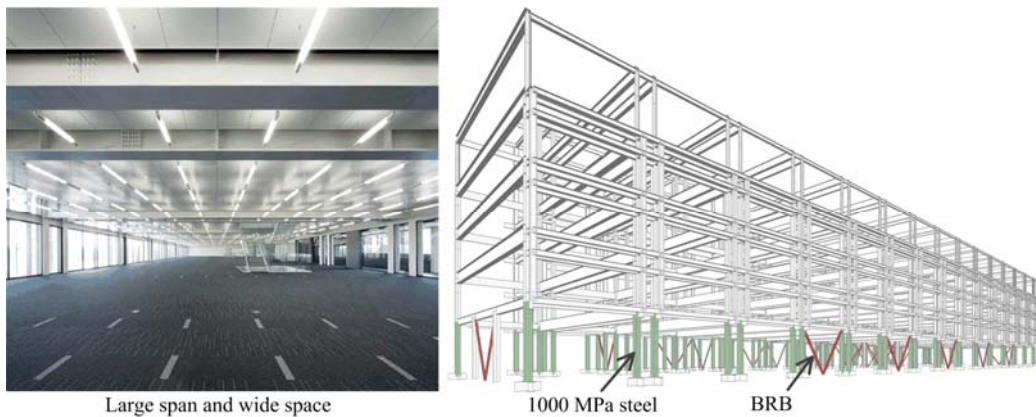


Figure 6. Application of 1000 MPa High Strength Steel (adapted from [32])

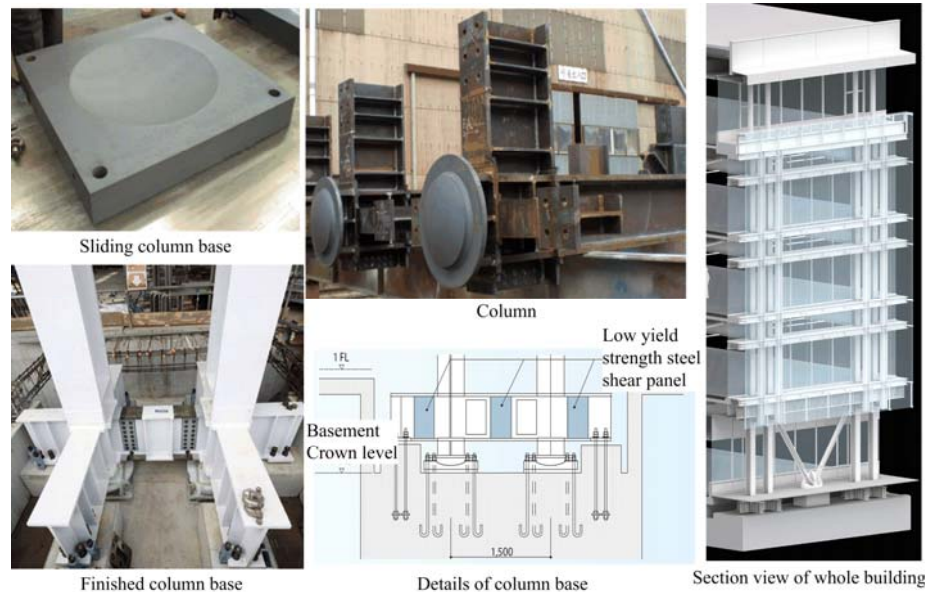


Figure 7. Details of Column Base in a Building Made of 1000 MPa High Strength Steel (adapted from [32])

2.3 Ductility Related HPSs

In recent several decades, a number of energy dissipation components, e.g., BRBs, oil dampers and shear fuses, have been developed and prevalently applied to seismic design of both building and bridge structures, where metallic dampers dissipating energy through plastic deforming of materials are a main category. Energy dissipation capacities of this type of dampers are mainly dependent on ductility of the material. A series of low-yield strength steels are developed aiming to improve the energy dissipation capacities of metallic dampers. In the year of 2000, low yield strength steels LY100 and LY225 for application to building structures were recognized by the Japanese government. The main characteristics of the two steels are:

- (1) strict control for the yield strength ranges (LY100: 80-120 MPa; LY225: 200-245 MPa);
- (2) high ductility in terms of elongation (LY100: $\geq 50\%$; LY225: $\geq 40\%$).

The ductility of the low strength steels is approximately twice of a common structural steel with an elongation of 20%. Meanwhile, the YRs for LY100 and LY225 are also respectively restrained to be less than 0.6 and 0.8. Some dampers such as BRBs have relatively large load-carrying capacities, which may induce premature failure of the attached connections and frames. The low yield strength steels have a tensile capacity one third to half of common steels, which can thus greatly reduce the demanding load-carrying capacities of the attached structural components.

2.4 Fireproofing HPS

Fire resistant property is one of the main concerns in steel structures, and commonly fireproofing coating is required to prevent sudden loss of load-carrying capacity of steel structural components. However, it takes time and expense to carry out fireproofing coating, and it also impairs architectural values of structures. To overcome these deficiencies, fireproofing steel is developed to shorten construction period, enlarge effective architectural space and reduce costs of maintenance etc. The steel has equivalent mechanical properties with common structural steel under normal temperature, while lower decreasing rate of load-carrying capacity compared with common steel under high temperature as shown in Figure 8 [33]. The fireproofing steel SN490-FR under 600 °C

can sustain more than two thirds of the yield strength under normal temperature. It has been employed in parking lots, atriums, external steel structures, art galleries, gyms etc., and an application to external steel structure is illustrated in Figure 9 [33].

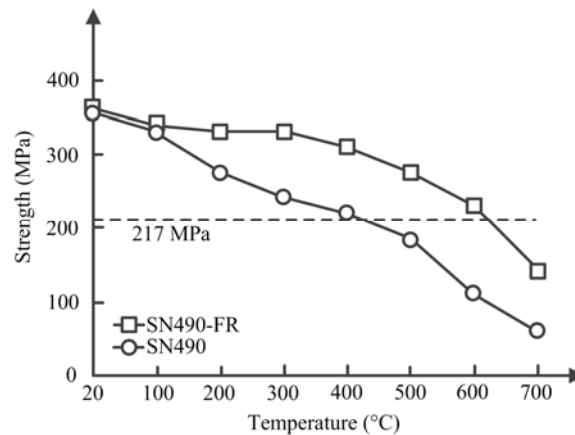


Figure 8. Comparison of Fireproofing Steel and Common Steel (adapted from [33])



Figure 9. Application of Fireproofing Steel in a Building Structure (adapted from [33])

3. HIGH PERFORMANCE STEELS IN BRIDGE STRUCTURES

3.1 General Comments

Vehicle dynamic load make fatigue cracking a main issue in steel bridges, which is different from steel buildings. Meanwhile, steel bridges are frequently exposed to more corrosive environments, and this corrosion is significantly enhanced due to marine (salt spray) exposures especially in Japan. Another issue is that many aging bridges constructed over 50 years ago require maintenance or rehabilitation. Design concept based on LCC [1] is increasing popular in new constructed and rehabilitated steel bridges, along with the aforementioned characteristics make durability related properties of steel more demanding in bridge structures.

The application history of steel to bridges along with the revisions of specifications for highway bridges is presented in Figure 10 [6], which indicates that weathering steels have been employed for a long history since around the year of 1973. A significant progress in manufacturing technology is the thermo-mechanical control process (TMCP) initiating in 1980s. Fine microstructures produced using the controlled-rolling and controlled-cooling method as shown in Figure 11 [34] can greatly improve the strength and toughness properties of steel. Main

advancement of HPSs in bridge structures occurred in 1990s, and a large variety of HPSs have been developed using the TMCP technology and employed in practice based on the revised specification.

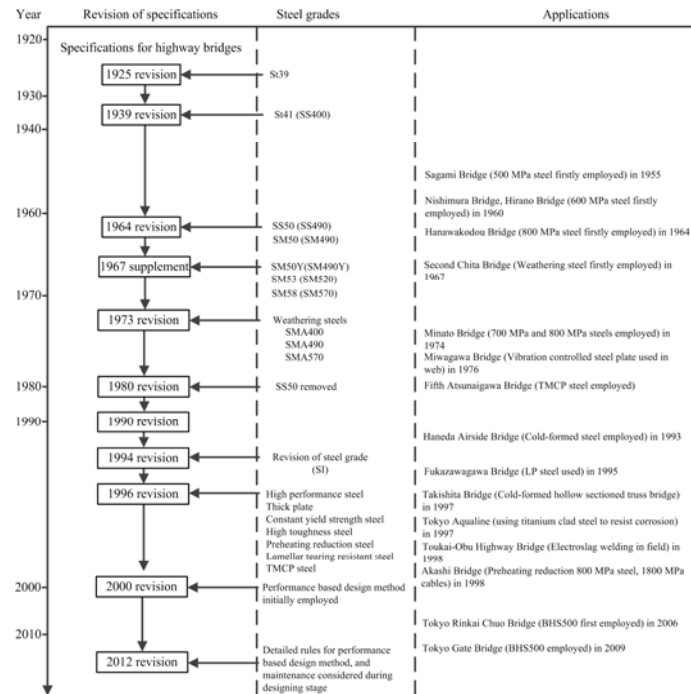


Figure 10. History of High Performance Steel in Steel Bridges (adapted from [6])

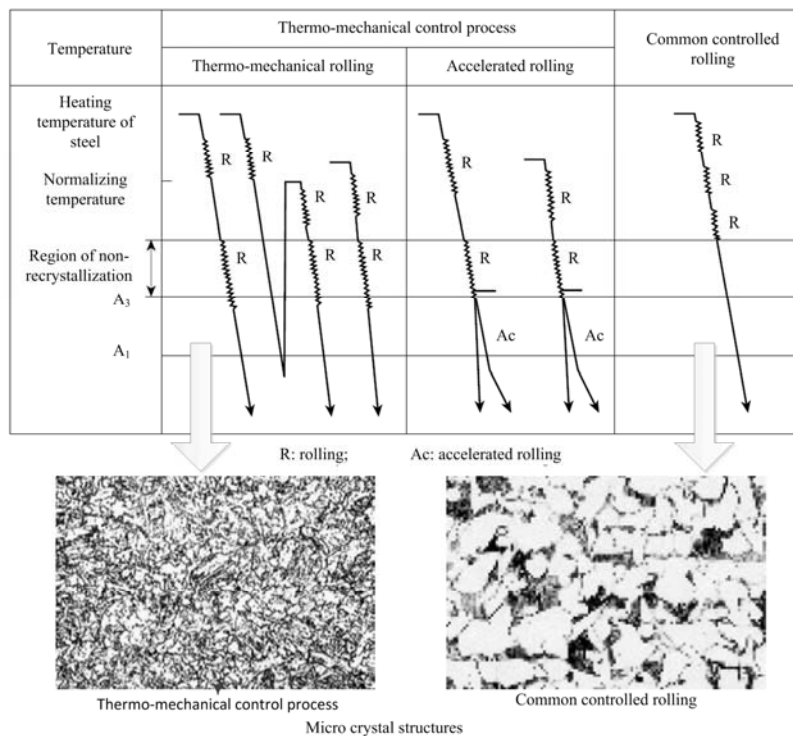


Figure 11. Thermo-mechanical Control Process for Plate Rolling (JIS G0201)

3.2 Strength Related HPS

3.2.1 Constant yield strength steels

Yield strength of common steel generally decreases as plate thickness increases. For example, yield strength decreases when plate thickness is over 40 mm for most Japanese structural steels. A new series of constant yield strength steels listed in Table 3 for plate thickness within 40-100 mm are developed. Yield strength versus plate thickness curve of a constant yield strength steel, SM520-H [35], is compared with a common steel, SM520, in Figure 12. The constant yield strength steels have the following two virtues:

- (1) constant yield strength for various plate thickness makes design simpler;
- (2) yield strength of a thick plate is increased, which can reduce self-weight and makes design more economical.

3.2.2 High strength cables

Suspension bridge and cable stayed bridge are two popular structural types for long span bridges. In recent decades, strength of the cables is increasing gradually as illustrated in Figure 13. The high strength cables have the following merits:

Table 3 Yield strength of constant yield strengths steel and common steels

Constant yield strength steel	Plate thickness (mm)	SM400C-H SMA400CW-H	SM490C-H	SM520C-H SMA490CW-H	SM570-H SM570W-H
	40$t\leq 100$	140	185	210	255
Common JIS steel	Plate thickness (mm)	SM400 SMA400W	SM490	SM520 SMA490W	SM570 SM570W
	16$t\leq 40$	140	185	210	255
	40$t\leq 75$	125	175	195	245
	75$t\leq 100$	125	175	190	240

- (1) reduce self-weight of the slabs;
- (2) reduce self-weight of other structural components;
- (3) more feasibility in structural design;
- (4) shorten construction period and reduce cost of a whole project.

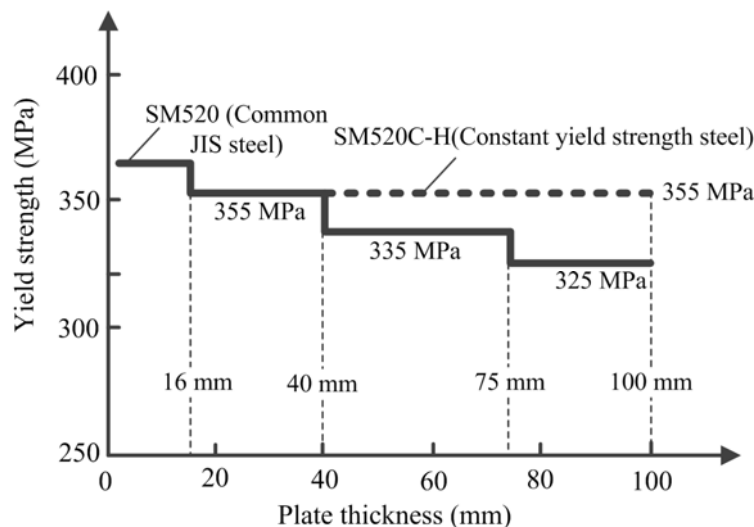


Figure 12. Yield Strength of Constant Strength Steel and Common Steel

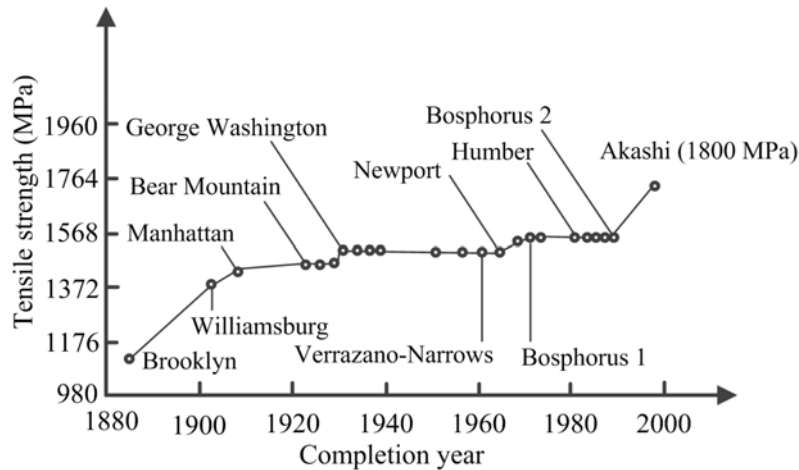


Figure 13. Development of High Strength Cables in Bridges

The strength of the two main cables employed in the Akashi bridge can reach 1800 MPa. It is reported that four main cables are required if 1600 MPa cables are employed. Not only the self-weight of the cables, but also the self-weight of the main towers and the bridge deck is reduced by approximately 10%. Meanwhile, the height of the main towers is also reduced from 320 m to 283 m for the increase of the cable strength.

3.3 Toughness Related HPS

Several properties are correlated with toughness of structural steel, such as cold forming properties and brittle fracture-resistant properties under low temperatures. It is known that cold forming will greatly reduce the ductility and toughness at regions with large bending curvatures (small bending radii). A material can fracture even during cold forming if the toughness is too low or the bending radius is too small. For common structural steel, a large bending radius of 15 times of the plate thickness is required. A series of high toughness steels are developed, and the bending radius can be reduced to 5 or 7 times of the plate thickness depending on the toughness of the material as shown in Figure 14 [35]. Besides, in cold areas such as Hokkaido in Japan, the temperature can decrease as low as -40°C , and high toughness steels are required to resist brittle fracture under the low temperature and meanwhile maintain ductility under a strong earthquake.

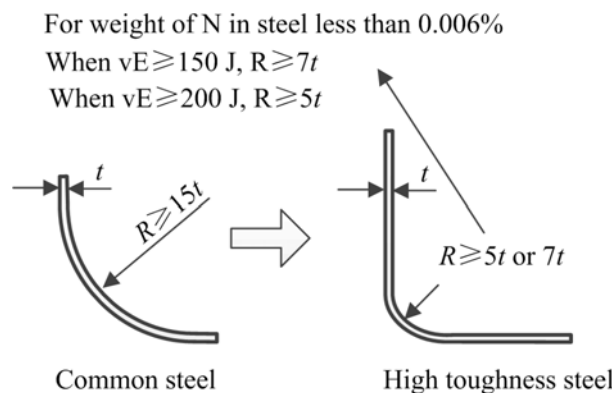


Figure 14. Favorable Cold Forming Properties of High Toughness Steel

3.4 Weldability Related HPS

3.4.1 Steel for high heat input welding

Generally, tungsten inert gas (TIG) welding, metal inert gas (MIG) welding and electro-slag welding (ESW) are widely employed in bridge engineering. For common structural steel, a large amount of heat input will induce low toughness at the heat affected zone, and premature brittle fracture may occur. Therefore, strict control of the heat input is required in some design specifications, e.g., the maximum heat input for SM570 and SM490 are respective 70 J and 100 J in Japan [35]. On the other hand, welding using high heat input method such as the single pass welding process, ESW, is more productive compared with the multi-pass welding methods such as TIG and MIG, while the heat input is generally more than 370 J, which is more than the specified value of the design code. A series of steel for high heat input welding is thus developed. Besides the high efficiency, the steel can also reduce the construction cost, especially for thick-walled steel plates. The welded connections using the steel also have high Charpy impact energy compared with common steel as illustrated in Figure 15. The micro-structure of the heat-affected zone using the steel for high heat input is much finer than those using conventional steel, and the weld thus has a superior fracture-resistant capacity. The micro-structure of a welded joint using the ESW process is shown in Figure 16 [36].

3.4.2 Reduced preheating steel

Weldability is commonly evaluated by the P_{cm} in Japan, and a large value of P_{cm} is correlated with poor weldability. Therefore, weldability becomes poor as the alloy content increases, and a thick-walled plate also has poor weldability. To avoid welding cracks, preheating is commonly required for thick-walled steel plates, especially in steel bridges where thick-walled plates are widely employed. However, it is not only inefficient but also difficult to carry out high temperature preheating in practice. A series of steel is developed to lower the required preheating temperature, and the steel has a relatively small value of P_{cm} as shown in Figure 17, where the required preheating temperature can be controlled within 50 °C.

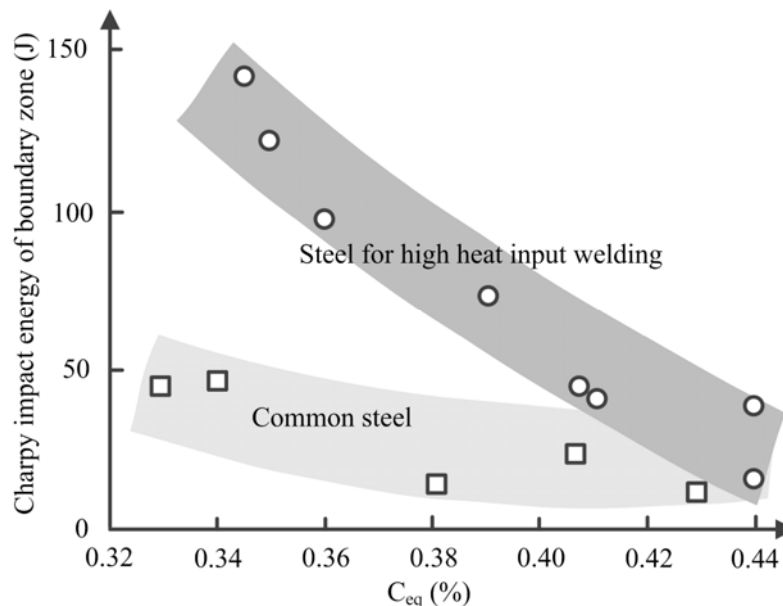


Figure 15. Comparison of toughness at Boundary Zone between Steel for High Heat Input Welding and Common Steel

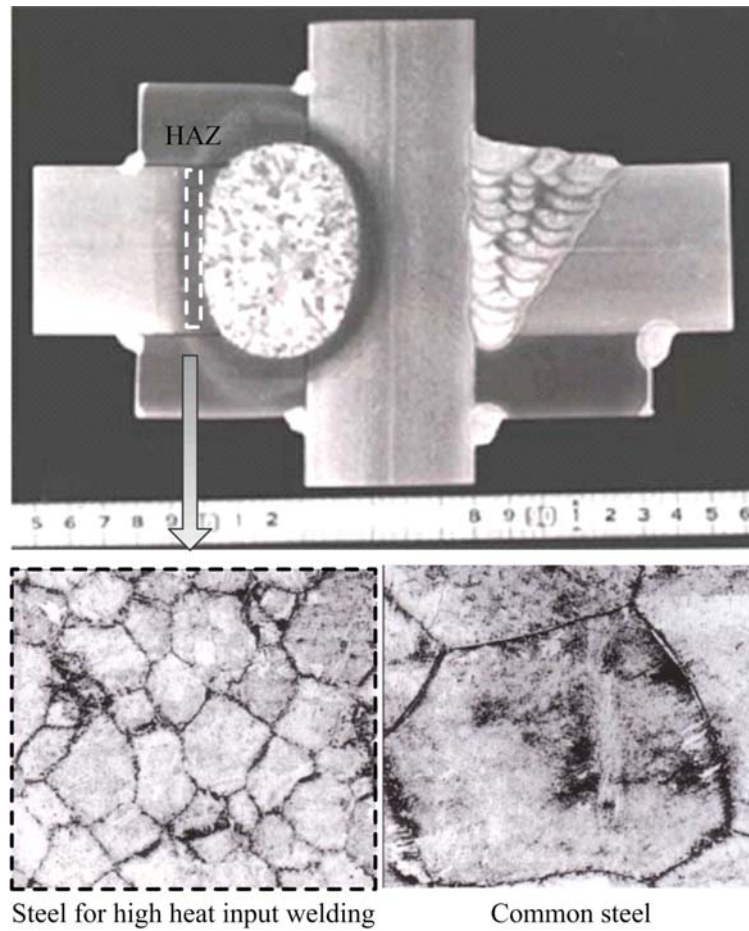


Figure 16. Application of Steel for High Heat Input Welding (adapted from [36])

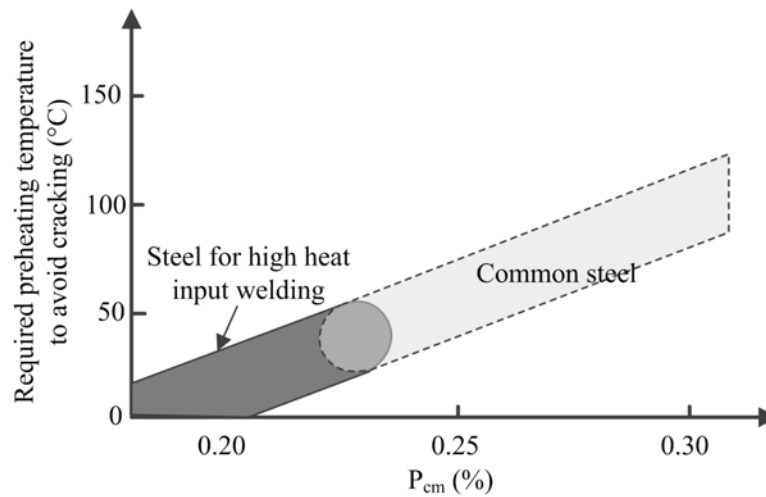


Figure 17 Preheating Requirements of Common Steel and Steel for High Heat Input Welding

3.4.3 Lamellar tearing-resistant steel

Impurities tend to accumulate at mid-thickness of a steel plate, and a thick-walled steel plate subjected to tensile stress along the thickness direction is susceptible to lamellar tearing as

illustrated in Figure 18. The main affecting impurity for lamellar tearing is MnS. A series of lamellar tearing-resistant steel is developed by limiting the S content within 0.006% to 0.01%, which corresponds to a reduction of area at fracture along the thickness direction within 15% to 35% [37]. The steel is applicable to welded thick-walled steel joints such as column flanges of beam-column connections.

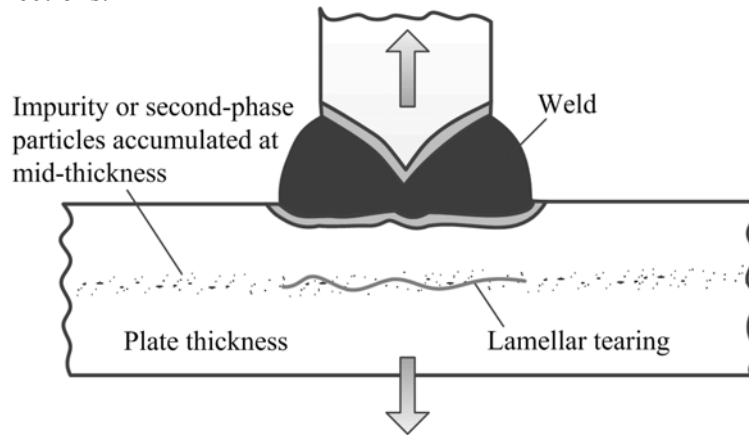
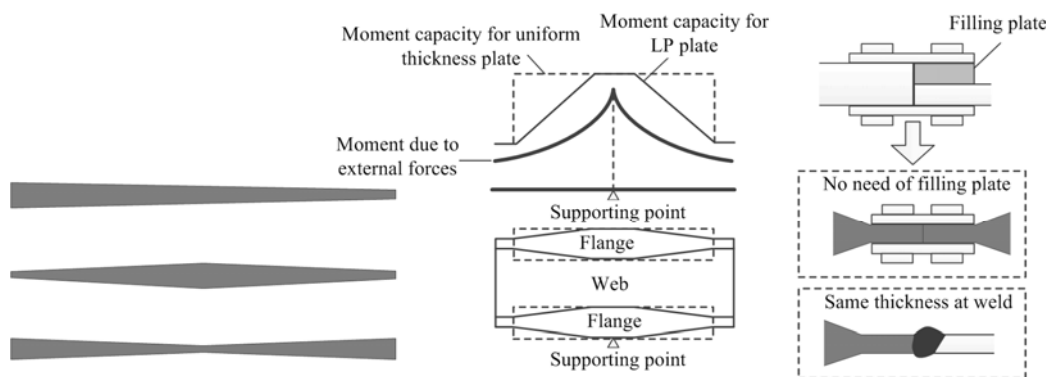


Figure 18. Illustration of Lamellar Tearing at Thick Steel Plates

3.5 Connection Feasibility Related HPS

Longitudinally profiled (LP) steel plates as shown in Figure 19 is another series of HPS developed for steel bridges. The LP steel plates have tapered sections along the thickness direction, which makes connections between two plates with different thickness simple. The stress conditions within the LP steel plates are also improved for the changing plate thickness. For these two virtues, less manufacturing work is required to connect two steel plates with different thickness, and the self-weight is also greatly reduced compared with common steel plates, which thus lower the construction fee.



(a) Profile along longitudinal direction (b) More economical solutions at supporting point and joints

Figure 19. Longitudinally Profiled Steel Plates and its Applications

3.6 Durability Related HPS

Weathering properties are very important for steel bridges, where commonly painting is required to protect the bridges from corrosion. Weathering steels are developed to enhance the corrosion-resistant properties of steel bridges, which have equivalent mechanical properties with common structural steel. These steels are commonly low alloy steels containing chemicals such as Cu, Cr and Ni etc. The steels will form a fine rust layer in the presence of moisture and air as

illustrated in Figure 20, which will prevent the inner material from further corrosion. For this mechanism, the rusting rate will be greatly slowed down compared with conventional steel. There are several benefits for application of the weathering steels, such as rapid construction, attractive appearance, minimal maintenance, and flexibility in future use. The steel bridges using weathering steels are more economical from the viewpoint of LCC.

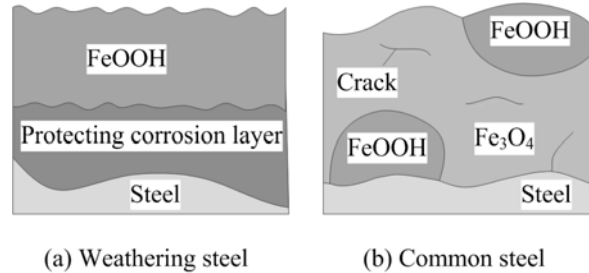


Figure 20. Illustration of Corrosion Mechanisms for Weathering Steel and Common Steel

3.7 New HPSs for Steel Bridges

A series of new HPSs termed BHS (bridge high performance steel) [38] have been developed to reduce the construction and maintenance costs of steel bridges. There are two steel grades, BHS500 and BHS700 (the current names are respective SBHS500 and SBHS700) [39], respectively with yield strengths no less than 500 MPa and 700 MPa. The main characteristics of the BHS include:

- (1) high yield strength;
- (2) favorable construction feasibility such as large welding heat input as much as 10 kJ/mm and reduced preheating temperature as listed in Table 4;
- (3) high toughness;
- (4) good weathering properties such as BHS500W and BHS700W, where “W” denotes weathering.

The BHS has been firstly employed in the construction of Tokyo Rinkai Chuo bridge in 2006, where most of the members in the truss bridge uses the new steel as shown in Figure 21 [40]. It is reported that the self-weight and manufacturing cost have been respectively reduced by approximately 3% and 12%.

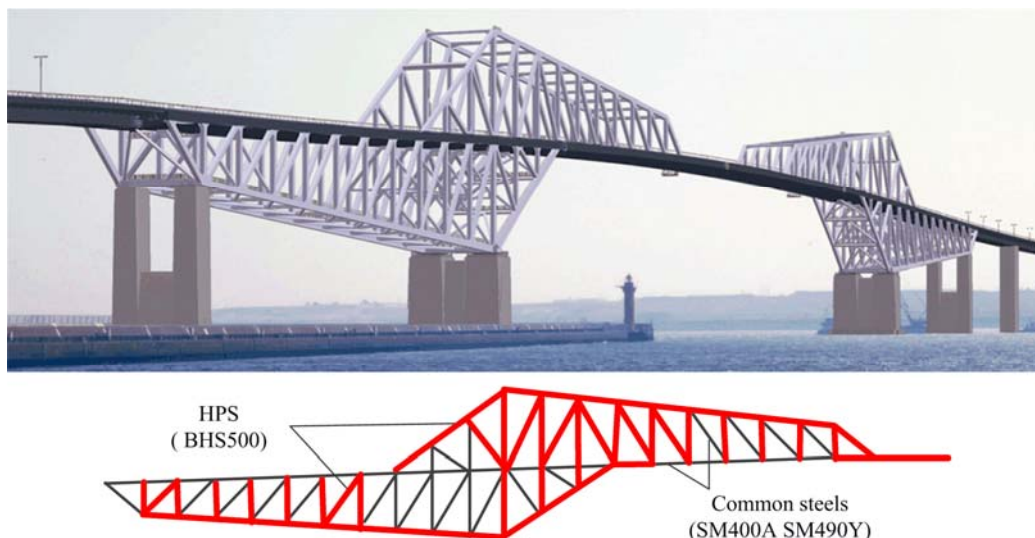


Figure 21. Application of High Performance Steel in Tokyo Rinkai Chuo Bridge (adapted from [40])

Table 4. Preheating Requirements for BHS Steels and Common Steels

Strength (MPa)	Type	Classification	Thickness			
			t≤25	25<t≤40	40<t≤50	50<t≤100
570	SM570	Standard P _{cm}	0.26 (no preheating)	0.27 (80°)		0.27 (100°)
		No need to preheating P _{cm}	-	0.24	0.22	
	BHS500	P _{cm}	≤0.20 (no need to preheating)			
	BHS500W	P _{cm}	≤0.20 (no need to preheating)			
780	HT80		t≤25	25<t≤38	38<t≤50	50<t≤75
		Standard temp. (°)	100	100	100	120
	BHS700W	Min. preheating temp. (°)	50			

4. SOCIAL AND ACADEMIC IMPACTS OF HPSS

A number of high performance steels (HPSs) in Japan have been discussed in this study. These steels have great impacts on the whole society, such as:

- (1) low construction and maintenance costs for steel structures;
- (2) safer structures for the improved mechanical properties such as more stable yield strength and higher toughness;
- (3) rapid construction speed;
- (4) more feasibility for challenging structural proposals, e.g., high strength steel makes larger scaled structures possible.

There are also significant impacts on academic research of structural engineering, such as:

- (1) new design methods for structures made of HPS;
- (2) innovative structural systems;
- (3) new energy dissipation components;
- (4) new connecting technologies.

More research efforts are still required to promote the developments of these new technologies, and there is great potential for the application of HPS in future.

ACKNOWLEDGEMENTS

The study is supported in part by grants from the Advanced Research Center for Natural Disaster Risk Reduction, Meijo University, which supported by Ministry of Education, Culture, Sports, Science and Technology (MEXT), Japan. This study is also partially supported by National Nature Science Foundation of China (51508401) and the Fundamental Research Funds for the Central Universities.

REFERENCES

- [1] Kitada, T., "Considerations on Recent Trends in, and Future Prospects of, Steel Bridge Construction in Japan", Journal of Constructional Steel Research, 2006, Vol. 62, No. 11, pp. 1192-1198.
- [2] Bjorhovde, R., "Development and Use of High Performance Steel", Journal of Constructional Steel Research, 2004, Vol. 60, No. 3-5, pp. 393-400.
- [3] Raoul, J. and Günther, H.-P., "Use and Application of High-performance Steels for Steel Structures", IABSE, 2005.
- [4] Bjorhovde, R., "Performance and Design Issues for High Strength Steel in Structures", Advances in Structural Engineering, 2010, Vol. 13, No. 3, pp. 403-411.

- [5] Miki, C., Homma, K. and Tominaga, T., "High Strength and High Performance Steels and Their Use in Bridge Structures", *Journal of Constructional Steel Research*, 2002, Vol. 58, No. 1, pp. 3-20.
- [6] JSCE, "High Performance Steel for Seismic Design and High Ductility Structures". Japan Society of Civil Engineers, 2000.
- [7] Ohata, M., "New Structural System Constructed Using New High-strength Steel Aiming for Non-damage during a Large Earthquake", *Proceedings of 10th Korea-China-Japan Symposium on Structural Steel Construction*, Seoul, South Korea, 2009, pp. 193-204.
- [8] Mahin, S.A., "Lessons from Damage to Steel Buildings during the Northridge Earthquake", *Engineering Structures*, 1998, Vol. 20, No. 4-6, pp. 261-270.
- [9] Bruneau, M., Wilson, J.C. and Tremblay, R., "Performance of Steel Bridges during the 1995 Hyogo-ken Nanbu (Kobe, Japan) Earthquake", *Canadian Journal of Civil Engineering*, 1996, Vol. 23, No. 3, pp. 678-713.
- [10] AIJ, "Fracture in Steel Structures during a Severe Earthquake", Architectural Institute of Japan, Tokyo, 1995.
- [11] Kuwamura, H., "Fracture of Steel during an Earthquake—State-of-the-Art in Japan", *Engineering Structures*, 1998, Vol. 20, No. 4-6, pp. 310-322.
- [12] Kuwamura, H. and Yamamoto, K., "Ductile Crack as Trigger of Brittle Fracture in Steel", *Journal of Structural Engineering (ASCE)*, 1997, Vol. 123, No. 6, pp. 729-735.
- [13] Usami, T. and Ge, H.B., "A Performance-based Seismic Design Methodology for Steel Bridge Systems", *Journal of Earthquake and Tsunami*, 2009, Vol. 3, No. 03, pp. 175-193.
- [14] Ge, H.B. and Kang, L., "A Damage Index-based Evaluation Method for Predicting the Ductile Crack Initiation in Steel Structures", *Journal of Earthquake Engineering*, 2012, Vol. 16, No. 5, pp. 623-643.
- [15] Ge, H.B. and Kang, L., "Ductile Crack Initiation and Propagation in Steel Bridge Piers Subjected to Random Cyclic Loading", *Engineering Structures*, 2014, Vol. 59, pp. 809-820.
- [16] Ge, H.B., Kang, L. and Tsumura, Y., "Extremely Low-cycle Fatigue Tests of Thick-walled Steel Bridge Piers", *Journal of Bridge Engineering*, 2013, Vol. 18, No. 9, pp. 858-870.
- [17] Ge, H.B., Ohashi, M. and Tajima, R., "Experimental Study on Ductile Crack Initiation and Its Propagation in Steel Bridge Piers of Thick-walled Box Sections", *J. Struct. Eng. JSCE A*, 2007, Vol. 53, pp. 493-502.
- [18] Kang, L. and Ge, H.B., "Predicting Ductile Crack Initiation of Steel Bridge Structures due to Extremely Low-cycle Fatigue using Local and Non-local Models", *Journal of Earthquake Engineering*, 2013, Vol. 17, No. 3, pp. 323-349.
- [19] Chi, W., Deierlein, G. and Ingraffea, A., "Fracture Toughness Demands in Welded Beam-column Moment Connections", *Journal of Structural Engineering (ASCE)*, 2000, Vol. 126, No. 1, pp. 88-97.
- [20] Dexter, R. and Melendrez, M., "Through-thickness Properties of Column Flanges in Welded Moment Connections", *Journal of Structural Engineering (ASCE)*, 2000, Vol. 126, No. 1, pp. 24-31.
- [21] JISF, "Safety of Steel Structures Concerning Seismic Design, Tsunami Resistant Design and Steel", The Japan Iron and Steel Federation (JISF), Tokyo, 2013.
- [22] El-Tawil, S., Mikesell, T. and Kunnath, S., "Effect of Local Details and Yield Ratio on Behavior of FR Steel Connections", *Journal of Structural Engineering (ASCE)*, 2000, Vol. 126, No. 1, pp. 79-87.
- [23] JIS. G3163, "Rolled Steels for Building Structure", Japanese Industrial Standards Committee, Tokyo, 2012.
- [24] Nakamura, Y., Kambara, H., Nakai, M. and Maeda, Y., "Proposal for Design Method of Damage Free Structure Utilizing Super High Strength Steel: Part I: Study on Design Input Earthquakes of JMA Seismic Intensity 7". *Summaries of Technical Papers of Annual Meeting Architectural Institute of Japan*, Architectural Institute of Japan, 2007, pp. 201-202.

- [25] Aburakawa, M. and Nakai, M., "Design Method of New Building System (The Collaborative Project by Cabinet and Ministries)", Journal of the Japan Welding Society, 2009, Vol. 78, No. 7, pp. 605-611.
- [26] Nakai, M., Tsuda, K., Mase, S., Narihara, H., Okayasu, T., Asai, H. and Suzuki, Y., "Performance Verification Through Full-scale Static Loading Tests for a Structural System using High Strength Steel", Journal of Structural and Construction Engineering (Transactions of AIJ), 2013, Vol. 78, No. 687, pp. 1007-1016.
- [27] Kawabata, T., Arimochi, K., Hashida, T., Numata, T., Kohzu, I., Tada, M., Kuwahara, S. and Taga, K., "Investigation on Application of 1000N Class Ultra High Strength Steel for Buildings : Part 1. Evaluation of Properties of Base Plate", Summaries of Technical Papers of Annual Meeting Architectural Institute of Japan. A-1, Materials and construction, 2005, pp. 97-98.
- [28] Sasaki, M., Ichinohe, Y., Nishio, M., Numata, T., Hashida, T., Kohzu, I., Tada, M., Kuwahara, S. and Taga, K., "Investigation on Application of 1000N Class Ultra High Strength Steel for Buildings : Part 4. Outline of Tests and Performance of Developed Steel", Summaries of Technical Papers of Annual Meeting Architectural Institute of Japan. C-1, Structures III, Timber Structures Steel Structures Steel Reinforced Concrete Structures, 2007, pp. 889-890.
- [29] Yasumura, M., Mukaide, S., Tada, M., Kohzu, I., Ichinohe, Y., Sasaki, M., Taga, K. and Numata, T., "Investigation on Application of 1000N Class Ultra High Strength Steel for Building: Part 8. Analytical Investigation on Local Buckling Properties of H-section Column", Summaries of Technical Papers of Annual Meeting Architectural Institute of Japan. C-1, Structures III, Timber Structures Steel Structures Steel Reinforced Concrete Structures, Vol. 2007, pp. 897-898.
- [30] Murakami, Y., Sugimoto, M. and Fukuda, K., "Recent Trend of Structural Steel Development: Application of Ultra-high Strength Steel to Building Structures", Journal of Steel Structures & Construction (JSSC), 2014, No. 17, pp. 42-46.
- [31] Suzui, Y., Niwa, H., Fuchita, Y., Tokinoya, H., Yamanaka, M. and Endo, F., "Ultra High Strength Concrete-filled Steel Tube Column", Report of Obayashi Corporation Technical Research Institute, Tokyo, 2010.
- [32] JISF, "Amagasaki Research and Development Center—Employing 1000 N-grade Steel", Steel Construction Today & Tomorrow, 2010, No. 38, pp. 2.
- [33] Steel Club. "Fireproofing Structural Steel for Building Structures", The Japan Iron and Steel Federation, Tokyo, 2000.
- [34] JIS. G0201, "Glossary of Terms used in Iron and Steel (Heat Treatment)", Japanese Industrial Standards Committee, Tokyo, 2000.
- [35] JRA. "Specification for Highway Bridges", Japan Road Association, Tokyo, 2012.
- [36] Fujisawa, K., "State of Art for High Performance Steel", Steel Construction Symposia, Tokyo, 2013.
- [37] JIS. G3199, "Specification for Through-thickness Characteristics of Steel Plate, Wide Flat and Sections", Japanese Industrial Standards Committee, Tokyo, 2009.
- [38] Miki, C., Ichikawa, A., Kusunoki, T. and Kawabata, F., "Proposal of New High Performance Steels for Bridges (BHS500, BHS700)", Journal of Structural Mechanics and Earthquake Engineering, Japan Society of Civil Engineers, 2003, No. 738, pp. 1-10.
- [39] JIS. G3140, "Higher Yield Strength Steel Plates for Bridges", Japanese Industrial Standards Committee, Tokyo, 2011.
- [40] Wada, K., Tanaka, K. and Kodama, Y., "Project of Tokyo-Port Seaside Bridge", Kawada Technical Report, Tokyo, 2009.

STATIC BEHAVIOR OF AXIALLY COMPRESSED CIRCULAR CONCRETE FILLED CFRP-STEEL TUBULAR (C-CF-CFRP-ST) COLUMNS WITH MODERATE SLENDERNESS RATIO

Q.L. Wang^{1,*}, S.E. Qu², Y.B. Shao³ and L.M. Feng⁴

¹ Professor, School of Civil Engineering, Shenyang Jianzhu University, Shenyang, P. R. China

² Graduate Student, School of Civil Engineering, Shenyang Jianzhu University, Shenyang, P. R. China

³ Professor, School of Mechatronic Engineering, Southwest Petroleum University, Chengdu, P. R. China

⁴ Graduate Student, School of Civil Engineering, Shenyang Jianzhu University, Shenyang, P. R. China

*(Corresponding author: E-mail: ceqlwang@sjzu.edu.cn)

Received: 19 January 2015; Revised: 7 October 2015; Accepted: 5 January 2016

ABSTRACT: Thirty-two specimens are experimentally tested in this paper to study the static performance of axially compressed circular concrete filled CFRP-steel tubular (C-CF-CFRP-ST) columns. The tested results indicate that, for columns with relative small slenderness ratio, failure is dominated by the strength loss of the materials. However, for columns with relative large slenderness ratio, failure is controlled by instability. The load versus deflection curves at the mid-height of the composite column can be divided into three stages, i.e., elastic, elasto-plastic and softening stage. Analyses of the tested results show that distribution of longitudinal strains in the steel tube over depth on the cross-section is approximately linear, and the steel tube and its outer CFRP material can cooperate both longitudinally and transversely. The longitudinal strain and the transverse strain at a point have opposite signs, and the steel tube under longitudinal tension has no transverse confinement effect on its concrete. The Deformed modes of the columns, the axial load versus deflection curves at the mid-height, the axial load versus axial shortening curves and the stresses in the steel tube are simulated by using finite element method. The calculated results agree well with the experimental results to prove the accuracy of the finite element model. Stresses in the concrete, the steel tube and the CFRPs are analyzed by using finite element method. The numerical results show that the interaction force between the steel tube and the concrete decreases gradually from compressive region to tensile region. The adhesive strength between the concrete and the steel tube has little effect on the critical buckling load and on the elastic stiffness of the columns. Equation for calculating the critical buckling load of the composite columns is presented, and the estimated results agree well with the experimental results.

Keywords: Circular CFRP-steel tube, In-filled concrete, Axially compressed columns with moderate slenderness ratio, Static performance, Critical buckling load

DOI:10.18057/IJASC.2016.12.3.4

1. INTRODUCTION

Fiber Reinforced Plastic (FRP) has been used in many engineering structures due to its advantages of high strength/weight ratio, good corrosion resistance, ease of installation, more and more cheaper cost and so on, in which Concrete Filled FRP Tubular (CF-FRP-T) structure or FRP strengthened concrete structure is a typical example. There are many research reports on CF-FRP-T (Wang and Restrepo [1]; Fam and Rizkalla [2]; Teng et al. [3]; Karabinis et al. [4]; Rousakis et al. [5]; Yu. et al. [6]; Yu. et al. [7]; Jiang and Wu [8]). CF-FRP-T structures have better corrosion resistance. However, the failure mode of CF-FRP-T structures has brittle characteristics in most cases, and the load carrying capacity in the transverse direction for this structure is weak.

As one typical style of the steel-concrete composite structures, Concrete Filled Steel Tubular (CFST) structures are widely used in civil engineering, and they show good constructional efficiency. The research work in this field has been studied systematically in the literature. Besides the systematic investigations on the static and the hysteretic behavior of the components and the connections (Han [9]; Han et al. [10]; Han et al. [11]; Han et al. [12]; Han and Li [13]), fire resistance (Han [14]), torsion performance (Han et al. [15]) and local compression (Han et al. [16])

of this structure are also reported. Comparing with the CF-FRP-T, CFST has higher shearing load carrying capacity. However, the outer surface corrosion of the steel tube cannot be ignored when CFST is used in a corrosive environment, and some corresponding research studies in this field have been reported in recent years (Han et al. [17]; Han et al. [18]).

In many engineering fields, the FRP-metal composite tanks or tubes have been used widely, such as gas tank used in motor vehicle (as shown in Figure 1, where GFRP refers to Glass Fiber Reinforced Plastic) and pipeline system for transporting high pressure gas or liquid used in municipal engineering or chemical engineering. Sometimes, petroleum pipeline system after corrosion is also reinforced with CFRP (Carbon Fiber Reinforced Plastic), which can save much cost compared to the measure of replacing the corroded tube with a new one. CFRP-metal tube can also be used in civil engineering, for example, by infilling concrete into CFRP-steel composite tube (Che et al. [19]), or by using CFRP to strengthen damaged CFST (Tao et al. [20]). Both of the above methods can form the so-called Concrete Filled CFRP-Steel Tubular (CF-CFRP-ST) structures. CF-CFRP-ST structures have the advantages of both the CFST and the CF-FRP-T structures, and the CF-CFRP-ST structures can also avoid the respective deficiency of the CFST and the CF-FRP-T structures to some degree. Recent study shows that CF-CFRP-ST has satisfactory fire endurance time when adequate fire resistant measures have been taken (Tao et al [21]).

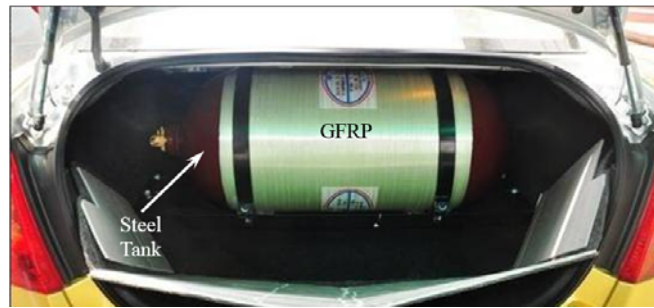


Figure 1. Gas Tank Used in Motor Vehicle



Figure 2. An Engineering Practice of C-CF-CFRP-ST Columns Used in Nanjing City, Jiangsu Province, P. R. China

There are many research studies about CF-CFRP-ST structures in the literature, and these studies mostly focus on Circular CF-CFRP-ST (C-CF-CFRP-ST) stub columns (Xiao et al. [22]; Choi and Xiao [23]; Park et al. [24]; Hu et al. [25]; Li et al. [26]; Teng et al. [27]), C-CF-CFRP-ST flexural members (Wang and Shao [28]), Square CF-CFRP-ST (S-CF-CFRP-ST) stub columns (Tao et al

[29]; Park et al. [30]; Sundararaja and Ganesh [31]; Sundararaja and Ganesh [32]; Sundararaja and Ganesh [33]; Wang and Shao [34]) and S-CF-CFRP-ST flexural members (Sundararaja and Ganesh [35]; Wang et al. [36]). More applications in practical engineering are columns with large slenderness ratio (as shown in Figure 2) although corresponding research is quite scarce. For axially compressed stub columns (slenderness ratio $\lambda \leq 3$), compressive buckling does not occur in general, and its load carrying capacity is determined by the material properties and the combination effect, while for axially compressed columns with moderate slenderness ratio, i. e., $\lambda > 3$, its critical buckling load is generally determined by stability, which is necessary to be studied specially.

To understand the static performance of the axially compressed C-CF-CFRP-ST columns with moderate slenderness ratio, 32 composite specimens with both transverse CFRP and longitudinal CFRP are tested and the details are introduced in this paper. Axial load (N) versus deflection at the mid-height (u_m) curves, cooperation between the steel tube and the CFRP and plane section assumption of the composite specimens are analyzed. Furthermore, the finite element software ABAQUS is used to simulate the deformed modes and the N - u_m curves of the composite columns. The distributions of the stress and the strain, the effects of adhesive strength between the steel tube and the concrete, and the interaction force (p) between the concrete and the steel tube are also analyzed. Finally, the equation for calculating the critical buckling load of the axially compressed C-CF-CFRP-ST columns with moderate slenderness ratio is given.

2. EXPERIMENTAL PROGRAM

2.1 General

In overall, tests on 32 axially compressed C-CF-CFRP-ST columns are conducted, and the basic parameters considered for these specimens include λ and strengthening factor of the longitudinal CFRP (η) (Wang and Shao [28]), respectively, where

$$\lambda = 4L/D_s \quad (1)$$

$$\eta = A_{\text{cfl}} f_{\text{cfl}} / (A_s f_y) \quad (2)$$

$$f_{\text{cfl}} = E_{\text{cf}} \varepsilon_{\text{cflr}} = 2300 \text{MPa} \quad (3)$$

where L is the length of the column; D_s is the outer diameter of the steel tube. A_{cfl} and f_{cfl} are the cross-sectional area and the ultimate tensile strength of the longitudinal CFRP, respectively. A_s and f_y are the cross-sectional area and the yield strength of the steel tube, respectively. E_{cf} and $\varepsilon_{\text{cflr}}$ are the elasticity modulus of CFRP and the rupture strain of the longitudinal CFRP, respectively. In this study, $\varepsilon_{\text{cflr}} = 10000 \mu\epsilon$, and the determination of $\varepsilon_{\text{cflr}}$ can be referred to the corresponding reference (Wang and Shao [28]).

The specimens' details are provided in Table 1. In the nomenclature of the specimens as listed in Table 1, CC means Circular Column. Letters A, B, C, D, E, F, G and H denote the different lengths of the columns: 400mm, 530mm, 600mm, 800mm, 1200mm, 1800mm, 2400mm and 3000mm, respectively. Number 0, 1, 2 or 3 refers to the number of the longitudinal CFRP layer(s) (m'). m is

number of the transverse CFRP layer. t_s is the wall thickness of the steel tube, and $N_{u,cr}^t$ is the tested value of the critical buckling load of the C-CF-CFRP-ST columns. ξ_s is the confinement factor of the steel tube (Han [9]). ξ_{cf} is the confinement factor of the transverse CFRP tube (Che et al. [19]), where

$$\xi_s = A_s f_y / (A_c f_{ck}) \quad (4)$$

$$\xi_{cf} = A_{cft} f_{cft} / (A_c f_{ck}) \quad (5)$$

$$f_{ck} = 0.67 f_{cu} \quad (6)$$

$$f_{cft} = E_{cf} \varepsilon_{cfr} = 1265 \text{ MPa} \quad (7)$$

where A_c and f_{ck} are the cross-sectional area and the characteristic axial compressive strength of the concrete, respectively. A_{cft} and f_{cft} are the cross-sectional area and the ultimate tensile strength of the transverse CFRP, respectively. f_{cu} is the cubic strength of the concrete specimen. ε_{cfr} is the rupture strain of the transverse CFRP ($\varepsilon_{cfr} = 5500 \mu\epsilon$) and the determination of ε_{cfr} can be referred to the corresponding reference (Che et al. [19]).

2.2 Specimen Preparations

Fabrication of Circular CFST (C-CFST) specimens can be found in relative reference (Han [9]). Carbon fiber sheets are applied using a hand lay-up method. The longitudinal CFRP is glued firstly, and then the transverse CFRP is glued. The finishing end of a sheet is overlapped to the starting end of the other sheet with an overlapped length of 150 mm.

Table 1. Specimen Labels and Capacities

No.	Specimens label	L (mm)	λ	m' (layer(s))	η	m (layer)	ξ_{cf}	D_s (mm)	t_s (mm)	ξ_s	$N_{u,cr}^t$ (kN)
1	CC A-0	400	12	0	0	1	0.13	133	5	1.3	2085
2	CC A-1	400	12	1	0.18	1	0.13	133	5	1.3	2118
3	CC A-2	400	12	2	0.35	1	0.13	133	5	1.3	2119
4	CC A-3	400	12	3	0.53	1	0.13	133	5	1.3	2206
5	CC B-0	530	16	0	0	1	0.13	133	5	1.3	2040
6	CC B-1	530	16	1	0.18	1	0.13	133	5	1.3	1947
7	CC B-2	530	16	2	0.35	1	0.13	133	5	1.3	2016
8	CC B-3	530	16	3	0.53	1	0.13	133	5	1.3	2094
9	CC C-0	600	18	0	0	1	0.13	133	4.5	1.3	1721
10	CC C-1	600	18	1	0.18	1	0.13	133	4.5	1.3	1756
11	CC C-2	600	18	2	0.35	1	0.13	133	4.5	1.3	1831
12	CC C-3	600	18	3	0.53	1	0.13	133	5	1.3	2090
13	CC D-0	800	24	0	0	1	0.13	133	4.5	1.3	1682

14	CC D-1	800	24	1	0.18	1	0.13	133	4.5	1.3	1724
15	CC D-2	800	24	2	0.35	1	0.13	133	4.5	1.3	1780
16	CC D-3	800	24	1	0.53	1	0.13	133	5	1.3	2035
17	CC E-0	1200	36	2	0	1	0.13	133	4.5	1.3	1445
18	CC E-1	1200	36	1	0.18	1	0.13	133	4.5	1.3	1500
19	CC E-2	1200	36	2	0.35	1	0.13	133	4.5	1.3	1560
20	CC E-3	1200	36	3	0.53	1	0.13	133	5	1.3	1914
21	CC F-0	1800	54	0	0	1	0.13	133	4.5	1.3	1222
22	CC F-1	1800	54	1	0.18	1	0.13	133	4.5	1.3	1281
23	CC F-2	1800	54	2	0.35	1	0.13	133	4.5	1.3	1358
24	CC F-3	1800	54	3	0.53	1	0.13	133	5	1.3	1704
25	CC G-0	2400	72	0	0	1	0.13	133	5	1.3	1387
26	CC G-1	2400	72	1	0.18	1	0.13	133	5	1.3	1409
27	CC G-2	2400	72	2	0.35	1	0.13	133	5	1.3	1428
28	CC G-3	2400	72	3	0.53	1	0.13	133	5	1.3	1613
29	CC H-0	3000	90	0	0	1	0.13	133	5	1.3	1296
30	CC H-1	3000	90	1	0.18	1	0.13	133	5	1.3	1174
31	CC H-2	3000	90	2	0.35	1	0.13	133	5	1.3	1243
32	CC H-3	3000	90	3	0.53	1	0.13	133	5	1.3	1467

2.3 Material Properties

Seamless steel tube is in the columns. Tensile tests on steel coupons cut from the original steel tubes are conducted. The measured properties of the steel tubes obtained from these tests are given in Table 2, where E_s and ν_s are the elasticity modulus and the Poisson's ratio of the steel tube, respectively.

Table 2. Material Properties of Steel Tube

t_s (mm)	E_s (GPa)	f_y (MPa)	ν_s
4.5	206	333	0.27
5	204	303	0.26

The in-filled concrete of all the specimens has same material property. In the concrete mixture, Portland cement is used, and the fine aggregate is silica-based sand. The coarse aggregate is limestone with a largest size of 20mm, and 1% (in weight) water reducing agent is added. The mixture proportions of the concrete are summarized in Table 3.

Table 3. Mixture Proportions of Concrete ($\text{kg}\cdot\text{m}^{-3}$)

Cement	Water	Sand	Course aggregate
485	150	703	1062

To determine the compressive strength of the in-filled concrete, six cubes with a side length of 150 mm are cast and cured in conditions similar to those of the related specimens. The averaged cubic

strength (f_{cu}) at 28 days is 48.8 MPa. At the testing time (six months later due to the delay of the test program), the cubic strength of 57.4 MPa is achieved and is adopted in later FE simulation and calculation. Elasticity modulus of the concrete (E_c) is 35.9 GPa.

Carbon fiber sheet used in the specimens is a kind of one-way sheet, and the properties of the CFRP determined from tensile tests of six flat coupons are given in Table 4, in which f_{cf}' , δ_{cf} and w_{cf} are the tensile strength, the elongation percentage and the density of the carbon fiber sheet, and t_{cf} is the thickness of one-layer carbon fiber sheet.

Table 4. Main Technical Properties of Carbon Fiber Sheets

Model number	f_{cf}' (GPa)	E_{cf} (GPa)	δ_{cf} (%)	w_{cf} (g·m ⁻²)	t_{cf} (mm)
C200/200	4.83	230	2.1	200	0.111

It should be pointed out that the rupture strain of the coupon CFRP is 21000 $\mu\epsilon$ while the rupture strains of the longitudinal CFRP $\epsilon_{cfr}=10000\mu\epsilon$ and that of the transverse CFRP $\epsilon_{cfr}=5500\mu\epsilon$. Such difference is possibly caused by different curvatures at CFPR positions, and the relative research (Yu et al. [37]) provided similar conclusion.

JGN-C, a typical kind of epoxy resin, which is produced by Building Science Research Institute of Liaoning Province of China and is used for building structures, is selected for adhering the CFRP to the steel tube. Another kind of epoxy resin, JGN-P, is used for gluing CFRPs together.

2.4 Test Setup and Instrumentation

The experimental test is carried out in the Structural Laboratory of Shenyang Jianzhu University, P. R. China. The critical buckling load of the specimen is predicted before the specimen is loaded: the transverse and the longitudinal CFRPs are simplified to equivalent steel tube, and then the critical buckling load can be calculated by using corresponding equations of C-CFST columns (Han et al. [11]). However, the equivalent steel tube besides longitudinal CFRP is not considered in calculating the confinement factor of the steel tube ξ_s .

The test setup is shown in Figure 3. The specimen is pinned at both ends. A instrument with a loading capacity of 5,000kN is used to apply axial compressive load N . The load is applied in many loading steps. In the elastic stage, each loading step is 1/10 of the estimated critical buckling load. When the applied load is about 60% of the estimated critical buckling load, the magnitude of the loading step is reduced to 1/15-1/20 of the estimated critical buckling load. After the deflection at the mid-height exceeds $L/50$, displacement control is used till the deflection at the mid-height reaches about $L/25$. The interval between two continuous loading steps is maintained for about 2 to 3 min.

As shown in Figure 3, 3-5 Linear Variable Differential Transformers (LVDTs) are placed in the bending plane with equal distance in the height direction according to different heights of the specimens to measure the lateral deflection. Simultaneously, two LVDTs are used to measure the longitudinal compression of the specimens. Overall, 11 strain gauges are glued on the surfaces of each steel tube and on the CFRP at the mid-height of the specimens respectively, as shown in Figure 4, where points 1-7 are the locations for measuring the longitudinal strains and points 1, 3, 5 and 8 are the locations for measuring the transverse strains.

The data is captured by Data Acquisition System U-CAM-70A, and the $N-u_m$ curve is achieved simultaneously.



Figure 3. Test Arrangement (Specimen CC H-1)

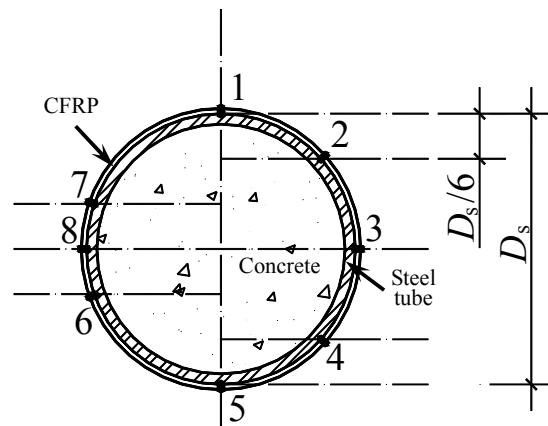


Figure 4. Location of Strain Gauges

2.5 Test Observations and Failure Modes

The failure of the specimens is mainly determined by the slenderness ratio (λ). For specimens with small λ , transverse CFRP located in longitudinal compressive region at the mid-height begins to fracture at a loading about $0.85 N_{u,cr}^t$. With the increase of the applied load, the amount of fractured transverse CFFPs becomes bigger (as shown in Figure 5 (a)) till the applied load reaches $N_{u,cr}^t$. Longitudinal CFRP located in longitudinal tensile region at the mid-height is not fractured in general, and the specimens have local outward buckling (as shown in Figure 5 (a)) which indicates a symbol of strength failure. For specimens with large λ , transverse CFRP located in longitudinal compressive region at the mid-height begins to fracture after $N_{u,cr}^t$. With the increase of the deflection, the longitudinal CFRP located in longitudinal tensile region at the mid-height begins to fracture (as shown in Figure 5 (b)). Finally, the specimens fail and the steel tube does not buckle outward and forms an instability failure. All specimens after failure are shown in Figure 6.

The CFRP-steel composite tubes are cut off after test. As shown in Figure 7, it is found that the concrete could be divided into both tensile and compressive regions. For specimens with small λ ,

the failure of the concrete is severe, and the concrete in the compressive region is crushed (as shown in Figure 7 (a)). In the tensile region, the concrete crack has a big width, and the distance between any two adjacent cracks is small (as shown in Figure 7 (b)). For specimens with large λ , the concrete failure is not severe, and thus the concrete in compressive region is almost not damaged (as shown in Figure 7 (c)). The crack in tensile region has a narrow width, and the distance between any two adjacent cracks is bigger (as shown in Figure 7 (d)).

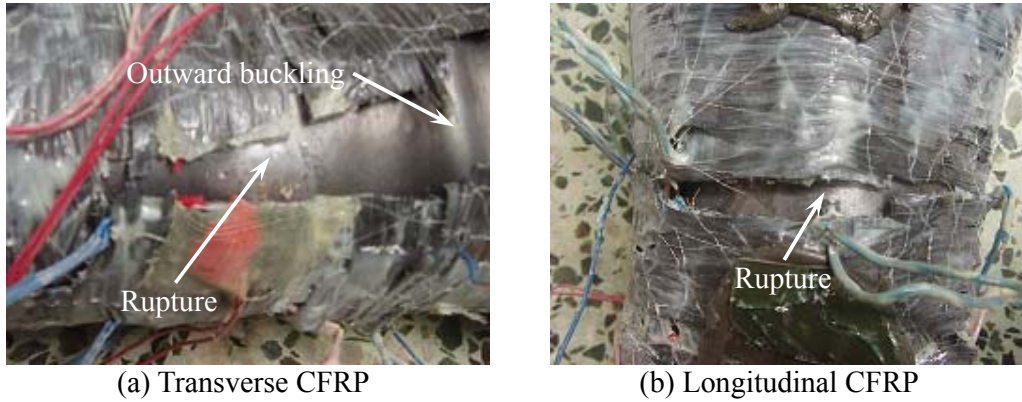


Figure 5. Rupture of CFRPs and Local Buckling



Figure 6. All Specimens after Testing

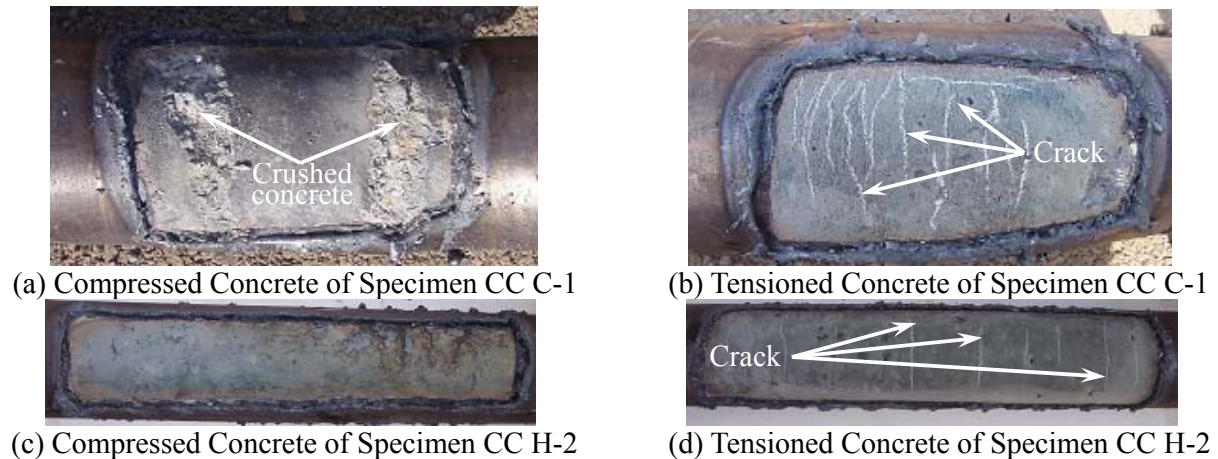


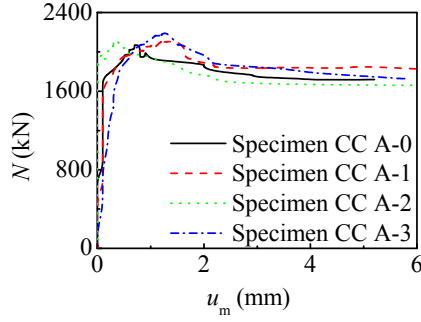
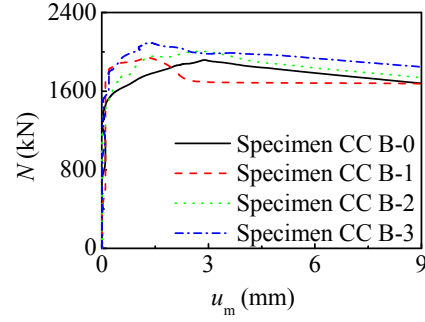
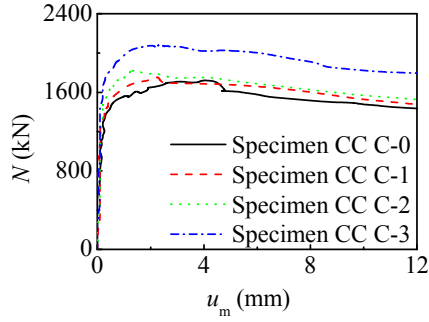
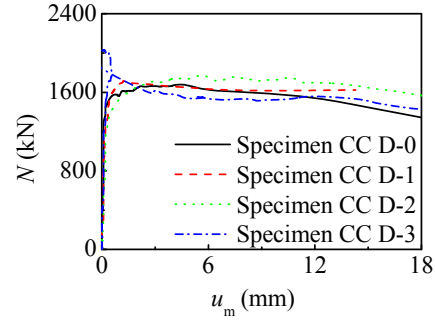
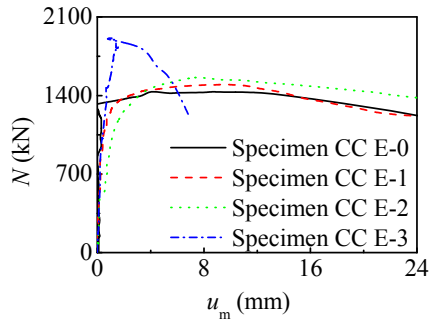
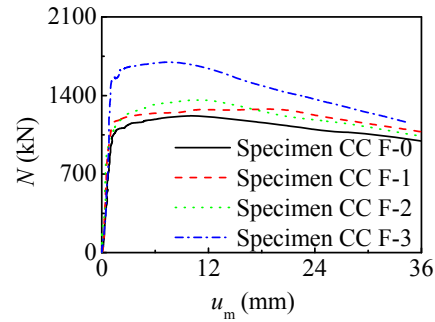
Figure 7. Failure Modes of Concrete

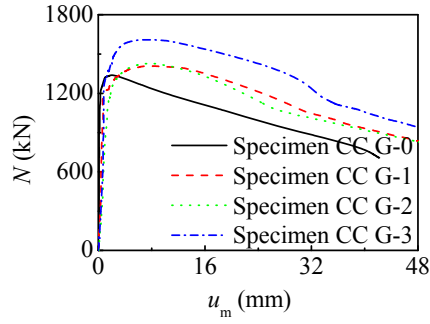
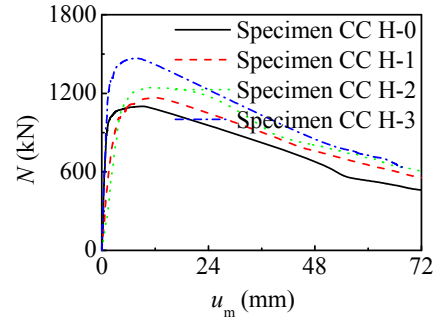
2.6 Test Results and Analysis

2.6.1 Tested $N-u_m$ curves

Figure 8 shows the $N-u_m$ curves of the specimens, and it can be found that these $N-u_m$ curves

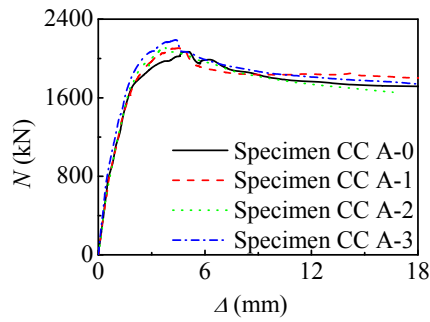
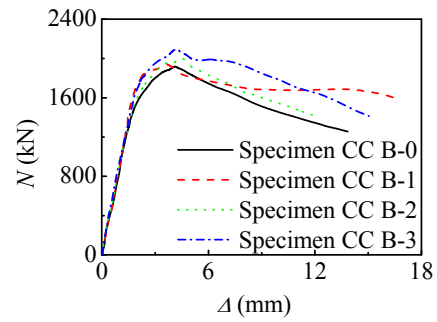
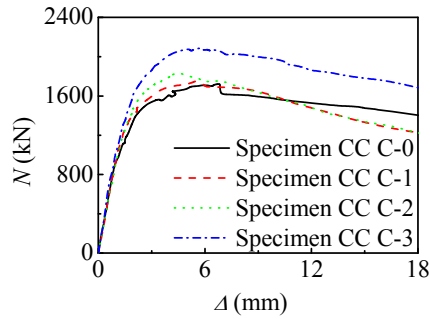
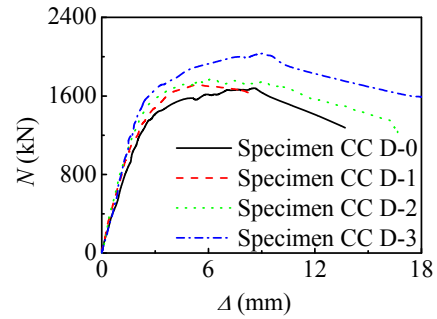
have the following characteristics: the curves develop linearly in initial loading stage, and this period belongs to an elastic stage. The following stage is elasto-plastic stage in which the developing rate of u_m is apparently faster than that of N . The curves begin to drop after $N_{u,cr}^t$, and in this stage the increase of u_m is much faster while the decrease of N is gradual.

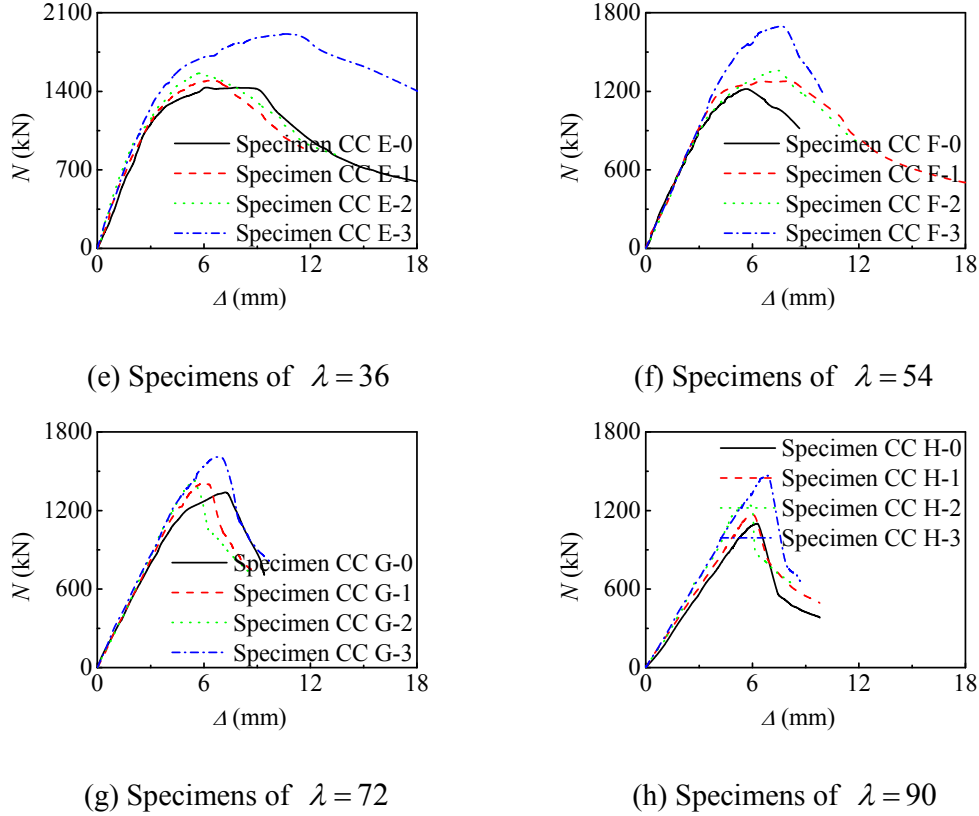
(a) Specimens of $\lambda = 12$ (b) Specimens of $\lambda = 16$ (c) Specimens of $\lambda = 18$ (d) Specimens of $\lambda = 24$ (e) Specimens of $\lambda = 36$ (f) Specimens of $\lambda = 54$

(g) Specimens of $\lambda = 72$ (h) Specimens of $\lambda = 90$ Figure 8. Tested $N-u_m$ Curves

2.6.2 Tested $N-\Delta$ curves

Figure 9 shows the $N-\Delta$ curves of the specimens, where Δ is the axial shortening of the specimen.

(a) Specimens of $\lambda = 12$ (b) Specimens of $\lambda = 16$ (c) Specimens of $\lambda = 18$ (d) Specimens of $\lambda = 24$

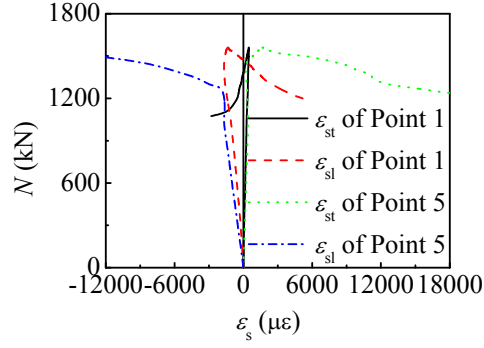
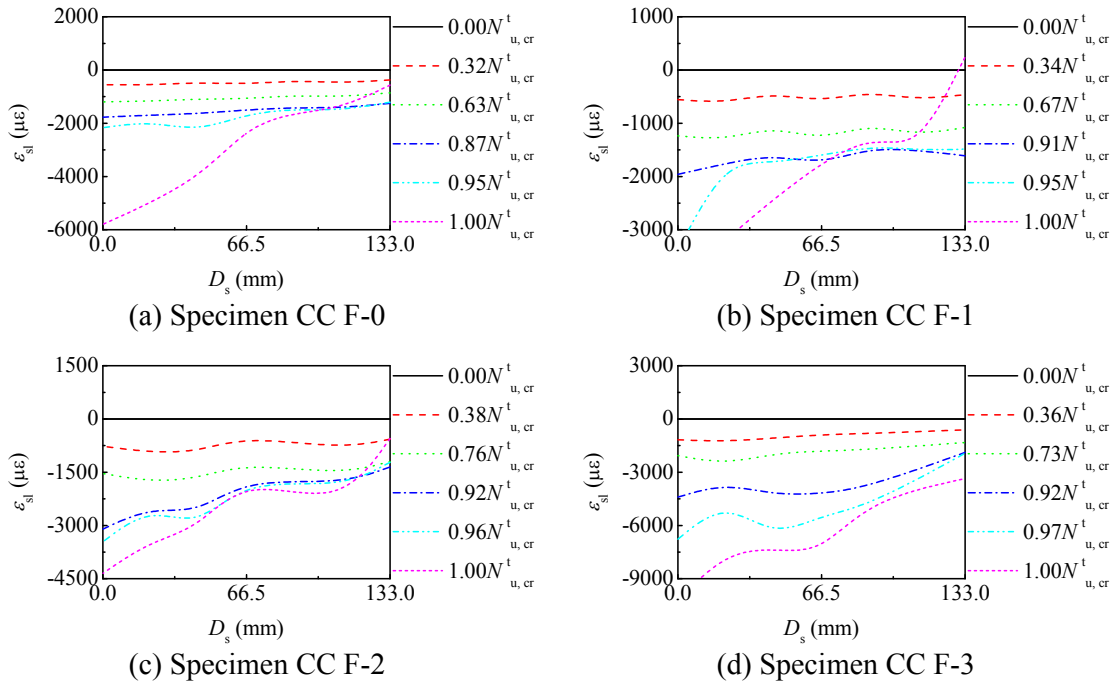
Figure 9. Tested N - Δ Curves

2.6.3 Comparison between longitudinal Strain and Transverse Strain

Figure 10 shows comparison between ε_{sl} (longitudinal strain of the steel tube) and ε_{st} (transverse strain of the steel tube) at point 1 and point 5 for specimen CC E-2, where ε_s is the strain of the steel tube. The signs of ε_{sl} and ε_{st} at same point are different: it is negative in longitudinal direction while positive in transverse direction and vice versa. Studies on CF-CFRP-ST stub column (Che et al. [19]; Wang and Shao [34]) and CF-CFRP-ST flexural member (Wang and Shao [28]; Wang et al. [36]) provided same conclusions. It can also be found that point 1 on the steel tube is under tension longitudinally and under compression transversely after $N_{u,cr}^t$, which makes it clear that this point together with the around steel tube has no confinement to concrete, and the reason may be listed as follow: the nearby concrete is also in a tensile state when the steel tube is under tension in longitudinal direction, and thus it does not need transverse confinement provided from steel tube. The transverse strain of the steel tube is under compression due to the corresponding tension in longitudinal direction.

2.6.4 Plane Section Assumption

Figure 11 shows the distribution of ε_{sl} over the depth on the cross-section of the specimen with a slenderness ratio $\lambda = 24$. As shown in Figure 11, the distribution of ε_{sl} is basically satisfied with the plane section assumption. Studies on CF-CFRP-ST flexural member (Wang and Shao [28]; Wang et al. [36]) provided same conclusions.

Figure 10. Comparisons between ε_{sl} and ε_{st} of Point 1 and Point 5 for Specimen CC E-2Figure 11. Distribution of ε_{sl} over Depth of Cross-Section for $\lambda = 24$ Specimens

3. FE SIMULATION

3.1 Stress-Strain Relationship of Materials

A 5-stage stress-strain relationship of steel material (Han et al. [10]) is used in the FE simulation. The constitutive relationships of the concrete confined by circular CFRP-steel tube under compression as well as under tension (Che et al. [19]) are adopted. The CFRP is assumed to be subjected to tension only, and the stresses in other directions are assumed to be 0.001MPa. Before fracture, the stress-strain relationship is in accordance with Hooke's Law

$$\sigma_{cf} = E_{cf} \varepsilon_{cf} \quad (8)$$

where σ_{cf} and ε_{cf} are the stress and the strain of CFRP, respectively. When longitudinal CFRP reaches its rupture strain (ε_{cflr}), it loses longitudinal strengthening effect to the specimens. When transverse CFRP reaches its rupture strain (ε_{cfr}), it loses transverse confinement to the steel tube.

3.2 FE Model

3.2.1 Element type selection and mesh discretization

The adopted element in the mesh of the steel tube is shell element S4 with full integration. Simpson integration with 9 integrating points in the shell thickness direction is used. For the mesh of the concrete, 3-D brick elements C3D8R with reduced integration is used. Membrane element M3D4 with 4-nodes is used for modelling CFRP. The convergent analysis is carried out by using refined mesh in finite element analysis, details can be found in Ref. (Che et al. [19]).

3.2.2 Interface model

Hard contact is used for contact interface between the steel tube and the concrete, i.e., the pressure perpendicular to the contact surfaces (p) can be transferred completely between the two surfaces. The tangential force between the steel tube and the concrete is simulated by using Columb model, i.e., shear force can be transferred between two contact surfaces. In the tangential direction of the contact surfaces between the end plate and the concrete, there is no slipping, and hard contact assumption is used in normal direction of the contact surfaces.

Figure 12 shows the comparison of the strains between the steel tube and the CFRP, where, ε_l and ε_t are the longitudinal strain and the transverse strain respectively, and ε_{cfl} and ε_{cft} are the strains of the longitudinal CFRP and the transverse CFRP, respectively. As shown in Figure 12, ε_{sl} and ε_{cfl} , as well as ε_{st} and ε_{cft} , are approximately same. Additionally, after cutting the CFRP-steel tubes into halves after the tests, it is found that the adherence between the CFRP and the steel tube is still intact except at the region where CFRP ruptured. All above indicate that the steel tubes and the CFRP could cooperate well in both longitudinal and transverse directions. Studies on CF-CFRP-ST stub column (Che et al. [19]; Wang and Shao [34]) and CF-CFRP-ST flexural member (Wang and Shao [28]; Wang et al. [36]) provided same conclusions.

According to the above test results, the CFRP is bound to the steel tube in the finite element model, and it is assumed that no slip exists between the CFRP and the steel tube. Same nodal freedoms are used for the contact elements between the CFRP and the steel tube.

3.2.3 Boundary conditions

Boundary conditions (as shown in Figure 13) are simulated as the same situations in the experimental process. According to the symmetry of both the geometry and the boundary condition, 1/4 of the entire model is selected for FE analysis. On the symmetrical plane of the model, symmetrical constraints are applied. At one end, the displacements in x -, y - and z - directions are all restrained. At the other end, line loading is applied (considering initial eccentricity of $L/1000$). Increment iteration method is used to solve the problem in which controlled displacement loading method is used.

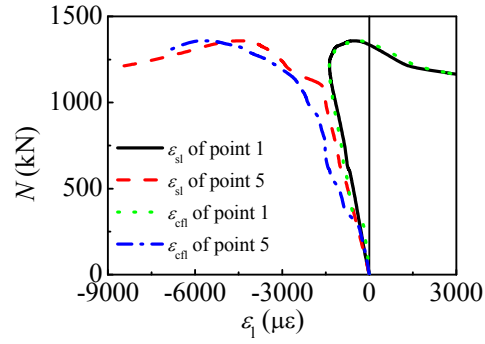
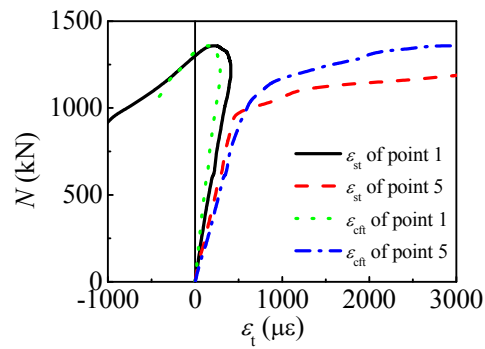
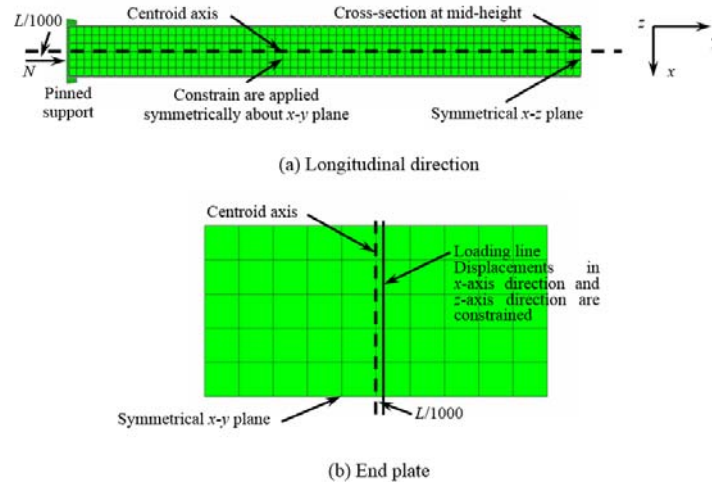
(a) N - ε_l Curves(b) N - ε_t CurvesFigure 12. Comparisons between ε_s and ε_{cf} for Specimen CC F-2

Figure 13. Boundary Conditions

3.3 FE Results

3.3.1 Failure modes

To verify the reliability of the above presented FE method, overall 32 axially compressed C-CF-CFRP-ST columns are analyzed by using ABAQUS software. Figure 14 shows the deformation modes of the specimen in the test and in FE simulation. From Figure 14, it can be

found that the simulated results agree reasonably well with the experimental results.

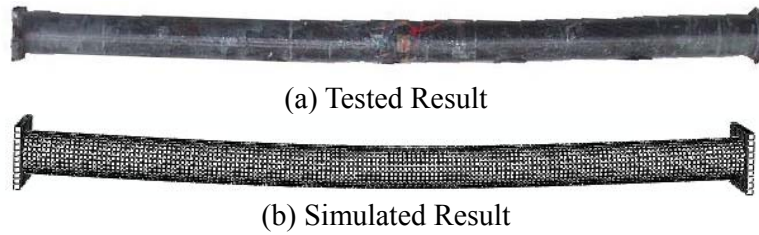
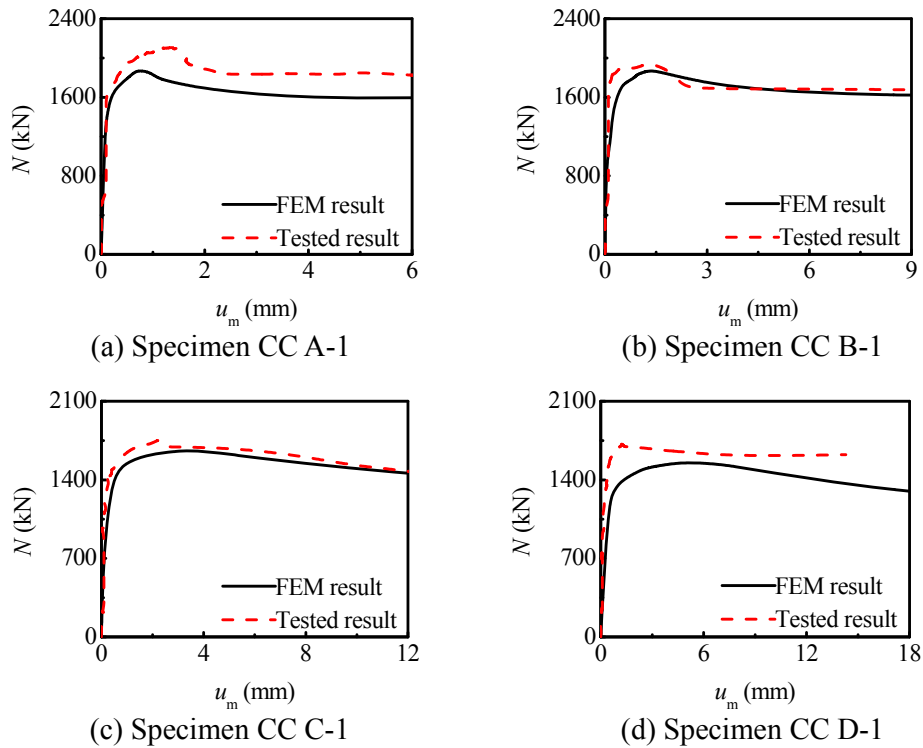
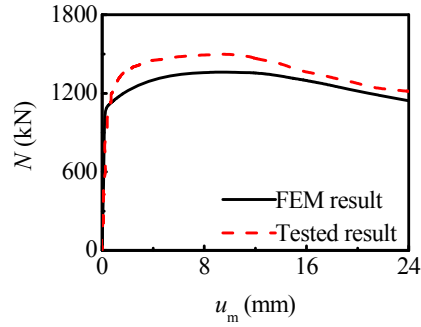


Figure 14. Deformation Modes

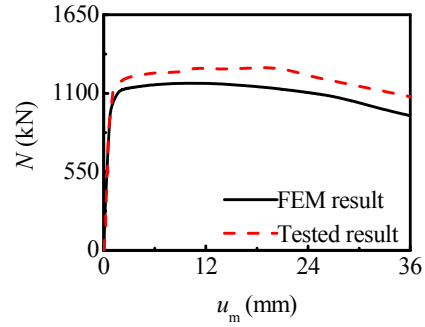
3.3.2 $N-u_m$ curves

The FE $N-u_m$ curves together with the measured results of several specimens are plotted in Figure 15. The FE results agree reasonably well with the experimental results. The average ratio of the critical buckling load between the FE and the experimental results ($N_{u,cr}^t$) is 0.848, and the COV is 0.092. The simulated results for the specimens with large slenderness are relatively smaller, and it is mainly caused by the following reason: The initial eccentricities for all the tested specimen are roughly equal in the experiment. However, such initial eccentricity is prescribed to be $L/1000$, which implies that the specimen with a larger slenderness has a bigger initial eccentricity and hence it has a lower simulated result.

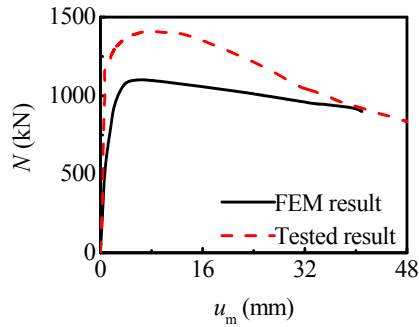




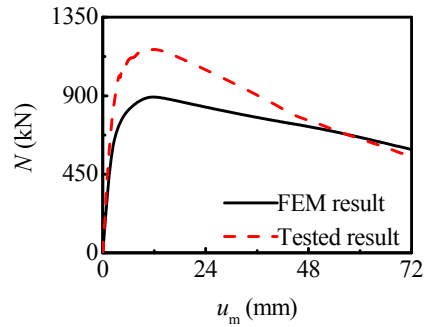
(e) Specimen CC E-1



(f) Specimen CC F-1



(g) Specimen CC G-1

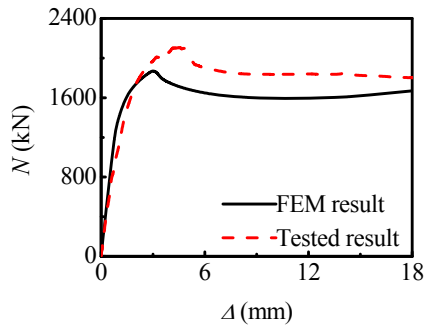


(h) Specimen CC H-1

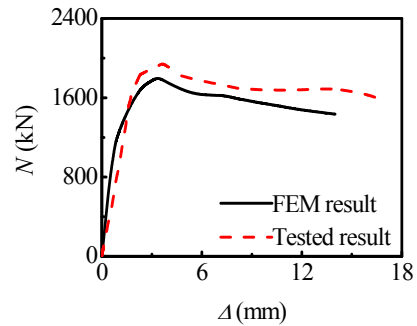
 Figure 15. Comparisons of $N-u_m$ Curves between FEM Result and
 Tested Result for Several Specimens

3.3.3 $N-\Delta$ curves

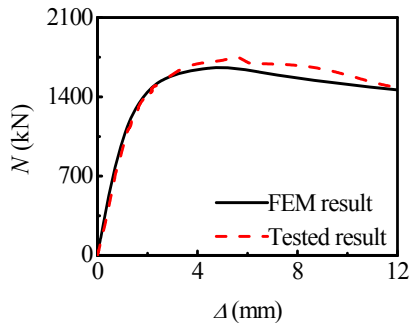
The FE $N-\Delta$ curves together with the measured results of several specimens are also given in Figure 16. The FE results agree reasonably well with the experimental results.



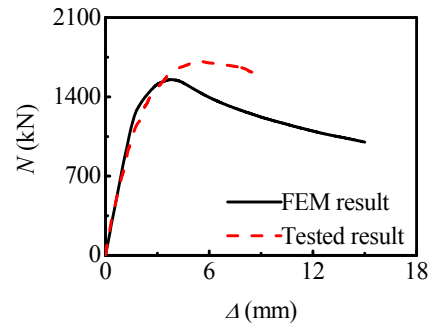
(a) Specimen CC A-1



(b) Specimen CC B-1



(c) Specimen CC C-1



(d) Specimen CC D-1

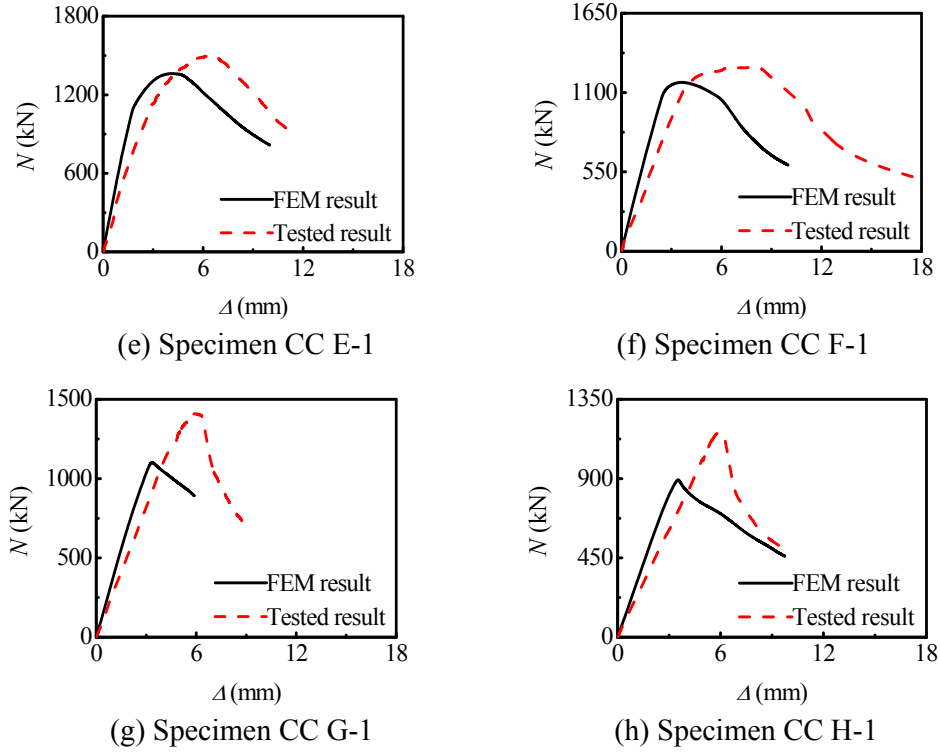


Figure 16. Comparisons of N - Δ Curves between FEM Result and Tested Result for Several Specimens

3.3.4 N - ϵ_s curves

The comparison of the strains in the steel tube of specimen CC E-1 is shown in Figure 17. Experimental and FE results are denoted in thin line and in thick line respectively, and the simulated results of the tube strains agree well with the experimental results.

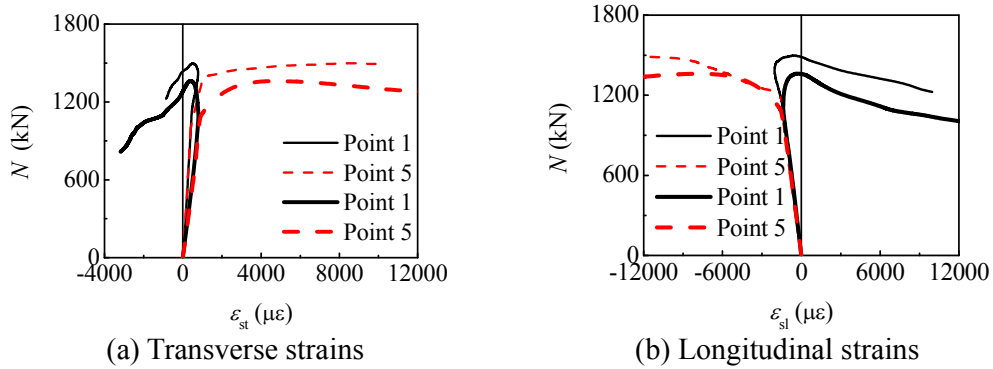


Figure 17. Comparison between Steel Tube Strains of Specimen CC E-1

4. THEORETICAL ANALYSIS

On the basis of the above model and approach, a large number of parametric analyses show that the validity range of the models in the presented approach is: $f_y = 200 - 400 \text{ MPa}$, $f_{cu} = 30 - 120 \text{ MPa}$, $\xi_s = 0.2 - 4$, $\xi_{cf} = 0 - 0.6$, $\eta = 0 - 0.9$. In the above validity range, a typical model is selected to carry out theoretical analysis, and the details of the typical model are listed as follows:

$D_s = 400\text{mm}$, $t_s = 9.3\text{mm}$, $f_y = 345\text{MPa}$, $f_{cu} = 60\text{MPa}$, $\lambda = 80$, $\xi_{cf} = 0.0383$, $\eta = 0.163$, elasticity Poisson's ratio of concrete $\nu_c = 0.2$, $E_c = 4700\sqrt{f'_c}$ (where f'_c is the compressive strength of cylinder concrete specimens and its unit is in MPa). Five typical points as shown in Figure 18 are selected for further analysis. In Figure 18, the load is proportional to the lateral deflection before point 1, and the stress of the steel tube reaches its proportional limit at point 1. Plastic region occurs on the cross-section at the mid-height between point 1 and point 2, and the critical buckling load is reached at point 2. Area of the plastic region increases gradually after point 2, and the transverse CFRP on the longitudinally compressive region ruptures at point 3. The longitudinal CFRP on the longitudinally tensile region ruptures at point 4. Deflection at the mid-height is very large (about $L/25$) at point 5.

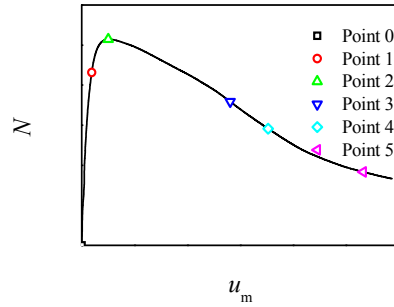


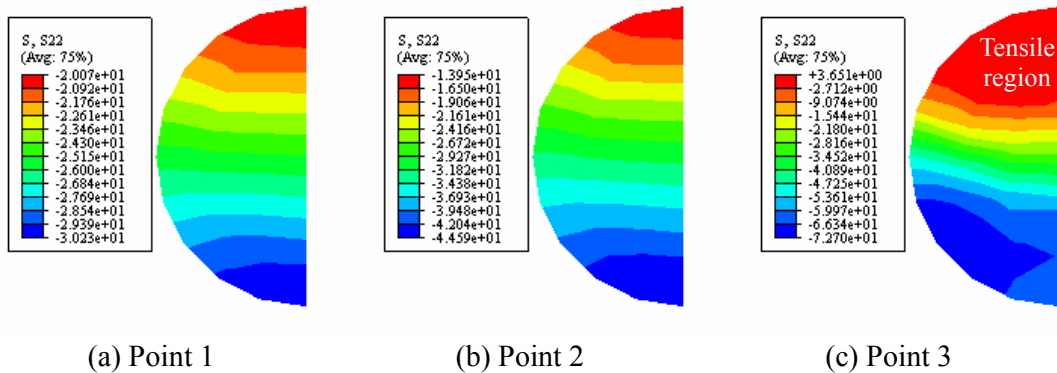
Figure 18. Typical $N-u_m$ Curve of Axially Compressed C-CF-CFRP-ST Columns with Moderate Slenderness Ratio

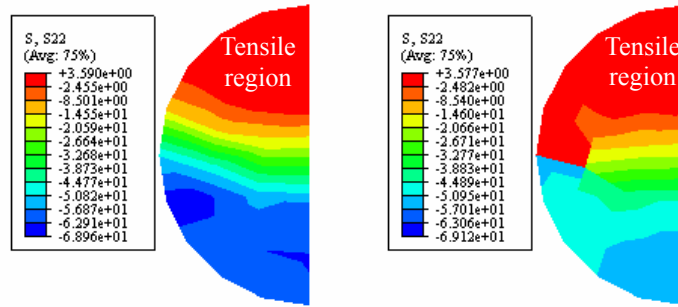
4.1 Stress analysis

4.1.1 Stress in concrete

Figure 19 illustrates the distribution of the longitudinal stress in the concrete on the cross-section at the mid-height for axially compressed C-CF-CFRP-ST column with moderate slenderness ratio. All the cross-section of the concrete is found to be under compression before the critical buckling load is reached. After the critical buckling load, tensile region initiates on the concrete section. With the increasing deflection at the mid-height of the column, the area of the compressive region reduces and the area of the tensile region enlarges continuously.

Figure 20 shows the distribution of the longitudinal stress in the concrete in axial direction. It can be found that such distribution is not uniform and the stresses of the concrete in the compressive region on the cross-section at the mid-height increase gradually.

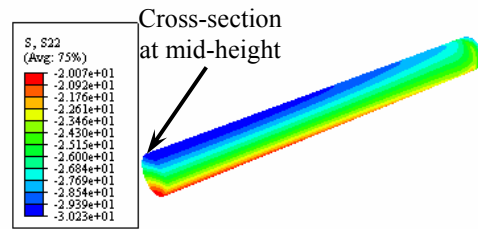




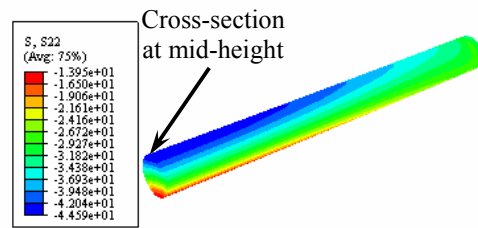
(d) Point 4

(e) Point 5

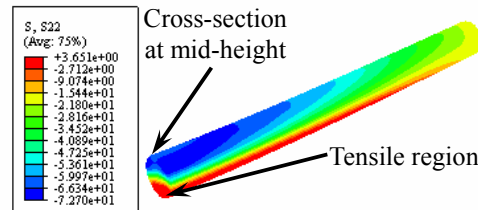
Figure 19. Distribution of Longitudinal Stress in Concrete on Cross-Section at Mid-Height



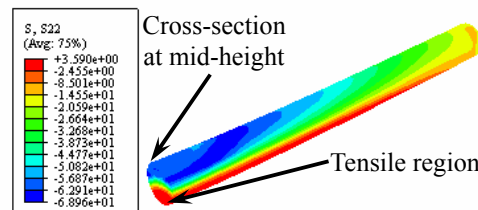
(a) Point 1



(b) Point 2



(c) Point 3



(d) Point 4

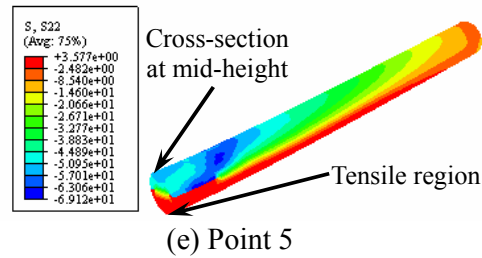
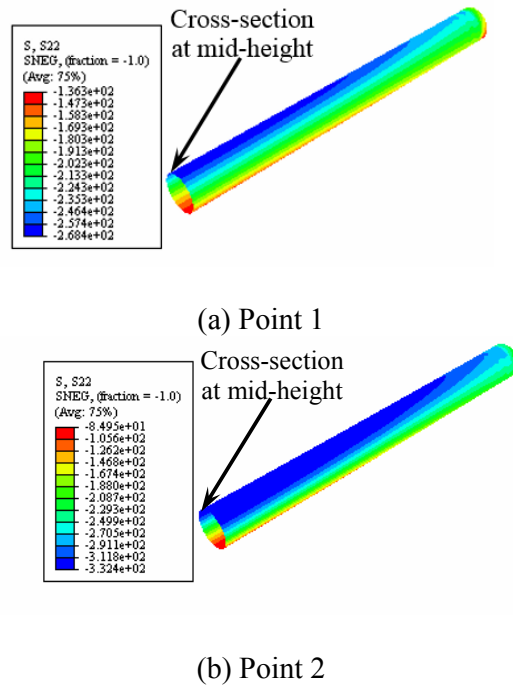


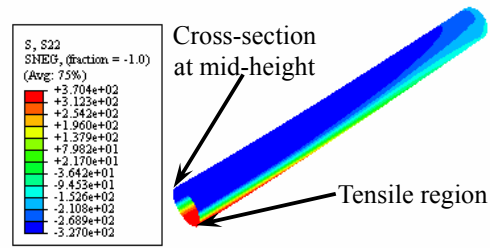
Figure 20. Distribution of Longitudinal Stress in Concrete in Axial Direction

4.1.2 Longitudinal stress in steel tube

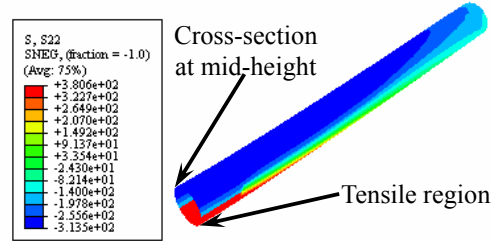
Figure 21 shows the distribution of the longitudinal stress in the steel tube in axial direction. The cross-section of the concrete is under compression before the critical buckling load (point 2), while the longitudinal stress on the cross-section varies from compression to tension over the depth on the cross-section after point 3, which process performs from a positive to a negative value of the stresses. The maximum compressive and the maximum tensile stresses are located at the top and at the bottom surfaces respectively.

Figure 22 shows the distribution of the Mises stress in the steel tube. The loading at point 1 is relatively smaller and the steel tube is in elastic stage. At point 2, the compressed steel tube begins to yield and the cross-section at the mid-height yields firstly. At this time, the tensioned steel tube does not yet yield. Before the fracture of the transverse CFRP, the compressed steel tube is still in a yielding state. After the fracture of the transverse CFRP, the steel tube enters into a hardening stage.

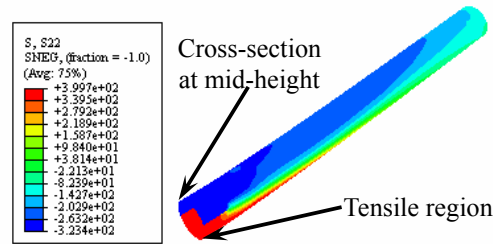




(c) Point 3

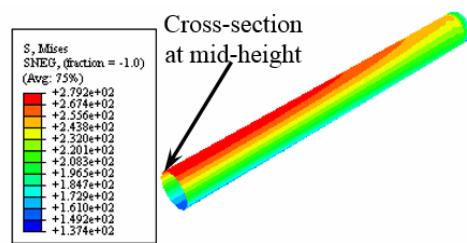


(d) Point 4

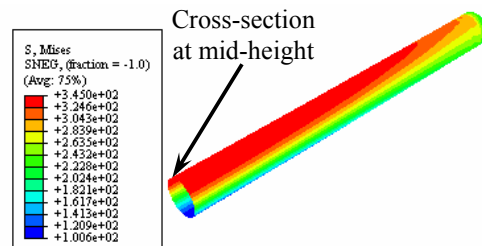


(e) Point 5

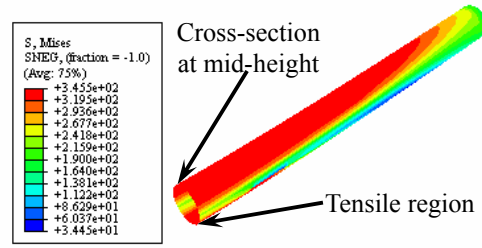
Figure 21. Distribution of Longitudinal Stress in Steel Tube in Axial Direction



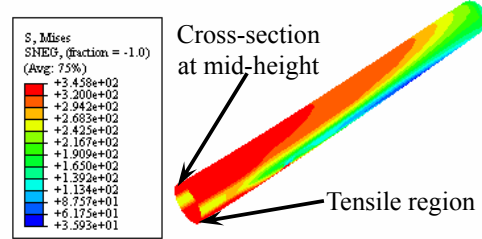
(a) Point 1



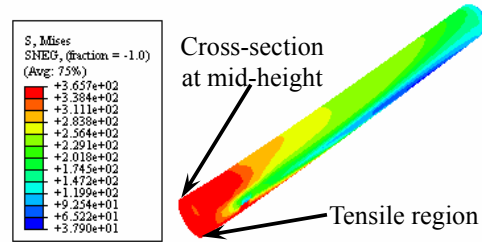
(b) Point 2



(c) Point 3



(d) Point 4



(e) Point 5

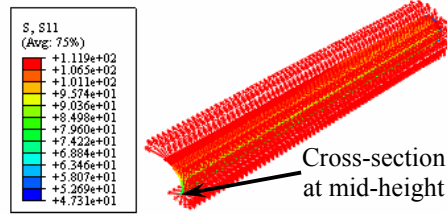
Figure 22. Distribution of Mises Stress in Steel Tube

4.1.3 Stress in CFRPs

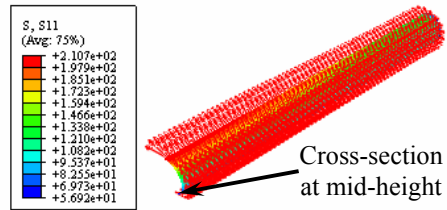
Figure 23 shows the distribution of the stress in the transverse CFRP. Such stress has a uniform distribution in the longitudinal direction in the elastic stage (point 1). Before the critical buckling load, the stress in the compressive region on the cross-section at the mid-height increases gradually. However, the transverse CFRP is still not fractured (the maximum value of stress is about $0.17 f_{ct}$). With the increasing deflection at the mid-height, such stress increases continuously till the CFRP is fractured and does not work (point 3) which indicates that the transverse CFRP in the compressive region in longitudinal direction provides confinement but the transverse CFRP in the tensile region cannot produce such action in the entire loading process.

Figure 24 shows the distribution of the stress in the longitudinal CFRP. It is found that the stress in the longitudinal CFRP has a uniform distribution in the elastic stage (point 1). Before the critical buckling load (point 2), the stress in the tensile region on the cross-section at the mid-height is very small (about 0.001MPa) because the deflection is about only $L/250$, which indicates that the longitudinal CFRP does not provide strengthening effect to the column at this time. At point 3, the deflection is about $L/50$ and the stress in the longitudinal CFRP increases remarkably (the maximum value of the stress is about $0.57 f_{ct}$). With the increasing deflection at the mid-height, the

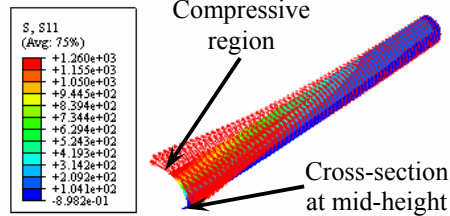
stress in the tensile region increases continuously till the CFRP is fractured and does not work. This shows the longitudinal CFRP in the tensile region detains the flexural deformation of the columns. The longitudinal CFRP in the compressive region cannot produce such action in the entire loading process.



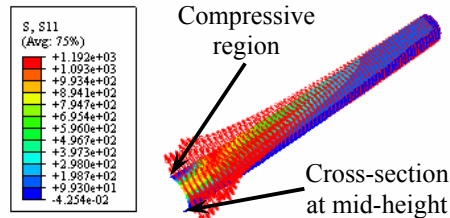
(a) Point 1



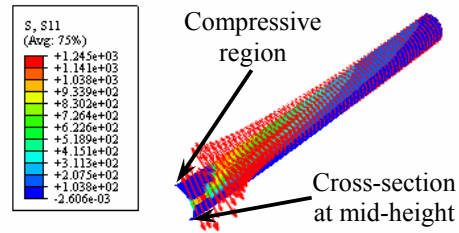
(b) Point 2



(c) Point 3

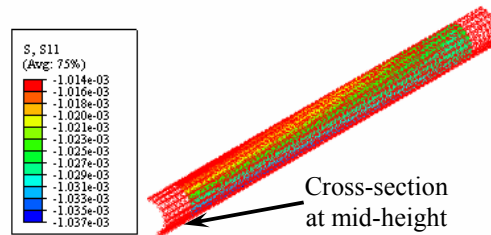


(d) Point 4

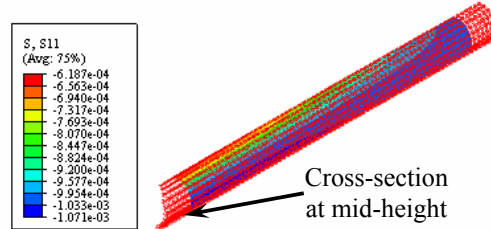


(e) Point 5

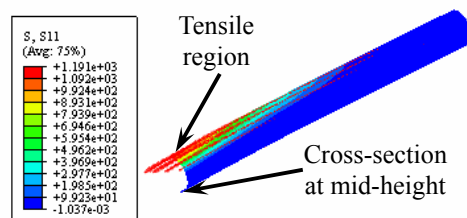
Figure 23. Distribution of Stress in Transverse CFRP



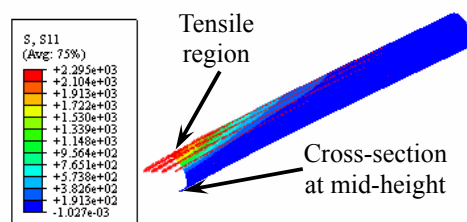
(a) Point 1



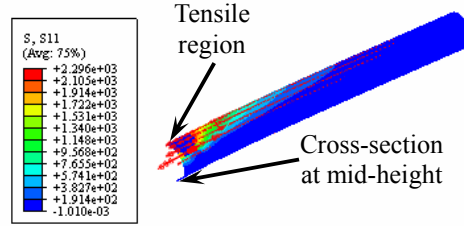
(b) Point 2



(c) Point 3



(d) Point 4



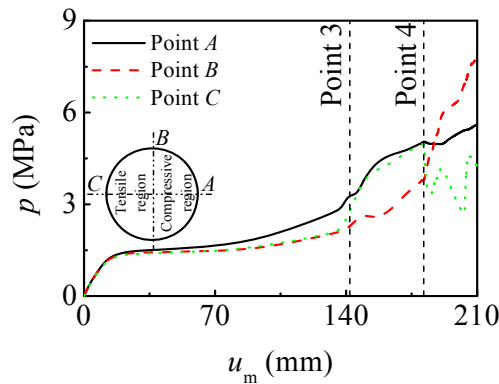
(e) Point 5

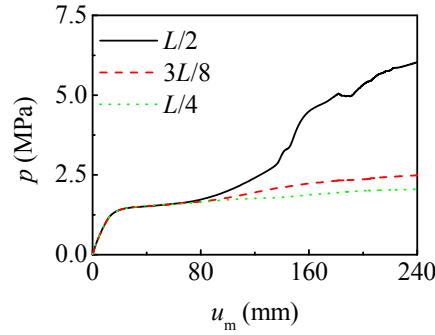
Figure 24. Distribution of Stress in Longitudinal CFRP

4.2 Interaction Force between Concrete and Steel Tube

The interaction force between the steel tube and the concrete (p)-deflection (u_m) curves for points A , B and C on the cross-section at the mid-height of the column is shown in Figure 25. The interaction force in the compressive region is bigger than the corresponding one in the tensile region before the transverse CFRP in the compressive region (point A) is fractured (point 3). After the longitudinal CFRP in the tensile region (point C) is fractured (point 4), the interaction force at point B becomes bigger than the one at point A because the transverse CFRP at point B is not fractured and it has still some confinements to the internal C-CFST.

The p - u_m curves of the columns at a height of $L/2$, $3L/8$ and $L/4$ to the end plate respectively in the compressive region are shown in Figure 26. The results show that the interaction force at the mid-height in the compressive region is bigger. With the increasing distance to the mid-height, the interaction force reduces gradually. As seen from Figures 25 and 26, for axially compressed C-CF-CFRP-ST columns with moderate slenderness ratio, the interaction force reduces continuously from the compressive region to the tensile region. In the compressive region, the interaction force also decreases gradually with the increasing distance to the mid-height of the specimens.

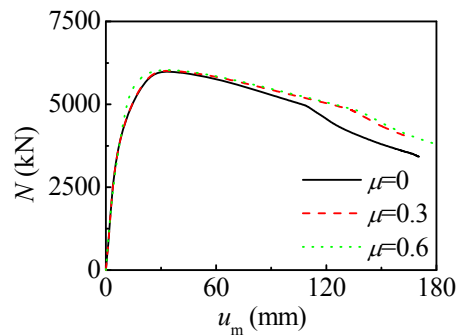
Figure 25. p - u_m Curves over Depth of Cross-Section of Column

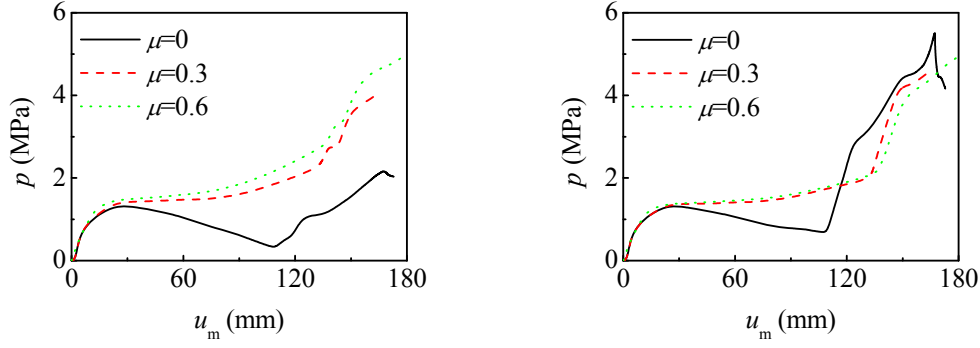
Figure 26. $p-u_m$ Curves along Height of Column

4.3 Analysis on Adhesive Strength

To investigate the effect of the adhesive strength between the steel tube and the concrete on the performance of the axially compressed C-CF-CFRP-ST columns with moderate slenderness ratio, different friction factors (μ) with the values of 0, 0.3 and 0.6 respectively are selected in the simulation. Figure 27 shows the effect of the adhesive strength on the $N-u_m$ curves of the column, which shows that the adhesive strength almost has no effect on the critical buckling load and the stiffness of the specimen in the elastic stage.

Figure 28 shows the effect of the adhesive strength on the $p-u_m$ curves of the column. In the compressive region, p increases with the increasing value of the friction factor (μ). A value from 0.3 to 0.6 seems to have no clear effect on p in the tensile region, which is some different with the case that the value of μ is zero.

Figure 27. Influence of Adhesive Strength on $N-u_m$ Curves of Column



(a) Compressive region (b) Tensile region
Figure 28. Influence of Adhesive Strength on p - u_m Curves of Column

5. CRITICAL BUCKLING LOAD

5.1 Calculation Expression

Many calculated results ($f_y = 200 - 400 \text{ MPa}$, $f_{cu} = 30 - 120 \text{ MPa}$, $\xi_s = 0.2 - 4$, $\xi_{cf} = 0 - 0.6$, $\eta = 0 - 0.9$, $E_s = 206 \text{ GPa}$, $\nu_s = 0.3$, $\nu_c = 0.2$, $E_c = 4700\sqrt{f'_c}$ MPa) show that the relationship between φ (stability coefficient of the axially compressed C-CF-CFRP-CT columns with moderate slenderness ratio) and λ can be described by using the curve that shown in Figure 29 (a). The curve can be divided into three stages: when $\lambda \leq \lambda_0$, $\varphi = 1$, the column fails in strength; when $\lambda_0 < \lambda \leq \lambda_p$, the column fails in elasto-plastic buckling; when $\lambda > \lambda_p$, the column fails in elastic buckling. λ_0 and λ_p are the limited slenderness ratios for an axially compressed C-CF-CFRP-ST column with moderate slenderness ratio in elasto-plastic buckling and elastic buckling respectively, and their values can be determined from the following equations (where the units of f_y and f_{ck} are in MPa):

$$\lambda_0 = \pi \sqrt{(420\xi + 550)/f_{cfscy}} \quad (9)$$

$$\lambda_p = 1743 / \sqrt{f_y} \quad (10)$$

where ξ is the global confinement factor (Che et al. [19]); f_{cfscy} is the index of load carrying capacity of the axially compressed C-CF-CFRP-ST stub columns (Che et al. [19]), where

$$\xi = \xi_s + \xi_{cf} \quad (11)$$

$$f_{cfscy} = [1.14 + 1.02(\xi_s + 3\xi_{cf})]f_{ck} \quad (12)$$

By using regression analysis method (Han et al. [11]), relationship of φ - λ can be expressed as follow

$$\varphi = \begin{cases} 1 & (\lambda \leq \lambda_0) \\ a\lambda^2 + b\lambda + c & (\lambda_0 < \lambda \leq \lambda_p) \\ d/(\lambda + 35)^2 & (\lambda > \lambda_p) \end{cases} \quad (13)$$

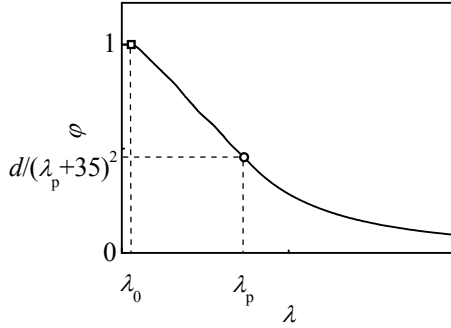
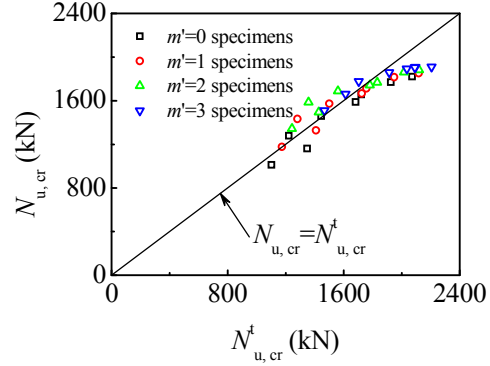
(a) $\varphi - \lambda$ curve(b) Comparisons between $N_{u,cr}$ and $N_{u,cr}^t$

Figure 29. Critical Buckling Load

where $a = [1 + (35 + 2\lambda_p - \lambda_0)e]/(\lambda_p - \lambda_0)^2$, $b = e - 2a\lambda_p$, $c = 1 - a\lambda_0^2 - b\lambda_0$, $e = -d/(\lambda_p + 35)^3$, the expression of the coefficient d is obtained from amounts of calculated results based on regression analysis, and it is listed as follow

$$d = \left[13000 + 4657 \ln \left(\frac{235}{f_y} \right) \right] \left(\frac{25}{f_{ck} + 5} \right)^{0.3} \left(\frac{\alpha}{0.1} \right)^{0.05} (1 + \eta)^{0.9} \quad (14)$$

where $\alpha = A_s/A_c$ is the steel ratio.

The expression for the critical buckling load of the C-CF-CFRP-ST columns with moderate slenderness ratio ($N_{u,cr}$) is then expressed as follow

$$N_{u,cr} = \varphi N_u \quad (15)$$

where N_u is the load carrying capacity of the C-CF-CFRP-ST stub columns (Che et al. [19]),

$$N_u = A_{cfsc} f_{cfscy} \quad (16)$$

where A_{cfsc} is the cross-sectional area of the C-CF-CFRP-ST columns with moderate slenderness ratio.

5.2 Validation of Expression

Figure 29 (b) displays the comparison between $N_{u,cr}$ and $N_{u,cr}^t$ for the tested specimens. The average value of $N_{u,cr}/N_{u,cr}^t$ is 0.97, and the mean square error is 0.08 which means the two results agree well and the calculated results are conservative in overall.

6. CONCLUSIONS

Based on the presented results in this study, the following conclusions can be drawn: (1) for the axially compressed C-CF-CFRP-ST columns with moderate slenderness ratio, the specimens tend to fail in strength when the slenderness ratio is small while the ones with large slenderness ratio tend to fail in buckling. Load-deflection curves at the mid-height of the specimens can be divided into three stages: elastic, elasto-plastic and dropping stages. (2) The steel tube and the CFRP tube could cooperate well both in the transverse and in the longitudinal directions. The distribution of the longitudinal strain of the specimens over the depth on the cross-section approximately meets the plane section assumption. The longitudinal and the transverse strains at same point have opposite signs, and the tensioned steel tube in longitudinal direction has no confinement to the concrete. (3) The finite element simulation results of the deformed mode, the $N-u_m$ curves and the $N-\Delta$ curves of the members as well as the stresses in the steel tube agree well with experimental results. The stress distributions of different composed materials have been analyzed, and the computed results have a good agreement with experimental results. (4) In the compressive region, with the increasing distance to the mid-height of the specimens, the interaction forces between the outer tube and the concrete reduces gradually. The adhesive strength has almost no effect on the critical buckling load and on the stiffness in the elastic stage of the specimens, but it can improve the confinement to the concrete. (5) The calculating equation of the critical buckling load of the axially compressed C-CF-CFRP-ST columns with moderate slenderness ratio is given.

ACKNOWLEDGEMENTS

The research reported in the paper is part of the Project 51378320 supported by Natural Science Foundation of China (NSFC) and the Project 2013003004 supported by Public Welfare Foundation of Liaoning Province, P. R. China. Their financial supports are highly appreciated.

NOMENCLATURE

A_c	: Cross-sectional area of concrete
A_{cfl}	: Cross-sectional area of longitudinal CFRP
A_{cfsc}	: Cross-sectional area of C-CF-CFRP-ST columns with moderate slenderness ratio
A_{cft}	: Cross-sectional area of transverse CFRP
A_s	: Cross-sectional area of steel tube
C-CF-CFRP-ST	: Circular concrete filled CFRP-steel tubes
C-CFST	: Circular concrete filled steel tubes
CF-CFRP-ST	: Concrete filled CFRP-steel tubes
CF-FRP-T	: Concrete filled FRP tubes
CFRP	: Carbon fiber reinforced plastic
CFST	: Concrete filled steel tubes
D_s	: Outer diameter of steel tube
E_c	: Elasticity modulus of concrete
E_{cf}	: Elasticity modulus of carbon fiber sheets
E_s	: Elasticity modulus of steel tube
f_{cfl}	: Ultimate tensile strength of longitudinal CFRP

f_{cfscy}	: Index of load carrying capacity of axially compressed C-CF-CFRP-ST stub columns
f_{cft}	: Ultimate tensile strength of transverse CFRP
f_{cf}'	: Tensile strength of carbon fiber sheet
f_{ck}	: Characteristic axial compressive strength of concrete
f_c'	: Compressive strength of cylinder concrete specimens
f_{cu}	: Cubic strength of concrete specimen
FRP	: Fiber reinforced plastic
f_y	: Yield strength of steel tube
GFRP	: Glass fiber reinforced plastic
L	: Length of specimens
LVDT	: Linear variable differential transformer
m	: Number of transverse CFRP layer
m'	: Number of longitudinal CFRP layer (s)
N	: Axial load
N_u	: Load carrying capacity of C-CF-CFRP-ST stub columns
$N_{u,cr}$: Calculated value of critical buckling load of C-CF-CFRP-ST columns with moderate slenderness ratio
$N_{u,cr}^t$: Tested value of critical buckling load of C-CF-CFRP-ST columns with moderate slenderness ratio
p	: Interaction force between concrete and outer tube
S-CF-CFRP-ST	: Square concrete filled CFRP-steel tubes
t_{cf}	: Thickness of 1 layer carbon fiber sheet
t_s	: Wall thickness of steel tube
u_m	: Deflection at mid-height of column
ν_c	: Elasticity Poisson's ratio of concrete
ν_s	: Elasticity Poisson's ratio of steel tube
w_{cf}	: Density of carbon fiber sheet
α	: Steel ratio
δ_{cf}	: Elongation percentage of carbon fiber sheet
Δ	: Axial shortening of specimen
ϵ_{cf}	: Strain of CFRP
ϵ_{cfl}	: Strain of Longitudinal CFRP
ϵ_{cflr}	: Rupture strain of longitudinal CFRP
ϵ_{cft}	: Strain of transverse CFRP
ϵ_{cflr}	: Rupture strain of transverse CFRP
ϵ_l	: Longitudinal strain
ϵ_s	: Strain of steel tube
ϵ_{sl}	: Longitudinal strain of steel tube
ϵ_{st}	: Transverse strain of steel tube
ϵ_t	: Transverse strain
ϕ	: Stability coefficient of axially compressed C-CF-CFRP-ST columns with moderate slenderness ratio

η	: Strengthening factor of longitudinal CFRP
λ	: Slenderness ratio
λ_0	: Limited slenderness ratio for an axially compressed C-CF-CFRP-ST column with moderate slenderness ratio in elasto-plastic buckling
λ_p	: Limited slenderness ratio for an axially compressed C-CF-CFRP-ST column with moderate slenderness ratio in elastic buckling
μ	: Friction factor
σ_{cf}	: Stress of CFRP
ξ	: Global confinement factor
ξ_{cf}	: Confinement factor of transverse CFRP
ξ_s	: Confinement factor of steel tube

REFERENCES

- [1] Wang, Y.C. and Restrepo, J.I., "Investigation of Concentrically Loaded Reinforced Columns Confined with Glass Fiber-reinforced Polymer Jackets", *ACI Structure Journal*, 2001, Vol. 98, No. 3, pp. 377-385.
- [2] Fam, A.Z. and Rizkalla, S.H., "Confinement Model for Axially Loaded Concrete Confined by Circular FRP Tubes", *ACI Structure Journal*, 2001, Vol. 98, No. 4, pp. 451-461.
- [3] Teng, J.G., Chen, J.F., Smith, S.T. and Lam, L., "FRP Strengthened RC Structures", John Wiley & Sons, 2002, Chichester, UK.
- [4] Karabinis, A.I., Rousakis, T.C. and Manolitsi, G.E., "3D Finite Element Analysis of Substandard Columns Strengthened by Fiber Reinforced Polymer Sheets", *ASCE Journal of Composites for Construction*, 2008, Vol. 12, No. 5, pp. 531-540.
- [5] Rousakis, T.C., Karabinis, A.I., Kioussis, P.D. and Tepfers, R., "Analytical Modelling of Plastic Behaviour of Uniformly FRP Confined Concrete Members", *Journal of Composites Part B: Engineering*, 2008, Vol. 39, No. 7-8, pp. 1104-1113.
- [6] Yu, T., Teng, J.G., Wong, Y.L. and Dong, S.L., "Finite Element Modeling of Confined Concrete-I: Drucker-Prager Type Plasticity Model", *Engineering Structures*, 2010, Vol. 32, No. 3, pp. 665-679.
- [7] Yu, T., Teng, J. G., Wong, Y. L. and Dong, S. L., "Finite Element Modeling of Confined Concrete-II: Plastic-Damage Model", *Engineering Structures*, 2010, Vol. 32, No. 3, pp. 680-691.
- [8] Jiang, J. F. and Wu, Y. F., "Identification of Material Parameters for Drucker-Prager Plasticity Model for FRP Confined Circular Concrete Columns", *International Journal of Solids and Structures*, 2012, Vol. 49, No. 3-4, pp. 445-456.
- [9] Han, L. H., "Tests on Concrete Filled Steel Tubular Columns with High Slenderness Ratio", *Advances in Structural Engineering*, 2000, Vol. 3, No. 4, pp. 337-344.
- [10] Han, L. H., Zhao, X. L. and Tao, Z., "Tests and Mechanics Model of Concrete-Filled SHS Stub Columns, Columns and Beam-Columns", *Steel and Composite Structures*, 2001, Vol. 1 No. 1, pp. 51-74.
- [11] Han, L. H., Yao, G. H. and Zhao, X. L., "Behavior and Calculation on Concrete-Filled Steel CHS (Circular Hollow Section) Beam-Columns", *Steel and Composite Structures*, 2004, Vol. 4, No. 3, pp. 169-188.
- [12] Han, L.H., Yao, G.H. and Zhao, X.L., "Tests and Calculations for Hollow Structural Steel (HSS) Stub Columns Filled with Self-Consolidating Concrete (SCC)", *Journal of Constructional Steel Research*, 2005, Vol. 61, No. 9, pp. 1241-1269.
- [13] Han, L. H. and Li, W., "Seismic Performance of CFST Column to Steel Beam Joint with RC Slab: Experiments", *Journal of Constructional Steel Research*, 2010, Vol. 66, No. 11, PP.

- 1374-1386.
- [14] Han, L. H., "Fire Resistance of Concrete Filled Steel Tubular Columns", *Advances in Structural Engineering*, 1998, Vol. 2, No. 1, pp. 35-39.
 - [15] Han, L.H., Yao, G.H. and Tao, Z., "Performance of Concrete-filled Thin-walled Steel Tubes under Pure Torsion", *Thin Walled Structures*, 2007, Vol. 45, No. 1, pp. 24-36.
 - [16] Han, L.H., Liu, W. and Yang, Y. F., "Behaviour of Concrete-filled Steel Tubular Stub Columns Subjected to Axially Local Compression", *Journal of Constructional Steel Research*, 2008, Vol. 64, No. 4, pp. 377-387.
 - [17] Han, L. H., Hou, C. and Wang, Q. L., "Square Concrete Filled Steel Tubular (CFST) Members under Loading and Chloride Corrosion: Experiments", *Journal of Constructional Steel Research*, 2012, Vol. 71, No. 1, pp. 11-25.
 - [18] Han, L. H., Hou, C. C. and Wang, Q. L., "Behavior of Circular CFST Stub Columns under Sustained Load and Chloride Corrosion", *Journal of Constructional Steel Research*, 2014, Vol. 103, No. 1, pp. 23-36.
 - [19] Che, Y., Wang, Q. L. and Shao, Y. B., "Compressive Performances of the Concrete Filled Circular CFRP-Steel Tube (C-CFRP-CFST)". *International Journal of Advanced Steel Construction*, 2012, Vol. 8 No. 4, pp. 311-338.
 - [20] Tao, Z., Han, L. H. and Wang, L. L., "Compressive and Flexural Behaviour of CFRP Repaired Concrete-filled Steel Tubes after Exposure to Fire", *Journal of Constructional Steel Research*, 2007, Vol. 63, No. 8, pp. 1116-1126.
 - [21] Tao, Z., Wang, Z. B., Han, L. H. and Uy B., "Fire Performance of Concrete-Filled Steel Tubular Columns Strengthened by CFRP", *Steel and Composite Structures*, 2011, Vol. 11, No. 4, pp. 307-324.
 - [22] Xiao, Y., He, W. H. and Choi, K. K., "Confined Concrete-filled Tubular Columns." *Journal of Structural Engineering*, 2005, Vol. 131, No. 3, pp. 488-497.
 - [23] Choi, K. K. and Xiao, Y., "Analytical Model of Circular CFRP Confined Concrete-filled Steel Tubular Columns under Axial Compression", *Journal of Composites for Construction*, 2010, Vol. 14, No. 1, pp. 125-133.
 - [24] Park, J. W., Hong, Y. K., Hong, G. S., Kim, J. H. and Choi, S. M., "Design Formulas of Concrete Filled Circular Steel Tubes Reinforced by Carbon Fiber Reinforced Plastic Sheets", *Procedia Engineering*, 2011, Vol. 14, pp. 2916-2922.
 - [25] Hu, Y. M., Yu, T. and Teng, J. G., "FRP-Confined Circular Concrete-Filled Thin Steel Tubes under Axial Compression", *Journal of Composites for Construction*, 2011, Vol. 15, No. 5, pp. 850-860.
 - [26] Li, S. Q., Chen, J. F., Bisby, L. A., Hu, Y. M. and Teng, J. G., "Strain Efficiency of FRP Jackets in FRP-Confined Concrete-Filled Circular Steel Tubes", *International Journal of Structural Stability and Dynamics*, 2012, Vol. 12, No. 1, pp. 75-94.
 - [27] Teng, J. G., Hu, Y. M. and Yu, T., "Stress-Strain Model for Concrete in FRP-Confined Steel Tubular Columns", *Engineering Structures*, 2013, Vol. 49, No. 4, pp. 156-167.
 - [28] Wang, Q. L. and Shao, Y. B., "Flexural Performance of Circular Concrete Filled CFRP-Steel Tubes". *Advanced Steel Construction*, 2015, Vol. 11, No. 2, pp. 127-149.
 - [29] Tao, Z., Han, L. H. and Zhuang, J. P., "Axial Loading Behavior of CFRP Strengthened Concrete-Filled Steel Tubular Stub Columns", *Advances in Structural Engineering*, 2007, Vol. 10, No. 1, pp. 37-46.
 - [30] Park, J. W., Hong, Y. K. and Choi, S. M., "Behaviors of Concrete Filled Square Steel Tubes Confined by Carbon Fiber Sheets (CFS) under Compression and Cyclic Loads", *Steel and Composite Structures*, 2010, Vol. 10, No. 2, pp. 187-205.
 - [31] Sundarraja, M. C. and Ganesh, P. G., "Investigation on Strengthening of CFST Members under Compression Using CFRP Composites", *Journal of Reinforced Plastics and Composites*, 2011, Vol. 30, No. 15, pp. 1251-1264.

- [32] Sundarraja, M. C. and Ganesh, P. G., "Experimental Study on CFST Members Strengthened by CFRP Composite under Compression", *Journal of Constructional Steel Research*, 2012, Vol. 72, No. 5, pp. 75-83.
- [33] Sundarraja, M. C. and Ganesh, P. G., "Behaviour of CFST Members under Compression Externally Reinforced by CFRP Composites", *Journal of Civil Engineering and Management*, 2013, Vol. 19, No. 2, pp. 184-195.
- [34] Wang, Q. L. and Shao, Y. B., "Compressive Performances of Concrete Filled Square CFRP-Steel Tubes (S-CFRP-CFST)", *Steel and Composite Structures*, 2014, Vol. 14, No. 5, pp. 455-480.
- [35] Sundarraja, M. C. and Ganesh, P. G., "Finite Element Modeling of CFRP Jacketed CFST Members under Flexural Loading". *Thin-walled Structures*, 2011, Vol. 49, No. 12, pp. 1483-1491.
- [36] Wang, Q. L., Li, J., Shao, Y. B. and Zhao, W. J., "Flexural Performances of Square Concrete Filled CFRP-Steel Tubes (S-CF-CFRP-ST)", *Advances in Structural Engineering*, 2015, Vol. 18, No. 8, pp. 1319-1344.
- [37] Yu, T., Wong, Y. L., Teng, J. G., Dong, S. L. and Lam, E. S. S., "Flexural Behavior of Hybrid FRP-Concrete-Steel Double-skin Tubular Members", *Journal of Composites for Construction*, 2006, Vol. 10, No. 5, pp. 443-452.

A PSEUDO-DYNAMIC TEST STUDY ON A SELF-CENTERING PREFABRICATED STEEL FRAME WITH A COLUMN BASE CONNECTED BY SEMI-RIGID JOINTS

Yanxia Zhang^{1*}, Zongyang Wang², Wei Zhao², Wenzhan Zhao² and Yuanyuan Chen²

¹ Associate Professor, Beijing Higher Institution Engineering Research Center of Structural Engineering and New Materials, Beijing University of Civil Engineering and Architecture, Beijing 100044, China

² Postgraduate, School of Civil and Transportation Engineering, Beijing University of Civil Engineering and Architecture, Beijing 100044, China

**(Corresponding author: E-mail: zhangyanxia@bucea.edu.cn)*

Received: 4 September 2015; Revised: 10 September 2015; Accepted: 19 September 2016

ABSTRACT: Self-centering steel frame structures are advantageous in that they can control structural damage, reduce or eliminate residual deformation, and are easy to repair after strong earthquakes. A self-centering prefabricated steel frame with a column base connected by semi-rigid joints (SPSF-SRJ) is proposed in the present study. The goal is to address the problem of excessive plasticity that a self-centering prefabricated frame with a column base connected by rigid joints exhibits. In addition, a pseudo-dynamic test is performed on the sub-structure of the proposed system to investigate and discuss the seismic performance of the system, which is then compared with the seismic performance of a self-centering prefabricated steel frame with a column base connected by rigid joints (SPSF-RJ). The test results show that the proposed performance-based design goal can be realized in the SPSF-SRJ. The semi-rigid joints effectively protect the column base and eliminate or reduce the damage to the columns; after an earthquake, only the steel beams require repairs, which significantly reduces the post-earthquake repair cost.

Keywords: Self-centering prefabricated steel frame, Column base connected by Semi-rigid joints, Pseudo-dynamic test, Performance-based design goal, Gap opening, Plastic strain

DOI:10.18057/IJASC.2016.12.3.5

1. INTRODUCTION

Self-centering steel frame structures are advantageous in that they can control structural damage, reduce or eliminate residual deformation, and are easy to repair after strong earthquakes. Rojas and Ricles et al. [1, 2, 3] studied friction-type self-centering steel frames. Lin et al. [4, 5] conducted a pseudo-dynamic test study on self-centering steel frames. Zhang et al. [6, 7] conducted experimental and theoretical studies on self-centering structural systems that dissipated energy through web friction devices and proposed a self-centering prefabricated steel frame system. The existing connection and plane frame tests showed that the system proposed by Zhang et al. [6, 7] exhibited the aforementioned advantages of self-centering steel frames; in addition, with this proposed system, post-tensioned (PT) strands could be tensioned on the ground of the construction site instead of being tensioned above the ground, and the beam-column connections only need to be connected using the mixed bolting-welding method, which is used to connect conventional beam-column connections. However, Zhang et al. [6, 7] also discovered that plastic deformation of the bottom columns of the self-centering prefabricated steel frame still occurred under medium-earthquake or large-earthquake conditions. Hoseok et al. [8, 9] proposed the use of prestressed column connectors at the column base of a self-centering frame; their finite element simulation and experimental study showed that the column base of the system could return to their original position automatically; in addition, the energy-dissipation device installed at the column base prevented plastic deformation from occurring; however, due to the gravitational effect, the vertical anchor cable structure was complicated and achieved self-centering abruptly and thus, was

not easily accepted by designers. Based on the research results of our research group as well as research groups in China and other countries, an self-centering prefabricated steel frame with a column base connected by semi-rigid joints (referred to as SPSF-SRJ hereinafter) is proposed in the present study with the goal of addressing the problem of excessive plasticity that a self-centering frame with a column base connected by rigid joints exhibits, and performance-based design goal of “no gap opening and no damage occurs during frequent earthquakes; gap openings are formed to dissipate energy, and no damage occurs to the main structure during design earthquakes; only extremely small structural damage occurs, and the structure can still normally operate during rare and extremely rare earthquakes (8.5 rare earthquake) is put forward. In addition, a pseudo-dynamic test is performed on the sub-structure of the SPSF-SRJ to investigate and discuss the seismic performance of the SPSF-SRJ, which is then compared with the seismic performance of an SPSF with a column base connected by rigid joints (referred to as SPSF-RJ hereinafter).

2. STRUCTURE OF A TYPICAL CONNECTION OF A SELF-CENTERING PREFABRICATED STEEL FRAME

A typical beam-column connection of a prefabricated prestressed steel frame system has a joint structure that connects a frame column and a prestressed steel beam (Figure 1). A prestressed steel beam consists of a middle beam portion, two short beam portions, a strengthening device, a connecting device, and an energy-dissipation device. The connecting device consists of a vertical plate and a prestressed strand. The strengthening device consists of a transverse stiffener and a longitudinal stiffener that are welded onto the short beam web. The energy-dissipation device uses a web friction damper and contains steel splice plates, which are positioned on the two sides of the web of the middle beam portion, and friction bolts for energy dissipation. Long holes are created at locations on the web of the middle beam portion that correspond to the friction bolts. A brass plate is sandwiched between the web of the middle beam portion and the splice plate to ensure a stable friction coefficient. Stiffeners are installed at the location where the steel frame column levels with the flange of the short beam segment.

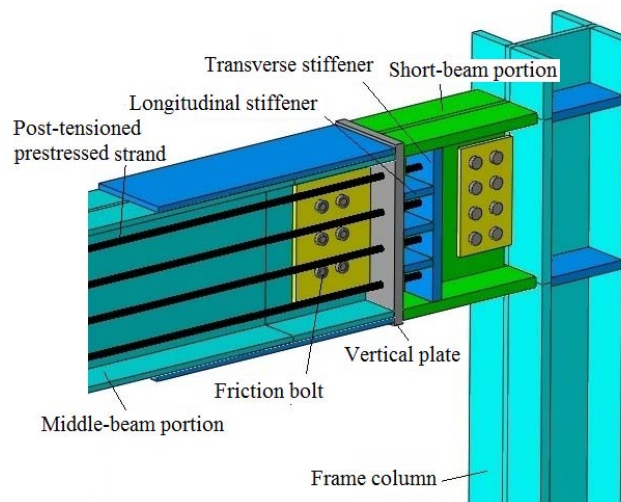


Figure 1. Typical Beam-column Connection of a Self-centering Prefabricated Steel Frame System

3. PROTOTYPE STRUCTURE AND TEST MODEL

3.1 Prototype Structure

Based on the proposed performance-based design goal, studies on self-centering connection structures conducted by Georgios et al. [10,11,12,13], characteristics of self-centering prefabricated steel frames, related design standards of other countries [14,15,16,17], and the *Code for Seismic Design of Buildings of China* [18], a 4-story SPSF-SRJ prototype structure that uses a web friction damper for energy dissipation was designed. Figure 2 shows the structural plane. Each span of the structural plane is 8 m; the first story is 3.8 m high, and the second to fourth stories are each 3.6 m high. The beam-column connections of the frame in the peripheral blue area are prefabricated prestressed steel frame. Box-section frame columns (section dimensions: $400\text{mm} \times 400\text{mm} \times 34\text{mm}$) were used in the present study. Each frame beam had section dimensions of $\text{H}588\text{mm} \times 300\text{mm} \times 12\text{mm} \times 20\text{mm}$. All other beam-column connections were articulated. Each column had dimensions of $400\text{mm} \times 400\text{mm} \times 30\text{mm}$. Each beam had dimensions of $\text{H}588\text{mm} \times 300\text{mm} \times 12\text{mm} \times 20\text{mm}$. M24 bolts were used as the bolts for energy dissipation and as the beam-column connecting bolts; 1×19 steel strands with a nominal area of 312.9 mm^2 were used.

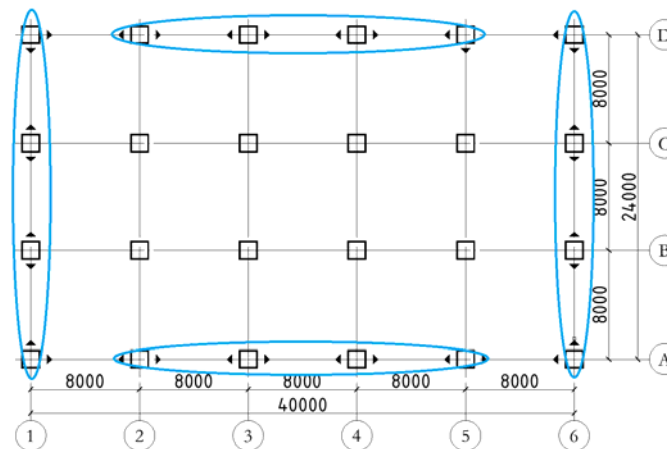


Figure 2. Plan Schematic of Prototype Structure

3.2 Test Model

The pseudo-dynamic test method for sub-structures was used in the present study. The SPSF in the middle of the bottom story of the prototype structure was selected as the sub-structure for testing. Considering the test conditions, the prototype structure was scaled down by 75%. The frame columns of the test model were under the same axial compression ratio as those of the prototype structure. In addition, the test model had the same ratio of imminent gap opening moment to the plastic limit moment of the section of the long beam as the prototype model. Figure 3 shows the detailed dimensions of the test model. The test model had a story height of 3.15 m and a span of 6 m. The model had $\text{H}300\text{mm} \times 300\text{mm} \times 20\text{mm} \times 30\text{mm}$ frame column, $\text{H}450\text{mm} \times 250\text{mm} \times 14\text{mm} \times 16\text{mm}$ middle beam segment, $\text{H}482\text{mm} \times 250\text{mm} \times 14\text{mm} \times 30\text{mm}$ short beam segment. Each column stiffener had a thickness of 30 mm. The transverse stiffener and longitudinal stiffener of the short beam thickness is 30 mm and 20 mm, respectively. The vertical plate had a thickness of 30 mm. The reinforcing plate of the flange of the middle beam segment had a thickness of 16 mm and a length of 800 mm. Eight grade 10.9 M24 bolts were used as the bolts for the energy dissipation. Eight grade 10.9 M20 bolts were used as the beam-column connecting bolts. Eight 1×19 steel strands were used as the PT strands; an initial PT force value of $0.25T_u$ was selected for a single

prestressed strand.

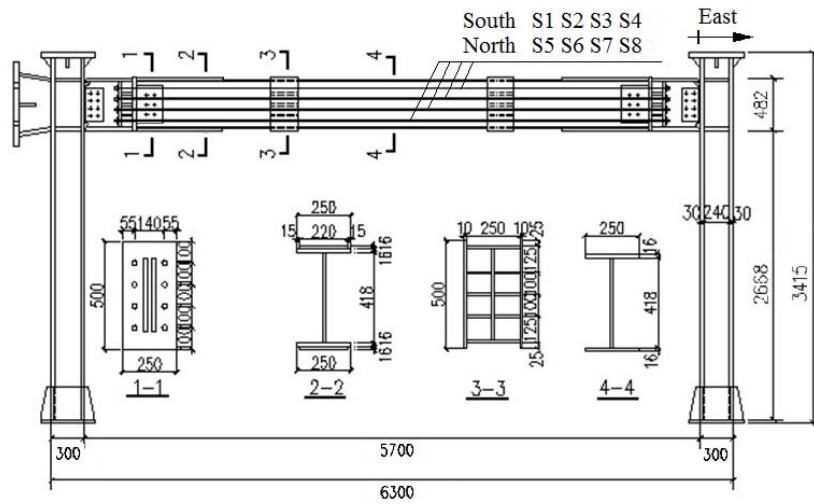


Figure 3. Detailed Dimensions of the Test Model
(Side strands:S1、S4、S5、S8, Middle strands:S2、S3、S6、S7)

3.3 Material Properties

Five sectional specimen thicknesses were used – 14 mm, 16 mm, 18 mm, 20 mm, and 30 mm. The steel product grade was Q345B. The mechanical properties of the specimen materials were tested and Table 1 lists the test results of the mechanical properties of the specimen materials. Table 2 lists the test results of the properties of the prestressed strand. Grade 10.9 bolts were used. The friction coefficient between the brass plate and steel plate was tested to be 0.34-0.38.

Table 1. The Mechanical Properties of the Specimen Materials

Thick (mm)	Yield strength (N/mm ²)	Ultimate strength (N/mm ²)	Elastic modulus (×10 ⁵ N/mm ²)	Percent elongation at fracture
14	384	561	2.15	27.0
16	392	555	2.06	23.3
18	381	555	2.22	25.3
20	384	550	2.09	25.7
22	388	574	2.09	26.8
30	350	505	2.07	26.5

Table 2. Prestressed Strand Material Properties

Strand	Specimen	Yield strength (kN)	Ultimate strength (kN)	Elastic modulus (×10 ⁵ N/mm ²)
1×19	1	1728.3	1894.5	2.03
	2	1727.1	1895.8	2.05
	3	1732.8	1875.4	2.00
	Average value	1729	1889	2.03

4. TEST SCHEME

4.1 Loading Device and Input Parameters

The multi-story structural remote cooperative pseudo-dynamic test platform (NetSLab_MSBSM1.0.0) developed by Hunan University was used in the present study. Due to the relatively large span of the SPSF-SRJ and the limited laboratory conditions, the axial pressure on the top of each column was applied through vertical prestressed strands, and 1×19 steel strands with a nominal diameter of 21.8 mm were still used for the test. Four prestressed strands were placed on each side of the structure. A single prestressed strand has a PT force of 189 kN. The lateral force was applied through a 200t actuator. Figures 4 and 5 show the schematics and a photograph of the loading device used in the test, respectively. Earthquake ground motions were used as inputs into the test platform structure to calculate the displacement, which was then exerted through the actuator. It was necessary to input the floor quality and theoretical inter-story restoring force model into the test platform to calculate the sub-structure. The floor quality, which was an input into the platform structure, was based on the floor quality of the prototype structure and the similarity relation between the test structure and prototype structure. The double-flag model provided by our research group was used as the theoretical inter-story restoring force model. The quality of each floor and the stiffness parameter were obtained through a finite element analysis of the planar frame. The column base connected by semi-rigid joints was realized by eliminating the pressure beam on the top of the column base and reducing the rotational stiffness of the column base (Figure 4).

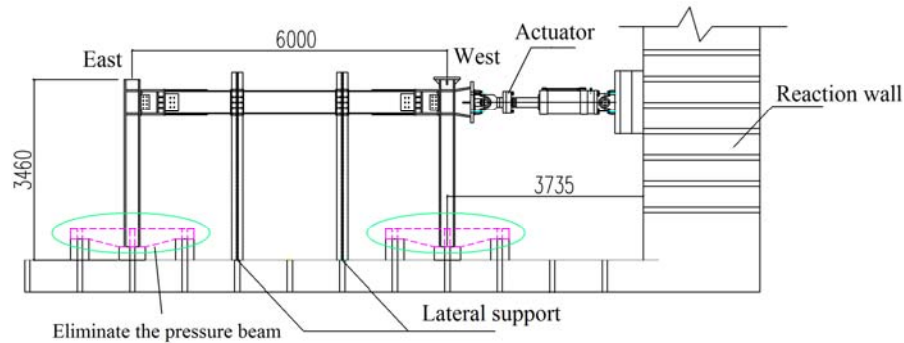


Figure 4. Test Setup



Figure 5. Photograph of the Loading Device used during the Test

4.2 Selection of Earthquake Ground Motions

Three earthquake ground motions, Taft, LOS000, and EL-Centro, were selected for the test. Figures 6-8 show the time history curves of the three selected earthquake ground motions. The peak ground acceleration (PGA) of the three earthquake ground motions were adjusted to $0.4g$. In addition, the time history curves were converted to acceleration response spectra using the SeismoSignal software (Figure 9). The first period of the test model was 1.23s. Each response spectrum curve essentially coincided with the standard response spectrum curve at the first period.

Seismic acceleration records with $PGA = 0.07g, 0.2g, 0.4g$, and $0.51g$ were inputs in the test according to earthquakes with four different levels: 8.0-degree frequent earthquake, design earthquake, rare earthquake, and 8.5-degree rare earthquake, according to *Chinese Code for Seismic Design of Buildings*(GB 50011-2010,2010). The three earthquake ground motions all had a time step of 0.01 s. Considering the reduced scale, the time step of each earthquake ground motion was adjusted to 0.0086s. A damping ratio of 0.05 was also selected. Before inputting the earthquake ground motions, preloading was performed to measure the actual stiffness of the test sub-structure, which was used as the basis for the subsequent calculation.

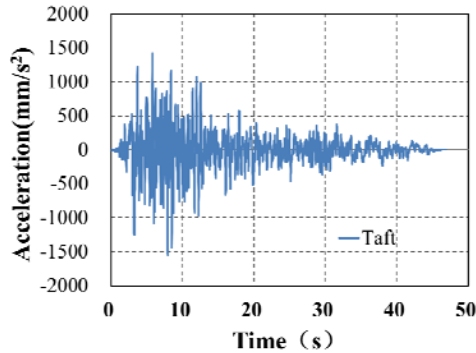


Figure 6. Taft Ground Motion Record

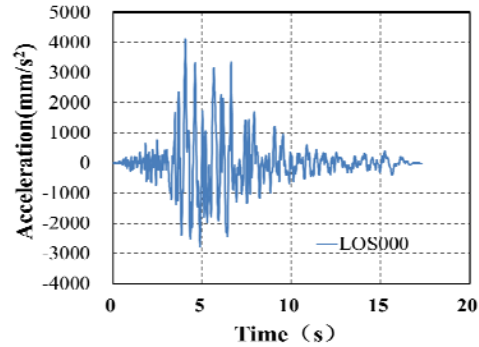


Figure 7. LOS000 Ground Motion Record

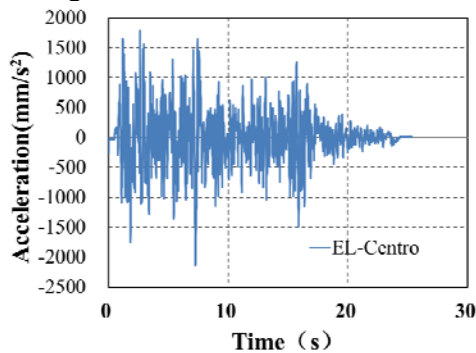


Figure 8. EL-Centro Ground Motion Record

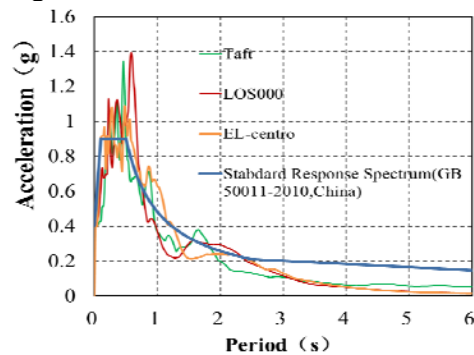


Figure 9. Acceleration Response Spectrum

4.3 Measurement Content

- (1) Measurement of the load: the change in the load during the test process was measured using the sensor that was installed in the actuator.
- (2) Measurement of the PT force of the prestressed strands: the changes in the PT force of the prestressed strands were recorded in real time using a 50t pressure load sensor.
- (3) Measurement of the displacements: as shown in Figure 10, eight linear displacement potentiometers were placed at the gap opening of each connection to measure the width of the gap opening of each connection; the changes in the displacements were measured using the sensor that

was installed in the actuator; a displacement meter with a measurement range of 150 mm was placed on top of the column on the east side to record the displacement of the top of the column; one displacement meter with a measurement range of 50 mm was placed on the east side of the column base, and another displacement meter with a measurement range of 50 mm was placed on the west side of the column base to record the horizontal slippage of the column base.

(4) Measurement of the strain: strain gauges were installed on the flange of the short beam, flange of the long beam, flange of the column base, web of the column base, flange in the connection region, and web in the connection region in the transverse and longitudinal directions to measure the change in the strain at each location during the loading process.

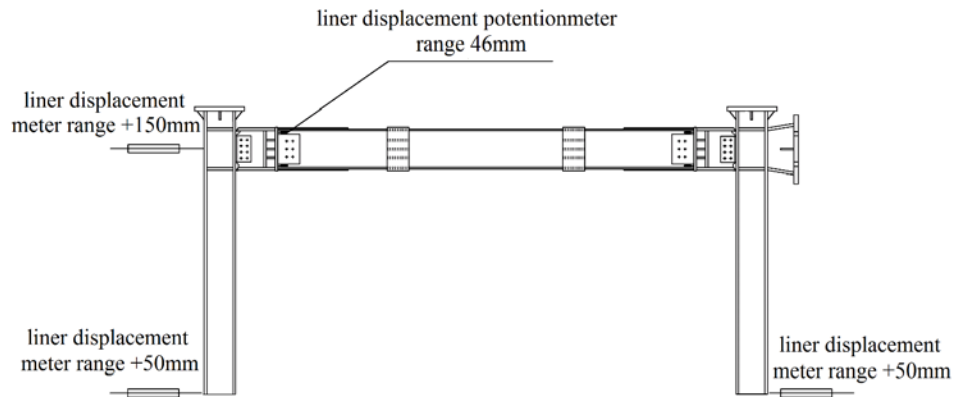


Figure 10. Arrangement of Displacement Meter

5. ANALYSIS OF THE TEST RESULTS

The dynamic characteristics of the SPSF-SRJ were studied by analyzing the displacement response of the structure, the gap openings of the connections, shear force of the base, hysteretic behavior, stiffness, PT force, and strain.

5.1 Deformation and Drift Response

Figure 11-12 shows a photograph of the lateral displacement of the column under the action of the EL-Centro ground motion ($PGA=0.4g$ and $PGA=0.51g$). The actuator acts on the column on the west side, which means that the east side and west side of the structure have asymmetrical stiffness; therefore, the displacement on the west side is often slightly greater than that on the east side. In the present study, the structural displacement response analysis is performed using the non-loaded east side of the structure as an example. The structural displacement-time histories under the actions of the EL-Centro ground motion of different earthquake levels are shown in Figures 13 where all displacement histories return to zero at the end of the tests, demonstrating self-centering behavior.

Table 3 lists the maximum displacement responses of the east side of the structure and the inter-story drifts. Under the action of the EL-Centro ground motion of $PGA=0.07g$, the SPSF-SRJ exhibits the maximum displacement response (18.94 mm), which is slightly larger than that of the SPSF-RJ (17.21 mm), because the lateral rigidity of SPSF-SRJ is usually less than that of SPSF-RJ. The SPSF-SRJ and SPSF-RJ have maximum inter-story drifts of 1/218 and 1/166, respectively; even though these maximum inter-story drifts exceed the elastic inter-story drifts limit defined in the *Code for seismic design of buildings* (1/250), the frames can essentially return to their original positions after an earthquake. Similarly, due to the rigidity reason, the displacement of SPSF-SRJ (40.5 mm) is greater than that of SPSF-RJ (30.65 mm) under the action of the EL-Centro ground motion of $PGA=0.2g$.

The maximum displacement response of SPSF-SRJ under the action of the three ground motions of $\text{PGA}=0.4\text{g}$ is 77.01 mm, greater than that of SPSF-RJ (62.2 mm). The maximum inter-story drifts under the action of the Taft, LOS000 and EL-Centro ground motions of $\text{PGA}=0.4\text{g}$ are 1/63, 1/57, and 1/41, respectively. The displacement response under the action of the EL-Centro ground motion is the largest and already exceeds the elastic inter-story drift limit of a frame defined in the *Code for seismic design of buildings* (1/50), but the frame can still return to its original position after an earthquake. Under the action of the Taft, LOS000, and EL-Centro ground motion of $\text{PGA}=0.51\text{g}$, the maximum displacement responses are 55.43 mm, 64.32 mm, and 89.71 mm, respectively, still exhibit the maximum displacement response than that of SPSF-RJ.

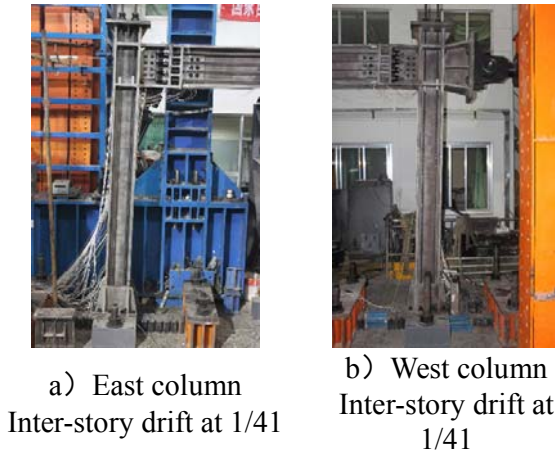


Figure 11. Column Lateral Displacement Photographs from El-Centro ($\text{PGA}=0.4\text{g}$)

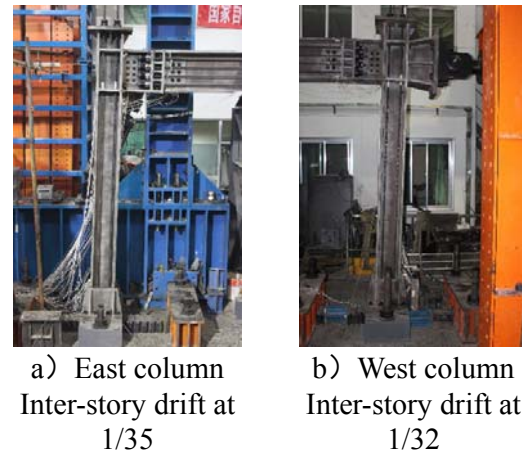


Figure 12. Column Lateral Displacement Photographs from El-Centro ($\text{PGA}=0.51\text{g}$)

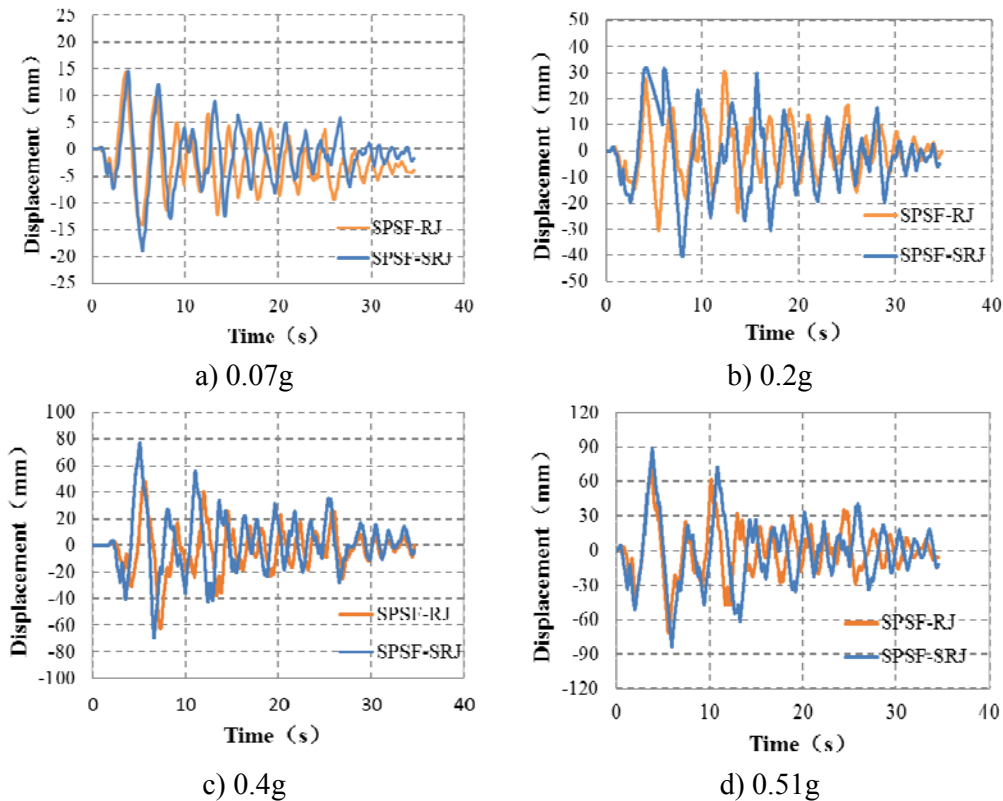


Figure 13. Lateral Displacement Time History from EL-Centro at East Side

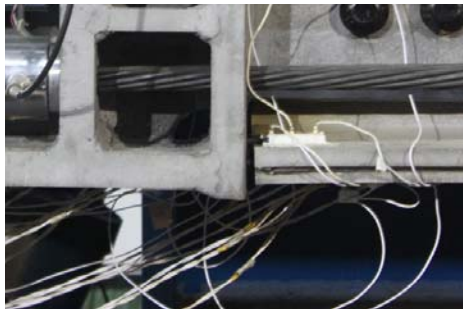
Table 3. Displacement Responses and Inter-Story Drifts of SPSF-RJ and SPSF-SRJ

Seismic events		Displacement (mm)				Inter-story drifts (rad)			
		0.07 g	0.2 g	0.4 g	0.51 g	0.07 g	0.2 g	0.4 g	0.51 g
SPSF-RJ	Taft	8.28	20.28	33.24	43.73	1/380	1/155	1/95	1/78
	LOS000	12.65	24.67	44.02	53.91	1/249	1/128	1/72	1/58
	EL-Centro	17.21	30.65	62.2	71.53	1/218	1/103	1/50	1/44
SPSF-SRJ	Taft	8.24	20.95	49.86	55.43	1/382	1/150	1/63	1/57
	LOS000	11.63	27.92	55.19	64.32	1/271	1/113	1/57	1/49
	EL-Centro	18.94	40.5	77.01	89.71	1/166	1/78	1/41	1/35

5.2 Connections Gap Opening

Figure 14~16 give photographs of the connections under the action of the EL-Centro ground motion of different earthquake levels and Tables 4 and 5 list the gap opening rotation (θ) and residual rotation (θ_{res}) of the connections on the east and west sides. Under the action of ground motion of PGA=0.07g, the connections gap openings are not formed. Under the action of ground motions of PGA=0.2g, 0.4g, 0.51g, the maximum gap opening rotations of the connections of the SPSF-SRJ are close to or slightly greater than that of the SPSF-RJ due to the rotation of column base of SPSF-SRJ. The maximum residual rotation (obtained by dividing the difference in residual displacements of adjacent floors by the story height) of the connections of the SPSF-SRJ is only 0.13%, which indicate the frame can return to its original position after an earthquake.

It can be observed from the above analysis that the connections do not open under the action of a frequent earthquake. Under the action of a design earthquake or a more intense earthquake, the connections begin to open; in addition, the gap opening rotation of the connections of the SPSF-SRJ are greater than those of the SPSF-RJ, and the residual rotation are extremely small; furthermore, The test results prove that the connections of the SPSF-SRJ exhibit a relatively good opening/closing mechanism and have a good self-centering capability, similar to the SPSF-RJ.

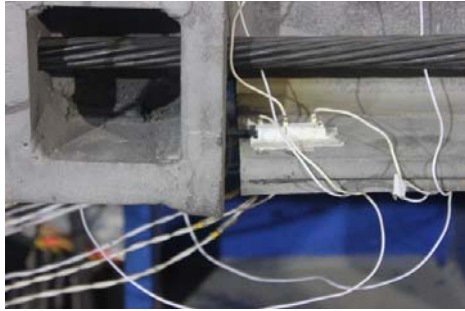


a) The gap opening width of the connection on the east side: 3.97 mm; gap opening rotation: 0.91%



b) The gap opening width of the connection on the west side: 4.52 mm; gap opening rotation: 1.04%

Figure 14. Connections photograph from EL-Centro(PGA=0.2g)

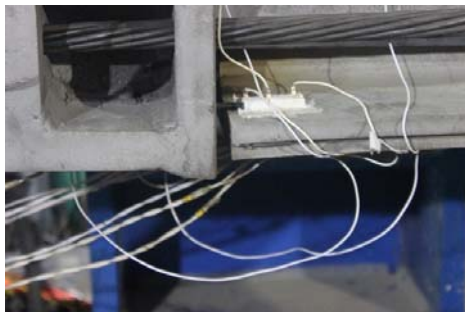


a) The gap opening width of the connection on the east side: 9.96 mm; gap opening rotation: 2.29%



b) The gap opening width of the connection on the west side: 11.79 mm; gap opening rotation: 2.72%

Figure 15. Connections Photograph from EL-Centro (PGA=0.4g)



a) The gap opening width of the connection on the east side: 13.37mm; gap opening rotation: 3.08%



b) The gap opening width of the connection on the west side: 14.28mm; gap opening rotation: 3.29%

Figure 16. Connections Photograph from EL-Centro (PGA=0.51g)

Table 4. Gap Opening Rotation and Residual Rotation of the Connections on the East Side

Seismic events		Gap opening rotation (rad)			Residual rotation (rad)		
		0.2g	0.4g	0.51g	0.2g	0.4g	0.51g
SPSF-RJ	Taft	0.26%	0.81%	1.04%	0.02%	0.18%	0.06%
	LOS000	0.41%	0.78%	1.53%	0.03%	0.06%	0.11%
	EL-Centro	0.63%	1.92%	2.54%	0.02%	0.04%	0.24%
SPSF-SRJ	Taft	0.29%	1.27%	1.58%	0.00%	0.03%	0.13%
	LOS000	0.42%	1.12%	1.68%	0.02%	0.00%	0.00%
	EL-Centro	0.91%	2.29%	3.08%	0.05%	0.02%	0.08%

Table 5. Gap Opening Rotation and Residual Rotation of the Connections on the West Side

Seismic events		Gap opening rotation (rad)			Residual rotation (rad)		
		0.2g	0.4g	0.51g	0.2g	0.4g	0.51g
SPSF-RJ	Taft	0.41%	1.06%	1.65%	0.03%	0.01%	0.02%
	LOS000	0.65%	1.23%	2.00%	0.07%	0.13%	0.31%
	EL-Centro	0.89%	2.78%	3.23%	0.03%	0.09%	0.07%
SPSF-SRJ	Taft	0.65%	1.23%	1.62%	0.03%	0.06%	0.02%
	LOS000	0.64%	1.19%	1.68%	0.00%	0.01%	0.00%
	EL-Centro	1.04%	2.72%	3.29%	0.08%	0.01%	0.03%

5.3 Base Shear Force

Figure 17 shows the base shear force-time histories of the SPSF-SRJ and SPSF-RJ under the action of the EL-Centro ground motion of different earthquake levels. Under the action of $PGA=0.07g$, the maximum base shear force of SPSF-SRJ is close to that of SPSF-RJ. Under the action of $PGA=0.2g, 0.4g, 0.51g$, The maximum base shear forces of the SPSF-SRJ are almost less than those of the SPSF-RJ, still because the rigidity of SPSF-SRJ is usually less than that of SPSF-RJ

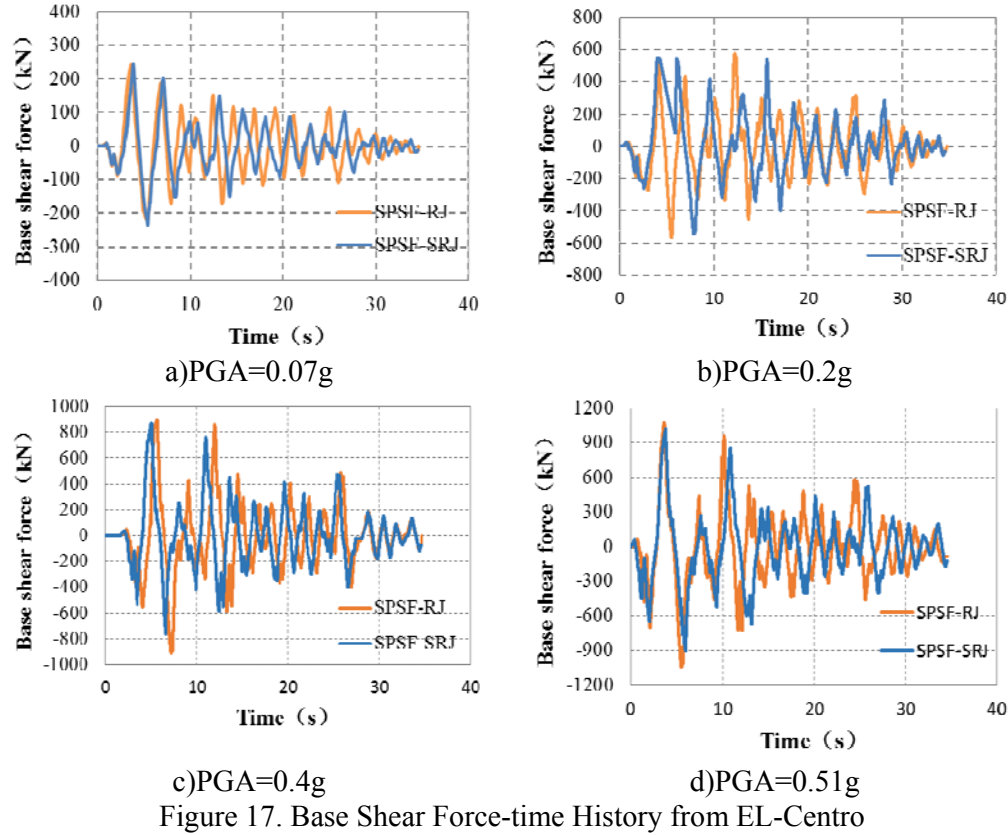


Figure 17. Base Shear Force-time History from EL-Centro

5.4 Hysteretic Behavior

Figure 18 gives the base shear force-displacement hysteretic curves of the SPSF-SRJ and SPSF-RJ under the action of the EL-Centro ground motion of different earthquake levels. In the present study, the hysteretic behavior of the SPSF-SRJ and SPSF-RJ under the action of the EL-Centro ground motion was analyzed. Under the action of ground motion of $PGA=0.07g$, the hysteretic curves are linear. Hysteretic loops begin appearing because of the beam-column connections opening and the friction dampers dissipating energy under the action of ground motion of $PGA=0.2g$. Hysteretic loops have essentially formed under the action of ground motion of $PGA=0.4g$; in addition, the energy dissipated by the friction damper increased when compared with that under the action of ground motion of $PGA=0.2g$. Hysteretic loops have completely formed under the action of ground motion of $PGA=0.51g$.

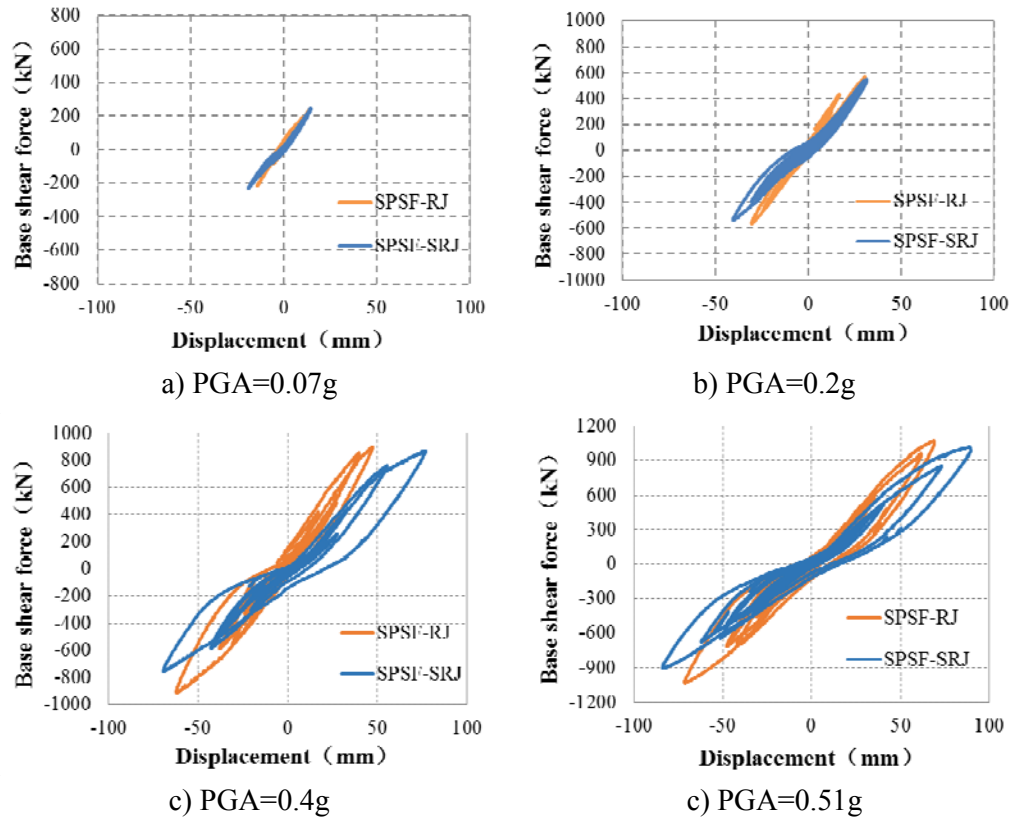


Figure 18. Base Shear Force-displacement Response from EL-Centro

The effective energy dissipation coefficient (β_E) can be used to quantitatively analyze the hysteretic behavior and energy dissipation capability of the SPSF-SRJ and SPSF-RJ. The β_E refers to the ratio of the actual energy dissipation of a system to the energy dissipation for a bilinear elastic-plastic system with the same capacity. To enable a satisfactory response for the SC-MRF under seismic loading to be achieved, Seo and Sause [19] recommend that $\beta_E \geq 0.25$.

Table 6 lists the β_E of the SPSF-SRJ and SPSF-RJ under the action of different earthquakes levels. When PGA is 0.07g, there is no energy dissipation, and the β_E are all zero. When PGA increases to 0.2g, the maximum β_E of SPSF-SRJ and SPSF-RJ are 0.288 and 0.209. When PGA increases to 0.4g, the maximum β_E of SPSF-SRJ and SPSF-RJ are 0.349 and 0.314. The β_E are close to or greater than 0.25. When PGA increases to 0.51g, the maximum β_E of SPSF-SRJ and SPSF-RJ are 0.296 and 0.295, respectively. The β_E are all greater than 0.25. However, the β_E of SPSF-SRJ are always greater than that of SPSF-RJ.

Table 6. The Effective Energy Dissipation Ratios (β_E)

Seismic events		0.07g	0.2g	0.4g	0.51g
SPSF-RJ	Taft	0	0	0.248	0.270
	LOS000	0	0	0.264	0.282
	EL-Centro	0	0.209	0.314	0.295
SPSF-SRJ	Taft	0	0	0.219	0.292
	LOS000	0	0.220	0.265	0.276
	EL-Centro	0	0.288	0.349	0.296

5.5 Analysis of Secant Stiffness

The stiffness of a structure reflects the deformability of the structure. Due to the gap openings of the beam-column connections of the test frame, the stiffness of the test frame decreases with increasing number of test cycles and increasing deformation of the test frame during the test process; such a phenomenon is called the stiffness degradation. The secant stiffness (K_i) is used to express the stiffness of the frame and is calculated using the following Eq. 1:

$$K_i = \frac{|+F_i| + |-F_i|}{|+\Delta_i| + |-\Delta_i|} \quad (1)$$

where F_i represents the value of the force at the i^{th} peak point; Δ_i represents the value of the displacement at the i^{th} peak point.

Table 7 lists the secant stiffness of the SPSF-SRJ and SPSF-RJ. The stiffness of each structure exhibits a decreasing trend with increasing energy dissipated by the openings of the connections. The stiffness of the SPSF-RJ degrades from 19210 kN/m (PGA=0.2g) to 15021 kN/m (PGA=0.51g), whereas the stiffness of the SPSF-SRJ degrades from 15455 kN/m (PGA=0.2g) to 11119 kN/m (PGA=0.51g). The stiffness of the SPSF-SRJ is always lower than that of the SPSF-RJ.

Table 7. Secant stiffness of structure (kN/m)

Seismic events		0.2g	0.4g	0.51g
SPSF-RJ	Taft	18844	18694	17391
	LOS000	19210	18596	16546
	EL-Centro	18687	17358	15021
SPSF-SRJ	Taft	15455	13692	14020
	LOS000	15190	13542	13294
	EL-Centro	15106	11146	11119

5.6 PT Force Analysis

5.6.1 PT force on the column

Four prestressed strands were placed on one column and the total initial PT force was 756kN (axial compression ratio is about 0.2). During the loading process, the maximum vertical PT force ranged from 6 kN at the peak ground acceleration of 0.07 g to 25kN at the peak ground acceleration of 0.51 g; the axial force remained essentially stable, as shown in Figure 19.

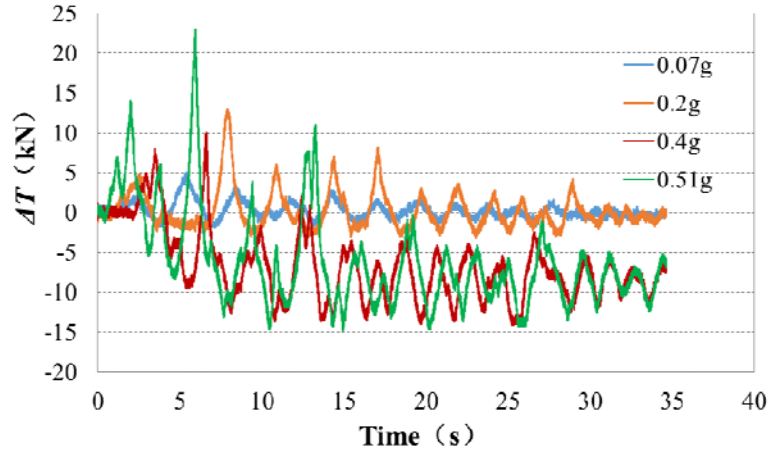


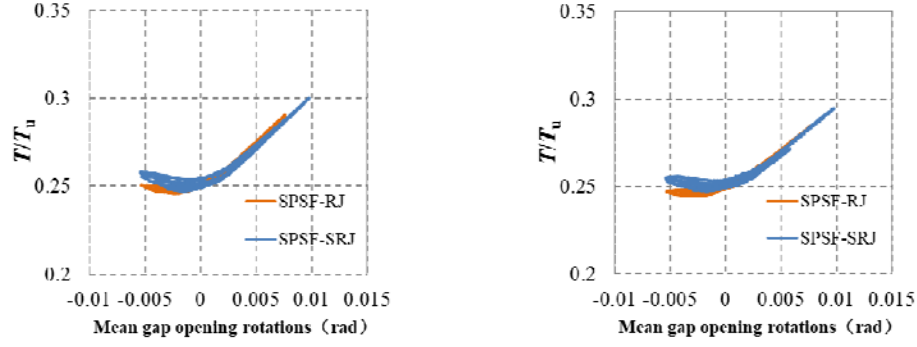
Figure 19. PT Force on the Column from EL-Centro

5.6.2 PT force on the beam

The SPSF-SRJ has a span of 6 m. Each prestressed strand has an effective length of 5.06 m. After the gap openings of the connections were formed, the PT force of each prestressed strand increased with the increasing length of the prestressed strand. The extension of each prestressed strand is related to the gap opening rotation of the connections on the east and west sides. Therefore, the curves of the relationships between the PT forces and mean gap opening rotations are plotted for analysis. Figure 20-22 shows the changes in the PT forces of the SPSF-SRJ and SPSF-RJ with the mean gap opening rotations when the SPSF-SRJ and SPSF-RJ are under the action of the EL-Centro ground motion of PGA=0.2g,0.4g,0.51g. The mean gap opening rotation is set as the abscissa, and T/T_u is set as the ordinate (T is the mean PT force during the test, T_u is the ultimate PT force, its value is 591 kN which is obtained based on the material properties of the prestressed strand.), the PT force of the side strand is the mean PT force of strands 1, 4, 5, and 8; and the PT force of the middle strand is the mean PT force of strands 2, 3, 6, and 7; Take the side strands for an example. The side strands of the SPSF-RJ and SPSF-SRJ have initial PT forces of 148 kN and 150 kN ($0.25T_u$), respectively, and maximum PT forces of 172 kN and 178 kN ($0.30T_u$), respectively. After the tests have terminated, the PT forces return to 148 kN and 148 kN ($0.25T_u$), respectively; thus, there is essentially no loss of the PT forces of the side strands.

As shown in Figure 21, when PGA increases to 0.4g, The prestressed strands of the SPSF-RJ and SPSF-SRJ have initial PT forces of 148 kN ($0.25T_u$) and 160 kN ($0.27T_u$), respectively, and maximum PT forces of 229 kN ($0.39T_u$) and 245 kN ($0.42T_u$), respectively. After the tests have terminated, the PT force of the SPSF-RJ and the SPSF-SRJ returned to 148 kN ($0.25T_u$) and 153 kN ($0.26T_u$), respectively; thus, there are nearly no losses in the PT forces.

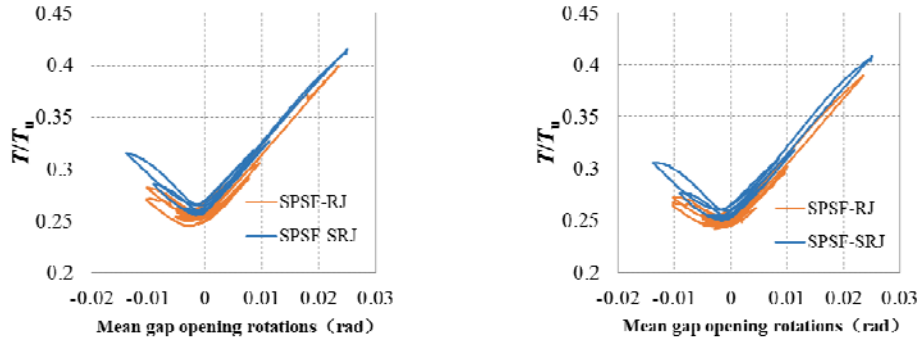
As shown in Figure 22, when PGA increases to 0.51g, The prestressed strands of the SPSF-RJ and SPSF-SRJ have initial PT forces of 141 kN ($0.24T_u$) and 154 kN ($0.26T_u$), respectively, and maximum PT forces of 254 kN ($0.43T_u$) and 266 kN ($0.45T_u$), respectively. After the tests have terminated, the PT force of the SPSF-RJ and the SPSF-SRJ returned to 141 kN ($0.24T_u$) and 148 kN ($0.25T_u$), respectively; which indicates that the prestressed strands of the SPSF-SRJ, the performance of the anchorage device, and the prestress tensioning method are reliable, providing a good basis for the SPSF-SRJ to normally operate and shows that it can bear the impacts from relatively large, multiple aftershocks after the occurrence of rare and extremely rare earthquakes.



a) Side strand

b) Middle strand

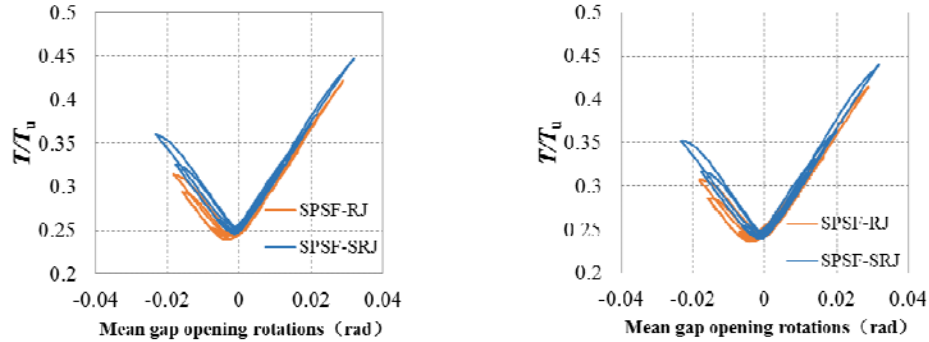
Figure 20. PT Force from EL-Centro(PGA=0.2g)



a) Side strand

b) Middle strand

Figure 21. PT Force from EL-Centro (PGA=0.4g)



a) Side cables

b) Middle cables

Figure 22. PT Force from EL-Centro (PGA=0.51g)

5.7 Analysis of Strain

Table 10 lists the maximum values of the strain at different parts of the SPSF-SRJ and SPSF-RJ when the SPSF-SRJ and SPSF-RJ were under the action of earthquakes with different degrees. Under the action of ground motion of PGA=0.07g, no plastic development occurred in the entire SPSF-SRJ and SPSF-RJ. Under the action of ground motion of PGA=0.2g, each part of the SPSF-SRJ and SPSF-RJ was still under an elastic state; the values of the strain at the flange of the short beam, flange of the long beam, flange in the connection region, and the web plate of the SPSF-SRJ were slightly greater than those of the SPSF-RJ; in addition, the values of the strain at the flange and web plate of the column base of the SPSF-SRJ were far smaller than those of the SPSF-RJ. The performance-based goal of “no structural damage” was realized in the SPSF-SRJ when the SPSF-SRJ was under the action of a frequent earthquake as well as under the action of a design earthquake.

Under the action of ground motion when PGA is 0.4g, the flange of the long beam and web plate in the connection region of the SPSF-RJ were under the elastic state; the flange of the short beam, flange in the connection region, flange and web of the column base of the SPSF-RJ all began to yield; however, the values of the strain at these parts did not exceed twice the value of the yield strain($2\varepsilon_y$); the value of the plastic strain at the reinforcing plate near the vertical plate on the long beam flange exceeded $2\varepsilon_y$. During the test, the flange of the short beam, reinforcing plate, flange and web in the connection region of the SPSF-SRJ entered the plastic state; the values of the strain at the flange of the short beam, reinforcing plate near the vertical plate on the long beam, and web plate in the connection region of the SPSF-SRJ are larger than those of the SPSF-RJ and exceeded $2\varepsilon_y$. Figures 23 and 24 show the strain-time history curves of the flanges of the short beams and web plates in the connection regions of the SPSF-SRJ and SPSF-RJ. The value of the strain at the flange in the connection region of the SPSF-SRJ did not exceed $2\varepsilon_y$ and was smaller than that of the SPSF-RJ. The flange of the long beam, flange and web of the column base of the SPSF-SRJ were all under the plastic state, the strain-time history curves of the flanges of the column bases of the SPSF-SRJ and SPSF-RJ are shown in Figure 25.

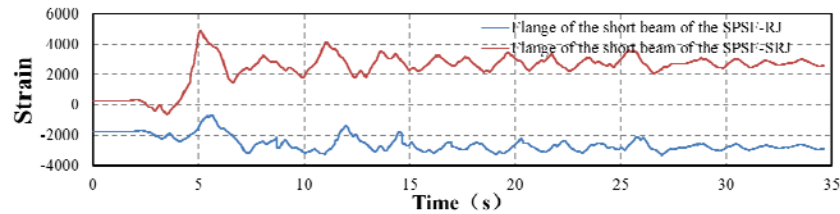


Figure 23. Strain-time History Curves of the Flanges of the Short Beams of the SPSF-SRJ and SPSF-RJ under the Action of the EL-Centro (PGA=0.4g)

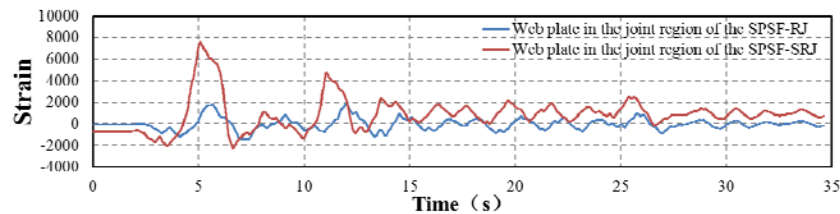


Figure 24. Strain-time History Curves of the Web Plates in the Connection Regions of the SPSF-SRJ and SPSF-RJ under the Action of the EL-Centro (PGA=0.4g)

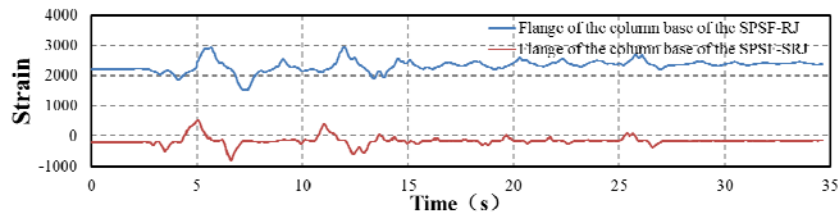


Figure 25. Strain-time History Curves of the Flanges of the Column Base of the SPSF-SRJ and SPSF-RJ under the Action of the EL-Centro (PGA=0.4g)

Under the action of ground motion of PGA=0.51g, the plasticity of each part of the SPSF-SRJ and SPSF-RJ continues to develop. In addition to the flange of the long beam of the SPSF-RJ being under the elastic state, all other parts of the SPSF-RJ had entered the plastic state; the strain at the location where the reinforcing plate is near the vertical plate on the long beam had a maximum value of $7273\mu\varepsilon$; the maximum yield strain at the flange of the short beam had a value as high as

4507 $\mu\epsilon$. During the test, the flange of the short beam, reinforcing plate, flange and web in the connection region of the SPSF-SRJ had entered the plastic state; the flange of the long beam had just entered the plastic state; the strain at the flange in the connection region did not exceed $2\varepsilon_y$. Figures 26 and 27 show the strain-time histories of the flange of the short beams and the web plates in the connection regions of the SPSF-SRJ and SPSF-RJ. However, the flange and web of the column base of the SPSF-SRJ were all under the elastic state. Figure 28 gives the strain-time histories of the flanges of the column bases of the SPSF-SRJ and SPSF-RJ. The performance-based goal of “only relatively small damage occurs and the structure can still normally operate” was realized in the SPSF-SRJ under the action of a rare earthquake as well as a rare 8.5-degree earthquake.

Hence, the use of semi-rigid joints to connect the column base of a self-centering steel frame can effectively protect the column base; however, the plasticity of the flange of the short beam and web plate of the column in the connection region will increase. The web plate in the connection region can be strengthened via a steel plate in future designs to eliminate or reduce the damage on the entire column; only the steel beam would require repairs after an earthquake, significantly reducing the post-earthquake repair cost.

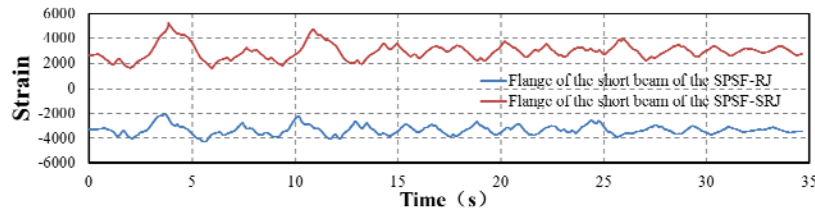


Figure 26. Strain-time History Curves of the Flanges of the Short Beams of the SPSF-SRJ and SPSF-RJ when the SPSF-SRJ and SPSF-RJ are under the Action of the EL-Centro (PGA=0.51g)

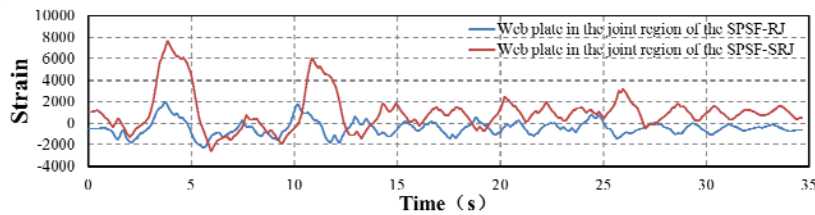


Figure 27. Strain-time History Curves of the Web Plates in the Connection Regions of the SPSF-SRJ and SPSF-RJ when the SPSF-SRJ and SPSF-RJ are under the Action of the EL-Centro (PGA=0.51g)

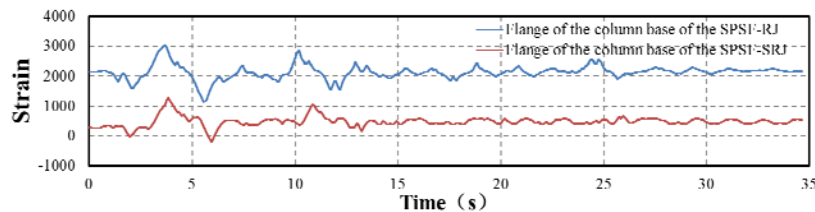


Figure 28. Strain-time History Curves of the Flanges of the Column base of the SPSF-SRJ and SPSF-RJ when the SPSF-SRJ and SPSF-RJ are under the Action of the EL-Centro (PGA=0.51g)

Table10. Maximum Values of the Strain at Different Parts of Structure

 $\mu\epsilon$

			Short beam flange	Long beam flange	Reinforcing plate	Flange of connection zone	Web plate of connection plate	Flange of column foot	Web plate of column foot
0.2 g	SPSF-R J	Taft	1166	263	528	736	772	397	229
		LOS000	1280	635	1381	800	930	1116	1078
		EL-Centro	1389	822	2350	1333	1189	1327	1103
	SPSF-S RJ	Taft	1159	815	446	805	1019	289	207
		LOS000	1629	1112	1043	1089	1393	356	272
		EL-Centro	1729	1010	1583	1434	1487	478	395
0.4 g	SPSF-R J	Taft	2037	909	3219	2389	1244	2335	2076
		LOS000	2396	938	3852	2850	1563	2768	2119
		EL-Centro	3296	1265	4734	2984	1806	2951	2240
	SPSF-S RJ	Taft	2104	1369	1518	1868	3241	682	460
		LOS000	2058	1608	1643	1830	4686	633	304
		EL-Centro	4908	1656	6297	2271	7603	805	536
0.5 1g	SPSF-R J	Taft	3797	1400	5914	2611	2155	3009	2417
		LOS000	4204	1318	5943	2742	2184	3038	2533
		EL-Centro	4507	1394	7273	2695	3094	3167	2663
	SPSF-S RJ	Taft	3828	1545	5494	1993	4414	782	531
		LOS000	4342	1565	6689	2041	6087	899	534
		EL-Centro	5247	1585	9854	2865	7695	1282	619

6. CONCLUSIONS

In the present study, a 3×5 bays 4-story SPSF-SRJ prototype structure was scaled down by 75%. A pseudo-dynamic test was performed on the planar frame sub-structure under the action of different levels of earthquake degrees. In addition, the pseudo-dynamic test results of the SPSF-SRJ are compared with those of the SPSF-RJ that were previously obtained in our research group. The following conclusions were obtained:

- (1) The performance-based design goal – “no opening and no damage occurs during frequent earthquakes; openings are formed to dissipate energy, and no damage occurs to the main structure during design earthquakes; only extremely small structural damage occurs, and the structure can still normally operate during rare and extremely rare earthquakes” – was realized in the SPSF-SRJ.
- (2) The stiffness of the SPSF-SRJ was lower than that of the SPSF-RJ. Therefore, the displacement responses and openings of the connections of the SPSF-SRJ were greater than those of the SPSF-RJ. The base shear force of the SPSF-SRJ was smaller than that of the SPSF-RJ.
- (3) Similar to the SPSF-RJ, the SPSF-SRJ also exhibited a good opening/closing mechanism. The SPSF-SRJ had a double-flag-shaped hysteretic curve. The SPSF-SRJ exhibited relatively good post-earthquake self-centering and energy dissipation capabilities. With increasing seismic acceleration peak values, the energy dissipation coefficient generally exhibited an increasing trend, and the energy dissipation capability of the SPSF-SRJ increased to a certain degree.
- (4) After the test, there were relatively small losses in the PT forces of the prestressed strands, indicating that the prestressed strands of the SPSF-SRJ, performance of the anchorage device, and prestress tensioning method are reliable, which provides a good basis for the SPSF-SRJ to normally operate and bear impacts from relatively large, multiple aftershocks after the occurrence of rare and extremely rare earthquakes.
- (5) There is a relatively large difference in the development of plasticity between the SPSF-SRJ and SPSF-RJ. The reinforcing plate of the SPSF-RJ enters the plastic state first when the SPSF-RJ is under the action of a design earthquake; afterwards, the flange of the short beam, flange and web of the column base, and web and flange in the connection region, connection of the SPSF-RJ enter the plastic state successively with increasing earthquake degree; under the protection of the reinforcing plate, the flange of the long beam maintains its elasticity throughout the process. Different from the SPSF-RJ, the SPSF-SRJ maintains its elastic state when the SPSF-SRJ is under the action of an 8-degree frequent earthquake as well as under the action of an 8-degree design earthquake. Under the action of an 8-degree rare earthquake, the web plate in the beam-column connection region of the SPSF-SRJ enters the plastic state first, after which, the reinforcing plate, flange of the short beam, and flange in the connection region enter the plastic state successively. Under the action of an 8.5-degree rare earthquake, the plasticity of the each part of the SPSF-SRJ continues to develop; however, the flange of the column base, web plate of the column base, and flange of the long beam all still maintain their elasticity.
- (6) Overall, using semi-rigid joints to connect the column base of a self-centering steel frame effectively protects the column base and allows the column base to maintain its elastic state; however, the plasticity of the web plate of the column in the joint region of the SPSF-SRJ will increase when compared with that of the SPSF-RJ. The column joint region should be strengthened in future designs to eliminate or reduce damage to the column; only the steel beam would require repairs after an earthquake, significantly reducing post-earthquake repair costs.

ACKNOWLEDGMENTS

The research reported herein is supported by the National Natural Science Foundation of China under Grant No. 51278027, the Key Project of Beijing Natural Science Foundation under Grant No.8131002 and the Project of Constructing Beijing Energy Saving and Emission Reduction Technology Collaborative Innovation Center.

REFERENCES

- [1] Rojas, P., Ricles, J. M. and Sause, R., "Seismic Performance of Post-tensioned Steel Moment Resisting Frames With Friction Devices", *Journal Structural Engineering*, 2005, Vol. 131, No. 4, pp. 529-540.
- [2] Lin, Y. C., Ricles, J. M. and Sause, R., "Earthquake Simulations on Self-centering Steel Moment Resisting Frame with Web Friction Devices", *Structures Congress 2009*, Reston Virginia: American Society of Civil Engineers, 2009.
- [3] Ricles, J. M., Sause, R., Lin, Y. and Seo, C., "Self-centering Moment Connections for Damage-free Seismic Response of Steel MRFs", *Structures Congress 2010*, Orlando, Reston Virginia: American Society of Civil Engineers, 2010.
- [4] Lin, Y. C., Sause, R. and Ricles, J. M., "Seismic Performance of Steel Self-centering, Moment-resisting Frame: Hybrid Simulations under Design Basis Earthquake", *Journal of Structural Engineering*, 2013, Vol. 139, No. 5, pp. 1823-1832.
- [5] Lin, Y. C., Sause, R. and Ricles, J. M., "Seismic Performance of a Large-scale Steel Self-centering Moment-resisting Frame: MCE Hybrid Simulations and Quasi-static Pushover Tests", *Journal of Structural Engineering*, 2013, Vol. 139, No. 7, pp. 1227-1236.
- [6] Zhang, Y. X., Ye, J. J., Yang, F. and Chen, Y. Y., "Dynamic Behavior and Time-history Analysis of Integral Self-centering Moment Resisting Frames", *China Civil Engineering Journal*, 2015, Vol. 48, No. 7, pp. 30-40. (in Chinese)
- [7] Zhang, Y. X., Zhang, A. L. and Sun, W.L., "Behavior Study of Self-centering Beam-column Connections in Resilient Steel Frames after Earthquake", *Industrial Construction*, 2014, Vol. 44, No. 502, pp. 160-167. (in Chinese)
- [8] Chi, H., Liu, J. and Garlock M., "Design and Analytical Validation of Post-tensioned Column Bases", *Vancouver, British Columbia, Canada: Structures 2008: Crossing Borders 2008*, ASCE.
- [9] Chi, H., "Development of Post-tensioned Column Base Connection for Self-centering Seismic Resistant Steel Frame", *West Lafayette, Indiana: Purdue University*, 2009.
- [10] Georgios, A., Gary, F. and Andre, F. "Computational Framework for Automated Seismic Design of Steel Frames with Self-Centering Connections", *Journal of Computing in Civil Engineering*, 2014, Vol. 28, pp.170-181.
- [11] Matthew, R. and Xiang, M. "Design Concepts for Controlled Rocking of Self-Centering Steel-Braced Frames", *Struct. Eng.*, 2014, Vol. 140, pp. 1-11.
- [12] Gandomi, A. and Roke, D., "Seismic Response Prediction of Self-Centering Concentrically Braced Frames Using Genetic Programming", *Structures Congress. 2014*, pp.1221-1232.
- [13] Darling, S., Eatherton, M. and Maurya, A., "Self-Centering Beams for Seismically Resilient Moment Frames" *Structures Congress*, 2013, pp.1701-1712.
- [14] Pacific Earthquake Engineering Research Center. "Guidelines for Performance-based Seismic Design of Tall Buildings", *California: University of California, Berkeley*, 2010.
- [15] Structural Engineers Association of California, "2012 IBC SEAOC Structural/seismic Design Manual", Vol. 4, *California*, 2012.
- [16] American Institute of Steel Construction, "Seismic Provisions for Structural Steel Buildings", *Chicago: AISC Committee on Specifications*, 2010.
- [17] American Institute of Steel Construction, "Prequalified Connections for Special and Intermediate Steel Moment Frames for Seismic Applications", *Chicago: AISC Board of Directors*, 2010.
- [18] GB 50011-2010, "Code for Seismic Design of Buildings", *Beijing: China Architecture & Building Press*, 2010 (in Chinese)
- [19] Seo, C. Y., and Sause, R., "Ductility Demands on Self-centering Systems under Earthquake Loading." *ACI Struct. J.*, 2005, Vol. 102, No. 2, pp. 275-285.

ANALYSIS OF DOOR-TYPE MODULAR STEEL SCAFFOLDS BASED ON A NOVEL NUMERICAL METHOD

Zhijia Chen^{1,2,*} and Zhongwei Zhao²

¹ State Key Laboratory of Hydraulic Engineering Simulation and Safety, Tianjin University, Tianjin 300072, China

² Department of Civil Engineering, Tianjin University, Tianjin, 300072, China

*(Corresponding author: E-mail: zhchen@tju.edu.cn)

Received: 21 August 2015; Revised: 28 August 2015; Accepted: 4 October 2015

ABSTRACT: As supporting scaffolds, door-type modular steel scaffolds are commonly used in construction. They were repeatedly used in practical project. Member imperfection often occurs when scaffolds were used repeatedly. Influence of member imperfection and joint stiffness on ultimate load of door-type modular steel scaffolds was systematically investigated in this paper. A novel numerical method was adopted and it can be conveniently used based on general finite element software. The method can be adopted for all kinds of scaffold systems. Reliability of the method was validated firstly. Then influence of splice joint stiffness and screw jack stiffness on ultimate load capacity was investigated. Influence of member imperfection was investigated in the end.

Keywords: Double element method, member imperfection, door-type scaffold, buckling behavior, semi-rigid joints

DOI:10.18057/IJASC.2016.12.3.6

1. INTRODUCTION

Modular steel scaffolds are temporary structures and they are commonly used as supporting scaffolds to support buildings under construction or constructors in construction site. As a kind of temporary structures, reliability of modular steel scaffolds has not been brought to the forefront. Many accidents caused by scaffold collapse happened all over the world.



Figure 1. Scaffold Collapse Occurred at a Construction Site in Taichung, Taiwan [1]

Yu investigated the influence of boundary conditions on instability of multi-storey door-type modular steel scaffolds[2]. In this investigation the boundary condition was idealized as pinned or fixed condition. But in most cases, the door-type modular steel scaffolds were semi-rigidly restrained or connected. Chu et al.[3] studied single storey double bay scaffolds. In the presence of

restraints on the loading beam and the jack bases, the top and base were modelled with various boundary conditions, and the scaffold connections were assumed to be rigid [4]. But scaffold joints are complex in nature due to the need for rapid assembly and reassembly in construction. The cuplok connections behave as semi-rigid joints, and show looseness with small rotational stiffness at the beginning of loading. Once the joints lock into place under applied load, the joints become stiffer[5].

So many studies have been conducted to investigate mechanical of scaffold both by experimental test and numerical test [6]. In terms of analytical study on steel scaffolds, Zhang and Rasmussen et al.[9] analyzed the variability of parameters related to steel scaffolds, including joint stiffness, initial geometric imperfection, yield stress, and load eccentricity. That study also obtained the structural strength of the steel scaffolding structures based on Monte Carlo simulation. Zhang and Rasmussen et al.[10] also investigated the failure modes of steel scaffolds, the effect of different random variables on structural strength and the reliability analysis of scaffolding structures. Chan et al.[11] conducted nonlinear analyses on the shoring structures that did not assume an effective length. Based on stability functions, while adopting the notional disturbance force and considering the $P-\delta$ and $P-\Delta$ effects, the analytical method accurately estimates the load-carrying capacities of scaffolding structures with nonlinear analyses.

By means of available commercial finite element software such as ANSYS [12] 13] and NIDA [14], recent studies on scaffold behavior have been carried out using three-dimensional models such as those presented by Prabhakaran et al. [15], Milojkovic et al.[16], and Godley and Beale[17].

Eigenvalue (buckling) analysis of the structural model was often conducted and the lowest eigen mode was taken to create an initially imperfect structural frame for the second-order structural analysis. For scaffold systems, these same approaches can be applied to model the effects of initial imperfections in the analysis. For example, Yu et al.[2] and Chu et al. [18] integrated lowest eigen mode with the magnitude of the column out-of-straightness of 0.001 of the height of the scaffold units into the model. This method is simple and convent, but it neglects the nature of initial imperfection: randomness. The ultimate load obtained by this method may be too conservative.

The height of scaffolds used in large-span structures is often large, for example the scaffold system used in YUJIAPU railway station, shown as in Figure 2. In this case, the joint stiffness and member imperfection may influence its ultimate load in a certain degree.

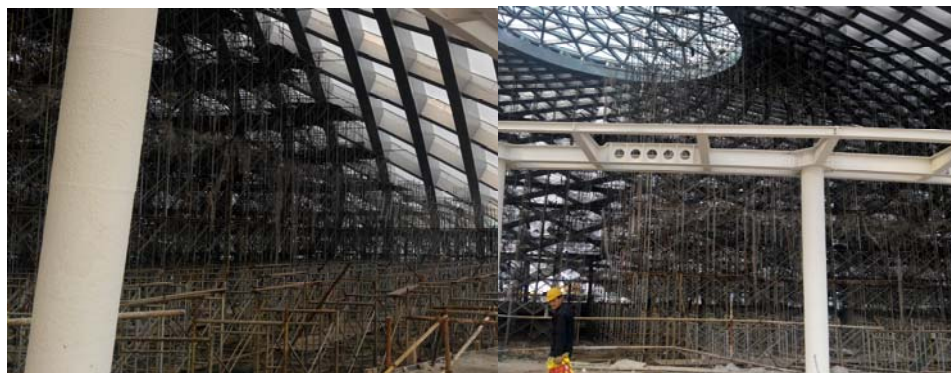


Figure 2. Door-type Modular Steel Ascaffold at YUJIAPU

2. IMPERFECT COMPONENTS WITH DOUBLE ELEMENT

2.1 Establishment of Imperfect components

General finite element software ANSYS [12, 13] was also employed to establish imperfect elements. In traditional analysis, straight line was generated and meshed to simulate components of latticed shell. The member imperfection cannot be considered in this case. In this research, straight line was replaced by curved line through 'BSPLIN' command. In the middle location of the component, magnitude of imperfection was set. In most analysis, the imperfection is assumed to be of a half-wave sinusoid. This can be achieved by adding imperfection value at other points to make the b-spline close to half-wave sinusoid, as shown in Figure 3. To set the imperfection value conveniently, local coordinate system was created. The x axis is in member direction, y axis is in vertical direction. Imperfection value can be generated by adopting sine function in ANSYS [12, 13]. All of the imperfect member can be generated through looping statements. The whole process can be performed easily and it is easy for engineers to master.

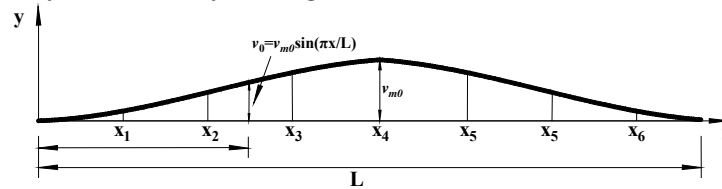


Figure 3. Imperfection Member and Local Coordinate System

2.2 Components with Double Element

Research on the stiffness of joints and their effects on the behavior of structures has been an area of interest to engineers and scientists in recent years and many applicable conclusions have been achieved. But until now, there has been no applicable method to consider joint stiffness in general finite element software. A simplified method considering joint stiffness was proposed in this paper.

This method assumed that joints of latticed shell were composed by two elements: Beam element with only bending stiffness and beam element without bending and torsional stiffness which act as a link element, shown as in Figure 4.

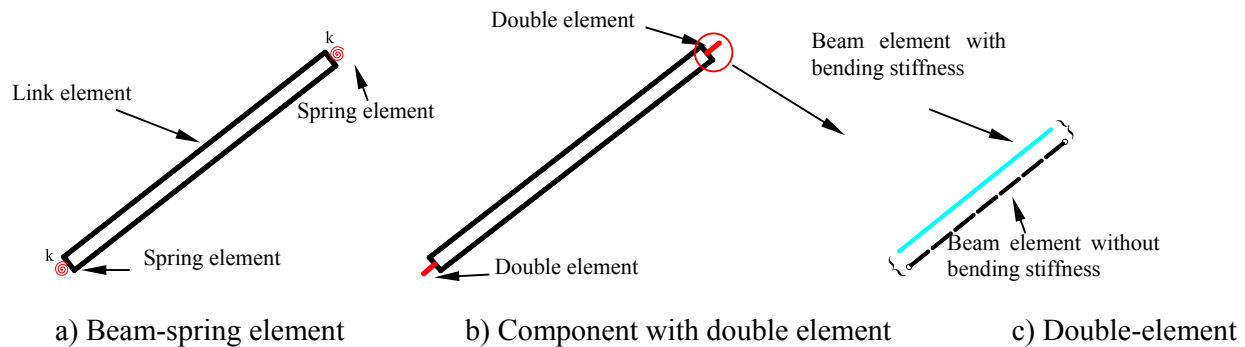


Figure 4. Numerical Model Considering Joints Stiffness

Assuming that the joint stiffness is k and the length of joint domain is l . Then the joint was replaced by double element and its length was set equal to the joint dimension. The rotation angle of joint and double element under action of moment M should be the same.

Rotation angle of the beam under action of moment M , shown as in Figure 5, can be calculated through Eq. 1 for the beam with a constant cross section. Then the bending stiffness of the beam can be represented by Eq. 2.

Let the bending stiffness of double element equal to joint stiffness k , then Eq. 3. can be derived.



Figure 5. Beam under Action of Moment

$$\theta = \int \frac{M}{EI} dl = \frac{Ml}{EI} \quad (1)$$

$$\frac{M}{\theta} = \frac{EI}{l} \quad (2)$$

$$I = \frac{kl}{E} \quad (3)$$

Investigations presented in this paper was conducted based on general finite element software ANSYS [12, 13]. BEAM4 element in ANSYS [12, 13] is a uniaxial element with tension, compression, torsion, and bending capabilities. The element has six degrees of freedom at each node: translations in the nodal x, y, and z directions and rotations about the nodal x, y, and z axes. The equilibrium equation and stiffness matrix of BEAM4 in element coordinates is shown as in Eq. 4 [13].

$$F = \begin{bmatrix} F_x \\ F_y \\ F_z \\ M_x \\ M_y \\ M_z \\ F'_x \\ F'_y \\ F'_z \\ M'_x \\ M'_y \\ M'_z \end{bmatrix} = [K_e] \begin{bmatrix} u_x \\ u_y \\ u_z \\ \theta'_x \\ \theta'_y \\ \theta'_z \\ u'_x \\ u'_y \\ u'_z \\ \theta'_x \\ \theta'_y \\ \theta'_z \end{bmatrix} = \begin{bmatrix} AE/L & 0 & 0 & 0 & 0 & 0 & -AE/L & 0 & 0 & 0 & 0 & 0 \\ 0 & a_z & 0 & 0 & 0 & c_z & 0 & -a_z & 0 & 0 & 0 & c_z \\ 0 & 0 & a_y & 0 & -c_y & 0 & 0 & 0 & -a_y & 0 & -c_y & 0 \\ 0 & 0 & 0 & GJ/L & 0 & 0 & 0 & 0 & 0 & -GJ/L & 0 & 0 \\ 0 & 0 & -c_y & 0 & e_y & 0 & 0 & 0 & 0 & 0 & f_y & 0 \\ 0 & c_z & 0 & 0 & 0 & e_z & 0 & -c_z & 0 & 0 & 0 & f_z \\ -AE/L & 0 & 0 & 0 & 0 & 0 & AE/L & 0 & 0 & 0 & 0 & 0 \\ 0 & -a_z & 0 & 0 & 0 & -c_z & 0 & a_z & 0 & 0 & 0 & -c_z \\ 0 & 0 & -a_y & 0 & 0 & 0 & 0 & 0 & a_y & 0 & c_y & 0 \\ 0 & 0 & 0 & -GJ/L & 0 & 0 & 0 & 0 & 0 & GJ/L & 0 & 0 \\ 0 & 0 & -c_y & 0 & f_y & 0 & 0 & 0 & c_y & 0 & e_y & 0 \\ 0 & c_z & 0 & 0 & 0 & f_z & 0 & -c_z & 0 & 0 & 0 & e_z \end{bmatrix} \begin{bmatrix} u_x \\ u_y \\ u_z \\ \theta'_x \\ \theta'_y \\ \theta'_z \\ u'_x \\ u'_y \\ u'_z \\ \theta'_x \\ \theta'_y \\ \theta'_z \end{bmatrix} \quad (4)$$

Where A , E , L , G and J are cross-section area, Young's modulus, element length, shear modulus and torsional moment of inertia.

$$a_{y(z)} = \frac{12EI_{y(z)}}{L^3(1+\phi_{z(y)})}, \quad c_{y(z)} = \frac{6EI_{y(z)}}{L^2(1+\phi_{z(y)})}, \quad e_{y(z)} = \frac{(4+\phi_{z(y)})EI_{y(z)}}{L(1+\phi_{z(y)})}, \quad \phi_{z(y)} = \frac{12EI_{y(z)}}{GA^s_{y(z)}L^2}$$

I_i is moment of inertia about direction i , $A^s_{y(z)}$ is shear area normal to direction $y(z)$ axes.

For beam element with bending stiffness in double-element, only the bending stiffness was assigned by real constant. The equilibrium equation and stiffness matrix of this element in element coordinates is shown as in Eq.5. For Beam element without bending stiffness in double-element, it was also BEAM4 element in ANSYS [12, 13], but the bending stiffness was set a very little value, that the beam element can be assumed as a link element. The equilibrium equation and stiffness matrix of this element in element coordinates is shown as in Eq. 6.

$$F = \begin{bmatrix} F_x \\ F_y \\ F_z \\ M_x \\ M_y \\ M_z \\ F'_x \\ F'_y \\ F'_z \\ M'_x \\ M'_y \\ M'_z \end{bmatrix} = [K_{beam}] \begin{bmatrix} u_x \\ u_y \\ u_z \\ \theta_x \\ \theta_y \\ \theta_z \\ u'_x \\ u'_y \\ u'_z \\ \theta'_x \\ \theta'_y \\ \theta'_z \end{bmatrix} = \begin{bmatrix} 0 & 0 & 0 & 0 & 0 & 0 & 0 & 0 & 0 & 0 & 0 & 0 \\ 0 & 0 & 0 & 0 & 0 & c_z & 0 & 0 & 0 & 0 & 0 & c_z \\ 0 & 0 & 0 & 0 & -c_y & 0 & 0 & 0 & 0 & 0 & -c_y & 0 \\ 0 & 0 & 0 & 0 & 0 & 0 & 0 & 0 & 0 & 0 & 0 & 0 \\ 0 & 0 & 0 & 0 & 0 & e_y & 0 & 0 & 0 & 0 & 0 & f_y \\ 0 & 0 & 0 & 0 & 0 & e_z & 0 & 0 & 0 & 0 & 0 & f_z \\ 0 & 0 & 0 & 0 & 0 & 0 & 0 & 0 & 0 & 0 & 0 & 0 \\ 0 & 0 & 0 & 0 & 0 & -c_z & 0 & 0 & 0 & 0 & 0 & -c_z \\ 0 & 0 & 0 & 0 & 0 & 0 & 0 & 0 & 0 & 0 & c_y & 0 \\ 0 & 0 & 0 & 0 & 0 & 0 & 0 & 0 & 0 & 0 & 0 & 0 \\ 0 & 0 & 0 & 0 & 0 & f_y & 0 & 0 & 0 & 0 & e_y & 0 \\ 0 & 0 & 0 & 0 & 0 & f_z & 0 & 0 & 0 & 0 & e_z & 0 \end{bmatrix} \begin{bmatrix} u_x \\ u_y \\ u_z \\ \theta_x \\ \theta_y \\ \theta_z \\ u'_x \\ u'_y \\ u'_z \\ \theta'_x \\ \theta'_y \\ \theta'_z \end{bmatrix} \quad (5)$$

$$F = \begin{bmatrix} F_x \\ F_y \\ F_z \\ M_x \\ M_y \\ M_z \\ F'_x \\ F'_y \\ F'_z \\ M'_x \\ M'_y \\ M'_z \end{bmatrix} = [K_e] \begin{bmatrix} u_x \\ u_y \\ u_z \\ \theta_x \\ \theta_y \\ \theta_z \\ u'_x \\ u'_y \\ u'_z \\ \theta'_x \\ \theta'_y \\ \theta'_z \end{bmatrix} = \begin{bmatrix} AE/L & 0 & 0 & 0 & 0 & 0 & -AE/L & 0 & 0 & 0 & 0 & 0 \\ 0 & a_z & 0 & 0 & 0 & 0 & 0 & -a_z & 0 & 0 & 0 & 0 \\ 0 & 0 & a_y & 0 & 0 & 0 & 0 & 0 & -a_y & 0 & 0 & 0 \\ 0 & 0 & 0 & GJ/L & 0 & 0 & 0 & 0 & 0 & -GJ/L & 0 & 0 \\ 0 & 0 & -c_y & 0 & 0 & 0 & 0 & 0 & 0 & 0 & 0 & 0 \\ 0 & c_z & 0 & 0 & 0 & 0 & 0 & -c_z & 0 & 0 & 0 & 0 \\ -AE/L & 0 & 0 & 0 & 0 & 0 & AE/L & 0 & 0 & 0 & 0 & 0 \\ 0 & -a_z & 0 & 0 & 0 & 0 & 0 & a_z & 0 & 0 & 0 & 0 \\ 0 & 0 & -a_y & 0 & 0 & 0 & 0 & 0 & a_y & 0 & 0 & 0 \\ 0 & 0 & 0 & -GJ/L & 0 & 0 & 0 & 0 & 0 & GJ/L & 0 & 0 \\ 0 & 0 & -c_y & 0 & 0 & 0 & 0 & 0 & c_y & 0 & 0 & 0 \\ 0 & c_z & 0 & 0 & 0 & 0 & 0 & -c_z & 0 & 0 & 0 & 0 \end{bmatrix} \begin{bmatrix} u_x \\ u_y \\ u_z \\ \theta_x \\ \theta_y \\ \theta_z \\ u'_x \\ u'_y \\ u'_z \\ \theta'_x \\ \theta'_y \\ \theta'_z \end{bmatrix} \quad (6)$$

3. ESTABLISHMENT OF NUMERICAL MODEL

Analysis was conducted based on work specimens tested by Yu et al. [2]. The member configurations of the door-type modular steel scaffolds together with their dimensions were illustrated as in

Figure 6 .

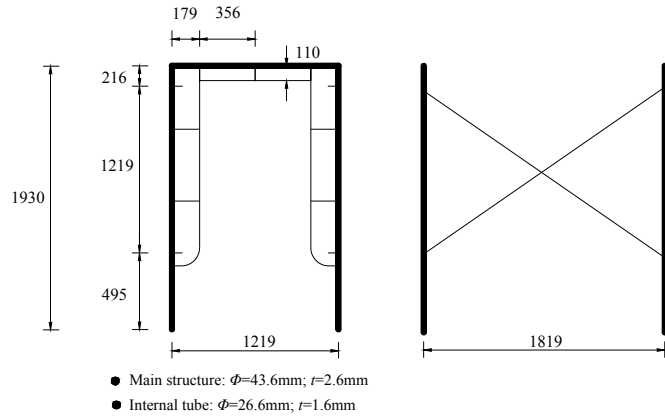


Figure 6. Typical Dimensions of Scaffolding Frame (unite: mm)

Beam188 element was adopted to establish finite element models of scaffold system. To model the mechanical behavior of x-brace, translational degrees of freedom of nodes located at middle of the two brace were coupled together. The bending degrees of node at two ends of brace were released by “ENDRELEASE” command. Double element was established to model connection between different modular scaffolds and the screw jack at bottom of scaffold.

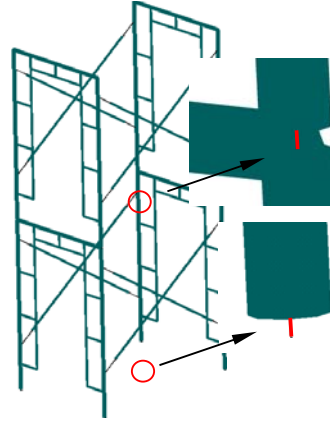


Figure 7. Finite Element Models of Two-storey Scaffold System

4. RESULTS AND DISCUSSIONS

4.1 Validation of Numerical Method

To validate the reliability of numerical method presented in this paper, two-storey scaffold system was analyzed. The boundary conditions with various degrees of positional and rotational restraints are classified into four categories.

- Pinned-Fixed condition,
- Pinned-Pinned condition,
- Free-Fixed condition, and
- Free-Pinned condition,

where the first condition refers to the positional restraint provided at the top of the scaffold while the second refers to the rotational restraint provided at the bottom of the scaffold, respectively.

The results derived was shown as in Figure 8 and it was compared to that derived by Yu et al.[2], shown as in Figure 9. It can be concluded that the boundary conditions of door-type scaffold system have great influence on its ultimate load capacity. The reliability of numerical model established based on method proposed in this paper was validated through comparison shown in Figure 9. It can be seen that the results were highly consistent with each other.

Figure 10 shows failure modes of two-storey scaffold system with different boundary conditions. It can be concluded that the boundary condition will also determine the failure modes.

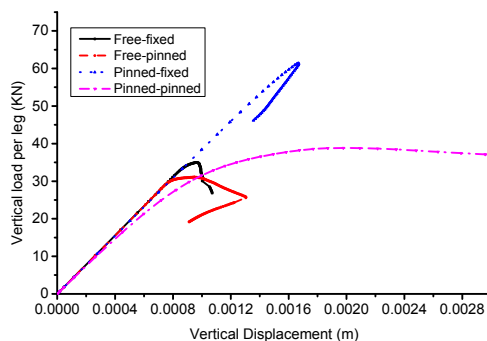


Figure 8. Load Deformation Curves of Modular Steel Scaffolds.

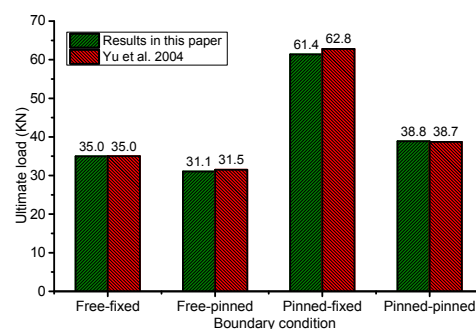


Figure 9. Ultimate Load of Modular Steel Scaffolds.

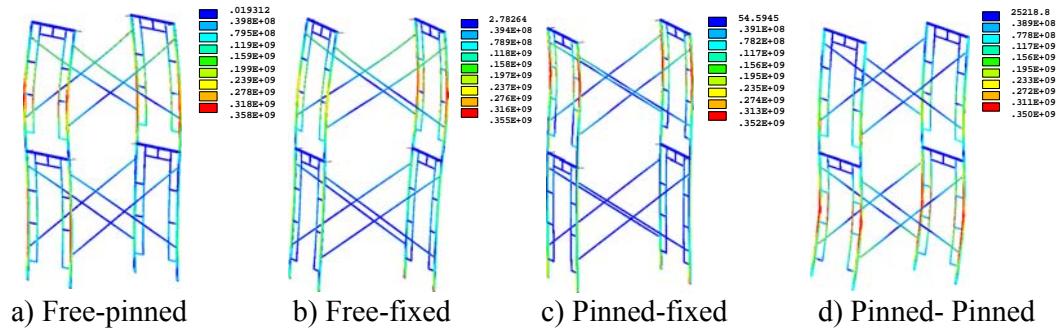


Figure 10. Failure Mode of Two-story, One-bay Scaffold System

4.2 Influence of Splice Stiffness

4.2.1 Free-fixed Condition

To investigate the influence of splice stiffness on ultimate load capacity of door-type scaffolds system, double element between different modular steel scaffolds were given different stiffness factor k to simulate influence of splice stiffness. Where k indicates ratio of splice stiffness to bending stiffness of stand column. The boundary was free-fixed condition.

The load-displacement curves with different splice stiffness were shown as in Figure 11. It can be concluded from the results that the splice stiffness has almost no influence on its ultimate load capacity. The influence is so slight that can be neglected. The splice stiffness will affect mechanical behavior of three-story, one-bay scaffold system after failure and will not for the three-story, two-bay scaffold system. The splice stiffness will also not influence initial structural stiffness.

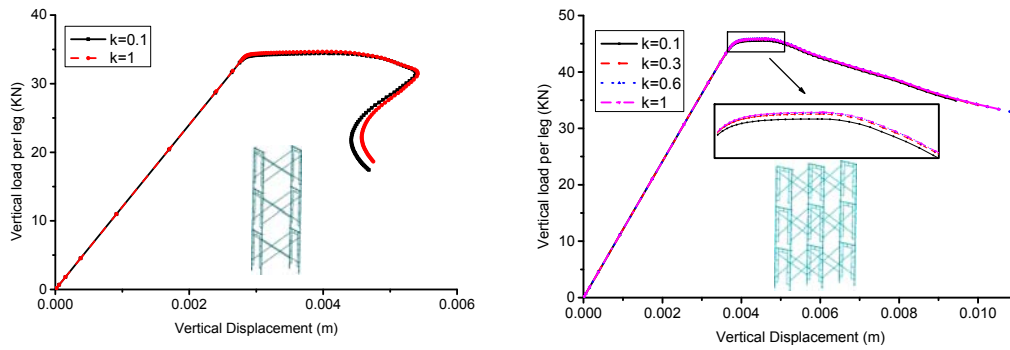


Figure 11. Influence of Splice Stiffness on Ultimate Load Capacity

Failure modes of three-story, two-bay scaffold system were shown as in Figure 12. It can be concluded that the splice stiffness will not influence failure mode. Failure was caused by buckling of stand column of the topmost storey. This may be caused by free condition of top nodes.

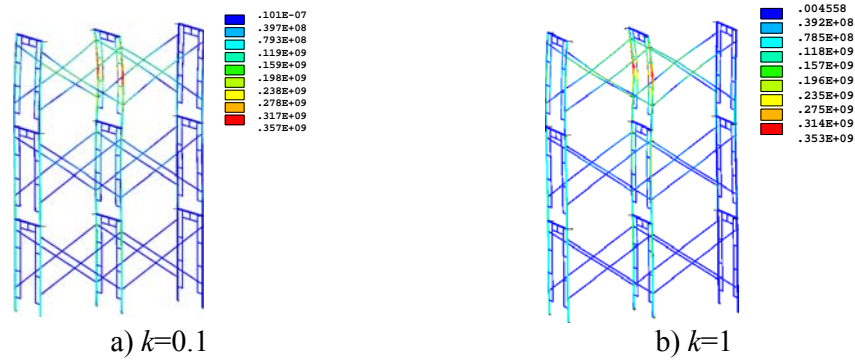


Figure 12. Failure Mode of Three-story, Two-bay Scaffold System

4.2.2 Pinned-fixed Condition

Analysis was conducted to investigate influence of splice stiffness on scaffold system with top nodes pinned constraint. Three-story, one-bay and three-story, four-bay scaffold system were analyzed. Load-displacement curves were shown as in Figure 13.

It can be seen from Figure 13 that the ultimate load was reduced from 92KN to 87.4KN when splice joint stiffness factor was set as 1 and 0.1 respectively for the three-story, one-bay scaffold system. For three-story, four-bay scaffold system, the ultimate load was reduced from 94KN to 90.26KN. It can be concluded that influence of splice stiffness on pinned-fixed condition is larger than that of free-fixed condition. This is caused by failure modes. The ultimate load was reduced by 5% and 4% for the two analyzed scaffold system.

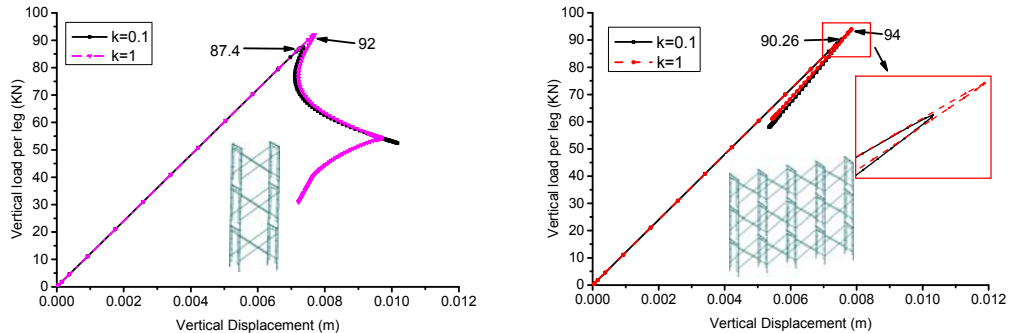


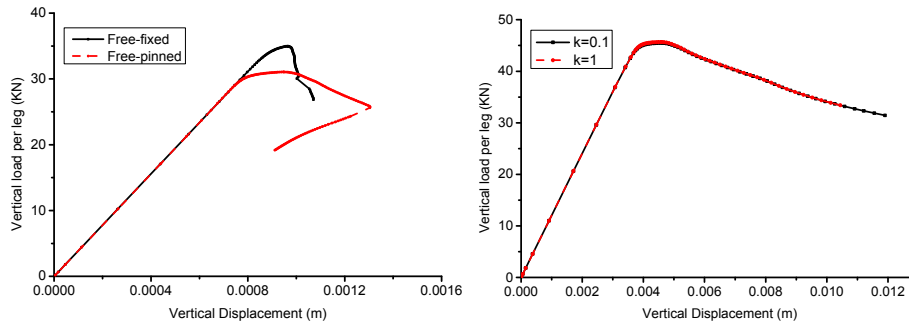
Figure 13. Influence of Splice Stiffness on Ultimate Load Capacity

4.3 Influence of Screw Jack Stiffness

4.3.1 Free-fixed condition

According to investigations conducted by Yu [2] that screw jack stiffness on ultimate load capacity of one-storey scaffold is the greatest. The ultimate load was reduced by 59% when the screw jack was changed from fixed condition to pinned condition. In this section, scaffold system that is in free-fixed condition was analyzed and the results were shown as in Figure 14. It can be concluded from Figure 14. a) that the reduced factor was 88.7% for two-storey scaffold system and it can also be concluded from Figure 14 b) that the screw jack stiffness almost has no influence on ultimate load for three-storey scaffold system. This is in consistent with the conclusions derived by Yu et al. [2].

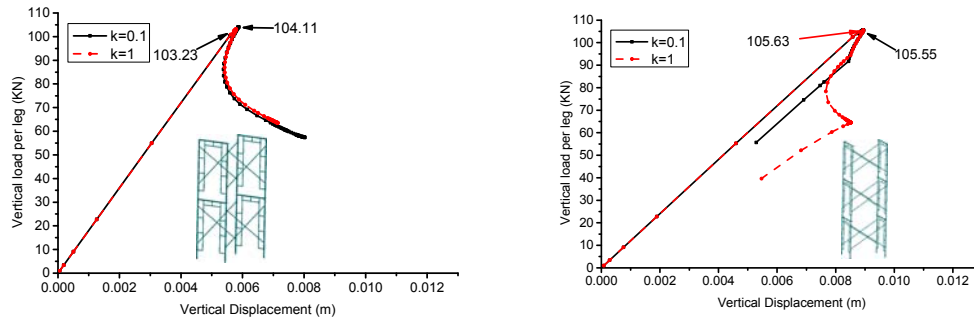
It can be deduced from the results mention above that the screw jack stiffness has influence on one-storey and two-storey scaffold system. The screw jack stiffness will has no influence on ultimate load capacity when the scaffold system is more than two stories.



a) Two-story, one-bay scaffold system b) Three-story, one-bay scaffold system
Figure 14. Influence of Screw Jack Stiffness (free-fixed)

4.3.2 Pinned-fixed condition

To investigate influence of screw jack stiffness on the scaffold systems in pinned-fixed condition. Analysis were conducted and the results were shown as in Figure 15. It can be concluded that the screw jack stiffness has little influence on ultimate load if the scaffold system was pinned-fixed constraint and more two stories.



a) Two-story, one-bay scaffold system b) Three-story, one-bay scaffold system
Figure 15. Influence of Screw Jack Stiffness (pinned-fixed)

5. INFLUENCE OF INITIAL IMPERFECTION

In practical project, it is inevitable that the scaffold systems have some initial imperfections, such as initial bending of member. The initial bending will decrease load capacity in a certain degree. So analysis was systematically conducted to investigate its influence. Different scaffold systems were analyzed and the results were shown as in Figure 16. M_0 and h indicate magnitude of initial bending and height of scaffold modular.

Figure 16 shows results of different scaffold system. It can be concluded from the results that when the initial bending magnitude M_0 was less than $h/1000$ which is the maximum allowable imperfection in [19], the influence of initial member bending has little influence on ultimate load capacity. The structural stiffness was also slightly influenced. So the maximum allowable member imperfection can also be determined as $h/1000$.

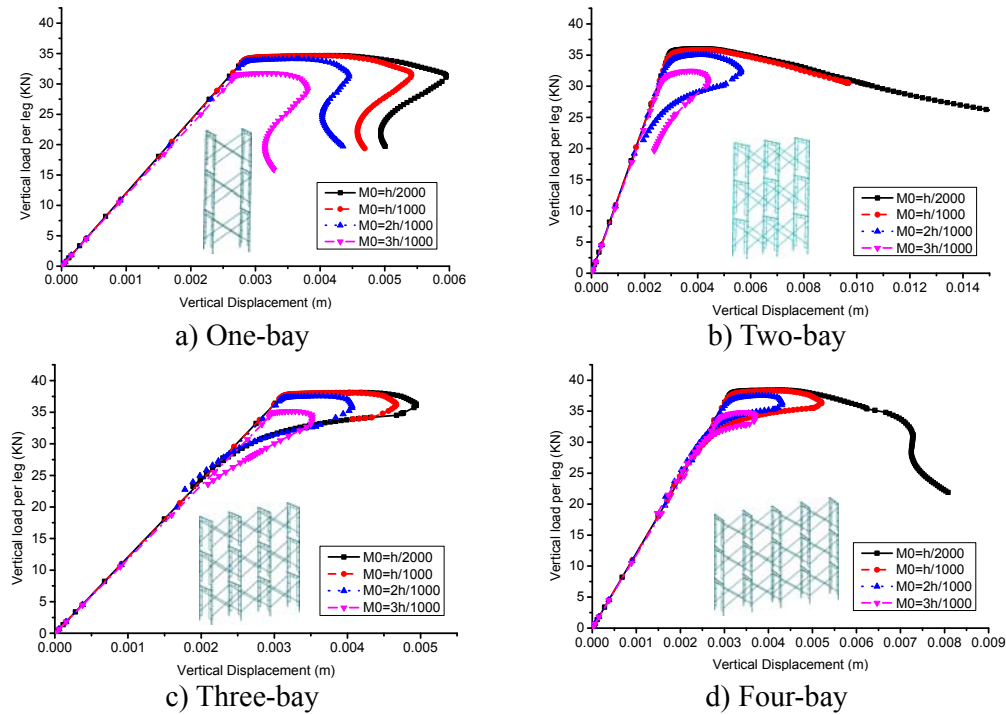


Figure 16. Influence of Initial Imperfection

Figure 17 shows failure modes of different scaffold systems with member imperfection. It can be concluded that failure occurs at the top storey. So it is easy to be understood that the screw jack stiffness almost has no influence on ultimate load when the scaffold system is more than two stories.

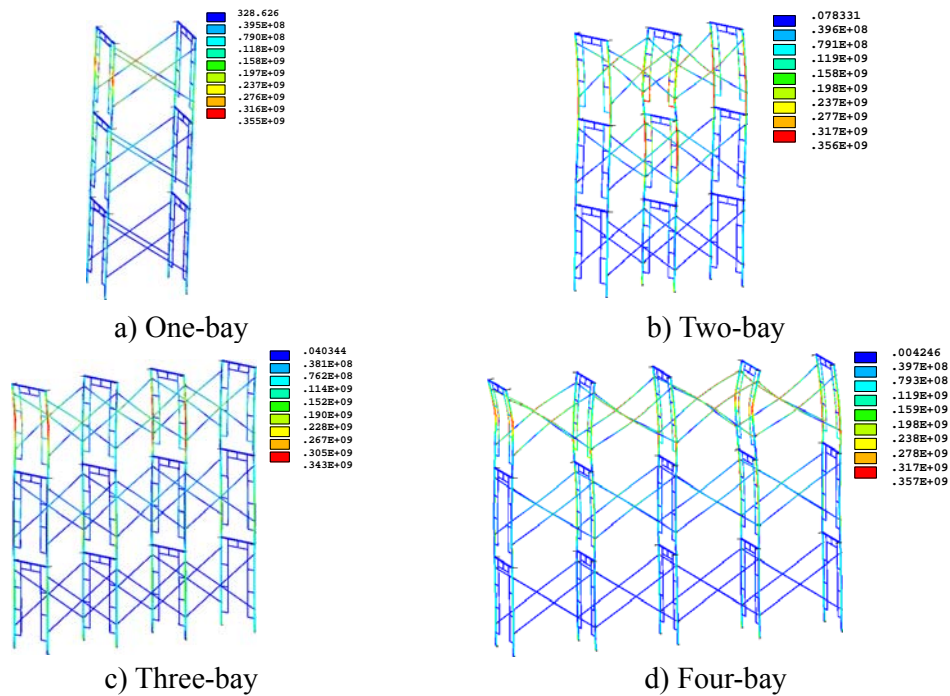


Figure 17. Failure Mode of Scaffold System

6. CONCLUSIONS

A novel numerical method was proposed in this paper. It can be easily adopted in analysis of joint stiffness and member imperfection. Reliability of the method was validated firstly. The method can be adopted for all kinds of scaffold systems. Then influence of splice joint stiffness was analyzed. It was concluded that splice joint stiffness has little influence on ultimate load in free-fixed condition and the influence is larger in pinned-fixed condition. The screw jack stiffness has great influence on ultimate load of lower scaffold system and the influence can be neglected when the scaffold system is more than two stories.

REFERENCES

- [1] Peng, J.L., Wu, C.W., Chan, S.L. and Huang, C.H., "Experimental and Numerical Studies of Practical System Scaffolds", *Journal of Constructional Steel Research*, 2013, Vol. 91, pp. 64–75.
- [2] Yu, W.K., Chung, K.F. and Chan, S.L., "Structural Instability of Multi-storey Door-type Modular Steel Scaffolds", *Engineering Structures*, 2004, Vol. 26, No. 7, pp. 867-881.
- [3] Chu, A.Y.T., Chan, S.L. and Chung, K.F., "Stability of Modular Steel Scaffolding Systems-theory and Verification", In: *Proceedings of International Conference Advances in Building Technology*, 2002, pp. 621-8.
- [4] Tayakorn, Chandransu and Kim, J.R. Rasmussen, "Structural Modelling of Support Scaffold Systems", *Journal of Constructional Steel Research*, 2011, No. 67, No. 5, pp. 866-875.
- [5] Godley, M.H.R. and Beale, R.G., "Sway Stiffness of Scaffold Structures", *Structural Engineer*, 1997, Vol. 75, pp. 4-12.
- [6] Chan, S.L., Huang, H.Y. and Fang, L.X., "Advanced Analysis of Imperfect Portal Frames with Semi-rigid Base connections", *Journal of Engineering Mechanics*, 2005, Vol. 131, pp. 633–40.
- [7] Weesner, L.B. and Jones, H.L., "Experimental and Analytical Capacity of Frame Scaffolding", *Engineering Structures*, 2001, Vol. 23, pp. 592–9.
- [8] Zhang, H., Chandransu, T. and Rasmussen, K.J.R., "Probabilistic Study of the Strength of Steel Scaffold Systems", *Struct. Saf.*, 2010, Vol. 32, pp. 393–401.
- [9] Zhang, H., Chandransu, T. and Rasmussen, K.J.R., "Probabilistic Study of the Strength of Steel Scaffold Systems", *Structural Safety*, 2010, Vol. 32, pp. 393-401.
- [10] Zhang, H., Rasmussen, K.J.R. and Ellingwood, B.R., "Reliability Assessment of Steel Scaffold Shoring Structure for Concrete Formwork", *Engineering Structures*, 2012, Vol. 36, pp. 81-89.
- [11] Chan, S.L., Chu, A.Y.T. and Albermani, F.G., "Stability and Simulation-based Design of Steel Scaffolding without Using the Effective Length Method", *Structural Stability and Dynamics*, 2003, Vol. 3, No. 4, pp. 443-460.
- [12] ANSYS. ANSYS Multiphysics, Version 14.0. ANSYS Inc., Canonsburg, Pennsylvania, USA. (www.ansys.com), 2011.
- [13] ANSYS user's manual. SAS IP inc.;2011
- [14] NIDA-9. Nonlinear Integrated Design and Analysis Software for Structures, Version 9, Department of Civil and Environmental Engineering, The Hong Kong Polytechnic University, Hong Kong, China, 2015.
- [15] Prabhakaran, U., Godley, M.H.R. and Beale, R.G., "Three-dimensional Second Order Analysis of Scaffolds with Semi-rigid Connections", *Welding in the World*, 2006, Vol. 50, pp. 187–94.

- [16] Milojkovic, B., Beale, R.G. and Godley, M.H.R., “Determination of the Factors of Safety of Standard Scaffold Structures”, In: Proceedings of International Conference Advances in Steel Structures, 2002, pp. 303–10.
- [17] Godley, M.H.R. and Beale, R.G., “Sway Stiffness of Scaffold Structures”, Structural Engineer, 1997, Vol. 75, pp. 4–12.
- [18] Chu, A.Y.T., Chan, S.L. and Chung, K.F., “Stability of Modular Steel Scaffolding Systems-theory and Verification”, In: Proceedings of International Conference Advances in Building Technology, 2002, pp. 621-8.
- [19] JGJ61-2003 Technical Specification for Latticed Shells, China Architecture & Building Press, Beijing, China, 2003. (in Chinese)

SAFETY ASSESSMENT OF EUROCODE 3 STABILITY DESIGN RULES FOR THE FLEXURAL BUCKLING OF COLUMNS

Luís Simões da Silva, Trayana Tankova*, Liliana Marques and Carlos Rebelo

*ISISE, Department of Civil Engineering, University of Coimbra, Coimbra, Portugal
Polo II, Pinhal de Marrocos
3030-290 Coimbra, PORTUGAL*

**(Corresponding author: E-mail: ttankova@uc.pt)*

Received: 25 September 2015; Accepted: 21 October 2015

ABSTRACT: This paper presents the safety assessment of Eurocode 3 – part 1-1 [1] rules for the flexural buckling columns using hot-rolled cross-sections (I and H cross-sections).

The safety assessment follows the procedure presented in Annex D of EN 1990 [2]. It is based on a large number (7332) of numerical simulations (GMNIA) covering various relevant parameters.

Firstly, it is concluded that the level of safety is consistent across the various types of I and H cross-sections and steel grades (maximum variation of 6.3%) except for S460 and minor axis buckling. It is therefore proposed to adjust the buckling curves for minor axis buckling for S460.

Secondly, the magnitude of the partial factor γ_{M1} is assessed. It is shown that depending on the random variables included in the analysis (just yield stress f_y ; yield stress f_y and cross-section geometry; or yield stress f_y , cross-section geometry and modulus of elasticity E) the average value of γ_{M1} varies from 0.941 to 1.049 with c.o.v varying from 4.3% to 6.3%.

Keywords: Column, flexural buckling, safety assessment, design rules, steel, Eurocode 3, stability

DOI:10.18057/IJASC.2016.12.3.7

1. INTRODUCTION

A main purpose of modern design codes is to provide design principles and application rules that lead to appropriate safety levels. The safety margin reflects the risk society is willing to accept yet that maximises economical design. Nowadays, it is possible to link quantitatively a specific design rule and the corresponding failure probability [3]. However, because design codes combine a very large number of design rules that evolved over many decades of expensive research work and their semi-probabilistic implementation was only effectively started in the 1990's [4], the safety level is not uniform across the various design rules and also within single design rules. Eurocodes 3, part 1-1 [1] is no exception, despite the enormous work that was put in its development and the wide past proven experience that it incorporates. In this paper focus is given to the stability verification of columns.

The design verification of the flexural buckling resistance of columns in Eurocode 3 is based on the buckling curve approach and the underlying European buckling curves that were established in the 1970's. Their development was based on an extensive experimental programme carried out by the European Convention for Constructional Steelwork (ECCS) in several European countries [5]. The theoretical background was summarized by Beer and Schulz [6] by thorough analysis of the experimental programme presented in Sfintesco [5], assessing various imperfections that can possibly occur and affect the resistance of compressed members. Furthermore, the safety of one of the curves was evaluated by Monte Carlo simulation accounting for the variability of various parameters [7]. Finally, Maquoi and Rondal [8] derived the analytical Ayrton-Perry format of the design verification and the curves were put into equation.

Recently, within the scope of the stability rules for steel members, it was recognized that the

extensions, corrections and improvements that evolved over a long period of time since the establishment of the column buckling curves, coupled with the development of new structural steels with largely improved mechanical and geometrical properties and dramatically improved quality control procedures, required a reassessment of the current safety levels of the stability design rules of EC3-1-1 [1]. Thus, this paper addresses a systematic assessment of the safety levels of the fundamental case of flexural buckling of I-shaped hot-rolled steel columns. Firstly, the adopted assumptions for the safety assessment are summarized. A parametric study for the evaluation of rules for flexural buckling of prismatic columns in EC3-1-1 is subsequently carried out. It covers several slenderness ranges, level of residual stresses, yield stress, and cross-section shapes, such that a thorough evaluation of the several members covered by the analysed stability design rules is possible, using advanced nonlinear numerical simulations. Finally, a discussion on the value of the partial factor γ_{M1} to be adopted based on the obtained results is proposed, leading to the proposal of adjustments to the buckling curves.

2. SAFETY ASSESSMENT OF STABILITY DESIGN RULES

2.1 Scope and Assumptions

The assessment encompasses the design rules for flexural buckling of columns given in EC3-1-1, given in clause 6.3.1 for hot-rolled sections. The partial factor γ_{M1} is obtained based on the methodology given in Annex D of EN 1990. Following [2] the procedure is briefly summarized in Section 2.2. The buckling strength of the members is obtained using advanced numerical finite element simulations (GMNIA). Numerical models are detailed in Section 2.4.

For each case (in plane and out-of-plane buckling), a wide range of I-shaped cross sections covering several buckling curves are analysed across practical ranges of slenderness. The parametric study is organized by buckling mode and it is defined in Section 3.1 for the flexural buckling of columns.

In the safety assessment of the design rules carried out in Section 3, the following assumptions are considered:

- The variability of the input variables in the design model is not considered for the calculation of V_{δ} ; the value is obtained from nominal properties since the “experimental” results are considered with nominal properties;
- The coefficient of variation of the basic variables, V_{rt} , considers only the variability of cross section dimensions, yield stress and modulus of elasticity; for these parameters more information is known and documented with recent data. The adopted distributions are summarized in Section 2.3.

2.2 Basis of Design

The framework for the statistical assessment of the steel members was presented and discussed in Tankova et al. [9]. The procedure proposed in Annex D of EN 1990 is summarized in Figure 1:

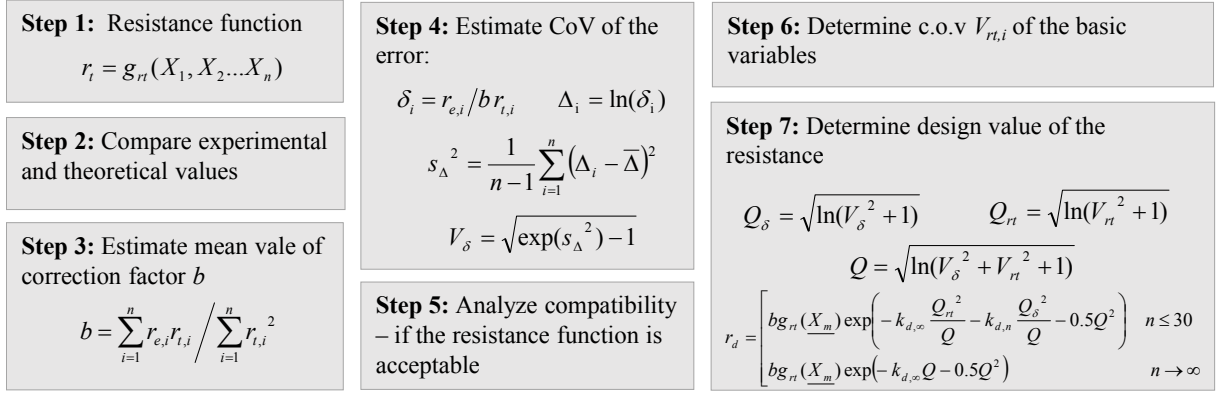


Figure 1. Flow Chart – Annex D

In Step 6, V_{rt} shall be determined as follows:

$$V_{rt}^2 = \frac{1}{g_{rt}(X_m)^2} \sum_{j=1}^k \left(\frac{\partial g_{rt}(X_j)}{\partial X_j} \sigma_j \right)^2 \quad (1)$$

The partial derivatives are computed numerically using expression (2) adopting a sufficiently small increment “ ΔX_i ” for each test specimen separately, leading to $\gamma_{M,i}$ for each specimen; finally the mean value for the subset is considered.

$$\frac{\partial r_t}{\partial X_i} \approx \frac{r_t(X_1, \dots, X_i + \Delta X_i, \dots, X_j) - r_t(X_1, \dots, X_i, \dots, X_j)}{\Delta X_i} \quad (2)$$

2.3 Adopted Distributions

In Step 6 of the procedure given in *Figure 1*, information about the scatter of the basic input parameters is required. The distributions summarized in *Table 1* were considered as a reference for the variability of the yield stress. The data was obtained from (*Simões da Silva et al. 2009*) [10] for S235 and S355; and from OPUS [11] for S460, for which there was sufficient number of coupon tests to give reliable distributions (see Annex A for further detail).

The parametric study given in Section 3.1 was defined in order to cover various parameters. Regarding the material properties, a well-known phenomenon is the variation of yield stress with thickness; hence, in this assessment, the provisions of EN 10025[12] have been adopted. Since there was not sufficient information about the distributions of the material properties with the thickness variation, the distributions from *Table 1* were extrapolated from the nominal yield stress for $t_f \leq 16\text{mm}$ and the coefficient of variation was kept constant.

Table 1. Adopted Reference Yield Stress Distributions

Steel	$f_{y,nom}$	$f_{y,m}$	c.o.v	Source
	Mpa	MPa	-	-
S235	235	297.3	5.8%	Silva et al [10]
S355	355	419.4	4.8%	Silva et al [10]
S460	460	520.0	5.2%	OPUS [11]

It is noted that the extrapolated distributions were then considered for computation of the γ_{Mi} value of each column, according to its cross-section flange thickness irrespective of whether EN 10025 or EC3-1-1 were used for the choice of nominal yield stress.

Regarding cross-section geometrical properties, statistical indicators from Alpsten [13] and results reported in Taras [14] were adopted for H or I sections and are given in *Table 2*:

Table 2. Adopted Geometrical Distributions

	Mean	c.o.v	Source
b_m/b_{nom}	1	0.9%	Alpsten, G. (1972) [13], Taras A. (2010) [14]
h_m/h_{nom}	1	0.9%	
t_{fm}/t_{fnom}	0.975	3.0%	
t_{wm}/t_{wnom}	1.025	4.0%	

b_m denotes the mean value of the flange width, b_{nom} denotes the nominal value of the flange width, h_m is the mean value of the cross-section height, h_{nom} is the nominal value of the cross-section height, t_f is the mean value of the flange thickness, $t_{f,nom}$ denotes the nominal value of the flange thickness, t_w denotes the mean value of the web thickness and $t_{w,nom}$ denotes the nominal value of the web thickness. Although the reports by Alpsten [13] and Taras [14] are not recent, the statistical characterization of the cross-section dimensions is in line with the statistical indicators for area, moment of inertia and bending modulus as given in the report from the research project PROQUA [15], see *Table 3*. Considering a normal distribution, the computation of the distributions of area and moment of inertia from the distributions of the cross-section dimensions from *Table 2* leads to values of mean and standard deviation that fall within the range of *Table 3*. Hence, the statistical description of the cross-section dimensions of *Table 2* are adopted in the calculation as input random variables.

Table 3. Statistical Distributions for Geometry (A, W, I) PROQUA [15]

	Mean, X_m	σ_x
A, W, I PROQUA [15]	$0.99X_{nom}$	$0.01 - 0.04 X_m$

A distribution for the modulus of elasticity is adopted based on recommendations given in DNV [16] that reports $E_m = E_{nom}$ and a c.o.v. of 5%. It is noted that the statistical characterization of the modulus of elasticity is not so strongly supported by experimental evidence. Furthermore, the testing procedures are not often as reliable with respect to this property. Hence, in Section 3 a sensitivity study is carried out with respect to this property by also considering a c.o.v. of 3%.

2.4 Numerical Modelling

Advanced finite element simulations were carried out to obtain “experimental” results. In this “experimental” programme, finite element software product Abaqus 6.12 [17] was used. Each column is modelled with four-node linear shell elements (S4) with six degrees of freedom.

Advanced analyses were performed using geometrical and material nonlinearities with imperfections, also known as GMNIA. This type of analysis allows capturing the second order effects which are essential for stability problems.

Material nonlinearity is incorporated in the model by using elastic-plastic constitutive law with strain hardening, according to Figure 2, following the recommendations from ECCS [18].

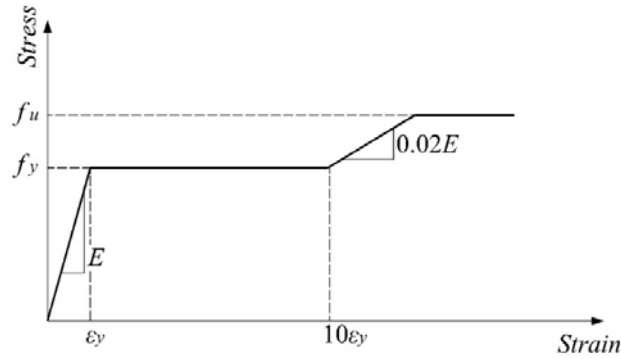


Figure 2. Constitutive Law

The yield stress, f_y , is considered either according to the provisions of the product standard EN 10025 [12], or from Table 3.1 of EC3-1-1. Since Table 3.1 of EC3-1-1 does not account for $t > 80$ mm, for such cases, the same value of f_y as in EN 10025 was considered, see Figure 3.

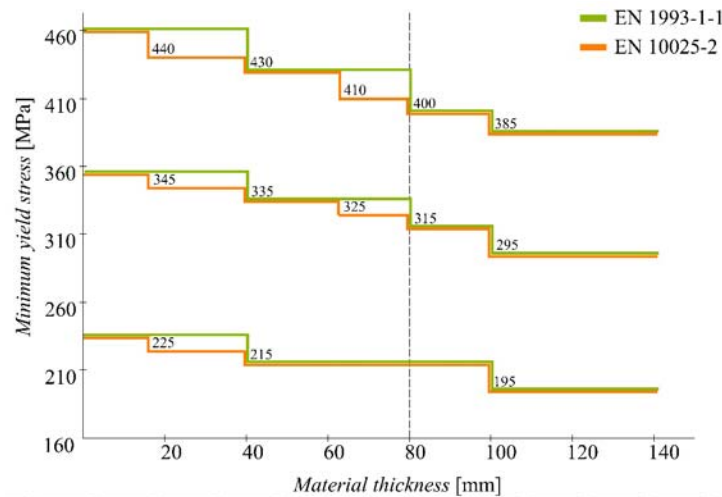


Figure 3. Variation of the Yield Stress with Thickness

Geometrical imperfections were modelled using an initial sinusoidal imperfection introduced in the weak or strong axis of the cross-section, with an amplitude $e_0 = L/1000$ at mid span. Residual stresses were considered according to Figure 4. The adopted value of f_y^* indicated in Figure 4 was $f_{y,235} = 235$ MPa. Nevertheless, for comparison, equivalent cases were included using the nominal value of the yield stress f_y .

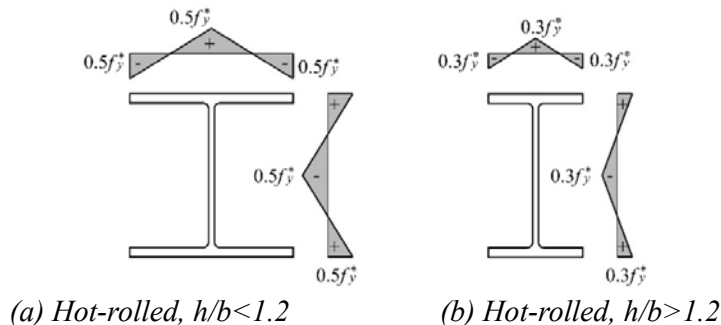


Figure 4. Residual Stresses (“+” Tension and “-” Compression)

The load is applied using load stepping routine, in which the increment size is chosen in order to meet the accuracy and convergence criteria. The equilibrium equations are solved for each increment using Newton-Raphson iteration technique. The adopted mesh comprises 16 sub-divisions in the web and flanges and 100 divisions along the member's axis per 10 m length.

The boundary conditions are implemented as end fork conditions in the shell model. The following restraints are used - vertical (δz) and transverse (δy) displacements and rotation about the xx -axis (ϕx) are prevented at the supports. In addition, the longitudinal displacement (δx) is prevented in one end. End cross-sections are constrained to remain straight. Whenever major axis buckling behaviour is to be studied, minor axis displacements are restrained at the tip of both flanges and centre of the web.

3. FLEXURAL BUCKLING OF PRISMATIC COLUMNS

As the main purpose of this study is the assessment of existing rules for flexural buckling of prismatic columns from EC3-1-1, in order to cover all types of hot-rolled sections according to Table 6.2 of EC3-1-1, a wide range of I-shaped cross-sections was selected so that flange thickness and the ratio h/b would vary.

In this section, firstly, the scope of the parametric study is introduced; subsequently, the methodology for assessment of results is given and finally, the results are discussed.

3.1 Parametric Study: Definition

Table 4 illustrates the hot-rolled section selected for the study, organized according to Table 6.2 of EC3-1-1. The selection includes 2 (two) American profiles.

Table 4. Sections of the Parametric Study for Columns

Fabrication	Limits		Sections		
			h/b	t_f [mm]	Profiles
Rolled	$h/b > 1.2$	$t_f \leq 40\text{mm}$	1.22	40	HEM340
			1.3	19	HEA400
			1.7	40	HEM500
			1.92	6.9	IPE140
			2.19	40	HEM650
			1.74	5.2	IPE80
			1.82	5.7	IPE100
			1.33	24	HEB400
			1.67	28	HEB500
			1.95	7.4	IPE160
			1.41	40	HEM400
			1.50	24	HEB450
			1.28	40	HEM360

Table 4. Sections of the Parametric Study for Columns (Continued)

Fabrication	Limits		Sections		
			h/b	t_f [mm]	Profiles
Rolled	h/b > 1.2	40mm < t_f ≤ 100mm	2.28	55.9	HL920x588
			2.29	62	HL920x656
			2.35	99.1	HL920x1077*
			3.36	64	HE1000x584
			2.31	73.9	HL920x787
			2.30	68.1	HL920x725
			3.08	65	W920x310x576
			2.56	70	HL1000x748
			2.05	69.1	W610x325x551
			2.06	54	HE600x399
			2.36	46	HE700x352
			2.69	54	HE800x444
			3.01	54	HE900x466
		t_f > 100mm	1.231	130	HD400x1202*
			2.4	109	HL920x1194*
			1.201	106	HD400x900
			1.23	115	HD400x990
			2.37	115.1	HL920x1269*
			2.31	115.1	HL920x1377*
			1.25	125	HD400x1086
			1.26	140	HD400x1299
	h/b ≤ 1.2	t_f ≤ 100mm	1.2	22.5	HEB360
			1.17	97	HD400x818
			0.96	8	HEA100
			1.0	19	HEB300
			1.1	39	HEM300
			1.0	10	HEB100
			1.0	15	HEB200
			1.17	17.5	HE360A
			1.09	67.6	HD400x551
			1.12	77.1	HD400x634
			1.04	52.6	HD400x421
			1.10	72.30	HD400x592
			1.00	17	HEB240
		t_f > 100mm	No sections exist		

*Heavy sections

The parametric study comprised 7332 numerical models, both for minor and major axis flexural buckling behaviour (3666 models for each mode). It includes several levels of slenderness, different steel grades, and two different levels of residual stresses, as given in Table 5.

Table 5. Parametric Study for Columns: Additional Parameters

Fabrication	$\bar{\lambda}$	Material and standard for f_y	Material imperfections
Rolled	0.5; 0.6; 0.7; 0.8 0.9; 1.0; 1.2; 1.4; 1.5 1.6; 1.8; 2.0; 2.5	EN 10025: S235 S355 S460	h/b ≤ 1.2: $f_{y,235}$ f_y h/b > 1.2: $f_{y,235}$ f_y

For the evaluation of the flexural buckling resistance of steel columns, clause 6.3.1 in EC3-1-1 is considered to represent the theoretical result, r_{ti} , in the safety assessment procedure. The design procedure is summarized in Table 6 for simply supported members of length L , whereas the imperfection factors are summarized in Table 7 for the cross section shapes covered by the parametric study. The latter imperfection factors are considered from Table 6.1 and 6.2 of EC3-1-1 and from (Snijder et al. [19], [20]) for hot-rolled heavy cross-sections with $t_f > 100\text{mm}$ and $h/b > 1.2$.

Table 6. Verification of Flexural Buckling of Columns, about Minor Axis ($i=z$) and Major Axis ($i=y$)

Parameter	Expression
N_{Rk}	$A \cdot f_y$ – class 1, 2 and 3 cross sections $A_{eff} \cdot f_y$ – class 4 cross sections
$N_{cr,z}$ or $N_{cr,y}$	$N_{cr,i} = \frac{\pi^2 EI_i}{L^2}$
$\bar{\lambda}_i$	$\bar{\lambda}_i = \sqrt{N_{Rk} / N_{CR,i}}$
α_i	See Table 7
η_i	$\alpha_i (\bar{\lambda}_i - 0.2)$
ϕ_i	$0.5 \times (1 + \eta_i + \bar{\lambda}_i^2)$
χ_i	$1 / (\phi_i + \sqrt{\phi_i^2 - \bar{\lambda}_i^2}) \leq 1$
Verification	$N_{Ed} \leq N_{b,i,Rd} = \chi_i \times N_{Rk} / \gamma_{M1}$

Additionally, for $\bar{\lambda}_i \leq 0.2$ and $\frac{N_{Ed}}{N_{cr,i}} \leq 0.04$, flexural buckling about axis i does not need to be verified and only cross sectional checks apply ($\chi_i = 1$).

In Section 3.3 and Section 3.4 the partial factors γ_{M1} for several subsets are obtained respectively for minor and major axes flexural buckling. Selected input variables for safety assessment and subsets are described in the corresponding sub-sections.

Table 7. Imperfection Factors and Generalized Imperfection Limits for Flexural Buckling

Fabrication	Limits		Axis	Source			
				EC3-1-1		(Cajot et al. (2013))	
				S235 S355	S460	S235 S355	S460
Rolled	$h/b > 1.2$	$t_f \leq 40\text{mm}$	y-y z-z	0.21 0.34	0.13 0.13	-	-
		$40\text{mm} < t_f \leq 100\text{mm}$	y-y z-z	0.34 0.49	0.21 0.21	-	-
		$t_f > 100\text{mm}$	y-y z-z	-	-	0.34 0.49	0.21 0.34
	$h/b \leq 1.2$	$t_f \leq 100\text{mm}$	y-y z-z	0.34 0.49	0.21 0.21	-	-
		$t_f > 100\text{mm}$	y-y z-z	0.76 0.76	0.49 0.49	-	-

3.2 Parametric Study: Methodology

In the subsequent sections the results for minor and major axis flexural buckling of columns are detailed. The following main topics are discussed:

- Influence of the specification of the minimum yield stress according to EN 10025 and Eurocode 3;
- Influence of the magnitude of residual stresses used in the numerical analyses;
- Influence of imperfection factor α for steel grade S460;
- Validation of the buckling curves for heavy sections;
- Influence of the number of random variables;

Throughout the following paragraphs, charts and tables, the following methodology is adopted:

- The partial factors for different subsets are computed considering the *Annex D* procedure summarized in Section 2.2.
- The assessment is performed using normalized values of the partial factor. The normalization is done with respect to the average value of γ_{M1} obtained for *S235 and S355, $t_f \leq 40\text{mm}$, $h/b > 1.2$ and major axis of flexural buckling*, considering the yield stress f_y as the only random variable.
- Whenever a subset according to slenderness is analysed, the following division is adopted:
 - Low slenderness – normalized slenderness $\bar{\lambda} \in [0.5; 0.8]$;
 - Medium slenderness – normalized slenderness $\bar{\lambda} \in (0.8; 1.5]$;
 - High slenderness – normalized slenderness $\bar{\lambda} \in (1.5; 2.5]$;
- For the first 4 topics listed above, only the variability of the yield stress is considered, as a relative assessment is sufficient to establish the influence of each parameter;
- In order to establish the influence of additional random variables, the following variables are considered: yield stress, geometrical dimensions of the cross-section and modulus of elasticity.

3.3 Results and Discussion – Minor axis Flexural Buckling

Hereby the results for minor axis flexural buckling are presented and discussed. Firstly, the reference cases for hot-rolled cross sections are analysed: the value of the yield stress both in r_e and r_t is considered according to EN 10025 and the level of the residual stresses is proportional to $0.3(0.5) \times 235\text{MPa}$ for $h/b > (\leq 1.2)$. Subsequently, the reference cases are analysed considering the value of the yield stress and r_t according to Table 3.1 of EC3-1-1, the experimental value r_e is

computed according to the EN 10025, assuming it as the “reality”. Finally, the reference cases are analysed considering the level of the residual stresses proportional to $0.3(0.5) \times f_y$ for $h/b > (\leq 1.2)$; More detailed results may be found in *Table B1* and *Table B2* of Annex B.

3.3.1 Results for hot-rolled cross sections

In the following all results are normalized (see Section 3.2). Partial factors are evaluated using the procedure from Annex D, as summarized in Section 2.2 and considering the variability of the yield stress only.

The parametric study was constructed aiming to cover all buckling curves for hot-rolled H and I sections and therefore, the sample includes members whose resistance is evaluated using different imperfection factors (α according to Table 7), different steel grades which are defined by different distributions, etc. Hence, further division into subsets is required, in order to avoid undesired bias of the results.

Since the reduction factor is mainly a function of slenderness, results should be assessed and organized by subsets of the slenderness ranges, as shown in Figure 5. The subsets are adopted according to Section 3.2: Low [0.5; 0.8]; Medium (0.8; 1.5]; and High (1.5; 2.5]. A larger partial factor is observed for S460 in *Figure 5* when compared to the other steel grades for all slenderness ranges. A possible explanation for this value is that the imperfection factors currently adopted for steel grade S460 may not be appropriate. This was independently confirmed by Lindner [21] and may thus require adjustment.

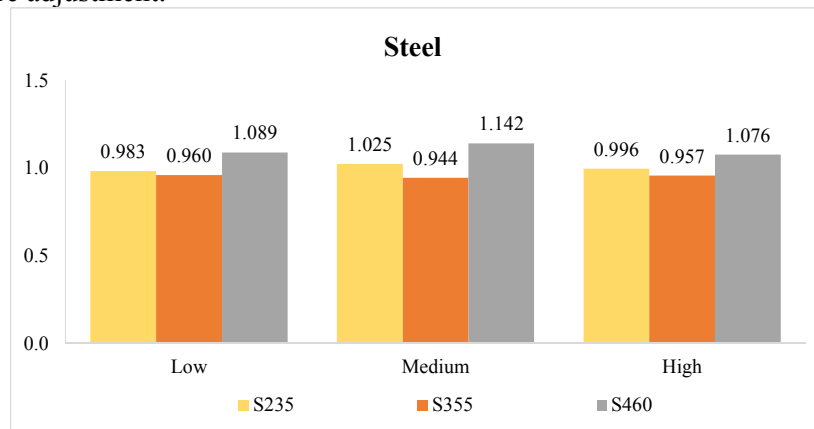


Figure 5. All Results Organized by Slenderness for Hot-rolled Cross Sections – γ_{M1} according to EN 10025 (Table B1, Annex B)

Figure 6 illustrates the results organized by the divisions given in Table 7, regardless of the slenderness range, thus allowing a direct comparison of the buckling curves in EC3-1-1. Firstly, it is clear that steel grade S355 leads to lower values of γ_{M1} . This is due to the relative amplitude of the residual stress with respect to the yield stress of the member when compared to S235 steel. Figure 6 again confirms that the imperfection factors for S460 may not be adequate, except for $h/b > 1.2$, $t_f > 100\text{mm}$ because they were recently proposed and calibrated as this range was not available in the code (Snijder et al. [19], [20]). Finally, note that no cases with $h/b \leq 1.2$ and $t_f > 100\text{mm}$ are included in the parametric study since no sections with these characteristics were found in catalogues.

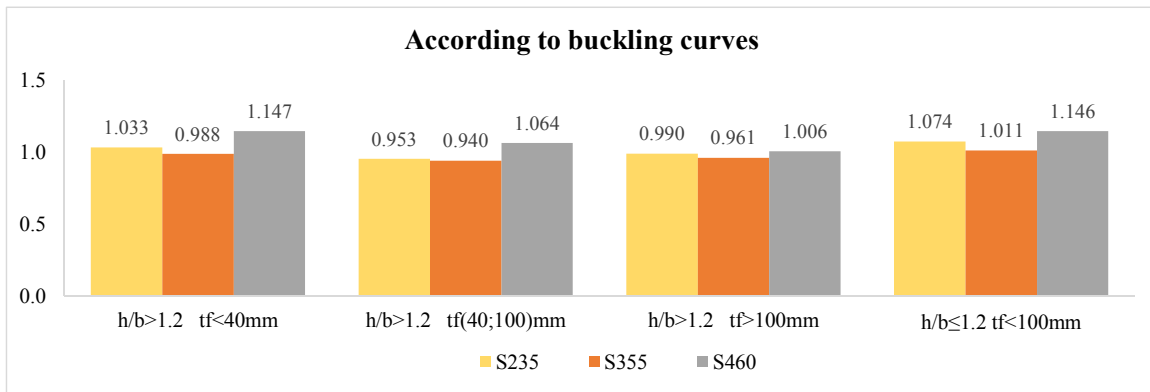


Figure 6. All Results organized by Buckling Curve Division for Hot-rolled Cross sections – f_y according to EN 10025 (Table B1, Annex B)

Additional subsets were considered for $h/b \leq 1.2$. The results are presented in Figure 7, the same trends being observed.

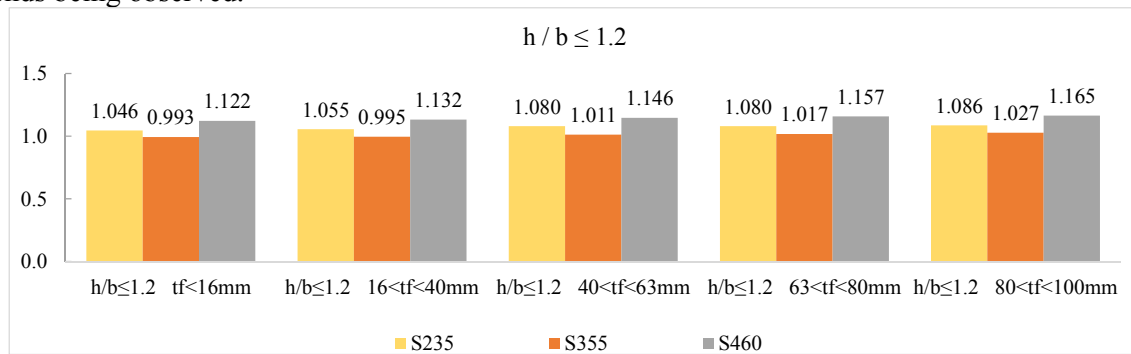


Figure 7. Subsets according to EN10025

3.3.2 Influence of the variation of the yield stress with thickness

The value of the yield stress in the theoretical value of the resistance r_t is now considered according to EC3-1-1, Table 3.1 and the “experimental” resistance r_e is computed considering the sub-divisions according to EN 10025, and presented in relative terms with respect to the results of EN 10025 (Figure 8). Results of Figure 8 are better interpreted together with Figure 3.

The second group for S235 and third group give the same values since the specifications of the yield stress in EN 10025 and EC3-1-1 are equal for the cross sections considered in the parametric study. On the other hand, for the first and fourth groups as well as second group for S355 and S460, differences are noted, for sections with thicknesses falling in the ranges (16; 40) and (63; 80), since the specifications in EC3-1-1 and EN 10025 are different in those ranges.

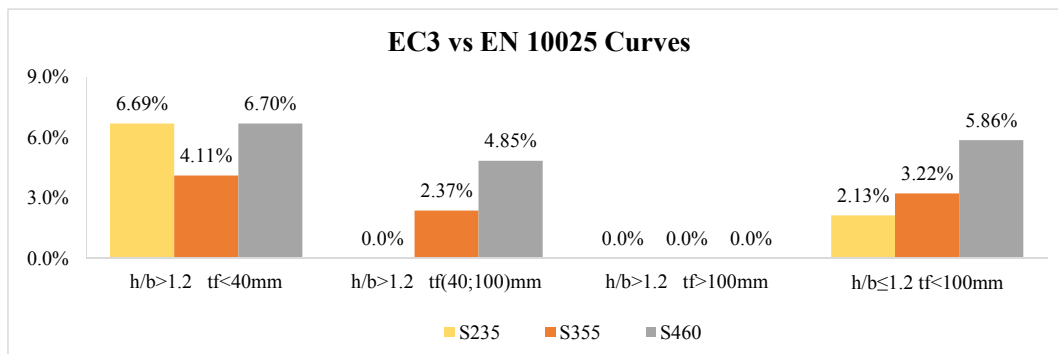


Figure 8. Percentage Difference for Normalized γ_{M1} between Yield Stress Calculated according to EC3-1-1 and EN 10025

The results in Figure 8 include thickness ranges that are different from the division according to EN 10025; hence, Figure 9 compares results between EN 10025 and EC3-1-1 for the intervals defined in EN 10025, highlighting maximum differences of about 8%.

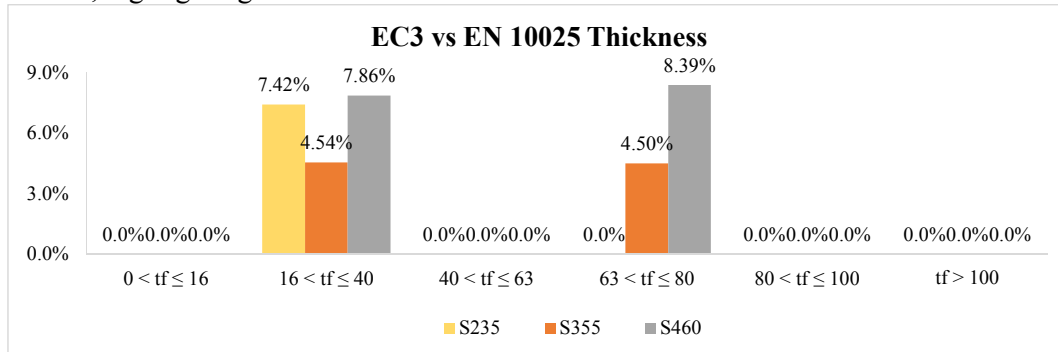


Figure 9. Percentage Difference for Normalized γ_{M1} between Yield Stress Calculated according to EC3-1-1 and EN 10025

3.3.3 Influence of the assumptions for the residual stress

Figure 10 and Figure 11 present relative results for the partial factor similarly to Figure 6, but assuming the conservative option that the level of the residual stresses is proportional to the yield stress $0.3(0.5) \times f_y$ for $h/b > (\leq 1.2)$. Since a higher level of the residual stresses is now considered (more conservative), the partial factor is expected to increase. This is observed both for steels S355 and S460, see Figure 10 and Figure 11 respectively. For steel grade S235, the analysis is not relevant.

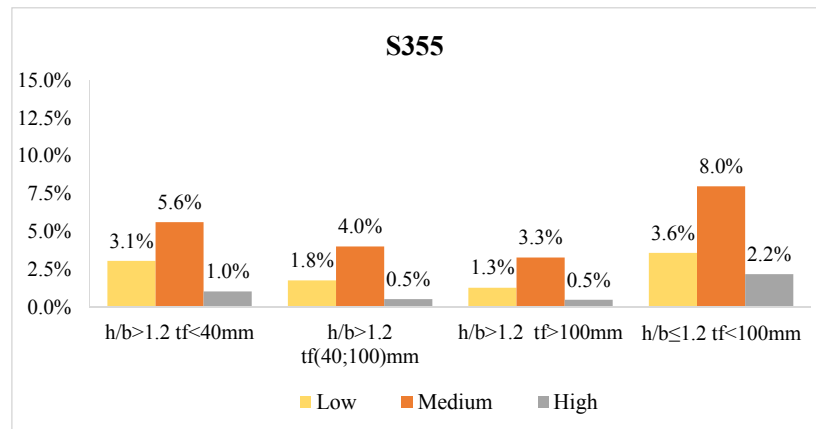


Figure 10. All Results organized by Buckling Curve and Slenderness Division for Hot-rolled Cross Sections and Steel Grade S355 – Residual Stress Proportional to the Actual Value of f_y (f_y according to EN 10025)

Figure 10 and Figure 11 represent the subsets by buckling curve, slenderness and steel grade. It is clearly seen that the influence of the residual stresses has higher impact in the medium slenderness range, as expected. Moreover, Figure 11 further shows that the adoption of residual stresses proportional to the yield stress $0.3(0.5) \times f_y$ is too conservative.

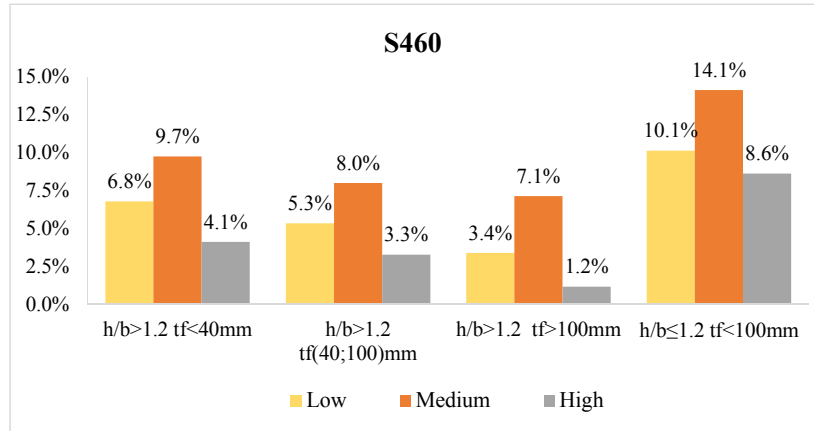


Figure 11. All Results organized by Buckling Curve and Slenderness Division for Hot-rolled Cross Sections and Steel Grade S460 – Residual Stress Proportional to the Actual Value of f_y (f_y according to EN 10025)

3.3.4 Evaluation of the partial factor considering new imperfection factors for S460

It was already seen that the results for steel grade S460 are significantly higher than those for the other steel grades. A possible improvement can be introduced by considering higher imperfection factors for minor axis flexural buckling as shown in Table 8 (values in bold).

Table 8. New Imperfection Factor for Steel Grade S460, Minor Axis

Fabrication	Limits		Axis	EC3-1-1		(Cajot et al. (2013))	
				S235 S355	S460	S235 S355	S460
Rolled	$h/b > 1,2$	$t_f \leq 40\text{mm}$	y-y z-z	0.21 0.34	0.13 0.21	-	-
		$40\text{mm} < t_f \leq 100\text{mm}$	y-y z-z	0.34 0.49	0.21 0.34	-	-
		$t_f > 100\text{mm}$	y-y z-z	-	-	0.34 0.49	0.21 0.34
	$h/b \leq 1,2$	$t_f \leq 100\text{mm}$	y-y z-z	0.34 0.49	0.21 0.34	-	-

* $h/b \leq 1,2$ and $t_f > 100\text{mm}$ is not included in the table, because no cross-sections were found

Figure 12 and Figure 13, similarly to Figure 5 and Figure 6 show the results according to slenderness and buckling curve division, respectively. The improvement of using higher imperfection factors for steel grade S460 is clear.

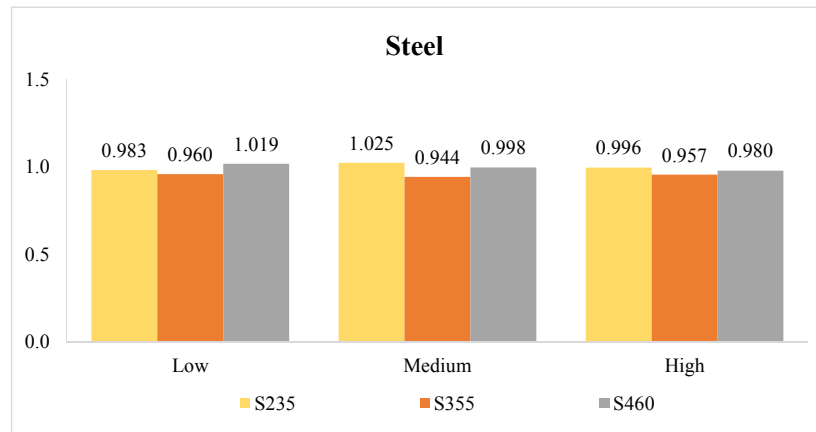


Figure 12. All Results organized by Slenderness for Hot-rolled Cross Sections – f_y according to EN 10025 (Table B1, Annex B)

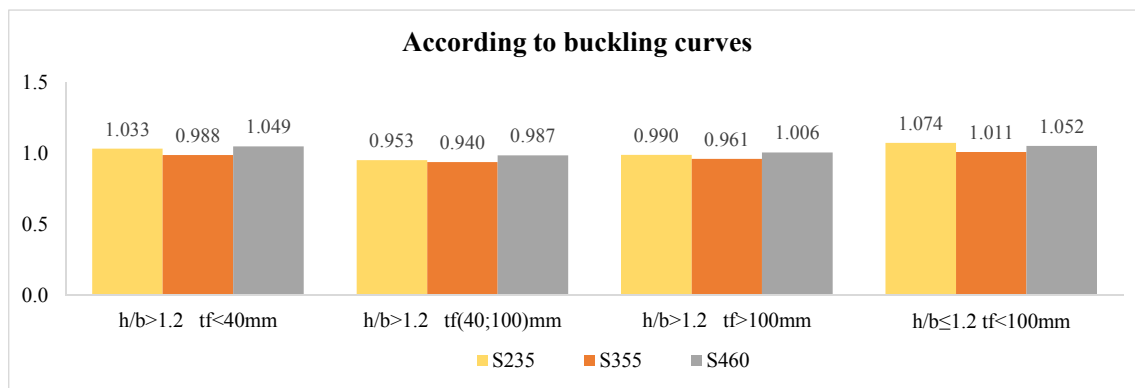


Figure 13. All Results organized by Buckling Curve Division for Hot-rolled Cross sections – f_y according to EN 10025 (Table B1, Annex B)

3.4 Results and Discussion – Major Axis Flexural Buckling

Identically to minor axis flexural buckling, the safety assessment is computed considering the Annex D procedure and variability of yield stress only, as stated in Section 3.2. The partial factors are also normalized with respect to the average value for *S235 and S355, $t_f \leq 40\text{mm}$, $h/b > 1.2$ and major axis of flexural buckling*. Firstly, the reference cases for hot-rolled cross sections are analysed: the yield stress both in r_e and r_t is considered according to EN 10025. Unlike minor axis flexural buckling, the relative values of the partial factor are more uniform for the different steel grades (Figure 14).

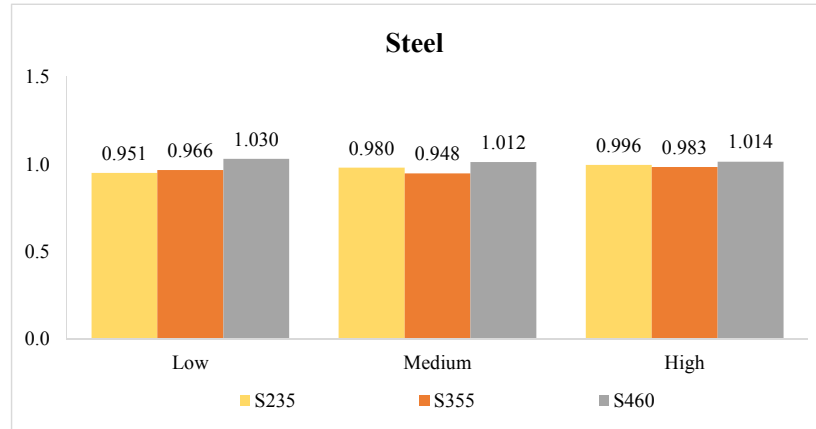


Figure 14. All Results organized by Slenderness for Hot-rolled Cross Sections – f_y according to EN 10025 (Table A1.1, Annex A1)

Similarly to Figure 6 for minor axis flexural buckling, Figure 15 illustrates the results organized according to the divisions presented in Table 7, regardless of the slenderness range, thus allowing a direct comparison of the buckling curves specified in EC3-1-1. All cases fall within an acceptable range of variation of the partial factor.

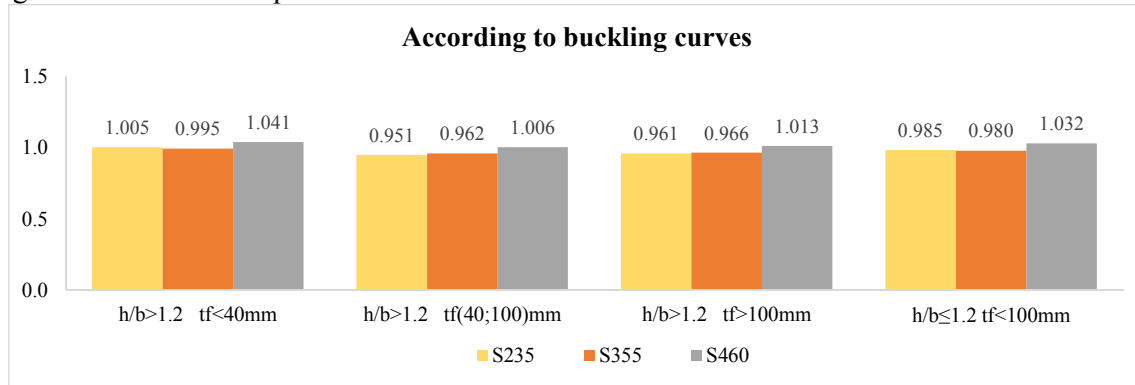


Figure 15. All Results organized by Buckling Curve Division for Hot-rolled Cross Sections – f_y according to EN 10025

Furthermore, when the influence of the variation of the yield stress with increasing flange thickness was analysed, similar conclusions were drawn. Identical results were found when the residual stresses were assumed proportional to the yield stress as in Section 3.3.3.

More detailed results are found in Table B1 and Table B2 in Annex B

3.5 Influence of the Number of Random Variables

In the previous sub-sections, only f_y was considered as a random variable. In reality, in the case on flexural buckling of columns, other basic variables also affect the behaviour of a column, such as the cross-section dimensions and the Young's modulus. It is noted that geometrical and material imperfections such as initial curvature and residual stresses are not included as basic random variables as they are included implicitly in the design model (Simões da Silva et al.) [22].

Hence, the following random variables are included in the analysis:

- Yield stress – f_y ;
- Geometrical dimensions – b , h , t_w , t_f ;
- Young's modulus – E ;

The distributions of the basic variables are considered as previously presented in Section 2.3. The partial factor is obtained using the procedure proposed in Annex D as presented in Section 2.2 of this document. The influence of the number of basic variables is accounted as their number is gradually increased. The following cases are considered:

- **Annex D (fy)** – considers the yield stress as the only basic variable, the other parameters are assumed as deterministic quantities with no variability;
- **Annex D (fy+CS)** – considers the yield stress and the geometrical dimensions of the cross-section as random variables;
- **Annex D (fy+CS+E)** – considers the yield stress, the geometrical dimensions of the cross-section and the modulus of elasticity as random variables;

γ_{M1} is calculated for both major and minor axis flexural buckling for all three cases.

3.5.1 Minor axis flexural buckling

Figure 16 summarizes the normalized partial factors obtained for minor axis and considering the assumptions previously made. Firstly, as expected, higher values of γ_{M1} are obtained. Secondly, the rate of increase of γ_{M1} increases with increasing slenderness: 3.9%, 8.0% and 12.9% for low, medium and high slenderness, respectively, as Young's modulus and geometrical dimensions (moment of inertia) become more relevant in the medium and high slenderness ranges.

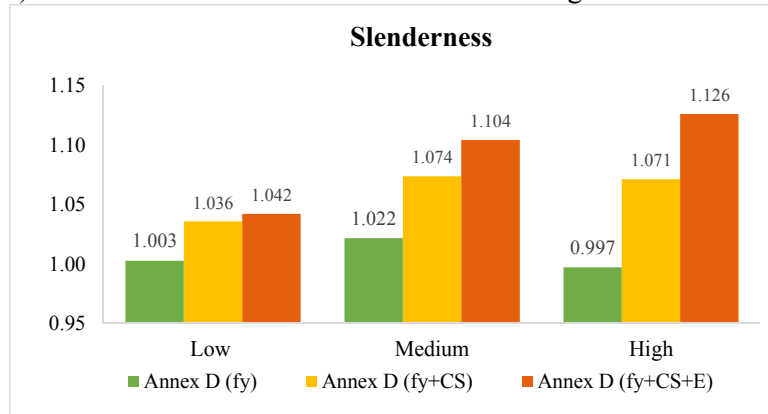


Figure 16. All Steels by Slenderness and using Different Number of Random Variables

Furthermore, results according to subsets of steel grade and slenderness are analysed in Figure 17 for Annex D (fy + CS + E).

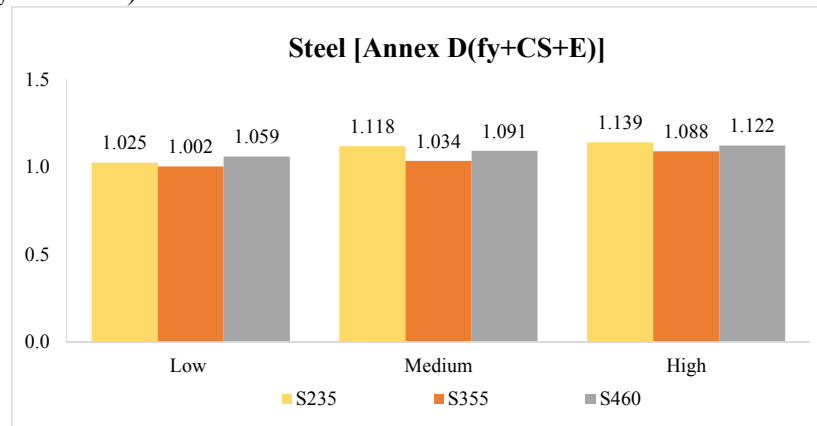


Figure 17. All Results organized by Slenderness and Steel Grade – using fy, Cross-section Dimensions and Modulus of Elasticity as Random Variables (Table B3, Annex B)

Similarly, results split according to buckling curve and steel grade are given in *Figure 18*. Detailed results for the intermediate case of Annex D ($f_y + CS$) are given in *Table B3* in Annex B.

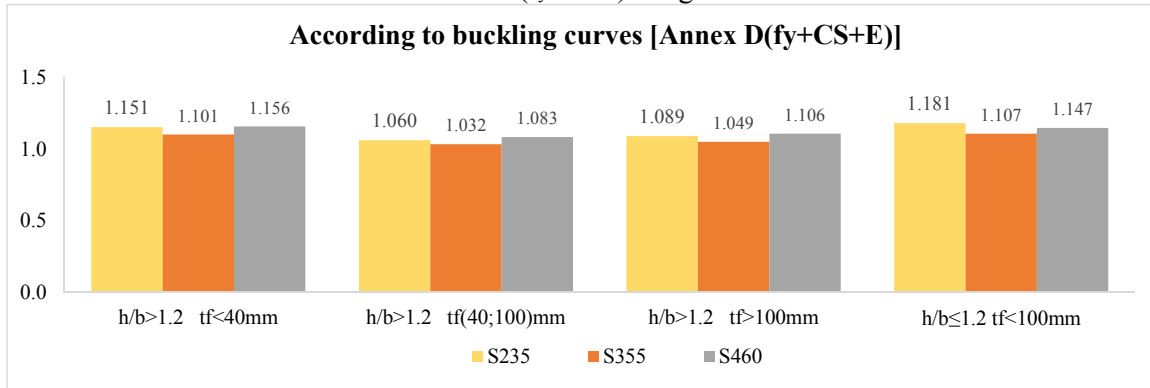


Figure 18. All Results organized by Buckling Curve for Hot-rolled Cross Sections – using f_y , Cross-section Dimensions and Modulus of Elasticity as Random Variables (see also Table B3, Annex B)

Table B4 in Annex B summarizes the results divided according to steel grade, buckling curve and slenderness range.

While for the yield stress and geometrical dimensions there is certain knowledge about their distributions, it is not the case for the modulus of elasticity. It is a variable, which is very difficult to measure, and additional variability may be added simply because of the measurement method. Therefore, additional calculations were performed for a coefficient of variation of 3% for the modulus of elasticity (see also Table B3 and Table B4 in Annex B). Differences up to 4% can be found in the high slenderness range as illustrated on Figure 19 for subsets according to slenderness.

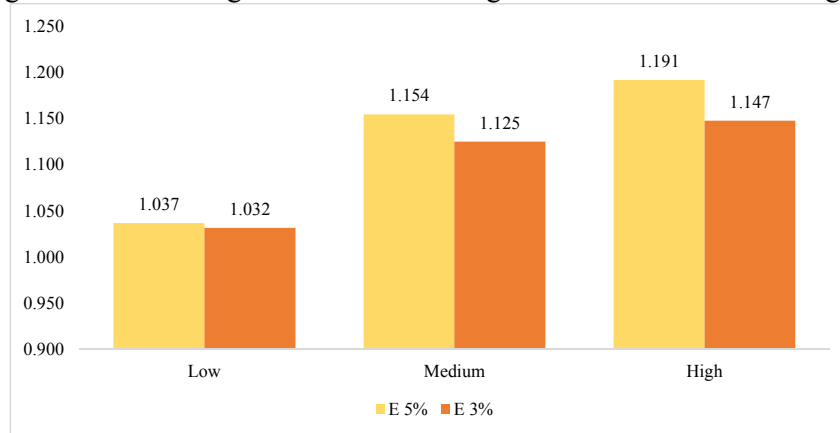


Figure 19. Difference between adopted Coefficients of Variation for E

3.5.2 Major axis flexural buckling

The same evaluation was performed for major axis of flexural buckling. The results are similar to the conclusions in the previous section, i.e. the presence of the modulus of elasticity leads to higher values for γ_{M1} (Figures 20 to 22). However, in general, the values of the γ_{M1} for major axis flexural buckling are lower than those for minor axis as presented in section 3.5.1 (3.1%, 7.1% and 11.4% for low, medium and high slenderness, respectively). Detailed results are given in *Table B3* and *Table B4* in Annex B.

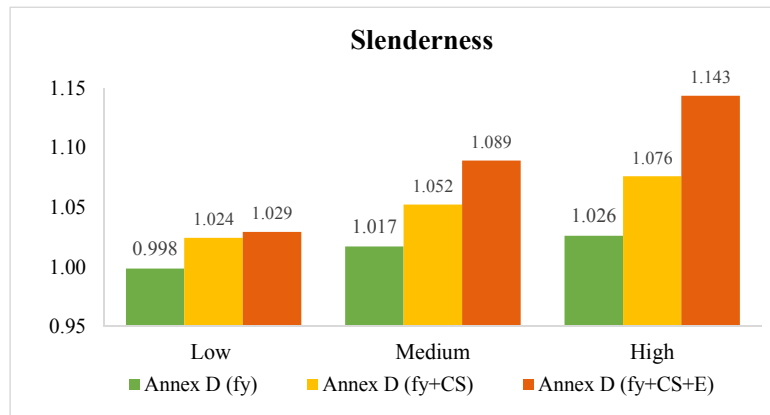


Figure 20. All Steels by Slenderness and using Different Number of Random Variables

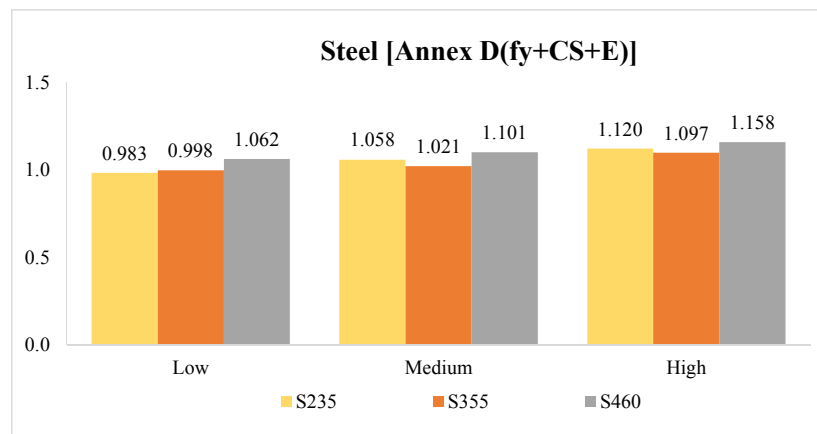


Figure 21. All Results organized by Slenderness and Steel Grade – using f_y , Cross-section Dimensions and Modulus of Elasticity as Random Variables (Table A1.3, Annex A1)

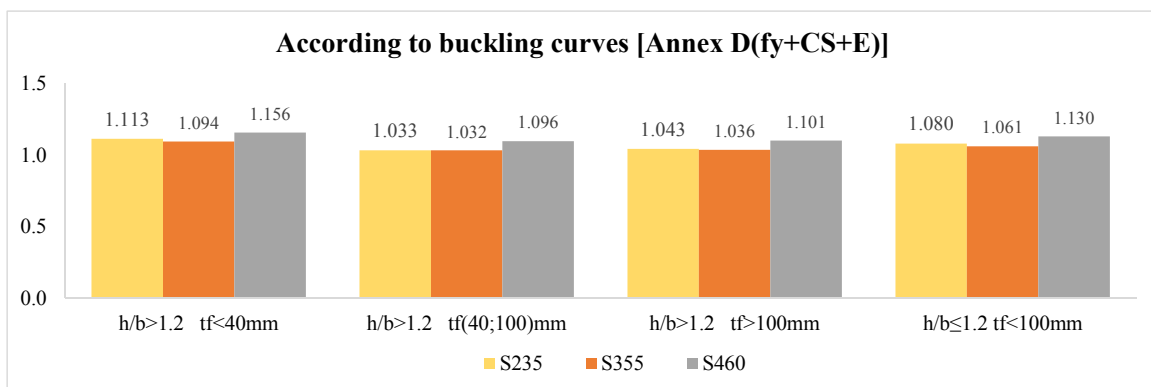


Figure 22. All Results organized by Buckling Curve for Hot-rolled Cross Sections – using f_y , Cross-section Dimensions and Modulus of Elasticity as Random Variables

3.6 Summary

A parametric study to assess the safety of the code prescriptions of the flexural buckling of columns was presented. *Table 9* summarizes the relative values obtained per buckling curve, the results being presented as normalized factors with respect to a specific sub-group.

Table 9. Values of Normalized γ_{M1} for Flexural Buckling of Columns*

Fabrication	Limits		Axis	EC3-1-1		[19], [20]	
				S235 S355	S460	S235 S355	S460
Rolled	$h/b > 1,2$	$t_f \leq 40\text{mm}$	y-y z-z	1.000 1.011	1.041 1.147	-	-
		$40\text{mm} < t_f \leq 100\text{mm}$	y-y z-z	0.956 0.946	1.006 1.064	-	-
		$t_f > 100\text{mm}$	y-y z-z	-	-	0.963 0.975	1.013 1.006
	$h/b \leq 1,2$	$t_f \leq 100\text{mm}$	y-y z-z	0.983 1.042	1.032 1.146	-	-

* The relative value for the partial factor for S235 and S355 is determined as the mean value obtained for S235 and S355

** $h/b \leq 1,2$ and $t_f > 100\text{mm}$ is not included in the table, because no cross-sections were found

The results were analysed in various subsets. The study revealed that the variation in the relative values of the partial factor is not high, except for steel grade S460 and minor axis of flexural buckling (the numbers in bold in *Table 9*). New imperfection factors were analysed and the results showed good agreement with the ones obtained for S235 and S355. *Table 10* summarizes the corresponding normalized partial factors.

Table 10. Values of Normalized γ_{M1} for Flexural Buckling of Columns*

Fabrication	Limits		Axis	EC3-1-1		[19], [20]	
				S235 S355	S460	S235 S355	S460
Rolled	$h/b > 1,2$	$t_f \leq 40\text{mm}$	y-y z-z	1.000 1.011	1.041 1.049	-	-
		$40\text{mm} < t_f \leq 100\text{mm}$	y-y z-z	0.956 0.946	1.006 0.987	-	-
		$t_f > 100\text{mm}$	y-y z-z	-	-	0.963 0.975	1.013 1.006
	$h/b \leq 1,2$	$t_f \leq 100\text{mm}$	y-y z-z	0.983 1.042	1.032 1.052	-	-

* The relative value for the partial factor for S235 and S355 is determined as the mean value obtained for S235 and S355

** $h/b \leq 1,2$ and $t_f > 100\text{mm}$ is not included in the table, because no cross-sections were found

Finally based on the analysis performed in Section 3.5, the normalized values of the partial factor, considering different random variables, is summarized in *Table 11*. The increase γ_{M1} varies from 7.9% to 11.4%.

Table 11. Values of Normalized γ_{M1} for Flexural Buckling of Columns*

Fabrication	Limits		Axis	Annex D (fy)		Annex D (fy+CS)		Annex D (fy+CS+E)	
				S235 S355	S460	S235 S355	S460	S235 S355	S460
Rolled	$h/b > 1,2$	$t_f \leq 40\text{mm}$	y-y	1.000	1.041	1.055	1.104	1.103	1.156
			z-z	1.011	1.049	1.084	1.117	1.126	1.156
		$40\text{mm} < t_f \leq 100\text{mm}$	y-y	0.956	1.006	0.994	1.052	1.033	1.096
			z-z	0.946	0.987	1.009	1.047	1.046	1.083
	$h/b \leq 1,2$	$t_f > 100\text{mm}$	y-y	0.963	1.013	0.999	1.055	1.039	1.101
			z-z	0.975	1.006	1.034	1.069	1.069	1.106
		$t_f \leq 100\text{mm}$	y-y	0.983	1.032	1.029	1.084	1.071	1.130
			z-z	1.042	1.052	1.108	1.114	1.144	1.147

* The relative value for the partial factor for S235 and S355 is determined as the mean value obtained for S235 and S355

** $h/b \leq 1,2$ and $t_f > 100\text{mm}$ is not included in the table, because no cross-sections were found

4. ASSESSMENT OF THE PARTIAL FACTOR

Section 3 analysed the design rules for the flexural buckling of columns in terms of the required value of the partial factors γ_{M1} to match the target probability of failure specified in EN 1990 [2]. The analysis was carried out by normalizing all values with respect to a reference case (major axis flexural buckling of I-section profiles in S235 to S355 with maximum flange thickness of 40 mm and $h/b > 1,2$) because the quality of the design rules is very dependent on the scatter of the γ_{M1} values for the various subsets that may be considered. It was shown that the design rules provide consistent results across the various possible subsets, with small scatter on the value of γ_{M1} .

In this section it is proposed to discuss the adoption of a single global γ_{M1} for flexural buckling of columns that is in line with the failure probability in EN 1990 and incorporates all the viewpoints that support code drafting and the choice of safety factors [23],[9].

Table 12 summarizes the partial factors obtained for minor and major axis, now given as absolute values instead of normalized values. It is noted that all values are smaller, since the normalizing γ_{M1} for the reference case is equal to 0.979. The results are presented according to subsets of steel grade and buckling curve.

Table 12. Values of γ_{M1} obtained using Different Random Variables for Major and Minor Axes Flexural Buckling

Fabrication	Limits		Axis	Annex D (f_y)		Annex D (f_y+CS)		Annex D (f_y+CS+E)	
				S235 S355	S460	S235 S355	S460	S235 S355	S460
Rolled	$h/b > 1,2$	$t_f \leq 40\text{mm}$	y-y	0.979	1.020	1.033	1.081	1.081	1.132
			z-z	0.990	1.028	1.062	1.094	1.103	1.133
		$40\text{mm} < t_f \leq 100\text{mm}$	y-y	0.937	0.985	0.974	1.030	1.011	1.074
			z-z	0.927	0.967	0.989	1.025	1.025	1.060
		$t_f > 100\text{mm}$	y-y	0.944	0.992	0.979	1.034	1.018	1.078
			z-z	0.955	0.985	1.013	1.047	1.047	1.084
	$h/b \leq 1,2$	$t_f \leq 100\text{mm}$	y-y	0.962	1.011	1.008	1.062	1.049	1.107
			z-z	1.021	1.030	1.085	1.091	1.120	1.124

In Annex B, Table B5 and Table B6, a further division into subsets according to slenderness is performed in order to be able to compare the different slenderness ranges. Even though finer subsets into slenderness, steel grade and buckling curve are adopted, the partial factors higher than unity are mostly only observed when the Young's modulus is included.

Table 13. Average γ_{M1} for Minor and Major Axis Flexural Buckling, according to Buckling Curves and Slenderness

	Axis	Annex D(f_y)	Annex D(f_y+CS)	Annex D(f_y+CS+E)
Mean value	y-y	0.943	0.995	1.040
	z-z	0.941	1.012	1.049
Coefficient of variation	y-y	4.28%	4.79%	6.31%
	z-z	4.33%	4.46%	5.54%

Table 13 summarizes the mean and standard deviation of γ_{M1} for the three different sets of random variable that were considered. It is concluded that depending on the random variables included in the analysis (just f_y ; f_y and cross-section geometry; or f_y , cross-section geometry and modulus of elasticity E) the average value of γ_{M1} varies from 0.941 to 1.049 with the c.o.v. varying from 4.3% to 6.3%. The mean value is lower than 1.05 for the more unfavourable case and the c.o.v. is low. Additionally, in general, the values of the γ_{M1} for major axis flexural buckling are similar to those for minor axis.

Recalling that the currently recommended value of γ_{M1} in Eurocode 3, part 1, is 1.0, and comparing with available data from the literature that led to the choice of $\gamma_{M1} = 1.0$, the results presented in this report for γ_{M1} are lower. In Muller (2003), a study on the flexural buckling resistance of hot-rolled sections was done and the corresponding partial factors were assessed, see Figure 23, corresponding to an average value of γ_{M1} for minor axis flexural buckling of 1.097 (cf. 0.941 as these results only considered the variability of f_y).

It is interesting to note that the observed trend (also in Muller (2003) [24]) of an increasing value of γ_{M1} in the intermediate slenderness range disappears when variability in cross-section and Young's modulus is included: in this case the value of γ_{M1} increases monotonically with slenderness. It is noted that the higher value of γ_{M1} for high slenderness is not so relevant because of practical reasons (practical range of column slenderness), as the parametric study included normalised slenderness ($\bar{\lambda}$) up to 2.5. It is therefore recommended to keep $\gamma_{M1}=1.0$ for columns.

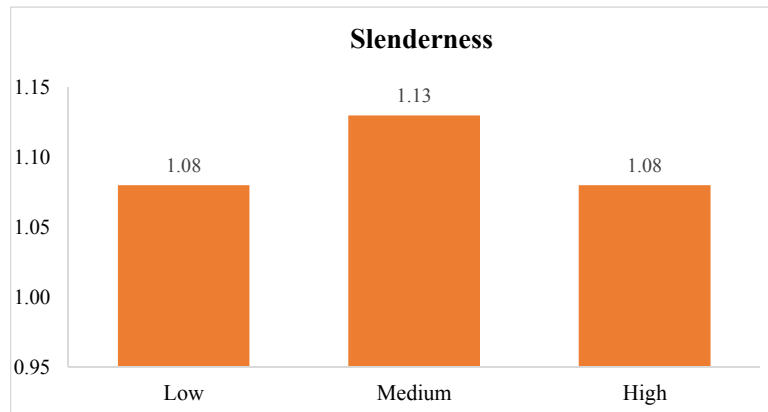


Figure 23. Results by Muller [24]

5. CONCLUSIONS

In this paper, the safety assessment of EC3-1-1 rules for flexural buckling of columns with hot-rolled I-shaped cross sections was performed and the partial factor was evaluated considering several subsets, including slenderness ranges, level of yield stress, EC3-1-1 buckling curves; flange thickness and respective variation of the yield stress; buckling axis.

The following conclusions were achieved:

- Influence of the adopted minimum yield stress using EN 10025 or Table 3.1 of Eurocode3;
The level of the minimum yield stress was assessed for both minor and major axis of flexural buckling of hot-rolled columns. It was shown that in both cases the values proposed in EC3 can be up to 8% non-conservative, which itself is not a negligible difference.
- Influence of the level of the residual stresses adopted in the numerical models;
The buckling curves are currently calibrated for level of residual stresses proportional to the yield stress f_y , which was shown to be conservative. When the results were divided into slenderness – in the medium slenderness range, where the residual stresses are actually important, high differences were obtained. These variations are relevant for the group of buckling curves S235-S420, with increasing difference as the steel grade increases; about 8% were noticed for S355.
- Imperfection factor for flexural-buckling of columns about minor axis which are made of steel grade S460;
It was shown that the imperfection factor currently prescribed for flexural buckling of steel columns made of S460 about the minor axis is not adequate. Alternative analysis was performed in order to check if other curves are more suitable and the results are summarized in Table 14:

Table 14. New Imperfection Factor for Steel Grade S460, Minor Axis

Fabrication	Limits		Axis	EC3-1-1		[19], [20]	
				S235 S355	S460	S235 S355	S460
Rolled	$h/b > 1,2$	$t_f \leq 40\text{mm}$	y-y z-z	0.21 0.34	0.13 0.21	-	-
		$40\text{mm} < t_f \leq 100\text{mm}$	y-y z-z	0.34 0.49	0.21 0.34	-	-
		$t_f > 100\text{mm}$	y-y z-z	-	-	0.34 0.49	0.21 0.34
	$h/b \leq 1,2$	$t_f \leq 100\text{mm}$	y-y z-z	0.34 0.49	0.21 0.34	-	-

- The recent study presented in [19], [20] about buckling curves for heavy sections was confirmed – the buckling curves chosen for sections with $h/b > 1,2$ and $t_f > 100\text{mm}$ are found suitable;

Finally, the value of the partial factor was discussed. With the proposed modifications, it is recommended to keep $\gamma_{M1} = 1.0$ for columns.

ACKNOWLEDGMENTS

The research leading to these results has received funding from:

- the European Community's Research Fund for Coal and Steel (RFCS) under grant agreement SAFEBRIC TILE RFS-PR-12103 – SEP no. 601596;
- the Portuguese Foundation for Science and Technology (FCT) under grant agreement TAPERSTEEL PTDC/ECM-EST/1970/2012 and
- the Portuguese Foundation for Science and Technology (FCT) under grant agreement SFRH/BD/99702/2014.

NOTATIONS

Latin upper case letters

A	is the gross cross sectional area;
A_{eff}	is the effective cross sectional area;
$N_{b,i,Rd}$	is the design buckling resistance about i axis of the compression member;
$N_{cr,i}$	is the critical compressive axial force for buckling about i axis;
N_{Ed}	is the design value of the axial force;
N_{Rk}	is the characteristic resistant axial force;
V_δ	Estimator for the coefficient of variation of the error term
V_X	Coefficient of variation
\underline{X}_m	Array of mean values of basic variables

Latin lower case letters

b	Correction factor
$g_{rt}(\underline{X})$	Resistance function used as a design model
$k_{d,n}$	Design fractile factor
n	Number of experiments or numerical results
r_d	Design value of the resistance
r_e	Experimental resistance value
r_n	Nominal value of the resistance
r_t	Theoretical resistance determined with $g_{rt}(\underline{X})$
s	Estimated value for the standard deviation σ
s_A	Estimated value for the standard deviation σ_A

Greek upper case letters

Δ	Logarithm of the error term δ
$\overline{\Delta}$	Estimated value for $E(\Delta)$

Greek lower case letters

α_i	is the imperfection factor for flexural buckling about i axis;
δ	Error term
δ_i	Observed error term for test specimen i
η_i	is the generalized imperfection for flexural buckling about i axis;
$\overline{\lambda}_i$	is the non-dimensional slenderness for flexural buckling about i axis;
χ_i	is the reduction factor for flexural buckling about i axis.
σ	Standard deviation
σ_A^2	Variance of the term Δ

REFERENCES

- [1] Eurocode – EN 1993-1-1, Eurocode 3: Design of Steel Structures - Part 1-1: General Rules and Rules for Buildings CEN, Brussels, 2005.
- [2] Eurocode – EN 1990, Eurocode – Basis of Structural Design, CEN, Brussels, 2002.
- [3] Simões da Silva, L., Marques, L., Tankova, T., “On the Safety of Stability Design Rules for Steel Members”, ICASS 2015, The Eight International Conference on Advances in Steel Structures, July 2015, Lisbon, Portugal
- [4] Dowling, P.J., “EC3, The New Eurocode for Steel Structures”, in IABSE Conference on Structural Eurocodes, Davos, 1992, pp.159-166.
- [5] Sfintesco, D., “Fondement Expérimental des Courbes Européennes de Flambement”, Construction Métallique, 1970, No. 3, pp. 5-12.
- [6] Beer, H. and Schulz, G., “Bases Théoriques des Courbes Européennes de Flambement”, Construction Métallique, 1970, No. 3, pp. 37-57.
- [7] Strating, J. and Vos, H., “Simulation sur Ordinateur de la Coubre C.E.E.M de Flambement à l’aide de la Méthode de Monte-Carlo”, Construction Métallique, 1973, No. 2, pp. 23-39.
- [8] Maquoi, R. and Rondal, J., “Mise en Équation des Nouvelles Courbes Européennes de Flambement”, Construction Métallique, 1978, No. 1 pp. 17-30.
- [9] Tankova, T., Simões da Silva, L., Marques, L., Rebelo, C. and Taras, A., “Towards a Standardized Procedure for the Safety Assessment of Stability Design Rules”, Journal of Constructional Steel Research, 2014, Vol. 103, pp. 290-302.
- [10] Simões da Silva, L., Rebelo C., Nethercot D. Marques, L., Simões, R. and Vila Real,

- P.M.M., “Statistical Evaluation of the Lateral-Torsional Buckling Resistance of Steel I-beams, Part 2: Variability of Steel Properties, *Journal of Constructional Steel Research*, 2009, Vol. 65, pp. 832-849.
- [11] Braconi, A., Finetto, M., Degee, H., Hausoul, N., Gundel, M., Hffmeister, B., Varelis, G., Pappa, P., Karmanos, S.A., Obiala, R., Rinaldi, V., Somja, H., Hjaij, M., Badalassi, M., Caprili, S. and Salvatore, W., “OPUS – Optimising the Seismic Performance of Steel and Steel-concrete Structures” Standardising Material Quality Control, Final Report, Research Fund for Coal and Steel, Contract Agreement RFSR-CT-2007-00039, 2013.
 - [12] CEN. European Committee for Standardization, EN 10025: 2004 – Hot Rolled Products of Structural Steels, 2004.
 - [13] Alpsten, G., “Variations in Mechanical and Cross-sectional Properties of Steel, State of the Art Report, Proceedings of the International Conference on the Planning and Design of Tall Buildings”, ASCE-IABSE, Lehigh University, August 1972.
 - [14] Taras, A., “Contribution to the Development of Consistent Stability Design Rules for Steel Members”, PhD Thesis, Technical University of Graz, Graz, Austria, 2010.
 - [15] Cajot, L.G., Haller, M., Conan, Y., Sedlacek, G., Kraus, O., Rondla, J., Cerfontaine, F., Johansson, B. and Lagerqvist, O., “PROQUA – Probabilistic Quantification of Safety of a Steel Structure Highlighting the Potential of Steel Versus Other Materials”, Final Report, Technical Steel Research, Contract No. 7210-PR/249, 2005.
 - [16] DNV, Guideline for Offshore Structural Reliability Analysis – Chapter 7, DNV Report No. 95-2018, Det Norske Veritas, Hovik, Norway, 1995.
 - [17] Abaqus, v.6.12, Dassault Systems/Simulia, Providence, RI, USA, 2012.
 - [18] ECCS, “European Recommendations for Steel Construction”, Brussels, 1978.
 - [19] Snijder, H.H., Cajot, L.G., Poppa, N. and Spoorenberg, R.C., “Buckling Curves for Heavy Wide Flange Steel Columns”, *Romanian Journal of Technical Sciences, Applied Mechanics*, 2014, Vol. 59, (1/2), pp. 178-204
 - [20] Spoorenberg, R.C., Snijder, H.H., Cajot, L.-G. and Popa, N., “Buckling Curves for Heavy Wide Flange QST Columns based on Statistical Evaluation”, *Journal of Constructional Steel Research*, 2014, Vol. 101, pp. 280-289.
 - [21] Lindner, J., “Classification of Rolled I-profiles Fabricated in Steel Grade S460 within Table 6.2 of EN 1993-1-1 - Rev.3. Report to Working Group 1-1, 21/02/2015.
 - [22] Simões da Silva, L., Simões, R., Gervásio, H. and Couchman, G., “Design of Steel Structures. Eurocode3: Design of Steel Structures. Part-1-1 - General Rules and Rules for Buildings. UK Edition ECCS - European Convention for Constructional Steelwork, John Wiley & Sons and SCI– Steel Construction Institute, 2014.
 - [23] Gulvanessian, H., Calgaro, J-A. and Holicky, M., “Designers' Guide to EN 1990. Eurocode: Basis of Design”, Thomas Telford, ISBN: 0727730118, 2002.
 - [24] Muller, C., “Zum Nachweis ebener Tragwerke aus Stahl gegen seitliches Ausweichen, PhD Dissertation”, Schriftenreihe Stahlbau - RWTH Aachen, 2003.

Annex A – Statistical Distributions for the Yield Stress

The statistical distributions of the yield stress were chosen based on real experiments. The variation adopted for S235 and S355 is based on a previously performed study at the University of Coimbra [10]. It is summarized in Table A1:

Table A1. Results from

Steel Grade	tf (mm)	fy (MPa)	n	Mean (MPa)	St. Dev (MPa)	CoV	Minimum Value (MPa)	Quantile for the nominal value	Value for 99.9% quantile
S235	≤16	235	837	310.03	31.29	10.09%	239.2	99.17	213.32
			347	279.78	18.79	6.72%	239.2	99.14	221.70
			342	297.30	17.11	5.76%	258	99.99	244.41
S275 (n=3625)	≤16	275	1991	327.93	18.96	5.78%	-	99.74	269.35
	>16 ≤40	265	2342	306.28	15.63	5.10%	-	99.59	257.97
	>40 ≤63	255	71	299.23	14.07	4.70%	-	99.92	255.74
	>63 ≤80	245	21	290.38	9.68	3.33%	-	100.00	260.46
S355 (n=1979)	≤16	355	733	419.38	20.25	4.83%	-	99.93	356.80
	>16 ≤40	345	1146	395.82	15.16	3.83%	-	99.96	348.96
	>40 ≤63	335	77	380.51	10.01	2.63%	-	100.00	349.58
	>63 ≤80	325	23	361.87	10.25	2.83%	-	99.98	330.20

For S460, recent results from OPUS [15] were used. They are summarized in Table A2.

Table A2. Results from OPUS

Steel Grade	tf (mm)	fy (MPa)	n	Mean (MPa)	St. Dev (MPa)	CoV	Minimum Value (MPa)	Quantile for the nominal value	Value for 99.9% quantile
S460 (n=982)	<16	460	113	495.26	17.2	3.47%	not available	97.98	442.11
	>16 ≤40	440	778	520.88	26.8	5.15%		99.87	438.06
	>40 ≤63	430	91	486.4	43.5	8.94%		90.26	351.97

Annex B - Results

Table B1. All Results for Minor and Major Axis of Hot-rolled Sections, Normalized γ_{M1} with respect to the Average Value for S235/S355 $t_f \leq 40\text{mm}$, $h/b > 1.2$ and Major Axis of Flexural Buckling (the Values in Green)

Sub-set		Minor axis					Major axis		
		n	EN10025	EN10025(S460)	EN10025		EN10025		
					f_{yi}	EC3	EN10025	f_{yi}	EC3
Total		1833	1.113	1.039	1.198	1.146	1.033	1.055	1.062
Low		564	1.056	1.003	-	-	0.993	-	-
Medium		705	1.127	1.022	-	-	1.012	-	-
High		564	1.075	0.997	-	-	1.021	-	-
S235		611	1.032	1.032	1.032	1.058	0.995	0.995	1.020
S355		611	0.988	0.988	1.033	1.010	0.993	1.001	1.013
S460		611	1.127	1.034	1.247	1.174	1.034	1.062	1.073
S235	Low	188	0.983	0.983	0.983	1.016	0.951	0.951	0.985
	Medium	235	1.025	1.025	1.025	1.045	0.980	0.980	0.999
	High	188	0.996	0.996	0.996	1.003	0.996	0.996	1.000
S355	Low	188	0.960	0.960	0.997	0.988	0.966	0.973	0.995
	Medium	235	0.944	0.944	1.008	0.960	0.948	0.970	0.960
	High	188	0.957	0.957	0.975	0.961	0.983	0.986	0.986
S460	Low	188	1.089	1.019	1.183	1.153	1.030	1.051	1.082
	Medium	235	1.142	0.998	1.275	1.175	1.012	1.057	1.035
	High	188	1.076	0.980	1.126	1.082	1.014	1.022	1.017
S235	$h/b > 1.2 \quad t_f < 40\text{mm}$	169	1.033	1.033	1.033	1.102	1.005	1.005	1.077
	$h/b > 1.2 t_f(40;100)\text{mm}$	169	0.953	0.953	0.953	0.953	0.951	0.951	0.951
	$h/b > 1.2 \quad t_f > 100\text{mm}$	104	0.990	0.990	0.990	0.990	0.961	0.961	0.961
	$h/b \leq 1.2 \quad t_f < 100\text{mm}$	169	1.074	1.074	1.074	1.097	0.985	0.985	1.006
S355	$h/b > 1.2 \quad t_f < 40\text{mm}$	169	0.988	0.988	1.034	1.029	0.995	1.009	1.036
	$h/b > 1.2 t_f(40;100)\text{mm}$	169	0.940	0.940	0.962	0.962	0.962	0.965	0.982
	$h/b > 1.2 \quad t_f > 100\text{mm}$	104	0.961	0.961	0.981	0.961	0.966	0.968	0.966
	$h/b \leq 1.2 \quad t_f < 100\text{mm}$	169	1.011	1.011	1.070	1.043	0.980	0.985	1.009
S460	$h/b > 1.2 \quad t_f < 40\text{mm}$	169	1.147	1.049	1.270	1.223	1.041	1.084	1.120
	$h/b > 1.2 t_f(40;100)\text{mm}$	169	1.064	0.987	1.155	1.115	1.006	1.017	1.048
	$h/b > 1.2 \quad t_f > 100\text{mm}$	104	1.006	1.006	1.064	1.006	1.013	1.027	1.013
	$h/b \leq 1.2 \quad t_f < 100\text{mm}$	169	1.146	1.052	1.332	1.213	1.032	1.074	1.090
S235	$0 < t_f \leq 16$	91	1.032	1.032	1.032	1.032	0.996	0.996	0.996
	$16 < t_f \leq 40$	182	1.043	1.043	1.043	1.120	1.026	1.026	1.099
	$40 < t_f \leq 63$	91	1.004	1.004	1.004	1.004	0.965	0.965	0.965
	$63 < t_f \leq 80$	117	1.042	1.042	1.042	1.042	0.977	0.977	0.977
	$80 < t_f \leq 100$	26	1.061	1.061	1.061	1.061	0.982	0.982	0.982
	$t_f > 100$	104	0.990	0.990	0.990	0.990	0.961	0.961	0.961
S355	$0 < t_f \leq 16$	91	0.995	0.995	1.044	0.995	0.998	1.002	0.998
	$16 < t_f \leq 40$	182	1.012	1.012	1.047	1.058	1.032	1.031	1.076
	$40 < t_f \leq 63$	91	0.955	0.955	1.000	0.955	0.964	0.972	0.964
	$63 < t_f \leq 80$	117	0.977	0.977	1.034	1.020	0.971	0.985	1.012
	$80 < t_f \leq 100$	26	0.993	0.993	1.051	0.993	0.972	0.986	0.972
	$t_f > 100$	104	0.961	0.961	0.981	0.961	0.966	0.968	0.966
S460	$0 < t_f \leq 16$	91	1.137	1.060	1.305	1.137	1.041	1.071	1.041
	$16 < t_f \leq 40$	182	1.152	1.066	1.287	1.243	1.067	1.091	1.148
	$40 < t_f \leq 63$	91	1.077	1.000	1.202	1.077	1.009	1.035	1.009
	$63 < t_f \leq 80$	117	1.105	1.000	1.250	1.197	1.016	1.053	1.095
	$80 < t_f \leq 100$	26	1.121	1.035	1.278	1.121	1.021	1.063	1.021
	$t_f > 100$	104	1.006	1.006	1.064	1.006	1.013	1.027	1.013

Notations:

- EN 10025 – minimum yield stress according to EN 10025
- EN 10025 (S460) - minimum yield stress according to EN 10025 and new buckling curves for S460;
- EN 10025 f_{yi} – yield stress proportional to f_y ;
- EC3 - minimum yield stress according to EN 10025;

Table B2 All Results for Minor and Major Axis of Hot-rolled Sections, normalized γ_{M1} with the Average Value for S235/S355 $t_f \leq 40\text{mm}$, $h/b > 1.2$ and Major Axis of Flexural Buckling (the Values in Green in Table B1)

Sub-set				Minor axis		Major axis	
			n	EN10025	EN10025 f_{yi}	EN10025	EN10025 f_{yi}
S355	$h/b > 1.2$ $t_f < 40\text{mm}$	Low	52	0.971	1.001	0.981	0.992
		Medium	65	0.950	1.007	0.949	0.974
		High	52	0.960	0.970	0.980	0.984
	$h/b > 1.2$ $t_f(40;100)\text{mm}$	Low	52	0.925	0.942	0.949	0.950
		Medium	65	0.874	0.910	0.874	0.886
		High	52	0.917	0.922	0.942	0.946
	$h/b > 1.2$ $t_f > 100\text{mm}$	Low	32	0.937	0.949	0.949	0.951
		Medium	40	0.881	0.911	0.879	0.889
		High	32	0.912	0.917	0.944	0.945
	$h/b \leq 1.2$ $t_f < 100\text{mm}$	Low	52	0.975	1.011	0.958	0.964
		Medium	65	0.940	1.022	0.906	0.943
		High	52	0.923	0.943	0.947	0.954
S460	$h/b > 1.2$ $t_f < 40\text{mm}$	Low	52	1.123	1.204	1.054	1.080
		Medium	65	1.147	1.271	1.022	1.074
		High	52	1.067	1.113	1.009	1.022
	$h/b > 1.2$ $t_f(40;100)\text{mm}$	Low	52	1.061	1.121	1.014	1.026
		Medium	65	1.058	1.150	0.953	0.978
		High	52	1.012	1.047	0.983	0.987
	$h/b > 1.2$ $t_f > 100\text{mm}$	Low	32	1.000	1.035	1.019	1.031
		Medium	40	0.945	1.018	0.962	0.989
		High	32	0.954	0.965	0.983	0.986
	$h/b \leq 1.2$ $t_f < 100\text{mm}$	Low	52	1.116	1.241	1.033	1.062
		Medium	65	1.126	1.312	0.987	1.067
		High	52	1.022	1.118	0.988	1.002

Notations:

- EN 10025 – minimum yield stress according to EN 10025
- EN 10025 f_{yi} – yield stress proportional to f_y ;

Table B3. Normalized Partial Safety Factors, Minor and Major Axis Flexural Buckling, according to Buckling Curves

Sub-set	Minor axis					Major axis		
	n	Annex D (fy)	Annex D (fy+CS)	Annex D (fy+CS+E _{5%})	Annex D (fy+CS+E _{3%})	Annex D (fy)	Annex D (fy+CS)	Annex D (fy+CS+E)
Total	1833	1.039	1.091	1.121	1.102	1.033	1.069	1.104
Low	564	1.003	1.036	1.042	1.038	0.998	1.024	1.029
Medium	705	1.022	1.074	1.104	1.085	1.017	1.052	1.089
High	564	0.997	1.071	1.126	1.092	1.026	1.076	1.143
S235	611	1.032	1.089	1.123	1.102	0.995	1.033	1.071
S355	611	0.988	1.041	1.072	1.053	0.993	1.028	1.062
S460	611	1.033	1.090	1.122	1.102	1.034	1.077	1.120
S235	Low	188	0.983	1.017	1.025	0.951	0.976	0.983
	Medium	235	1.025	1.083	1.118	0.980	1.018	1.058
	High	188	0.996	1.080	1.139	0.996	1.050	1.120
S355	Low	188	0.960	0.995	1.002	0.966	0.992	0.998
	Medium	235	0.944	1.001	1.034	0.948	0.984	1.021
	High	188	0.957	1.033	1.088	0.983	1.032	1.097
S460	Low	188	1.019	1.054	1.059	1.030	1.058	1.062
	Medium	235	0.998	1.056	1.091	1.012	1.055	1.101
	High	188	0.980	1.062	1.122	1.014	1.078	1.158
S235	h/b>1.2 t _r <40mm	169	1.033	1.108	1.151	1.125	1.005	1.062
	h/b>1.2 t _r (40;100)mm	169	0.953	1.021	1.060	1.037	0.951	0.992
	h/b>1.2 t _r >100mm	104	0.990	1.052	1.089	1.066	0.961	1.000
	h/b≤1.2 t _r <100mm	169	1.074	1.143	1.181	1.157	0.985	1.035
S355	h/b>1.2 t _r <40mm	169	0.988	1.061	1.101	1.077	0.995	1.047
	h/b>1.2 t _r (40;100)mm	169	0.940	0.997	1.032	1.011	0.962	0.997
	h/b>1.2 t _r >100mm	104	0.961	1.017	1.049	1.029	0.966	0.999
	h/b≤1.2 t _r <100mm	169	1.011	1.073	1.107	1.086	0.980	1.023
S460	h/b>1.2 t _r <40mm	169	1.049	1.117	1.156	1.132	1.041	1.104
	h/b>1.2 t _r (40;100)mm	169	0.987	1.047	1.083	1.061	1.006	1.052
	h/b>1.2 t _r >100mm	104	1.006	1.069	1.106	1.084	1.013	1.055
	h/b≤1.2 t _r <100mm	169	1.052	1.114	1.147	1.126	1.032	1.084

Table B4. Normalized Partial Safety Factors, Minor Axis Flexural Buckling, according to Buckling Curves and Slenderness

Sub-set			Minor axis				Major axis			
			n	Annex D (fy)	Annex D (fy+CS)	Annex D (fy+CS+E5%)	Annex D (fy+CS+E3%)	Annex D (fy)	Annex D (fy+CS)	Annex D (fy+CS+E)
S235	h/b>1.2 tr<40mm	Low	52	0.990	1.029	1.037	1.032	0.972	1.001	1.007
		Medium	65	1.023	1.106	1.154	1.125	0.988	1.053	1.111
		High	52	0.991	1.118	1.191	1.147	0.993	1.087	1.175
	h/b>1.2 tr(40;100)mm	Low	52	0.926	0.961	0.971	0.964	0.924	0.948	0.955
		Medium	65	0.931	1.005	1.049	1.022	0.894	0.947	0.996
		High	52	0.936	1.043	1.108	1.069	0.949	1.017	1.092
	h/b>1.2 tr>100mm	Low	32	0.944	0.982	0.992	0.986	0.933	0.957	0.965
		Medium	40	0.950	1.022	1.063	1.038	0.909	0.958	1.010
		High	32	0.940	1.041	1.105	1.067	0.952	1.014	1.093
	h/b≤1.2 tr<100mm	Low	52	1.011	1.058	1.068	1.061	0.949	0.982	0.990
		Medium	65	1.049	1.126	1.170	1.143	0.964	1.019	1.070
		High	52	0.985	1.101	1.169	1.128	0.970	1.046	1.125
S355	h/b>1.2 tr<40mm	Low	52	0.971	1.010	1.018	1.013	0.981	1.012	1.017
		Medium	65	0.950	1.034	1.079	1.052	0.949	1.015	1.070
		High	52	0.960	1.074	1.144	1.102	0.980	1.064	1.149
	h/b>1.2 tr(40;100)mm	Low	52	0.925	0.959	0.967	0.962	0.949	0.972	0.978
		Medium	65	0.874	0.946	0.987	0.962	0.874	0.922	0.967
		High	52	0.917	1.007	1.067	1.031	0.942	1.001	1.072
	h/b>1.2 tr>100mm	Low	32	0.937	0.973	0.982	0.976	0.949	0.974	0.980
		Medium	40	0.881	0.952	0.991	0.967	0.879	0.925	0.972
		High	32	0.912	1.001	1.060	1.024	0.944	0.997	1.070
	h/b≤1.2 tr<100mm	Low	52	0.975	1.020	1.029	1.023	0.958	0.991	0.998
		Medium	65	0.940	1.014	1.053	1.029	0.906	0.961	1.009
		High	52	0.923	1.023	1.085	1.048	0.947	1.012	1.085
S460	h/b>1.2 tr<40mm	Low	52	1.041	1.079	1.083	1.080	1.054	1.084	1.087
		Medium	65	1.017	1.092	1.136	1.109	1.022	1.092	1.152
		High	52	0.982	1.080	1.149	1.107	1.009	1.109	1.202
	h/b>1.2 tr(40;100)mm	Low	52	0.984	1.017	1.024	1.020	1.014	1.040	1.044
		Medium	65	0.934	1.004	1.045	1.020	0.953	1.011	1.063
		High	52	0.952	1.039	1.101	1.064	0.983	1.060	1.144
	h/b>1.2 tr>100mm	Low	32	1.000	1.037	1.043	1.039	1.019	1.045	1.050
		Medium	40	0.945	1.021	1.063	1.037	0.962	1.013	1.067
		High	32	0.954	1.057	1.124	1.084	0.983	1.054	1.140
	h/b≤1.2 tr<100mm	Low	52	1.028	1.072	1.079	1.075	1.033	1.068	1.073
		Medium	65	0.979	1.050	1.090	1.065	0.987	1.048	1.102
		High	52	0.944	1.037	1.099	1.062	0.988	1.070	1.155

Table B5. Partial Safety Factors, Minor Axis Flexural Buckling, according to Buckling Curves

Sub-set	Minor axis					Major axis		
	n	Annex D (fy)	Annex D (fy+CS)	Annex D (fy+CS+E)	Annex D (fy)	Annex D (fy+CS)	Annex D (fy+CS+E)	
S235	h/b>1.2 t _r <40mm	169	1.012	1.085	1.127	0.984	1.040	1.090
	h/b>1.2 t _r (40;100)mm	169	0.934	1.000	1.039	0.932	0.972	1.012
	h/b>1.2 t _r ≥100mm	104	0.969	1.031	1.067	0.942	0.979	1.022
	h/b≤1.2 t _r <100mm	169	1.052	1.119	1.157	0.965	1.014	1.058
S355	h/b>1.2 t _r <40mm	169	0.968	1.039	1.079	0.975	1.026	1.072
	h/b>1.2 t _r (40;100)mm	169	0.920	0.977	1.011	0.942	0.976	1.011
	h/b>1.2 t _r ≥100mm	104	0.941	0.996	1.028	0.946	0.978	1.015
	h/b≤1.2 t _r <100mm	169	0.990	1.051	1.084	0.960	1.002	1.040
S460	h/b>1.2 t _r <40mm	169	1.028	1.094	1.133	1.020	1.081	1.132
	h/b>1.2 t _r (40;100)mm	169	0.967	1.025	1.060	0.985	1.030	1.074
	h/b>1.2 t _r ≥100mm	104	0.985	1.047	1.084	0.992	1.034	1.078
	h/b≤1.2 t _r <100mm	169	1.030	1.091	1.124	1.011	1.062	1.107

Table B6. Partial Safety Factors, Minor Axis Flexural Buckling, according to Buckling Curves and Slenderness, c.o.v. of Modulus of Elasticity 5%

Sub-set			Minor axis				Major axis		
			n	Annex D (fy)	Annex D (fy+CS)	Annex D (fy+CS+E)	Annex D (fy)	Annex D (fy+CS)	Annex D (fy+CS+E)
S235	h/b>1.2 tr<40mm	Low	52	0.970	1.008	1.015	0.952	0.981	0.987
		Medium	65	1.002	1.083	1.131	0.967	1.031	1.088
		High	52	0.970	1.095	1.167	0.972	1.064	1.151
	h/b>1.2 tr(40;100)mm	Low	52	0.907	0.941	0.951	0.905	0.929	0.936
		Medium	65	0.912	0.985	1.027	0.875	0.927	0.976
		High	52	0.917	1.021	1.086	0.930	0.996	1.070
	h/b>1.2 tr>100mm	Low	32	0.925	0.962	0.972	0.913	0.938	0.945
		Medium	40	0.931	1.001	1.041	0.890	0.938	0.989
		High	32	0.921	1.020	1.083	0.932	0.993	1.070
	h/b≤1.2 tr<100mm	Low	52	0.990	1.036	1.046	0.929	0.962	0.969
		Medium	65	1.027	1.103	1.146	0.944	0.998	1.048
		High	52	0.965	1.078	1.145	0.950	1.024	1.102
S355	h/b>1.2 tr<40mm	Low	52	0.951	0.990	0.997	0.961	0.991	0.996
		Medium	65	0.930	1.013	1.057	0.930	0.994	1.048
		High	52	0.940	1.052	1.120	0.960	1.042	1.125
	h/b>1.2 tr(40;100)mm	Low	52	0.906	0.939	0.947	0.929	0.952	0.958
		Medium	65	0.856	0.927	0.966	0.856	0.903	0.947
		High	52	0.898	0.987	1.045	0.923	0.981	1.050
	h/b>1.2 tr>100mm	Low	32	0.917	0.953	0.962	0.930	0.954	0.960
		Medium	40	0.863	0.932	0.970	0.860	0.906	0.952
		High	32	0.894	0.980	1.038	0.924	0.977	1.048
	h/b≤1.2 tr<100mm	Low	52	0.955	0.999	1.008	0.939	0.971	0.978
		Medium	65	0.921	0.993	1.032	0.888	0.942	0.988
		High	52	0.904	1.002	1.063	0.927	0.991	1.063
S460	h/b>1.2 tr<40mm	Low	52	1.020	1.056	1.061	1.032	1.062	1.065
		Medium	65	0.996	1.069	1.113	1.001	1.069	1.128
		High	52	0.962	1.058	1.125	0.988	1.087	1.177
	h/b>1.2 tr(40;100)mm	Low	52	0.964	0.996	1.003	0.993	1.018	1.022
		Medium	65	0.915	0.983	1.023	0.933	0.990	1.041
		High	52	0.933	1.018	1.079	0.962	1.038	1.120
	h/b>1.2 tr>100mm	Low	32	0.980	1.016	1.022	0.998	1.024	1.028
		Medium	40	0.926	1.000	1.041	0.942	0.992	1.045
		High	32	0.934	1.035	1.101	0.962	1.032	1.116
	h/b≤1.2 tr<100mm	Low	52	1.007	1.050	1.057	1.012	1.046	1.051
		Medium	65	0.959	1.029	1.067	0.967	1.027	1.079
		High	52	0.924	1.016	1.077	0.967	1.048	1.131

ICSAS 2016

The organizing committee is pleased to announce The Eighth International Conference on Steel and Aluminium Structures (ICSAS) 2016 to be held in Hong Kong, a dynamic metropolitan with thriving construction industry.

Introduction

Seven ICSAS Conferences have been successfully held in Cardiff, UK (1987), Singapore (1991), Istanbul, Turkey (1995), Helsinki, Finland (1999), Sydney, Australia (2003), Oxford, UK (2007) and Kuching, Malaysia (2011). The conference aims at bringing international experts and leaders together to disseminate recent research findings in the fields of steel and aluminium structures. It will also provide a forum for the discussion of the developments in the design and construction of steel and aluminium structures.

Who Should Attend

Steel and aluminium structure designers and manufacturers, trade associations, design engineers, steel fabricators, architects, owners or developers of steel and aluminium structures, researchers, academics and post-graduate students.

Key Dates

Abstract Submission	November 30, 2015
Acceptance of Abstract	January 15, 2016
Full Paper Submission	April 15, 2016
Acceptance of Full Paper	August 15, 2016
Conference	December 7–9, 2016

An aerial photograph of the Hong Kong skyline, showing a dense cluster of skyscrapers and buildings along the coast, with the Victoria Harbour in the background. The image is used as a background for the conference announcement.

**8TH INTERNATIONAL CONFERENCE ON STEEL AND ALUMINIUM STRUCTURES
DECEMBER 7 – 9, 2016 HONG KONG**

Call for Papers

Prospective authors are invited to submit abstracts before **November 30, 2015**, on the topics as follows (but not limited to):

- Analysis and Design of:
 - Structural Steel
 - Stainless Steel
 - Aluminium Alloy
- Architectural Uses
- Cold-formed Steel Structures
- Composite Structures
- Computational Modelling and Analysis
- Connection Behaviour
- Earthquake and Seismic Analysis
- Fire Engineering
- Material Properties and Structural Reliability
- Plates and Shell Structures
- Scaffoldings and Racks
- Specification and Standard Developments
- Sustainable Development
- Tubular Structures

Abstracts should be submitted electronically via the conference website: www.civil.hku.hk/ICSAS2016

Exhibition

Booths will be organised for exhibitors during the Conference, allowing companies and associations an excellent opportunity for marketing and promotion.

For exhibition information contact:
Prof. Ben Young
Department of Civil Engineering
The University of Hong Kong
Email: young@hku.hk

Prizes

Three papers will be selected for the following awards:

- *Best Steel Structures Paper Award*
- *Best Aluminium Structures Paper Award*
- *Best Composite Structures Paper Award*

Organised by

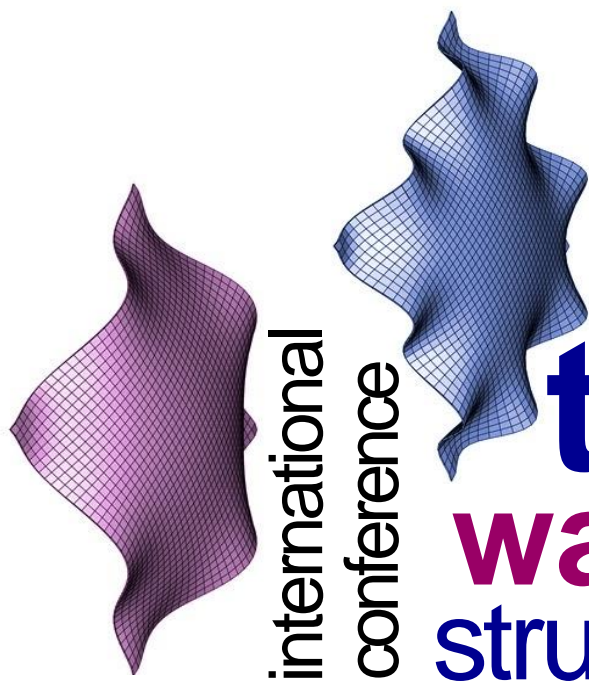
Department of Civil Engineering
The University of Hong Kong



The University of Hong Kong



www.civil.hku.hk/ICSAS2016



international
conference

thin walled structures

July 24-27, 2018 ● Lisbon, Portugal





Lisbon is a city with intense light and a deep blue sky. The almost constant presence of sunshine and the River Tagus transform the Portuguese capital into a mirror of a thousand colours that highlight the city's distinctive architecture and beauty.

Lisbon offers a wide array of different experiences: walks through ancient neighbourhoods, heritage monuments and riverfront leisure, pleasant strolls and stays in gardens, belvederes and esplanades, exciting nightlife, and unique gastronomy.

Key Dates

Abstract submission:

30 September 2017

Abstract acceptance:

15 November 2017

Full paper submission:

1 February 2018

Full paper acceptance:

31 March 2018

For further information

Prof. Dinar Camotim:

dcamotim@civil.ist.utl.pt

Prof. Nuno Silvestre:

nsilvestre@ist.utl.pt



**ORDER
FORM**

ISSN 1816-112X

**Advanced Steel Construction,
an international journal**Indexed by the Science Citation Index Expanded,
Materials Science Citation Index and ISI Alerting Services**From:****To:** Secretariat, Advanced Steel Construction, an international journal
Fax: (852) 2334-6389

I/ We would like to enter a subscription to the *International Journal of Advanced Steel Construction (IJASC)* published by The Hong Kong Institute of Steel Construction.

Please complete the form and send to:

International Journal of Advanced Steel Construction
c/o Department of Civil and Environmental Engineering
The Hong Kong Polytechnic University
Hung Hom, Kowloon, Hong Kong

Fax: (852) 2334-6389 Email: ceslchan@polyu.edu.hk

Published by : The Hong Kong Institute of Steel Construction
Website: <http://www.hkisc.org/>

Please tick the appropriate box

- ☐ Please enter my hard-copy subscription (**4 issues per year**).
☐ Please send me a complimentary copy of the *Advanced Steel Construction, an International Journal (IJASC)*.

Please tick the appropriate box(es)

	<u>Print</u>	<u>On-line is free</u>
Personal	<input type="checkbox"/> US\$ 125	
Institutional	<input type="checkbox"/> US\$ 280	

Total Amount US\$ _____

Methods of payment ☐ Please invoice me
(please tick the appropriate box(es)) ☐ Cheque enclosed for US\$ _____ payable to
Hong Kong Institute of Steel Construction Limited
(No personal cheque accepted)

Ship to

Name (Prof./ Dr./ Mr./ Ms.) _____
Address _____

City/ State/ Postal Code _____
Country _____
Email _____ Fax _____